IMPERIAL COLLEGE LONDON

DOCTORAL THESIS

Mathematical modelling of misfolded protein aggregation in neurodegenerative diseases using *in vivo* PET data

Author:
Alexander WHITTINGTON

Supervisor:
Prof. Roger N. GUNN
Prof. David J. SHARP

A thesis submitted in fulfillment of the requirements
for the degree of Doctor of Philosophy

in the

Division of Brain Sciences

June 21, 2018

Declaration of Authorship

I, Alexander WHITTINGTON, declare that this thesis titled, "Mathematical modelling of misfolded protein aggregation in neurodegenerative diseases using *in vivo* PET data" and the work presented in it are my own. I confirm that:

- This work was done wholly or mainly while in candidature for a research degree at this University.
- Where I have consulted the published work of others, this is always clearly attributed.
- Where I have quoted from the work of others, the source is always given. With the exception of such quotations, this thesis is entirely my own work.
- I have acknowledged all main sources of help.
- Where the thesis is based on work done by myself jointly with others, I have made clear exactly what was done by others and what I have contributed myself.

'The copyright of this thesis rests with the author and is made available under a Creative Commons Attribution Non-Commercial No Derivatives licence. Researchers are free to copy, distribute or transmit the thesis on the condition that they attribute it, that they do not use it for commercial purposes and that they do not alter, transform or build upon it. For any reuse or redistribution, researchers must make clear to others the licence terms of this work.'

"Supposing a tree fell down, Pooh, when we were underneath it?"

"Supposing it didn't," said Pooh after careful thought. "

A. A. Milne

IMPERIAL COLLEGE LONDON

Abstract

Faculty of Medicine

Division of Brain Sciences

Doctor of Philosophy

Mathematical modelling of misfolded protein aggregation in neurodegenerative diseases using *in vivo* PET data

by Alexander WHITTINGTON

Positron emission tomography (PET) is an imaging modality widely used in the study of neurodegeneration to image the accumulation of the misfolded proteins such as amyloid-β (Aβ) and tau. The aims of this thesis were to investigate Aβ accumulation in Alzheimer's disease (AD) using mathematical modelling and perform kinetic modelling of the novel tau radiotracer [^{18}F]-AV1451 in corticobasal degeneration (CBD) and traumatic brain injury (TBI). The main contributions of this thesis are:

Aβ - Modelling the spatiotemporal distribution of Aβ in AD

The spatiotemporal distribution of Aβ in AD was modelled using a network diffusion model and a four-parameter logistic growth model. Results suggest the spatiotemporal distribution of Aβ in AD results from properties of the local tissue environment rather than long-term spreading from seed regions.

Aβ - Amyloid Load

Using parametric images derived from the logistic growth model, a new outcome measure, amyloid load $A\beta_L$ was defined for a single [^{18}F]-AV45 Aβ PET

scan. It had greater sensitivity than the currently used mean cortical SUVr outcome measure and will improve the power to detect signal changes in future trials of novel anti-Aβ therapeutics.

Tau - Kinetic modelling of [^{18}F]-AV1451

Dynamic [^{18}F]-AV1451 PET data from a CBD study was effectively modelled with a reversible two-tissue compartmental model, the simplified reference tissue model (SRTM) and standardised uptake value ratio (SUVr). SRTM was used to quantify [^{18}F]-AV1451 uptake in a TBI study consisting of 32 subjects. There were no differences between patients and controls at the ROI level and the voxel level analysis revealed heterogeneous radiotracer uptake amongst patients. It is impossible to tell whether increased PET signal is due to tau or off-target binding.

Acknowledgements

This work was made possible by joint funding from the Medical Reasearch Council and Imanova Ltd.

I owe a great debt of gratitude to my supervisors, Professor Roger N. Gunn and Professor David J. Sharp, for their guidance and support during this project. Roger, your door was always open and your enthusiasm was one of the main reasons this turned out to be such an enjoyable project to work on. David, I thank you for the many helpful discussions and the opportunity you provided for me to broaden my knowledge beyond mathematical modelling.

To everyone at both C3NL and Imanova, thank you for your advice, support, understanding and encouragement. I was very lucky to be able to work in such a positive and kind environment. I owe particular thanks to Ayla Winklemann, Lysia Demetriou, Nick Keat, Graham Searle, Phil Noonan, Christopher Coello, Gaia Rizzo, John McGonigle and Courtney Bishop who were always around to offer encouragement and many of whom selflessly gave up hours of their time to teach me over the past three years.

This thesis would have never been completed without my friends who kept me laughing even when things weren't going as well as I had hoped. Thank you Adam, Chris, Lewis and Jim for all the weekends away and my teammates at COXA football club - I always looked forward to Saturdays. I am also greatly indebted to Ayla and Moritz and Lewis and Emily for all the amazing hospitality they provided whilst I was writitng up.

Finally, I wish to thank my parents and my brother Will for their everlasting love and care regardless of the situation.

Contents

Declaration of Authorship 3

Abstract 7

Acknowledgements 9

Contents 11

1 Magnetic resonance imaging and positron emission tomography 31

1.1 MRI . . . 32

1.1.1 Segmentation of structural MRI images into tissue types . 33

1.1.2 Diffusion tensor imaging . . . 34

1.2 PET . . . 37

1.2.1 PET signal and image reconstruction . . . 37

1.2.2 Subject motion in PET . . . 40

1.3 Quantification methods in PET . . . 41

1.3.1 Image registration . . . 41

1.3.2 Motion-correction, delineation of regions of interest and generation of time-activity curves . . . 42

1.3.3 Model-driven quantification of PET data . . . 44

1.3.4 Outcome parameters quantifying radiotracer uptake . . . 49

1.3.5 Simplified reference tissue model . . . 51

1.3.6 Standardised uptake tissue ratio . . . 54

1.3.7 Parametric images . . . 54

1.4 Conclusion . . . 55

2 PET in Alzheimer's disease, traumatic brain injury and corticobasal degeneration 57

2.1 Alzheimer's disease . . . 58
2.1.1 Pathophysiology of AD . . . 58
2.2 Aβ imaging in AD using PET . . . 61
2.3 Spatiotemporal modelling of Aβ in AD . . . 63
2.3.1 Spatiotemporal distribution of Aβ in AD . . . 63
2.3.2 Heterogeneity in Aβ concentration: spreading from seed regions or a result of differences in properties of the local tissue environment? . . . 65
2.3.3 Previous mathematical models for the spatiotemporal distribution of Aβ in AD . . . 66
2.4 Corticobasal degeneration . . . 68
2.5 Traumatic brain injury . . . 69
2.6 Imaging tau *in vivo* using PET . . . 71
2.6.1 Tau in neurodegenerative diseases . . . 71
2.6.2 Radiotracer design for tau PET . . . 73
2.6.3 [^{18}F]AV1451 in AD and non-AD studies . . . 77
2.7 Outline of the remainder of the thesis . . . 82

3 Datasets and preprocessing **85**
3.1 Static [^{18}F]AV45 Aβ PET imaging data . . . 85
3.1.1 Alzheimer's disease neuroimaging initiative . . . 85
Cross-sectional ADNI dataset . . . 86
Longitudinal ADNI dataset . . . 87
3.1.2 Dallas lifespan brain study . . . 87
3.1.3 Spatial normalisation of static [^{18}F]AV45 Aβ images into MNI152 space . . . 88
3.2 Calculating regional SUVr . . . 89
3.3 Dynamic [^{18}F]AV1451 PET imaging data . . . 89
3.3.1 Tau in CBD . . . 90
3.3.2 Tau in TBI . . . 91
3.4 Preprocessing and motion correction of [^{18}F]AV1451 PET images 91
3.4.1 Isotropic images . . . 91

3.4.2 Motion correction 92
3.4.3 Overview of subjects included in kinetic modelling of [^{18}F]AV1451 in CBD analysis (Chapter 7) 94
3.4.4 Overview of subjects included in kinetic modelling of [^{18}F]AV1451 in TBI (Chapter 8) 95
3.5 Conclusion 97

4 Spatiotemporal Modelling of Misfolded Proteins using a Network Diffusion Model 99
4.1 Outline and aims 99
4.2 Modelling the brain as a weighted graph 100
4.3 Network diffusion model 101
4.4 Investigating the model space 102
4.5 Creation of a dataset representing the spatiotemporal distribution of Aβ at the population level 103
4.5.1 Fitting the model to the chronological dataset 104
4.6 Results 105
4.6.1 Calculating t^* 105
4.6.2 Identifying the most parsimonious model 105
4.7 Limitations 107
4.7.1 Network diffusion model on a weighted graph 109
4.7.2 The parameter $Age - t^*$ 109
4.7.3 The optimum network diffusion model 110
4.8 Conclusion 111

5 Spatiotemporal modelling of Aβ using a four-parameter logistic growth model 113
5.1 Aims and outline 114
5.2 Logistic growth model of Aβ accumulation 114
5.3 Construction of a chronological dataset 115
5.3.1 Transformation of the functional form for use with [^{18}F]AV45 data 118

5.3.2 Finding the time through the disease process, t_i and generation of the chronological dataset . . . 119
5.4 Model space . . . 122
5.4.1 Fitting the logistic growth model to the chronological dataset and investigation of the model space . . . 124
5.5 ROI level results . . . 124
5.6 Alternative brain parcellations . . . 126
5.7 Parametric imaging . . . 126
5.8 Discussion . . . 133
5.9 Conclusion . . . 135

6 Amyloid load, $A\beta_L$: a novel outcome measure for the global Aβ burden in AD 137
6.1 Quantifying Aβ burden using mean cortical SUVr . . . 137
6.1.1 Limitations of mean cortical SUVr . . . 138
6.2 Aims and outline . . . 139
6.3 Definition of Amyloid Load, $A\beta_L$ . . . 139
6.4 Automated method of calculating $A\beta_L$ . . . 141
6.5 Evaluating **SUVr**$_{fit}$ images . . . 142
6.5.1 ADNI cross-sectional data . . . 142
6.5.2 Dallas lifespan study . . . 144
6.5.3 Using the difference image to QC the quality of **SUVr**$_{fit}$ in future studies . . . 144
6.6 $A\beta_L$ as an outcome measure in the cross-sectional ADNI data . . . 146
6.6.1 ns in the cross-sectional ADNI data . . . 149
6.7 $A\beta_L$ as an outcome measure in ADNI longitudinal data . . . 149
6.8 Discussion . . . 151
6.9 Conclusion . . . 153

7 Kinetic analysis of [^{18}F]AV1451 Tau PET 155
7.1 Aims and outline . . . 155
7.2 Optimum modelling pipeline for quantitative [^{18}F]AV1451 analysis 156
7.2.1 Determination of arterial plasma parent input function . . . 156

Blood data from a dynamic PET scan 156
Modelling blood data to create an arterial input function . 157
7.2.2 Generation of TACs 160
7.2.3 Optimum kinetic model 162
7.2.4 Grey matter cerebellum as a reference region 163
7.2.5 V_T and BP_{ND} in CBD and healthy controls 165
7.3 Validation of SRTM 166
7.4 Validation of SUVr 169
7.4.1 Finding the optimum SUVr time window 169
7.4.2 Assessing the optimum SUVr time window using individual scan time stability analysis 171
7.5 Conclusion 174

8 Application of Tau PET quantification to tau accumulation following a TBI 177

8.1 Aims and outline 177
8.2 Definition of regions of interest 178
8.2.1 Definition of grey matter 178
8.2.2 Registration of atlas image to individual MR space 178
8.2.3 Reference region 179
8.2.4 Target regions 179
8.3 Region of interest analysis using SRTM 180
8.3.1 SRTM fits to TACs 180
8.3.2 Distributions of BP_{ND} in healthy controls and TBI 181
8.4 Voxel-level analysis 183
8.4.1 Voxel level fitting of SRTM 184
8.4.2 Parametric BP_{ND} images 184
8.4.3 Z-score images 188
Characterising the normal distribution of healthy controls 188
Generating Z-score images for TBI subjects 188
8.4.4 Group comparison of Z-scores 190
8.5 Discussion 193

8.5.1 Quantifying specific binding of [^{18}F]AV1451 with the SRTM 195
8.5.2 Tracer specific binding in TBI 196
8.5.3 Quantifying tau in TBI with [^{18}F]AV1451 197
8.6 Conclusion 198

9 Conclusions and future work **201**

A List of PPF models fitted **205**

B Permissions summary table **207**

List of Figures

1.1 MRI images and 3 tissue probability maps after the MRI has been segmented. (GM: Grey matter, WM: White matter, CSF: cerebrospinal fluid) 35
1.2 An example tractography image generated from diffusion tensor imaging data (Image taken from O'Donnell and Westin 2011) . . . 36
1.3 Particle interactions leading to a PET signal being detected: Initially an unstable nucleus decays via beta decay producing a positron which annihilates with a nearby electron. This causes two nearly anti-parallel gamma rays to be produced, which are detected by the scanner. 39
1.4 An example TAC: each point represents the mean activity for the frame. Activity is quantified in SUV 44
1.5 Commonly used compartmental models 47
1.6 Simplified reference tissue model (SRTM) : The model assumes that the reference tissue is devoid of target and therefore all signal observed there is non-displaceable signal 52

2.1 MRI images at different stages of cognitive impairment; cognitively normal (CN), amnestic mild cognitive impairment (aMCI) and AD. [Image taken from Vemuri and Jack 2010] 59
2.2 Flow diagram representing the amyloid hypothesis. APP is cleaved causing Aβ aggregation and subsequently amyloid deposits. A combination of deposited amyloid and soluble amyloid causes tau pathology and then neuronal dysfunction, cell death and dementia. (Figure adapted from Karran, Mercken, and Strooper 2011) 60

2.3 PiB images in healthy controls and AD (Image taken from Klunk et al. 2004). There is increased tracer uptake in AD when quantified with SUV. 61

2.4 Braak Staging of amyloid pathology. The level of deposition is categorised into 3 stages. In stage A deposition is localised to the frontal, temporal and occipital lobe, stage B sees pathology spread to all regions apart from the primary sensory and primary motor field and at stage C all areas are affected. (Image adapted from H. Braak and E. Braak 1991) 64

3.1 Motion parameters for an example subject who had suffered a TBI. This subject passed QC. 93

3.2 Motion parameters from a subject taken from the study involving patients with CBD that wasn't included in the analysis in Chapter 7 due to excessive motion. 93

4.1 The workflow applied to model the brain as a weighted graph. . 101

4.2 A graphic illustrating the model space that was investigated . . . 103

4.3 Example scatter plots created after finding t^* for each subject. $Age - t^*$ is the estimated time since accumulation began. Each plot gives the estimated regional accumulation at the population level. 106

4.4 Plots for 9 regions showing the fit of Model 9 to the data. The model can accurately describe the data in regions with high and low uptake. 108

5.1 The logistic growth model describing the PET imaging signal over time as a function of the PET tracer's non-specific binding (NS), the carrying capacity (K), the time of half maximal Aβ concentration (T_{50}) and the uninhibited exponential growth rate (r). . 116

5.2 The cubic spline function found by Jack et al. 2013 which describes rates of change of mean cortical SUVr as a function of the baseline value. In this work, I followed the methodology described by Jack et al. 2013 to create a functional form for the temporal evolution of mean cortical SUVr in AD by integrating this cubic spline function with respect to time. 117

5.3 The functional form for the temporal evolution of mean cortical SUVr in AD over a 30 year period. The curve is produced by integrating the cubic spline function shown in Figure 5.2 and subsequently applying a linear transformation to account for differences between [^{11}C]PiB and [^{18}F]AV45 119

5.4 A histogram to show the distribution of the set $T = \{t_i\}$. This distribution is normal with mean of 11.8 years and standard deviation of 5.12 years. There are subjects in all the bins meaning that the cross-sectional data appears to have subjects at al stages of the accumulation process. 120

5.5 The chronological [^{18}F]-AV45 Aβ PET data in 9 regions. The trajectories in regions are coherent providing strong evidence that there is a stereotypical accumulation pattern for Aβ in AD. (D: Dorsal, A: Anterior, Inf: Inferior). 121

5.6 16 logistic growth models of Aβ accumulation with example curves from 3 distinct brain regions. Models in grey have regionally different T_{50} values and are consistent with spreading from seed regions whilst the models in white are consistent with local tissue properties driving the Aβ accumulation process. 123

5.7 Model fitting of the most parsimonious logistic growth model (Model 11) to the chronological [^{18}F]-AV45 Aβ PET data in 9 regions taken from the 90 region parcellation of the CIC atlas (Tziortzi et al. 2011) (D: Dorsal, A: Anterior, Inf: Inferior). The model accurately describes the data including regions of high accumulation (top row), medium accumulation (middle row) and low accumulation (bottom row). 127

5.8 The fit of Model 11 to the chronological dataset for ROIs 1-45 of the 90 region parcellation of the CIC atlas (Tziortzi et al. 2011). The model accurately describes all trajectories but the level of coherence in the data is variable across regions 128

5.9 The fit of Model 11 to the chronological dataset for ROIs 46-90 of the 90 region parcellation of the CIC atlas (Tziortzi et al. 2011). The model accurately describes all trajectories but the level of coherence in the data is variable across regions. In particular, the subcortical regions have a higher level of variability. 129

5.10 Parametric images displayed as orthographic projections for the carrying capacity K and the tracer non-specific binding (NS) obtained from fitting Model 11 at the voxel level. Grey matter (GM) and white matter (WM) maps are displayed for reference. The highest carrying capacities are found in the frontal lobe and the lowest are observed in the cerebellum, occipital lobe and the brain stem. The non-specific image is consistent with the known non-specific binding of [^{18}F]AV45 to white matter. 132

6.1 Workflow of how $A\beta_L$ is calculated: the input image is initially spatially normalised to MNI152 space and then a linear regression is performed using the two parametric maps. There are four outputs; α, $A\beta_L$, the fitted SUVr image $\mathbf{SUVr}_{fit}$ and a difference image equal to $\mathbf{SUVr} - \mathbf{SUVr}_{fit}$ 142

6.2 A figure showing the quality of the fit of $\mathbf{SUVr}_{fit}$ images. The top plot shows percentage of voxels in the brain which satisfied $|\mathbf{SUVr} - \mathbf{SUVr}_{fit}| > 0.3$ for each of the 769 subjects. The subjects are ordered by this percentage. 3 subjects (A, B, C) are labelled on the graph and below the corresponding **SUVr**, $\mathbf{SUVr}_{fit}$ and difference images are displayed. Overall, the linear combination of parametric images can effectively model the scans from the ADNI cross-sectional imaging data. 143

6.3 An equivalent figure to Figure 6.2 but using the cross-sectional Dallas Lifespan Brain study. As with the ADNI cross-sectional data, linear combinations of the parametric template images can effectively model the data 145

6.4 Using the difference image to check $A\beta_L$ calculation. **Left**: Two frontal ROIs have had the intensities set to zero to simulate a heavily lesioned brain. **Middle**: The fitted image calculated with this adaptation of the original image. **Right**: The difference image between $\mathbf{SUVr}_{fit}$ and the 'lesioned' brain. One can clearly identify the bright intensities in the simulated lesions showing the poor fitting here. 146

6.5 Boxplots of the distributions of mean cortical SUVr and $A\beta_L$ within four groups - HC: Healthy controls, EMCI: Early mild cognitive impairment, LMCI: Late mild cognitive impairment and AD: Alzheimer's disease. With increased progression through the disease process, there is an increase in both mean cortical SUVr and $A\beta_L$ but the effect sizes between the groups are all greater for $A\beta_L$ (see Tables 6.1 and 6.2). 148

6.6 Boxplots of the distributions of the calculated α for the 4 different groups with decreasing level of cognition. With increased progression through the disease process, there is a decrease in ns. 150

6.7 Boxplots for the distributions of changes in $A\beta_L$ and mean cortical SUVr between baseline and follow-up scans in the longitudinal ADNI data 150

6.8 Power curves for the ability of mean cortical SUVr and $A\beta_L$ to detect changes in global Aβ burden 152

7.1 Fit of the sigmoid function to the parent fraction data for all 10 subjects 159

7.2 Mean parent fraction curve across the whole study (error bars show the standard deviation). 160

7.3 Regional TACs for the 120 min scan for an example subject for the Precuneous cortex and the Cerebellum. Qualitatively, these regions exhibit different kinetics. 161
7.4 Regional TACs for the 120 min scan for an example subject for 5 ROIs. 162
7.5 Fits of the two-tissue compartment model (2-TCM) to time activity curves for a target region (Precuneous cortex) and the potential reference region (grey matter Cerebellum) 163
7.6 Fits of the two-tissue compartment model (2-TCM) to TACs from 5 cortical ROIs 164
7.7 Plots showing the TACs and 2-tissue compartment model fits for the grey matter Cerebellum region for all subjects. 165
7.8 Boxplots displaying calculated V_T values for CBD patients and healthy controls for six ROIs 166
7.9 Boxplots showing calculated BP_{ND} values for CBD patients and controls for six ROIs 167
7.10 The fit of SRTM to the TACs of two ROIs. The sum of squares of the residuals of the fit to the Cerebellum TAC is zero as this is the reference tissue TAC. 168
7.11 The fit of SRTM to the TACs of five ROIs. The model accurately describes the TACs in all regions. 168
7.12 Correlation between BP_{ND} derived from 2-tissue compartmental model and from SRTM 169
7.13 Correlation between BP_{ND} derived from 2-tissue compartmental model and SUVr-1 calculated from static images 171
7.14 Plot showing the time stability of regional SUVr values for six ROIs. The x-axis represents the mid-time window time. The values become stable at 40 min (30-50 min time window) 172
7.15 Plot showing the time stability of regional SUVr values for six ROIs. The values become stable at 70 min (60-0 min time window) 173

7.16 Plot showing the time stability of regional SUVr values for six ROIs. The values fail to become stable inside the duration of the 120 min scan. 174

8.1 Time activity curves for a target ROI (Precuneous cortex) and the reference region (Cerebellum). Both regions have been grey matter masked. 180

8.2 TACs for five grey matter ROIs 181

8.3 The fit of SRTM to two TACs for an example subject. The Cerebellum is the reference region in this analysis resulting in the sum of squares of residuals equalling zero by design. 182

8.4 The fit of SRTM to five TACs for an example subject. The model can accurately describe TACs in each region. 182

8.5 BP_{ND} values as calculated using STRM across six regions in healthy controls and TBI: At the region of interest level there is no difference in the tracer binding potentials between groups. In all regions, there is a higher range of BP_{ND} values in the TBI group than in controls suggesting that level of uptake in TBI is variable and potentially not spatially consistent across patients 183

8.6 Orthographic projections of parametric BP_{ND} images for healthy controls; consistent with previous studies, there is high uptake in the striatum which is likely to be due to off-target binding to neuromelanin and MAO-A. 185

8.7 Orthographic projections of parametric BP_{ND} images for TBI patients (1-12); tracer uptake is variable across patients with some showing a strong and widespread cortical signal such as TBI 03, TBI 04 and TBI 10 but others with few voxels having positive binding potentials such as TBI 06 and TBI 11. In the subjects with strong signal, the highest binding potentials occur in the temporal and parietal lobes 186

8.8 Orthographic projections of parametric BP_{ND} images for TBI patients (13-21); as with page 1, tracer uptake is variable across patients with some showing a strong and widespread cortical signal such as TBI 15 and TBI 16 but others with few voxels having positive binding potentials such as TBI 18. 187

8.9 Orthographic projections of the mean and standard deviation images of healthy controls; the highest binding potentials in the mean image are in the striatum which are likely to be caused by off-target binding to neuromelanin. Interestingly, in this location there is high variability across subjects as shown by the high intensities in the standard deviation image. 189

8.10 Orthographic projections of Z-score images for TBI patients (1-12) as calculated against the normal distribution of healthy controls. Both the location and z-values are variable across the patients. 191

8.11 Orthographic projections of Z-score images for TBI patients (13-21) as calculated against the normal distribution of healthy controls. Both the location and z-values are variable across the patients. 192

List of Tables

3.1 Size and ages of different groups in the cross-sectional ADNI dataset 87
3.2 Demographics for the healthy controls included in the Tau in CBD analysis in chapter 7. 94
3.3 Demographics for the CBD subjects included in the Tau in CBD analysis in chapter 7. 94
3.4 Demographics for the healthy controls included in the Tau in TBI analysis in chapter 8. 95
3.5 Demographics for the TBI subjects included in chapter 8. 96

4.1 A table showing the results of fitting each of the different models to the dataset. Models were ranked by the BIC value. The rightmost column shows the Delta BIC for each model where $\Delta BIC_i = BIC_i - \min(BIC)$ and $\min(BIC)$ is the lowest value across all the models. Model 9 has the lowest BIC values and all other models had a ΔBIC of greater than 3500. 107

5.1 The characteristics of the subjects taken from both the longitudinal study performed by Jack et al. and the cross-sectional data obtained from ADNI. These two datasets are combined to create a chronological dataset. 118

5.2 The 16 parameterisations of the logistic growth model of Aβ accumulation used to analyse the chronological [^{18}F]-AV45 SUVr PET data at a regional level with the corresponding sum of squared residuals (SSQ) and ΔBIC_i. 90 cortical and subcortical regions were included and parameters were either restricted to a single value across all regions (Global) or fitted individually for each region (Local). ΔBIC_i gives a measure of the parsimony of each model in relation to the smallest BIC value. Model 11 (Local K, Global r, Global T_{50} and Local NS) gives the most parsimonious fit to the data. 125

5.3 An equivalent table to Table 5.2 but using a set of 76 cortical ROIs only (this corresponds to the removal of the sub-cortical regions from the previous set of 90 ROIs where there is lower accumulation) 130

5.4 An equivalent table to Table 5.2 but using a set of 9 ROIs which are much larger regions and cover the whole brain 130

6.1 Effect sizes for SUVr. 147

6.2 Effect sizes for $A\beta_L$. 147

7.1 A table showing Pearson correlations of determination and the parameters from the best linear fit for the correlation of regional SUVr values with BP_{ND} values derived from the two-tissue compartment model for six regions of interest 170

8.1 A table showing the number of voxels in the Z-score images of each Healthy conrol over the threshold value of 1.96. 193

8.2 A table showing the number of voxels in the Z-score images of each Healthy conrol over the threshold value of 1.96. 194

List of Abbreviations

MR	**M**agnetic **R**esonance
MRI	**M**agnetic **R**esonance **I**maging
PET	**P**ositron **E**mission **T**omography
SUV	**S**tandardised **U**ptake **V**alue
SUVr	**S**tandardised **U**ptake **V**alue **r**atio
RF	**R**adio**f**requency
FID	**F**ree **I**nduction **D**ecay
Aβ	**A**myloid-β
CBD	**C**ortico**B**asal **D**egneration
TBI	**T**raumatic **B**rain **I**njury
ADNI	**A**lzheimer's **D**isease **N**euroimaging **I**nitiative
DLBS	**D**allas **L**ifespan **B**rain **S**tudy
SSQ	**S**um of **SQ**uares of the residuals
BIC	**B**ayesian **I**nformation **C**riteria
GM	**G**rey **M**atter
WM	**W**hite **M**atter
TAC	**T**ime **A**ctivity **C**urve
2-TCM	**Two**-**T**issue **C**ompartment **M**odel
SRTM	**S**implified **R**eference **T**issue **M**odel
PHF	**P**aired **H**elical **F**ilaments
NFT	**N**euroFibrillary **T**angles
CTE	**C**hronicTraumatic **E**ncephalopathy

List of Symbols

V_T	Volume of distribtution	unitless
BP_{ND}	Binding potential	unitless
K	Carrying capacity	SUVr units (unitless)
NS	Non-specific binding	SUVr units (unitless)
r	Exponential growth rate	years^{-1}
T_{50}	Time of half maximal Aβ concentration	years
SUVr	Spatially normalised SUVr image	
SUVr$_{fit}$	Fitted SUVr image	
ns	Non-specific binding scaling factor	Percentage (unitless)
NS	Parametric non-specific binding image	
$A\beta_L$	Amyloid Load	Percentage (unitless)
K	Parametric carrying capacity image	

Chapter 1

Magnetic resonance imaging and positron emission tomography

In vivo medical imaging is wide-ranging field which forms an integral part of both clinical and investigative medicine. By visualising both anatomy and biological processes occurring in the body, medical imaging can aid diagnosis, monitoring of disease pathology and understanding of anatomy. Molecular imaging can be defined to be the "noninvasive, visualisation of biochemical events at the cellular and molecular level within living cells, tissues, and/or intact subjects" (James and Gambhir 2012). There are a range of imaging modalities which can be used in molecular imaging which give complementary information. In this chapter, I introduce two imaging modalities; magnetic resonance imaging (MRI) and positron emission tomography (PET). I describe how the strengths of both can be combined to quantify concentrations of a molecular imaging targets *in vivo*. The imaging techniques presented in this chapter are used throughout this thesis to quantify molecular imaging targets relevant to neurodegenerative processes.

1.1 MRI

The physical phenomenon of nuclear magnetic resonance was first discovered in 1938 by Isobar Rabi but it wasn't until Damadian 1971 used it to detect tumours, that the field of MRI imaging was born. Today, MRI is a well established imaging modality that is used both clinically and in research. In neuroimaging, structural imaging gives high resolution soft tissue contrast images of anatomy (Plewes and Kucharczyk 2012) and the introduction of functional-MRI (Ogawa et al. 1990) has allowed researchers to study functional networks of the brain which are activated whilst performing a variety of activities or tasks.

The physics involved in generating MRI images are complex and only the fundamentals of generating a signal are covered here. A magnetic dipole is produced in every proton due to the proton's spin (Shung, M. B. Smith, and Tsui 1992). By placing a subject in an MRI scanner, one places the protons in the subject in a strong external magnetic field, B_0. Under these circumstances, protons either exist in a lower energy state where the magnetic dipole of the proton aligns with B_0 or in a higher energy state where the magnetic dipole is in the opposite direction to B_0 (Plewes and Kucharczyk 2012). A small majority of protons reside in the lower energy state which induces a small magnetic field in the same direction as B_0 known as longitudinal magnetisation (Möllenhoff, Oros-Peusquens, and Shah 2012; Schild 1990). Applying a radiofrequency (RF) pulse (with frequency close to the Lamor frequency of protons) transverse to B_0 excites protons with the result that some transfer from the lower energy state to the higher energy state which in turn causes the longitudinal magnetisation vector to decrease in magnitude (Schild 1990). Following the RF pulse, the system reverts to the original state in a process called relaxation. Relaxation produces an electrical signal because the overall magnetic vector from the protons is constantly changing in direction and cutting the magnetic flux of B_0. The electrical signal is termed free induction decay (FID) (Hendee and Ritenour 2003) and it is this signal that is detected in MRI. MRI scanners have gradients in B_0 which enable one to ascertain where a given FID signal originated from (Hendee and

Ritenour 2003).

The time taken for relaxation in the longitudinal direction is described by the T1 which is determined by the physical properties of the surroundings of the protons in question (Schild 1990). T1 is typically longer for structures containing more water and shorter for structures containing more fat and therefore different tissue types in the brain have different T1 (Möllenhoff, Oros-Peusquens, and Shah 2012). By applying repeated radiofrequency pulses (a radiofrequency pulse sequence) MRI scanners exploit this property as the different T1's in the different tissues will cause different FID signals and thus can be converted into different intensities in an image.

An example T1-weighted MRI scan can be seen in the top row of Figure 1.1. The main advantage of structural magnetic resonance images is that they provide high resolution anatomical information about the brain and magnetic resonance imaging is now frequently used in the clinic to find lesions and abnormalities. Structural magnetic resonance images do not provide any information on the function of the brain and they are not quantitative images; ie, they do not obtain "maps of meaningful physical or chemical variables that can be measured in physical units and compared between tissue regions and among subjects" (Basser and Pierpaoli 2011).

1.1.1 Segmentation of structural MRI images into tissue types

In this thesis, the anatomical information provided by MRI images is used to define regions of interest in the brain which can then be applied to other images acquired using PET.

Automated algorithms have been developed which segment T1-weighted MRI images into different tissue classes such as grey matter (GM), white matter (WM) and cerebrospinal fluid (CSF). In this thesis, all tissue segmentation will be performed using an algorithm called unified segmentation which was published by (Ashburner and K. J. Friston 2005). This method has demonstrated a high accuracy for tissue classification (Ashburner and K. J. Friston

2005) when tested on simulated data where the tissue classification of each voxel is known. Figure 1.1 shows example tissue probability maps for each of the tissue classes produced by the segmentation process.

1.1.2 Diffusion tensor imaging

T1-weighted MRI images provide useful information for classifying voxels in the brain into different tissue classes but the structure inside each of these classes cannot be assessed. From post-mortem studies it is known that grey matter regions of the brain are connected in a highly structured way through white matter connections (Blumenfeld 2010; Filley and Fields 2016; Fields 2010; Furst and Fellgiebel 2011). These white matter connections in the brain can be imaged *in vivo* with diffusion tensor imaging (DTI). DTI is a form of MRI where gradients are used to image the movement of water molecules in the brain. The apparent diffusion component in the direction of three gradients (in the x, y and z directions) can be fitted using an ellipsoid (Jellison et al. 2004). An ellipsoid can be completely characterised by the three eigenvalues and eigenvectors. The hypothesis is that in the direction of white matter tracts, the apparent diffusion component and therefore the eigenvalue will be higher as there are less obstructions. Therefore the eigenvector with the largest corresponding eigenvalue is most likely to be colinear with prominent white matter tracts at a given voxel (Basser, Mattiello, and LeBihan 1994; Basser 1995; Basser and Pierpaoli 1998). By combining these eigenvectors across an image, it is possible to generate maps of the white matter connections (Basser and Pierpaoli 2011) in a process called three-dimensional tractography. Introduced around the turn of the millennium, tractography reconstructs white matter connections (Basser, Pajevic, et al. 2000; Conturo et al. 1999; Mori, Crain, et al. 1999; Catani et al. 2002) and can be used to create striking visual representations of the whole brain white matter connectivity (see Figure 1.2) antemortem. An example diffusion tensor image can be see in Figure 1.2.

Unfortunately however, tractography is prone to both subjective and systematic errors (Assaf and Pasternak 2008). It can accurately delineate the "core

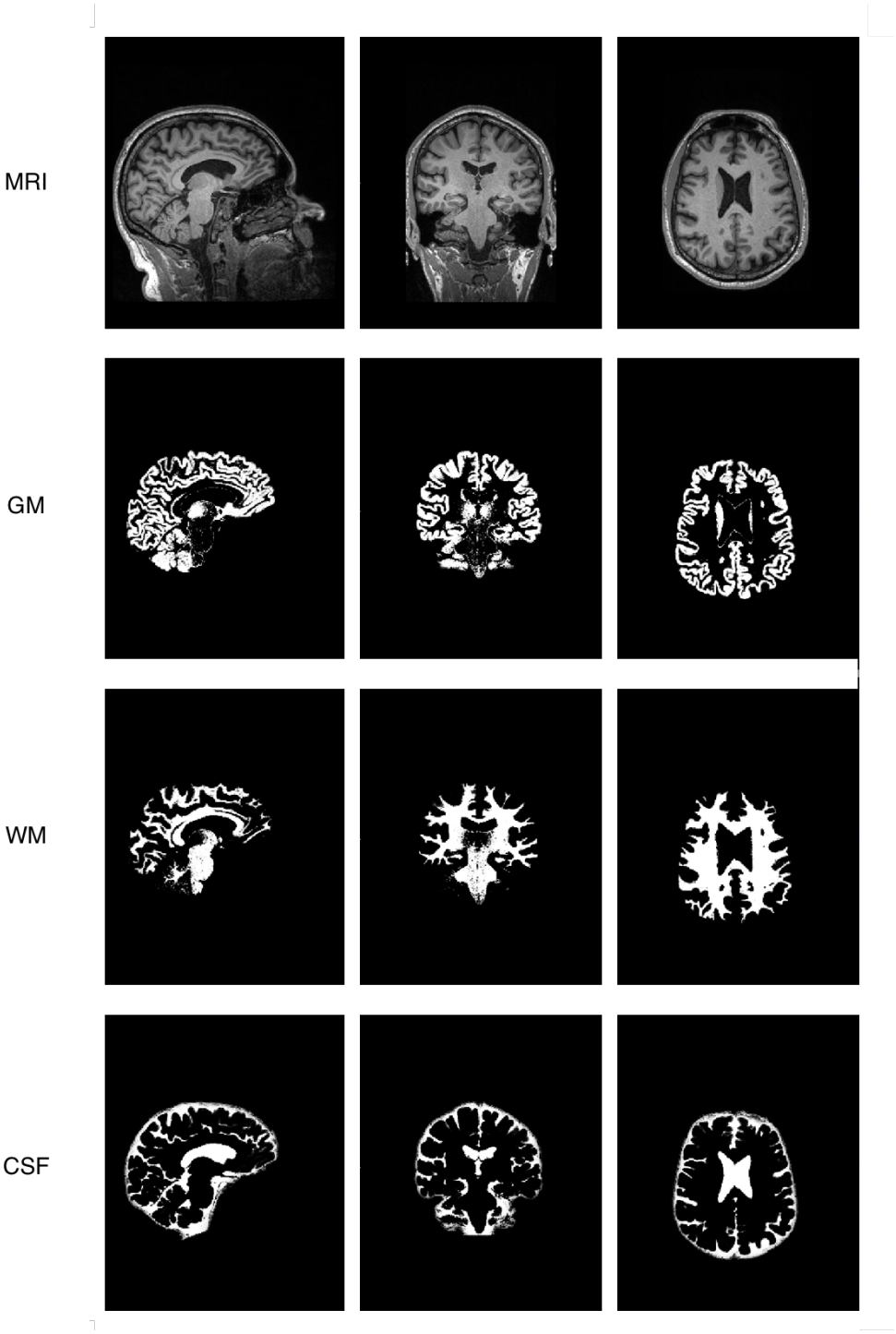


FIGURE 1.1: MRI images and 3 tissue probability maps after the MRI has been segmented. (GM: Grey matter, WM: White matter, CSF: cerebrospinal fluid)

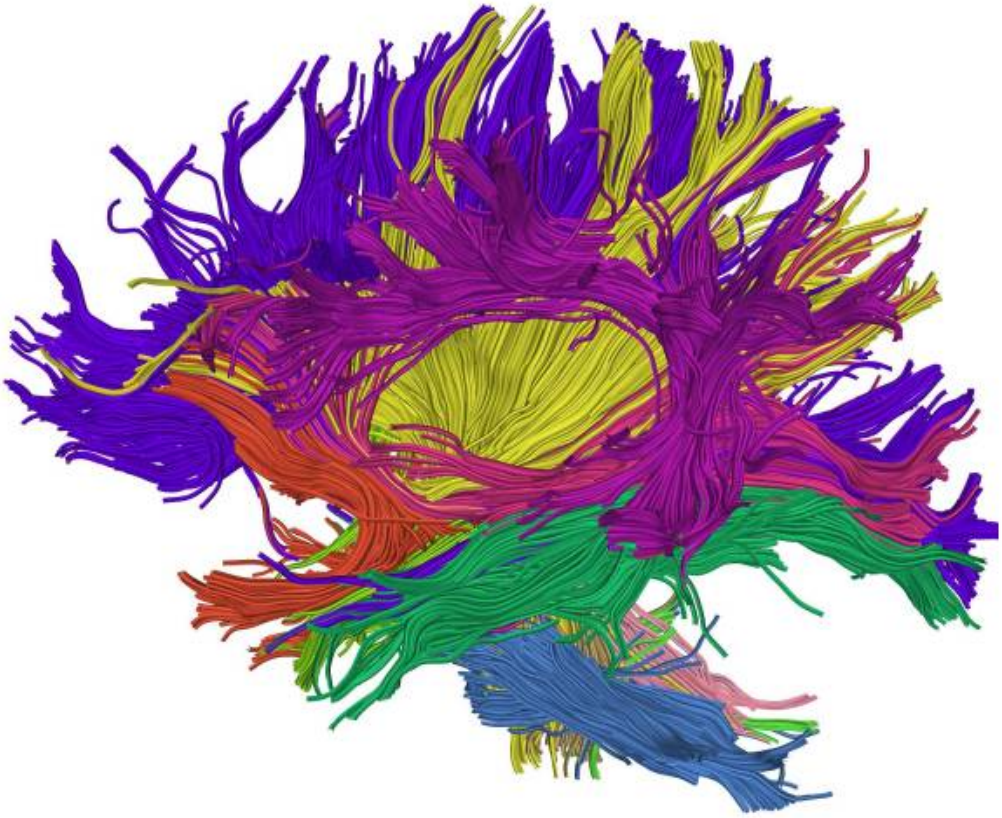


FIGURE 1.2: An example tractography image generated from diffusion tensor imaging data (Image taken from O'Donnell and Westin 2011)

of large white matter tracts" (Mori and Zijl 2002), however it is susceptible to image artefacts and caution should be used when using it to describe smaller tracts (Mori and Zhang 2006; O'Donnell and Westin 2011).

1.2 PET

PET is an imaging modality commonly used to research both normal brain function and pathophysiological processes and diagnose patients, monitor disease progression and assess treatment response *in vivo* (Nasrallah and Dubroff 2013; Heurling et al. 2017). A subject is injected with a positron emitting (β^+ decay) radioactive compound in solution which is specifically designed to selectively bind to a target of interest - a radiotracer (sometimes shortened to just tracer). By detecting photons generated (outlined in detail in subsection 1.2.1), PET scanners can be used to generate images which show the spatiotemporal distribution of the radiotracer over the course of the scan. By analysing the kinetics of the radiotracer, it is possible to calculate the concentration of the target of interest in a region of interest (ROI). This process is explained in section 1.3. Since the turn of the century, PET has been used ever increasingly (Heurling et al. 2017) with many studies focussing on neurodegenerative processes by imaging metabolism and misfolded protein aggregation.

1.2.1 PET signal and image reconstruction

A PET scanner consists of a bore surrounded by stacked rings of photon detectors (Fahey 2010; Kwee, Torigian, and Alavi 2013). To perform a scan, a subject is positioned in the scanner and injected with the radiotracer which is carried around the body in the bloodstream. Figure 1.3 is a schematic of the processes occurring in a PET scanner that enable photon detection. Unstable radioactive compounds decay to more stable states with one proton changing to a neutron which results in a neutrino and a positron being emitted (Saha 2016; James and Gambhir 2012). The positron travels a short distance according to brownian

motion until the positron annihilates with an electron causing two nearly anti-parallel photons to be produced (Schmitz, A. M. Alessio, and P. E. Kinahan 2009). These photons are detected at the edge of the bore of the scanner and are combined to create PET images.

When the two near anti-parallel photons hit the detectors, their energy is converted into an electrical signal and for a given annihilation, the two photons will be detected at two different detectors almost simultaneously (Krishnamoorthy, Schmall, and Surti 2016). Any time two different detectors detect a signal simultaneously, it is called a coincidence event. It is assumed that all coincidence events occur as a result of the process described above but it is important to note that in reality processes such as scatter and random coincidence events mean that this is not true (James and Gambhir 2012) and these need to be corrected for to enable quantitative imaging of the tracer concentration. A single frame of a dynamic PET scan is simply the collection of all coincidence events occurring in a frame time window.

Only by combining the record of all coincidence events, is it possible to gain information on the spatial location of the radiotracer. Some geometry is required to recover this information and for simplicity, I will consider the case of a single ring of detectors around a subject with each spatial co-ordinate being defined by the pair (x, y). Each coincidence event defines a line of response which in turn determines a unique pair (r, θ) where r is the displacement in the x-direction of the detector away from the centre and θ is the angular orientation (A. Alessio and P. Kinahan 2006). Each coordinate in the x, y plane determines a unique set of values for the pair r and θ in turn determine a unique half sine curve (S. Tong, A. M. Alessio, and P. E. Kinahan 2010). In a frame of a PET scan, each half sine wave is assigned an intensity equal to the number of decays which were assigned to happen at the x, y-coordinate to which it is associated. The result is a sinogram and this encodes the spatial uptake of the tracer in the time window of the frame (Saha 2016; Schmitz, A. M. Alessio, and P. E. Kinahan 2009; A. Alessio and P. Kinahan 2006). The sinogram can be reconstructed into

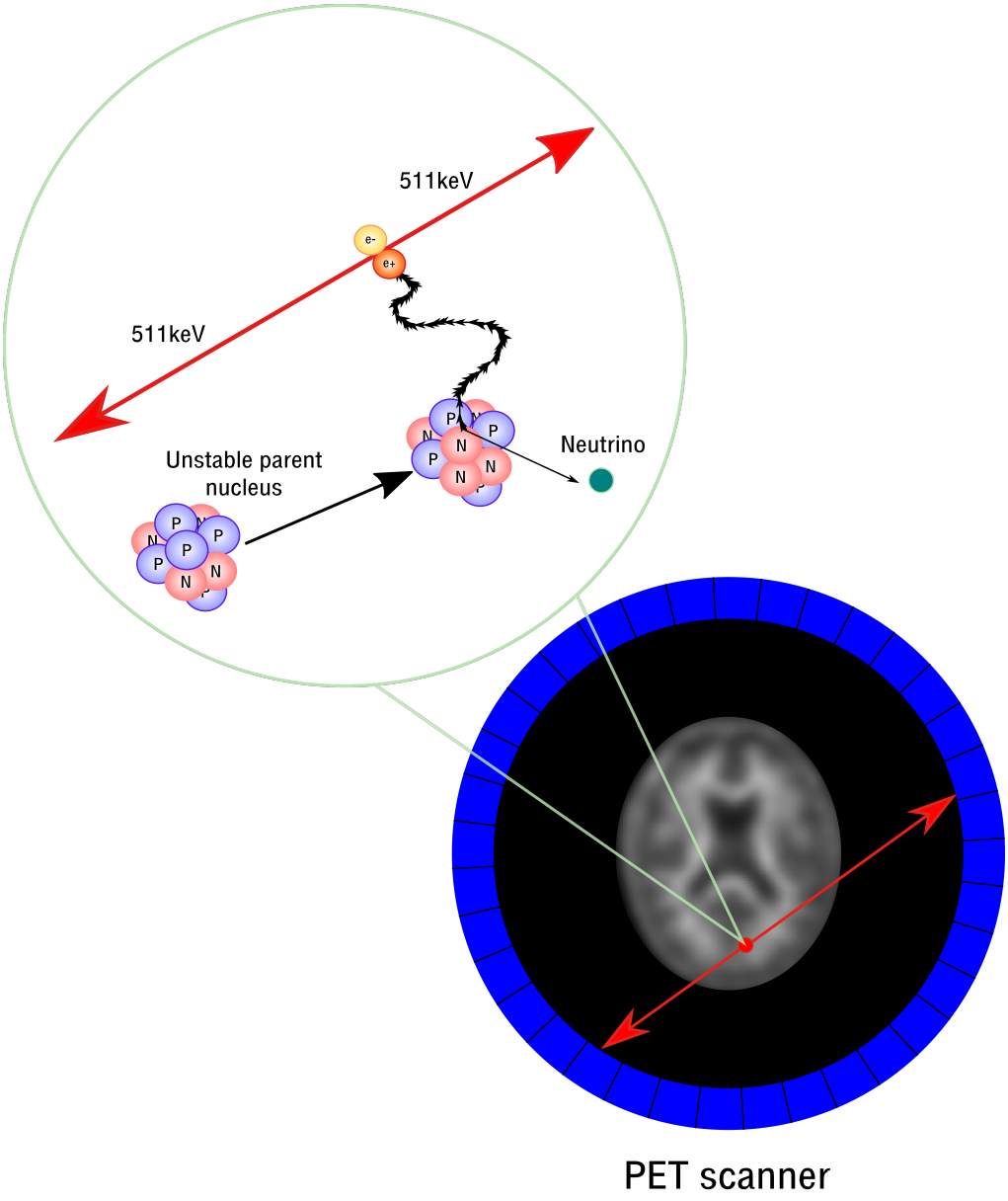


FIGURE 1.3: Particle interactions leading to a PET signal being detected: Initially an unstable nucleus decays via beta decay producing a positron which annihilates with a nearby electron. This causes two nearly anti-parallel gamma rays to be produced, which are detected by the scanner.

x, y-coordinates analytically using filtered back projection or via iterative reconstruction (A. Alessio and P. Kinahan 2006).

In a PET scan there are multiple sets of detector rings stacked along the bore of the scanner. Co-incidence events from all rings are combined to and reconstructed to produce a 2D image for each ring of detectors. The reconstructed 2D images, sometimes called slices, are stacked one on top of another to form a 3D image representing the spatial distribution of radiotracer in a given frame. As previously mentioned the full dynamic PET scan consists of a number of frames showing the spatial distribution of the tracer in some chosen time windows and as such, this data provides spatiotemporal information about the distribution of the radiotracer.

1.2.2 Subject motion in PET

Subject motion during a PET scan has important consequences for image quality and thus quantification. In an ideal scenario for quantification, the subject would not move throughout the duration of the scan, however scans often last over 90 minutes and it is inevitable that some motion will occur. I will explain two different types of motion here; between frame motion and within frame motion.

Between frame motion describes motion that occurs between one frame and the next. If left unaccounted for, this could heavily bias quantification of the concentration of the target. To explain why, consider the following thought experiment. Let's assume that we have two small regions of interest, ROI1 and ROI2 which are 5 mm apart with coordinates (a, b) and (c, d) respectively and that ROI1 has double the concentration of target than ROI2. Then, suppose further that, in between frames the subject moves 5 mm so that in the following frame ROI 2 now has coordinates (a, b). For quantification, it would be assumed that coordinates (a, b) would represent ROI1 but it would actually be of ROI2 which has half the concentration of target. This would lead to the quantification of target in ROI1 to be inaccurate.

Within frame motion occurs when the subject moves during the period a frame is being captured. The motion will mean that co-incidence events in the same (x, y)-coordinates will have resulted from annihilations in different regions of the brain. Like between frame motion, this can bias results although the level of motion occurring in the duration of a frame is likely to be lower than across the length of an entire scan.

1.3 Quantification methods in PET

This section is dedicated to describing methods by which the concentration of an imaging target, such as a neuroreceptor or form of disease pathology, can be derived using reconstructed dynamic PET data.

1.3.1 Image registration

In order to explain quantification in PET, it is necessary to understand the fundamentals of image registration. Two images are considered to be in the same space if voxels correspond to the same anatomical space in both images. The aim of image registration is to spatially transform an image so that it is in the same space as a reference image (Ashburner and K. Friston 2003). This could involve registering two images from the same subject (often from different modalities) or images from multiple subjects (sometimes referred to as co-registration) (K. J. Friston et al. 1995; Hill et al. 2001). A common practice for analysing common features across many subjects is to register images to one common space which is referred to as spatial normalisation.

There are many algorithms to perform image registration. Broadly, these can be classified into three different categories; rigid registration, affine registration and nonlinear registration. Rigid registration finds the optimum parameters for rotations around the three axes (pitch, roll and yaw) and translations along each of the three axes (Ashburner and K. Friston 2003). Importantly, rigid registration restricts the image to being the same size after registration or equivalently,

there is no scaling. In cases of registering images from the same subject with the same voxel sizes, this method is preferred. Rigid-body registrations are in fact a subset of the the class of affine registrations. Affine transformations of a vector $\mathbf{x} = (x_1, x_2, x_3)$ to a vector $\mathbf{y} = (y_1, y_2, y_3)$ are all transformations that can be expressed in the following form,

$$y_1 = m_{11}x_1 + m_{12}x_2 + m_{13}x_3 + m_{14} \tag{1.1}$$

$$y_2 = m_{21}x_1 + m_{22}x_2 + m_{23}x_3 + m_{24} \tag{1.2}$$

$$y_3 = m_{31}x_1 + m_{32}x_2 + m_{33}x_3 + m_{34} \tag{1.3}$$

where $m_{i,j} \in \mathbb{R}$.

These transformations are often expressed using matrix algebra,

$$\begin{pmatrix} y_1 \\ y_2 \\ y_3 \\ 1 \end{pmatrix} = \begin{pmatrix} m_{11} & m_{12} & m_{13} & m_{14} \\ m_{21} & m_{22} & m_{23} & m_{24} \\ m_{31} & m_{32} & m_{33} & m_{34} \\ 0 & 0 & 0 & 1 \end{pmatrix} \begin{pmatrix} x_1 \\ x_2 \\ x_3 \\ 1 \end{pmatrix} \tag{1.4}$$

Along with rotations and translations, affine registrations allow the moved images to undergo scaling and shears (Ashburner and K. Friston 2003).

Nonlinear registrations allow all continuous transformations of images (ie, those that do not produce new holes in the images). These types of registration are normally used to spatially normalise images from different subjects to a common space such as MNI152 space. It is common for an initial affine transformation of the image to be performed before the nonlinear warping of the image to avoid overfitting (Ashburner 2007).

1.3.2 Motion-correction, delineation of regions of interest and generation of time-activity curves

As was outlined above, it is required for reliable quantification that the same voxel in each frame of a PET scan corresponds to a consistent point in the

brain. One method frequently used to account for between frame motion in the reconstructed images is to register each of the frames to a reference frame. This produces a 'realigned' image in which all the frames are in the same space. Within frame motion is more problematic but by keeping frame duration times small, one can limit the amount that occurs.

Many studies will focus on quantifying the concentration of the target in a set of predefined voxels - an ROI. ROIs are delineated manually on structural MRI images of the same subject or using an atlas image. For manual ROI drawing, a rigid-body registration is used to register the MRI and PET images. When using an atlas, it is required to have the atlas and PET image data in the same space. One must choose whether to register the PET data to the standard space the atlas was defined in or register the atlas to the PET image space. If one wants to perform a population level analysis at the voxel level with static images then it is favourable to register the PET scans to the standard space so that each voxel in an image can be directly compared to others in the population. If one however, wants to perform kinetic modelling of a novel tracer, it is preferable to work in subject space as one doesn't alter the reconstructed PET data. The spatial resolution and anatomical information in PET images is inferior to structural MRI and therefore registering MRI is more reliable than registering PET scans. Because of this, it is common to register a standard template magnetic resonance image in the same space as the atlas image to the subjects' MRI (or reverse in the case of moving the PET to a standard space) and apply the transformation parameters to the atlas image. This step is commonly done using a nonlinear registration. At this point, a rigid-body registration of the PET scan to the MRI produces the desired atlas image in the same space as the PET.

The mean intensity of voxels from the delineated regions of interest in each frame is used to define a regional time activity curve (TAC) in which one plots the concentration of radioactivity versus the time after injection of the tracer. The radioactivity measured in kBq/ml can be normalised by the injected dose divided by the body weight of the subject to give standardised uptake values (SUV). An example TAC can be seen in Figure 1.4.

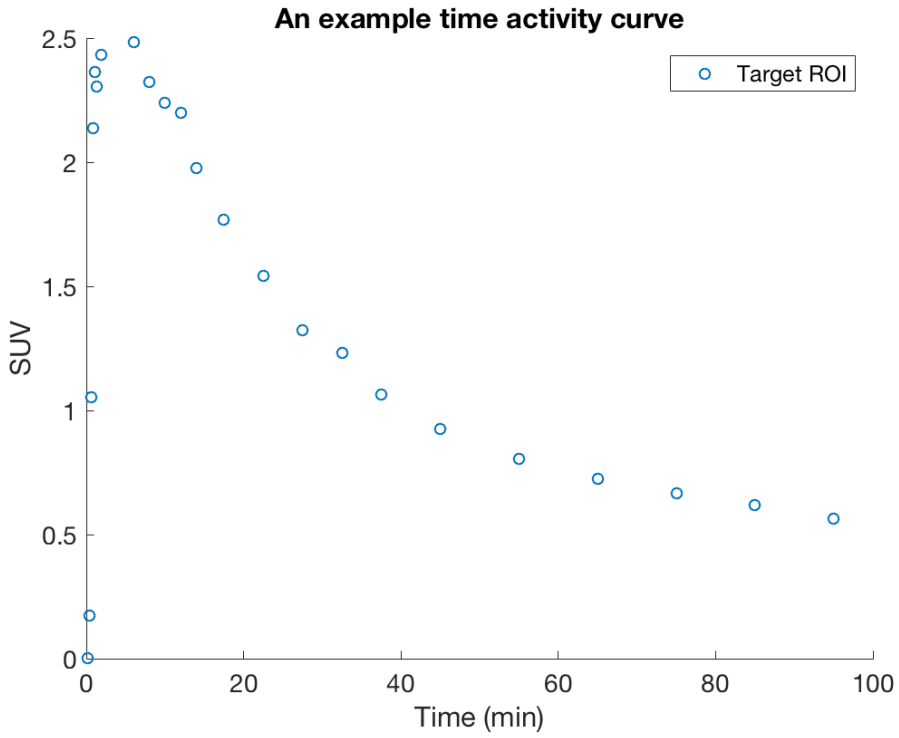


FIGURE 1.4: An example TAC: each point represents the mean activity for the frame. Activity is quantified in SUV

1.3.3 Model-driven quantification of PET data

Quantification methods for PET data can be split into two classes; data-driven methods and model-driven methods (R. N. Gunn, S. R. Gunn, Turkheimer, et al. 2002). Data driven methods such as those introduced by Patlak and Blasberg 1985 and Logan et al. 1990 do not assume any underlying model for the data. In this thesis, I will concentrate on model-driven methods which use known biological phenomena to construct models to describe radiotracer kinetics.

The gold standard for quantifying target concentration from ROIs with PET data is using compartmental models and an arterial input function. All compartmental models express the ROI time activity curve, $C_T(t)$ as a function of the plasma input function, $C_p(t)$ and rate constants between different states or 'compartments' that the tracer can be in (R. N. Gunn, S. R. Gunn, and Cunningham 2001).

$C_p(t)$ is obtained by placing an arterial cannula for the duration of the scan

and drawing blood samples. The blood samples can be analysed to obtain the concentration of radiotracer in the plasma which has not been metabolised and is therefore freely available to enter the brain.

Figure 1.5 shows four commonly used compartmental models. Compartmental models can be classified into two main type, irreversible and reversible models (R. N. Gunn, S. R. Gunn, and Cunningham 2001). Tracers that can be best modelled using an irreversible model have a state in which the tracer gets trapped. Reversible models by contrast assume that there are non-zero rates of flow away from all compartments (R. N. Gunn, S. R. Gunn, and Cunningham 2001). The commonly used radiotracer [^{18}F]Fludeoxyglucose ([^{18}F]FDG) is best described by an irreversible model because after the tracer enters the brain it becomes phosphorylated and then trapped (Phelps et al. 1979; Sokoloff et al. 1977). An example of a tracer with reversible kinetics is [^{11}C]Raclopride which targets dopamine receptors (Farde et al. 1989). The concentration in the tissue is monotonically increasing in all irreversible models (assuming the trapping compartment is in the tissue) and reversible models tend towards an equilibrium position where the concentration in each compartment is non-zero. Compartmental models hypothesise that the net rate of flow between two compartments at time t is proportional to the difference in concentrations of the two compartments (Kety 1951) which means that the systems can be described mathematically using ordinary differential equations and linear equations.

The one-tissue irreversible model can be seen on the top line of Figure 1.5. There is only one rate constant, K_1 which represents the rate of transfer of radiotracer from the plasma to the tissue - once in the tissue, it becomes trapped. The equations which describe the one-tissue irreversible model can be seen in Equation 1.5

$$\begin{aligned} \frac{dC_1(t)}{dt} &= K_1 C_P(t) \\ C_T(t) &= (1 - V_B)C_1(t) + V_B C_B(t) \end{aligned} \tag{1.5}$$

where V_B is the fractional volume of whole blood. The observed PET signal $C_T(t)$ is the sum of the concentrations in the tissue compartments and in the

whole blood $C_B(t)$.

The one-tissue reversible model can be seen on the second line of Figure 1.5. There are two rate constants, K_1 and k_2 which represent the rate of transfer of radiotracer from the plasma to the tissue and the efflux of the tracer from the tissue. The system is described by Equation 1.6

$$\begin{aligned} \frac{dC_1(t)}{dt} &= K_1 C_P(t) - k_2 C_1(t) \\ C_T(t) &= (1 - V_B) C_1(t) + V_B C_B(t) \end{aligned} \tag{1.6}$$

In the two-tissue irreversible model, there are two states the tracer can be in after it has crossed the blood-brain-barrier into the tissue from the plasma. However, once the tracer has entered compartment C_2, it becomes trapped and remains in that state. The equations describing the system are written in Equation 1.7

$$\begin{aligned} \frac{dC_1(t)}{dt} &= K_1 C_P(t) - (k_2 + k_3) C_1(t) \\ \frac{dC_2(t)}{dt} &= k_3 C_1(t) \\ C_T(t) &= (1 - V_B)(C_1(t) + C_2(t)) + V_B C_B(t) \end{aligned} \tag{1.7}$$

A commonly used model is the reversible two-tissue compartment model. The model equations are described by the set of equations in Equation 1.8.

$$\begin{aligned} \frac{dC_1(t)}{dt} &= K_1 C_P(t) - (k_2 + k_3) C_1(t) + k_4 C_2(t) \\ \frac{dC_2(t)}{dt} &= k_3 C_1(t) - k_4 C_2(t) \\ C_T(t) &= (1 - V_B)(C_1(t) + C_2(t)) + V_B C_B(t) \end{aligned} \tag{1.8}$$

Using a state space representation of compartmental models, R. N. Gunn, S. R. Gunn, and Cunningham 2001 has been shown that there is a general solution to a system with n compartments which is shown in Equation 1.9.

$$C_T(t) = V_B C_B(t) + (1 - V_B) \sum_{i=1}^{n} \alpha_i e^{\beta_i t} \otimes C_P(t) \tag{1.9}$$

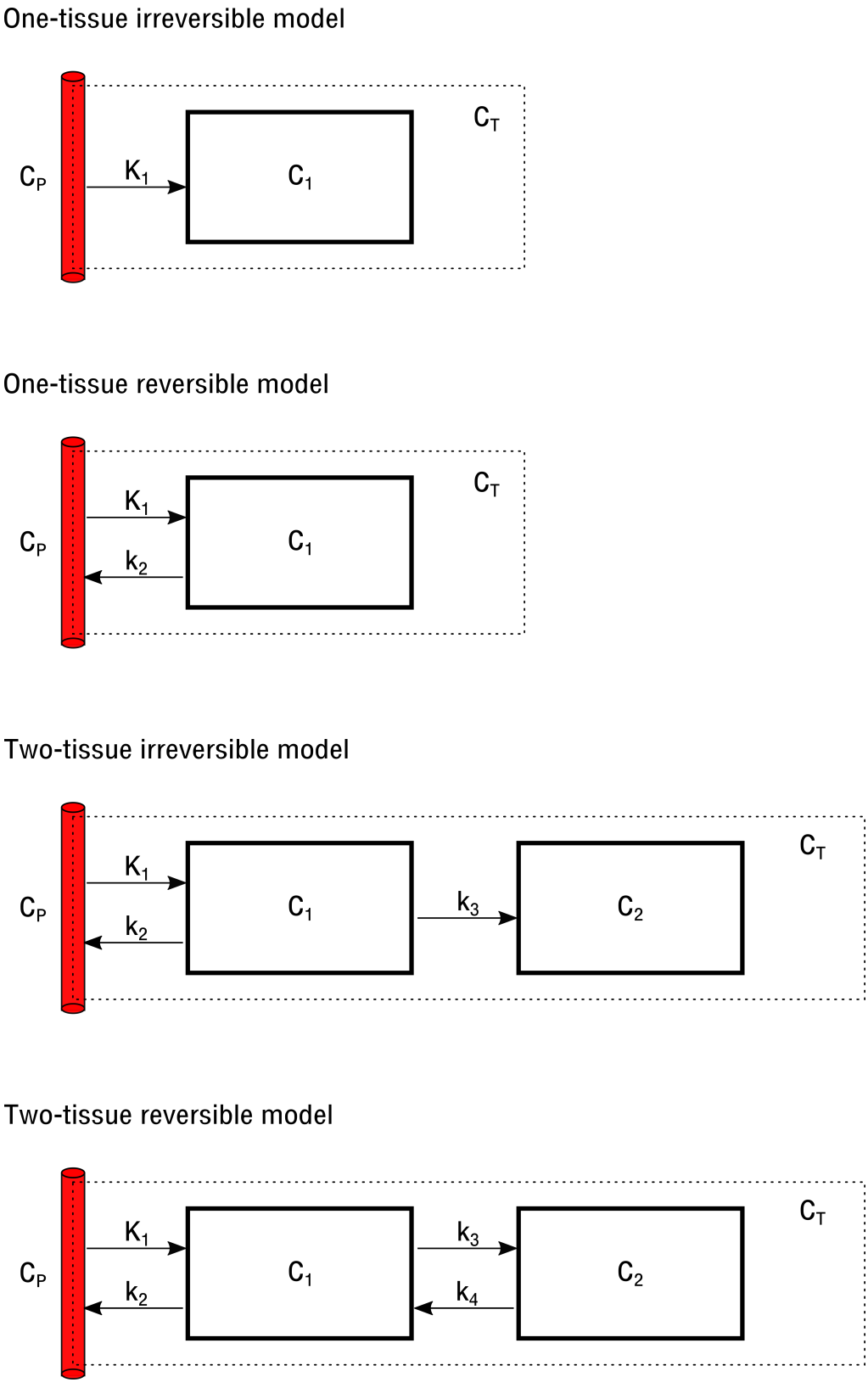


FIGURE 1.5: Commonly used compartmental models

where, $\alpha_i \in \mathbb{R}$ and β_i are combinations of the rate constants connecting the compartments.

If the model is a reversible model,

$$\alpha_i \in \mathbb{R} \text{ such that } \alpha_i > 0$$

$$\beta_i \in \mathbb{R} \text{ such that } \beta_i > 0$$

If the model is an irreversible model however $\beta_i = 0$ for some $1 \leq i \leq n$. Without loss of generality, this can be stated as

$$\alpha_i \in \mathbb{R} \text{ such that } \alpha_i > 0$$

$$\beta_i \in \mathbb{R} \text{ such that } \begin{cases} \beta_i > 0 \text{ for } i \neq n \\ \beta_i = 0 \text{ for } i = n \end{cases}$$

As an example, the solutions to the one-tissue irreversible model and the one-tissue reversible models are shown in Equations 1.10 and 1.11 respectively,

$$C_T(t) = V_B C_B(t) + (1 - V_B) K_1 \otimes C_P(t) \tag{1.10}$$

$$C_T(t) = V_B C_B(t) + (1 - V_B) K_1 e^{k_2 t} \otimes C_P(t) \tag{1.11}$$

In theses examples, $n = 1$, $\alpha_1 = K_1$, $\beta_1 = 0$ for the irreversible model because $i = n$ and $\beta_1 = k_2$ for the reversible model. The reader is referred to (Phelps et al. 1979) for the full solution of the two-tissue compartmental model.

For a novel radiotracer where the kinetics are not well established, a range of different compartmental models can be fitted to the TACs for the defined ROIs. Models are fitted by optimising the values for α_i and β_i so that the sum of squares of residuals between the TACs and the fitted $C_T(t)$ is minimised. The fits of these different models are assessed to decide which model describes that kinetics of the tracer in the most parsimonious manner. In addition to fitting

different compartmental models, one can fit each model with different options for the blood volume parameter V_B. V_B can be fixed (typically 5% in brain imaging), ignored or equivalently set to zero or optimised as a parameter in the model.

The fit of each model can be visually inspected, however a more robust method is to combine visual inspection with quantitative measures of parsimony in the form of information criteria. There are many different information criteria but all work similarly in that they trade off the fit of the model against how many parameters are in the model. One of the most commonly used information criteria is the bayesian information criteria (BIC) (Kass and Raftery 1995). With fitting to TACs, the fit of the model is evaluated using the residual sum of squares and therefore the BIC for a model i, BIC_i is calculated by,

$$BIC_i = \ln\left(\frac{RSS}{n}\right) + 2\ln(k) \tag{1.12}$$

where, RSS is the residual sum of squares in the region of interest, n is the number of datapoints (in this case the number of frames) and k is the number of parameters in the model.

The model with the lowest BIC value is the determined the most parsimonious model by the bayesian information criteria.

1.3.4 Outcome parameters quantifying radiotracer uptake

I will now turn my attention to how these analytical solutions to compartmental models describing tracer kinetics can be used to derive useful biological information about the tracer spatial distribution in the brain. If a bolus injection of radiotracer is administered, the compartmental systems presented will reach a steady state as $t \to \infty$.

In the case of the irreversible models, this steady state occurs when all the tracer has reached the compartment in which it is trapped. The net rate of trapping

from the plasma is given by the α_n in a general irreversible n-tissue compartment model and this value is often used as an outcome measure to quantify tracer uptake. For example, [^{18}F]FDG can be modelled effectively using an irreversible two-tissue compartmental model (Phelps et al. 1979) and here the net trapping rate is $\alpha_2 = \frac{K_1 k_3}{k_2 + k_3}$ (Li et al. 2014) (typically referred to as K_i).

For a reversible compartmental model, at equilibrium, the radiotracer is still moving between compartments but the total rate of efflux in each compartment is equal to the total rate of influx. The volume of distribution, V_T is defined to be the ratio of the concentration of radiotracer in the tissue to that in the plasma at equilibrium (Innis et al. 2007). For any irreversible model, $V_T = \infty$ and therefore holds little information. V_T is however, a frequently used outcome measure in pharmacokinetic studies to quantify radiotracer uptake when a reversible model provides the optimum fit to the TACs. For the reversible one-tissue compartmental model, $V_T = \frac{K_1}{k_2}$, for the reversible two-tissue compartmental model $V_T = \frac{K_1}{k_2}\left(1 + \frac{k_3}{k_4}\right)$ and more generally for the reversible n-compartmental model R. N. Gunn, S. R. Gunn, and Cunningham 2001 showed that,

$$V_T = \sum_{i=1}^{n} \frac{\alpha_i}{\beta_i} \tag{1.13}$$

where, α_i and β_i are defined in Equation 1.9.

Up until this point, I have only referred to compartments in each of the compartmental models as having different states. Mintun et al. 1984 introduced an outcome measure for PET neuroreceptor studies called binding potential which has the symbol BP_{ND} (Innis et al. 2007). The authors hypothesised that a tracer in the tissue was either specifically bound to the target or in some other state. The ratio of concentrations in the specifically bound compartment to all other states in the tissue at equilibrium defines the BP_{ND}. The tracer in these other states which is not specifically bound to the target have subsequently been defined to be non-displaceable (hence the ND in BP_{ND}). If the kinetics between all the states that make up the non-displaceable tracer are very fast, it is likely that a reversible two-tissue compartment model will best fit the data. When a reversible three-tissue compartment model best fits the data, it has been hypothesised that

the three compartments represent free, non-specifically bound and specifically bound tracer (Mintun et al. 1984).

Using V_T as the primary outcome measure in studies where the reversible two-tissue compartment model is the best fit is problematic as it is impossible to determine whether increased V_T is a consequence of a higher concentration of the target specific binding or a higher non-displaceable component. One can address this by using BP_{ND} as the outcome measure.

Calculating BP_{ND} can be done directly from the reversible two-tissue compartment model using $BP_{ND} = \frac{k_3}{k_4}$ but this has been shown to be unreliable especially when the kinetics between the non-displaceable and specifically bound compartments are fast (Lammertsma 2012). If a reversible one-tissue compartment model fits the data, direct calculation of BP_{ND} is infeasible. A more robust quantification can be achieved by calculating BP_{ND} indirectly using a reference region. A reference region is a region of interest defined which is known to have no target present and therefore can be hypothesised to have zero specific binding and so the signal in these regions results only from the non-displaceable states. The BP_{ND} for a target region is calculated indirectly Equation 1.14 (Lammertsma, Bench, et al. 1996).

$$BP_{ND} = \frac{V_T^{Target}}{V_T^{Ref}} - 1 \tag{1.14}$$

where V_T^{Target} is the volume of distribution in the target region and V_T^{Ref} is the volume of distribution in the reference tissue.

1.3.5 Simplified reference tissue model

Whilst compartmental models are the gold standard in terms of quantification, they require the placement of an arterial cannula which is an invasive procedure which can be uncomfortable to the patient. Reference tissue models can be used to obtain BP_{ND} without the requirement for an arterial cannula to be placed (R. N. Gunn, Guo, et al. 2011).

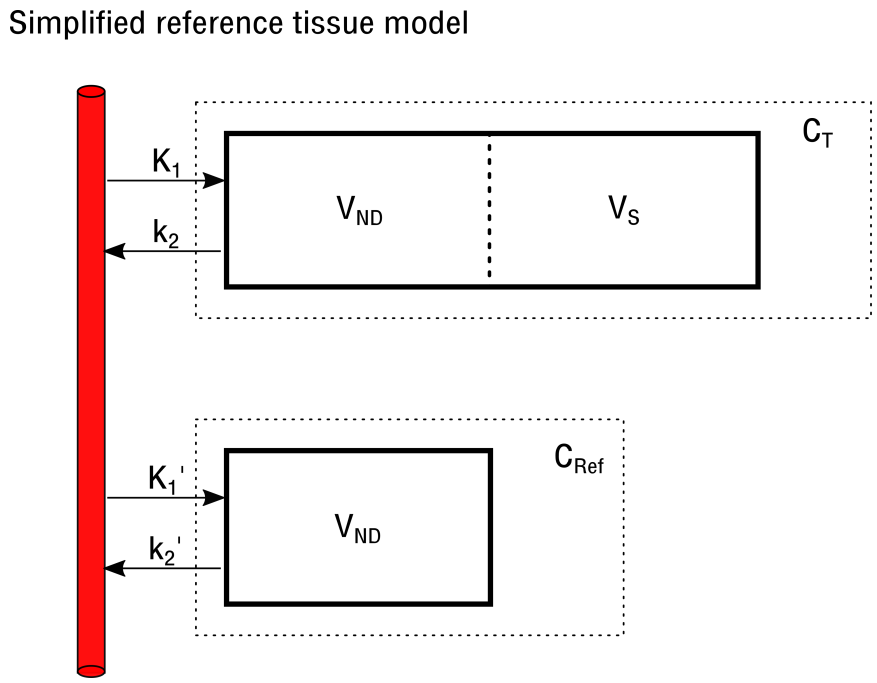


FIGURE 1.6: Simplified reference tissue model (SRTM) : The model assumes that the reference tissue is devoid of target and therefore all signal observed there is non-displaceable signal

The simplified reference tissue model (SRTM) introduced by Lammertsma and Hume 1996 is a model which is widely used in quantitative PET studies (Salinas, Searle, and R. N. Gunn 2015). A model schematic is shown in Figure 1.6. The model makes four key assumptions (Salinas, Searle, and R. N. Gunn 2015),

- The reference region is devoid of target
- The kinetics of the both the target and reference region can be described using a one-tissue compartmental model
- The contribution of whole blood to the signal is negligible
- The non-displaceable signal in the target region and the reference region are equal

Lammertsma and Hume 1996 showed that the observed signal in the target tissue, $C_T(t)$ can be described by Equation 1.15.

$$C_T(t) = R_1 C_{Ref}(t) + \left(k_2 - \frac{R_1 k_2}{1 + BP_{ND}}\right) C_{Ref}(t) \otimes e^{-\frac{k_2}{1+BP_{ND}}t} \tag{1.15}$$

where, $R_1 = \frac{K_1}{K_1'}$ is the ratio of the delivery of the tracer to the tissue in the target region and reference region, $C_{Ref}(t)$ is the reference region time activity curve, BP_{ND} is the binding potential in the target region and k_2 is the rate of transfer of radiotracer from the target tissue to the plasma. A value for BP_{ND} can be obtained by optimising the three parameters R_1, k_2 and BP_{ND} so that the sum of squares of residuals of the target tissue time activity curve and $C_T(t)$ is minimised. Reference tissue models offer an attractive option to quantify specific tracer uptake without the need for the invasive procedure of placing an arterial cannula but as R. N. Gunn, Guo, et al. 2011 note, validation of these methods is necessary and is paramount and particular attention should be paid "whether the reference region is truly devoid of the target, the model simplification is appropriate and the blood volume contribution to tissues is accounted for" (R. N. Gunn, Guo, et al. 2011). In their recent paper, Salinas, Searle, and R. N. Gunn 2015 ran simulations to show the impact of violating the assumptions made with SRTM. Both a reference tissue which is not completely devoid of the target and a reference tissue which does not have same level of non-displaceable binding as the target produce negative biases in the true binding potential of over 100% if the true $BP_{ND} < 1$ (Salinas, Searle, and R. N. Gunn 2015). Choice of reference is therefore paramount if reference tissue models are to be used for quantifying tracer uptake.

The BP_{ND} calculated using an arterial input compartmental model is often used to validate BP_{ND} values calculated using the SRTM. This method of validation is good for checking if the assumptions that the kinetic behaviour of the tracer in both the reference and target tissue can be represented by a reversible one-tissue compartment model and that the the blood volume component of the signal in negligible. However, indirect calculation of BP_{ND} requires a reference region and therefore assessment of the validity of that reference region is challenging. It is important to choose the reference region using interpretation from both imaging data and post-mortem data. Post-mortem studies reveal the distribution of target in a given disease and can guide the choice of reference region.

1.3.6 Standardised uptake tissue ratio

The SRTM does not require an arterial cannula to be placed but it does still require the subject to lie still in the scanner for the full duration of scan which is typically over 60 minutes. This can be uncomfortable for patients. In addition, this duration in the scanner is prohibitively long and expensive for high throughput studies involving large numbers of patients both. Static images provide a way of quantifying tracer uptake with the patient spending only around 20 minutes in the scanner.

The patient is scanned for a short period (often 20-30 min) of time typically 30-50 minutes after injection (although the optimal time window varies with tracer). The aim after reconstruction is to produce a 3D volume that represents the average tracer distribution in the scanning window. A regional standardised uptake value ratio (SUVr) is simply calculated by taking the mean value from voxels in the target region and dividing by the mean value of voxels in the reference region (Jagust, Landau, et al. 2016).

SUVr is frequently used as a cost-effective way to quantify tracer uptake in PET however as with reference tissue models, SUVr should only be used after it has been validated against full quantitative analysis using an arterial input function. SUVr does not take into account any signal resulting from the whole blood and importantly for studies in neurodegeneration it assumes that the delivery of radiotracer to the tissue is consistent across the brain (Lammertsma 2017).

1.3.7 Parametric images

All the methods presented above are concerned with quantifying tracer uptake in an ROI. It is possible to quantify tracer uptake at the voxel level using the same models. One can think of each voxel being an ROI with a TAC in exactly the same way as an ROI is defined as a group voxels. Fitting at the voxel level however, is computationally expensive and directly fitting compartmental models and the simplified reference tissue model would take too long for most

studies. The paper published by R. N. Gunn, S. R. Gunn, Turkheimer, et al. 2002 shows how basis functions can be used to speed up the fitting of each of the compartmental models and SRTM. The result is a 3D parametric image for each of the parameters in the model. For instance, for the reversible one-tissue compartment model, parametric maps for K_1 and k_2 are produced. One can then easily created a parametric map for V_T by dividing the K_1 map by the k_2 map.

For SRTM, fitting produces parametric maps for the three parameters, R_1, k_2 and BP_{ND}. The BP_{ND} map gives a voxel-level quantification of tracer specific binding. This is especially useful if the spatial distribution of the target (other than the fact it is not in the reference region) is unknown. BP_{ND} parametric maps are also provide information on the spatial consistency of the tracer uptake across subjects which can be lost when using larger ROIs. It should be noted however, that in fitting at the voxel level one assumes that the model is valid in all voxels. This assumption could be violated and therefore caution should be used when drawing conclusions on signal only from parametric images. In particular, high BP_{ND} in very small clusters or individual voxels can result from poor fitting (often caused by noisy data) rather than true signal.

1.4 Conclusion

In this chapter, I have introduced the imaging modalities of PET and MRI.

The physics of MRI were briefly explained and examples of structural T1-weighted structural images and diffusion tensor images were presented. T1-weighted structural images will be used throughout this thesis to define regions of interest in PET studies. Automated algorithms for segmenting the tissue classes in the brain were discussed and again these will be used extensively in Chapters 3, 7 and 8. Connections between cortical regions which have been imaged using diffusion tensor imaging are used in Chapter 4.

PET data is however the primary focus of this thesis. The physics underlying the production of the PET signal was explained in this chapter along with how this signal is reconstructed to create dynamic 4-dimensional images. One of the main themes of this thesis is quantifying tracer uptake; both from static and dynamic PET data. In this chapter, I discussed required motion correction to facilitate robust quantification and different model-driven methods for quantifying tracer uptake. Compartmental models and the SRTM outlined in this chapter are used in Chapters 7 and 8 with dynamic PET data both at the ROI and the voxel-level. SUVr is used as the primary outcome measure for disease progression modelling in Alzheimer's disease in Chapters 4 and 5 and in Chapter 6 a novel outcome measure for quantifying static images is introduced and compared to SUVr.

In the next chapter, I show how the modalities of MRI and PET have been used to study different neurodegenerative processes and outline how this thesis will add to the literature in this field.

Chapter 2

PET in Alzheimer's disease, traumatic brain injury and corticobasal degeneration

In Chapter 1, I introduced the imaging modalities of MRI and PET, explained how images were obtained and presented different methods of quantifying PET imaging data. In this chapter, I give background on AD, Corticobasal degeneration (CBD) and traumatic brain injury (TBI) and review how PET imaging data has been used to further our understanding of neurodegenerative diseases. Specifically, I concentrate on imaging of misfolded proteins in neurodegenerative diseases. I show how Aβ PET imaging has been used to investigate the spatiotemporal distribution of Aβ in AD previously and identify how previous mathematical models can be improved. I also review how novel ligands have been used to attempt to quantify the tau burden on patients suffering from neurodegenerative diseases. Finally, I present an outline of the remainder of the thesis.

2.1 Alzheimer's disease

AD is a chronic, progressive and ultimately fatal neurodegenerative disease (Masters et al. 2015) which is the most common cause of dementia worldwide (Scheltens et al. 2016). Patients commonly suffer from cognitive impairment and executive dysfunction and more rarely visual and language problems (Barnes et al. 2015; Murray et al. 2011; W M van der Flier et al. 2011).

5-7% of people over 60 years of age and an estimated 40 million people worldwide suffer from dementia and this number is projected to double in the next 20 years (Prince et al. 2013). This increase will put a heavy socio-economic burden on society. The financial cost of caring for these patients will become in many countries unaffordable and AD severely affects the quality of life of both the patient and the carer (Masters et al. 2015). The need for effective therapeutics is obvious however, it is my opinion that these are unlikely to be found without a greater understanding of the disease.

2.1.1 Pathophysiology of AD

In 1907, Alois Alzheimer identified proteinaceous deposits on brain in a histopathological study of a woman suffering from dementia (Alzheimer 1907) which were subsequently found to be neurofibrillary tangles (NFT) and neuritic plaques. The proteins making up these deposits are similar to healthy proteins but have a different 3D structure and so are commonly referred to as misfolded proteins (Gregersen et al. 2006). They are now considered the pathological hallmarks of AD and evidence suggests they play a key role in the disease (Scheltens et al. 2016). As neurodegenerative processes occur, cell deaths result in widespread atrophy which in turn are thought to cause the cognitive and behavioural decline seen in AD.

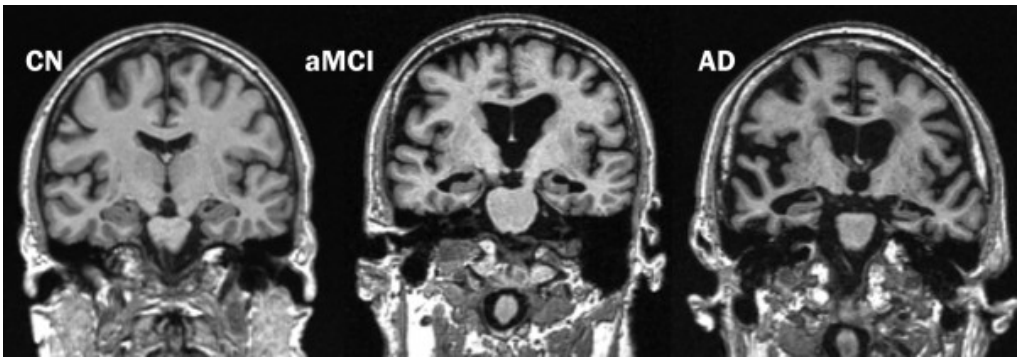


FIGURE 2.1: MRI images at different stages of cognitive impairment; cognitively normal (CN), amnestic mild cognitive impairment (aMCI) and AD. [Image taken from Vemuri and Jack 2010]

Figure 2.1 taken from a Vemuri and Jack 2010 shows coronal sections from structural T1-weighted MRI scans of typical subjects with different levels of cognition. The cognitively normal subject (CN) on the left shows little sign of any abnormalities, whereas the amnestic mild cognitive impairment (aMCI) and AD patients have enlarged ventricles and clear cortical atrophy. The level of atrophy is increased in AD compared to aMCI in line with neurodegeneration being a progressive and irreversible process (Fox et al. 1999; Sluimer, W M Flier, et al. 2009; Sluimer, Bouwman, et al. 2010).

Almost 80 years after Alois Alzheimer first noted the pathognomonic signs of AD, Glenner and C. W. Wong 1984 isolated amyloid-β (Aβ) peptide as being a major component of neuritic plaques. Work in the next 8 years provided evidence that Aβ plays a key role in the pathogenesis of AD (Goate et al. 1991; J. Hardy and Allsop 1991; Selkoe 1991). In 1992, the first articulation of the 'Amyloid cascade hypothesis' (J. A. Hardy and Higgins 1992) was published. It posits that Aβ is a driving factor in patients developing dementia. In it's current form (Figure 2.2), it is hypothesised that Aβ molecules are formed from the cleaving of the amyloid precursor protein (APP). Aβ then aggregates which leads to soluble oligomers and the deposited Aβ peptide as discovered by Alzheimer 1907. Further, the hypothesis states that, this not only occurs prior to, but causes the formation of NFT which in turn causes neuronal death and eventually dementia.

Whilst the hypothesis is appealing, it remains far from universally accepted.

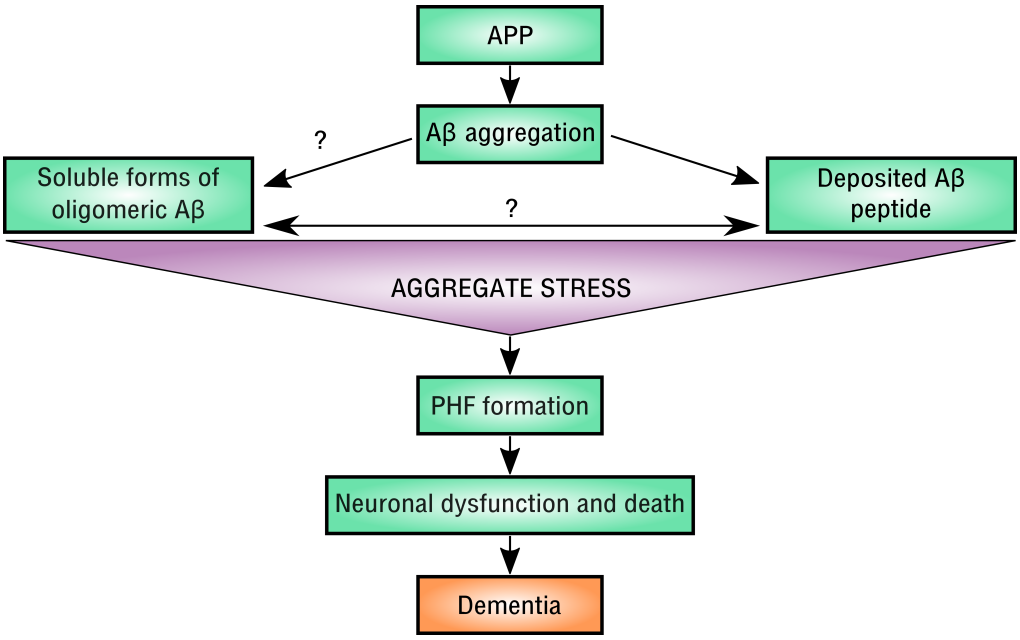


FIGURE 2.2: Flow diagram representing the amyloid hypothesis. APP is cleaved causing Aβ aggregation and subsequently amyloid deposits. A combination of deposited amyloid and soluble amyloid causes tau pathology and then neuronal dysfunction, cell death and dementia. (Figure adapted from Karran, Mercken, and Strooper 2011)

The hypothesis infers a cause and effect relationship generated from a correlation and with current data it is still possible that Aβ accumulation results from other processes rather than causes AD. Moreover, in the 20 years since its introduction, data has been published which contradicts the expected findings from the hypothesis. Firstly, there have been repeated findings of healthy controls showing deposits of Aβ similar to those found in AD patients (Crystal et al. 1988; Price and Morris 1999; Klunk et al. 2004). One potential explanation of this, is that these subjects are in the early stages of the disease and will go on to develop dementia in the future. Secondly, H. Braak and E. Braak 1991 have shown that tau pathology occurs in some regions of the brain in the absence of Aβ. It is possible that Aβ accumulation in one region could cause NFT formation in another but it is also possible that the two occur from parallel processes and don't interact at all (S. A. Small and Duff 2008).

It therefore seems likely that, the aggregation of Aβ and the formation of oligomeric Aβ and deposited Aβ peptide does play a role in AD and that Aβ aggregation does occur prior to the formation of NFT, however the interaction between Aβ

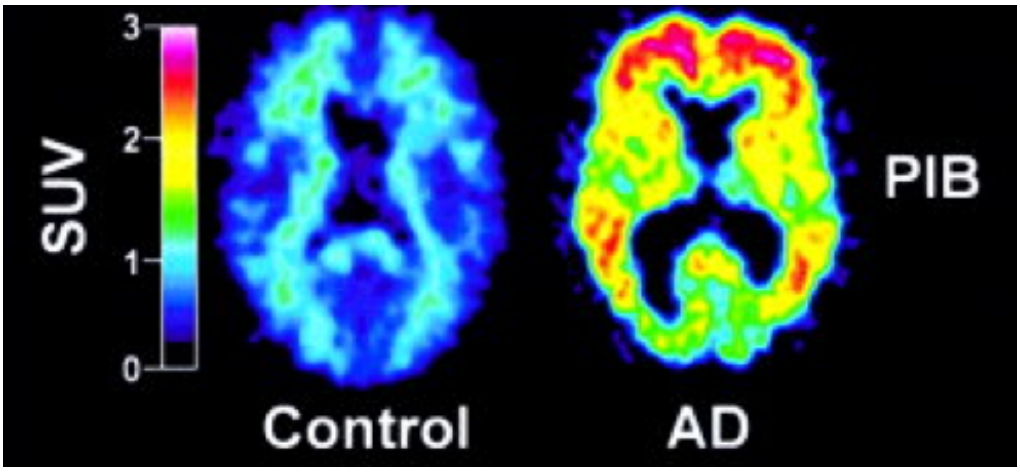


FIGURE 2.3: PiB images in healthy controls and AD (Image taken from Klunk et al. 2004). There is increased tracer uptake in AD when quantified with SUV.

and tau and neuronal loss is poorly understood and their relationship is likely to be complex rather than a simple linear cause and effect (S. A. Small and Duff 2008; Scheltens et al. 2016).

Only by elucidating these interactions and biological processes, will it be possible to fully understand the causes of AD and develop effective novel therapeutics to slow or even reverse decline.

2.2 Aβ imaging in AD using PET

A major step forward in AD research came with the ability to image Aβ pathology *in vivo* using PET. An explosion of Aβ imaging studies followed Klunk et al. 2004 after they showed the first use of the radiotracer [^{11}C]Pittsburgh compound B ([^{11}C]PiB) in humans. [^{11}C]PiB was developed to image Aβ *in vivo*. The paper showed that [^{11}C]PiB had a high specificity for Aβ and using SUV as a quantification method the authors showed increased binding in AD subjects in comparison to healthy controls (see Figure 2.3). Since it's introduction, [^{11}C]PiB has been extensively used to image Aβ pathology in a range of neurodegenerative diseases.

One obvious disadvantage of PiB is that it is labelled with ^{11}C which has a short half-life making it infeasible to use it in centres that don't have a cyclotron on

site. To address this, a group of tracers based on the a similar chemical structure but labelled with ^{18}F were developed such as Flutametamol, Florbetaben and Florbetapir (Saidlitz et al. 2014). Florbetapir (or equivalently [^{18}F]AV45) showed a sensitivity of 95% and a specificity of 95% (Newberg et al. 2012) which is the highest reported of all the aforementioned Aβ tracers and Clark, Schneider, and Bedell 2011 reported that binding had a strong agreement with post-mortem analysis.

Static Aβ PET data is now routinely collected in large cross-sectional and longitudinal studies (Mueller et al. 2005; Rowe et al. 2010; Haas et al. 2016). In the United States of America, static Aβ PET imaging has been approved by the food and drug administration (FDA) to decide whether a subject is "Amyloid positive" or "Amyloid negative". Importantly, on its own, it cannot provide a diagnosis of AD and in fact is more useful for "ruling out" AD (Kepe et al. 2013). Typically, scans are classified by visual inspection (Yang, Rieves, and Ganley 2012). Negative scans exhibit binding only in the white matter which is a consequence of known high levels of non-specific binding (Kepe et al. 2013) whereas positive scans have increased binding in cortical grey matter (Yang, Rieves, and Ganley 2012). Whilst this approach has shown a good level of reliability (Yang, Rieves, and Ganley 2012), there are still test-retest discrepancies and it is a financially costly way of classifying images. A more desirable option would be to have an automated way of classifying scans or perhaps even better, a reliable continuous outcome measure, calculated automatically which summarises the global Aβ burden.

Mean cortical SUVr and mean composite SUVr[1] have been used extensively as a method of quantifying the global Aβ burden (K. A. Johnson, Sperling, et al. 2013; Jagust, Landau, et al. 2016) in research. The reference region is often the grey matter Cerebellum (Jack et al. 2013; Jagust, Landau, et al. 2016) although recently using a composite white matter reference has been suggested with longitudinal data due to the observed lower lever of variability (Landau, Fero, et

[1] Mean cortical SUVr has the target region as all voxels in the cortex and mean composite SUVr has the union of 4-5 large ROI as its target region. Both aim to provide a single outcome measure for the scan which represents the global level of binding across the brain.

al. 2015). For clinical use, it has been suggested that a cut-off value should be used to quantitatively classify scans as positive or negative (Clark, Schneider, and Bedell 2011; K. A. Johnson, Sperling, et al. 2013). I believe this to be missing an opportunity; there is more information in retaining the continuous outcome measure of SUVr. By performing a binary classification, one loses most of the information which SUVr provides. This information could prove useful in tracking progression of disease and assessing the efficacy of novel therapeutics.

In summary, whilst Aβ PET imaging provides rich information on Aβ pathology, there is a way to go before a fully automated pipeline for quantification is used routinely both in research and in a clinical setting.

2.3 Spatiotemporal modelling of Aβ in AD

Mathematical modelling allows us to characterise Aβ accumulation and potentially provides information on the mechanism by which this occurs. Previous mathematical modelling in AD has provided a temporal characterisation of different biomarkers for AD (Jack Jr, Knopman, Jagust, Petersen, et al. 2013) but imaging biomarkers were confined to global measures. In this section, I focus on the spatiotemporal distribution of Aβ in AD progression and review relevant mathematical models for this application. Initially, I describe the known stereotypical spatiotemporal distribution which has been characterised using post-mortem data (H. Braak and E. Braak 1991). I then review two previous spatiotemporal models for AD and assess the strengths and weaknesses of each. Finally, I identify the ideal characteristics for a mathematical model for the spatiotemporal distribution of Aβ

2.3.1 Spatiotemporal distribution of Aβ in AD

In their seminal paper, H. Braak and E. Braak 1991, characterised the stereotypical regional accumulation pattern of Aβ neuritic plaques and NFT seen in AD using post-mortem data from 83 subjects. This Braak staging is still used today

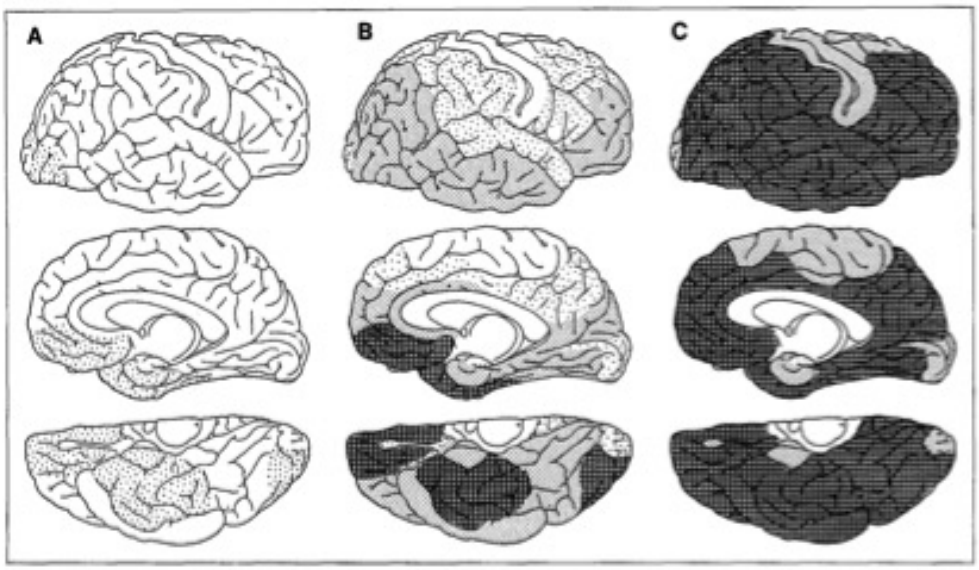


FIGURE 2.4: Braak Staging of amyloid pathology. The level of deposition is categorised into 3 stages. In stage A deposition is localised to the frontal, temporal and occipital lobe, stage B sees pathology spread to all regions apart from the primary sensory and primary motor field and at stage C all areas are affected. (Image adapted from H. Braak and E. Braak 1991)

as a way to track the pathological progression of the disease. Figure 2.4 defines three 'Braak stages'; Stage A, Stage B and Stage C. At Stage A, low densities of Aβ deposits are found in the isocortex, particularly in the basal portions of the frontal, temporal and occipital lobe. At Stage B there is an increase in concentration of Aβ in almost all isocortical association areas and only the primary sensory areas and primary motor field remain almost devoid of deposits. There is a mild involvement of the hippocampal formation and Aβ may be found in the entorhinal cortex. Stage C is mainly characterised by the fact that virtually all isocortical areas are affected, while deposits in the hippocampal formation show the same pattern as Stage B. This spatiotemporal distribution suggests that the regions are involved hierarchically (Thal, Rüb, et al. 2002) and potentially that Aβ could be spreading from seed regions of the brain (Iturria-Medina and Evans 2015).

The approach used by H. Braak and E. Braak 1991 provided the first real characterisation of where in the brain Aβ accumulates during neurodegeneration but there is an opportunity to improve this characterisation using *in vivo* PET data.

To date, large cohort cross-sectional Aβ PET studies have been performed (Jagust, Landau, et al. 2016) but analysis has mainly focused on classifying the distinct clinical phases of the disease. This approach has provided relatively little information about the way Aβ plaques accumulate over time. Longitudinal studies have either been restricted to short time windows of no more than 2 years (Jagust, Landau, et al. 2016) or to studying the average deposition across the whole cortex (Jack et al. 2013).

Therefore, it is difficult with the currently available data to study the spatiotemporal distribution of Aβ across the disease spectrum directly. However, mathematical modelling has been used to attempt to better understand the mechanism by which Aβ accumulates using datasets which are currently available.

2.3.2 Heterogeneity in Aβ concentration: spreading from seed regions or a result of differences in properties of the local tissue environment?

The stereotypical accumulation pattern of Aβ in AD exhibits heterogeneity in concentration of Aβ across the brain at all stages of disease but the cause of the different concentrations is yet to be elucidated.

One hypothesis is that, Aβ concentrations are determined by properties of the local tissue environment. That is, varying levels of a given property of the tissue in different regions facilitates different levels of Aβ accumulation (Buckner, Snyder, et al. 2005; Bero et al. 2011; Jagust and Mormino 2011; Hafkemeijer, Grond, and Rombouts 2012; Spires-Jones and Hyman 2014). An example property which has been investigated is neuronal activity. There is evidence that the level of Aβ accumulation is increased when neuronal activity is increased (Bero et al. 2011). Further, correlations have been drawn between the common Aβ accumulation pattern and regions in the default mode network (Buckner, Snyder, et al. 2005; Hafkemeijer, Grond, and Rombouts 2012; Buckner, Andrews-Hanna, and Schacter 2008). This network is a set of connected regions that are

active even when the brain is not focussed on the external environment (Buckner, Andrews-Hanna, and Schacter 2008). The hypothesis is that these regions have constant increased neuronal activity which then causes increased Aβ accumulation (Buckner, Snyder, et al. 2005).

A second hypothesis is that, Aβ originates in a small number of seed regions and over the duration of the disease spreads to other brain regions. In fact, this is a combination of two hypotheses. Firstly, that misfolded forms of Aβ induce misfolding in healthy forms of the molecule in what is called a prion-like manner and secondly, that Aβ spreads across the brain through white matter connections.

The hypothesis that Aβ behaves in prion-like manner is not a new one. More than 35 years ago, Prusiner 1984 published an article with the hypothesis. More recently, evidence from *in vitro* data has increased interest. Perhaps most importantly, Nussbaum et al. 2012 and Nath et al. 2012 report prion-like behaviour for Aβ and that the interaction with tau causes neurotoxicity. Domert et al. 2014 go further and associate the prion-like behaviour to be a consequence of poor clearance.

Evidence for Aβ spreading along white matter tracts is less compelling with most arguments showing a correlation between the known uptake of Aβ and the brains' white matter architecture (Brettschneider et al. 2015; Palop, Chin, and Mucke 2006).

2.3.3 Previous mathematical models for the spatiotemporal distribution of Aβ in AD

I will briefly review two previously published spatiotemporal models used for misfolded proteins in AD. Both models hypothesise that misfolded proteins spread along white matter tracts.

Raj, Kuceyeski, and Weiner 2012 were able to predict atrophy patterns as measured by MRI in AD using a network diffusion model. There were however, weaknesses to the work. Firstly, the network diffusion model did not directly

model accumulation of Aβ, tau or any other specific process but rather the flow of "disease pathology" through the brain. A higher concentration of disease pathology was hypothesised to give greater atrophy. The interactions between proteinaceous deposits and neuronal loss is complex, temporally nonlinear and not yet fully understood and therefore this assumption seems an oversimplification. Secondly, the model predicts that the global amount of "disease process" in the brain remains constant but is just distributed differently which is not what was observed in post-mortem data (H. Braak and E. Braak 1991).

An alternative model to the one proposed by Raj, Kuceyeski, and Weiner 2012 was published by Iturria-Medina, Sotero, et al. 2014. They applied an epidemic spreading model to Aβ PET data . Similar models have been used to describe a wide range of processes from modelling the spread of an infective disease across planet earth to the spread of forest fires (Barthelemy et al. 2005). In this setting, Iturria-Medina, Sotero, et al. 2014 model the spread of Aβ across the brain from an epicentre where accumulation is hypothesised to originate. Importantly however, the epicentre had a production rate and each individual region had it's own clearance rate meaning that the global load of Aβ in the model could increase. The validity of the model was tested on cross-sectional Aβ data. Initially, [^{18}F]-AV45 SUVr values for cortical regions were converted into a probability that each region was in an "infested state". These probabilities were the data that the model was fitted to. After fitting the model to the data results indicated that poor clearance rather than increased production may be the cause of Aβ aggregation (Iturria-Medina, Sotero, et al. 2014).

The model proposed by Iturria-Medina, Sotero, et al. 2014 is a great improvement however it does not predict SUVr values directly which means that interpretation of the findings can be difficult. One is forced to ask the question; if a region has a probability of 1 that it is in an infested state, what does that imply? A model which predicts SUVr values would be far more appealing and may lead to easier interpretation of the results. Finally, the model proposed by Iturria-Medina, Sotero, et al. 2014 didn't show a direct comparison between

production of Aβ in every region and production only occurring in an epicentre. To evaluate the hypothesis that distal spreading is a key process in the build up of Aβ pathology, it would be desirable to be able to compare an equivalent models which had only local processes and no distal spreading.

An ideal model for the spatiotemporal distribution of Aβ would accurately describe the spatiotemporal distribution of Aβ in AD similar to that of the one proposed by Iturria-Medina, Sotero, et al. 2014 but it should also SUVr values directly because then one would be able to provide a predicted SUVr for all stages of the accumulation process which makes the model easily applicable to other data and falsifiable. Additionally, it would be beneficial if results from the model could provide information regarding the processes that drive accumulation rather than just fit the data. As previously stated, Iturria-Medina, Sotero, et al. 2014 only presented a spreading model rather than comparing a spreading model to an equivalent non-spreading model and an ideal model would allow the importance of different processes to be tested.

2.4 Corticobasal degneration

CBD is a rare neurodegenerative disease associated with movement abnormalities or Parkinsonism, behavioural and cognitive symptoms. It was first identified by Rebeiz, Kolodny, and Richardson 1968 and now it has been classified as one type of a group of neurodegenerative diseases called FTD (V. M.-Y. Lee, Goedert, and Trojanowski 2001). Patients usually experience the first symptoms over the age of 40 and a typical disease duration is 7 years (Mahapatra et al. 2004).

Prevalence estimates of CBD are poor due to a shortage of high quality data. It is estimated there are 4.9–7.3 cases per 100,000 individuals (Mahapatra et al. 2004; Winter et al. 2010) however these results only come from a small number of studies and these numbers should be treated with caution.

It is difficult to accurately diagnose CBD due to the overlapping symptoms with other neurodegenerative diseases such as AD and other FTDs. Often, a reliable diagnosis can only be achieved with a neuropathological examination (Kouri et al. 2011). It been estimated that 25-56% of cases are correctly diagnosed ante-mortem (Litvan et al. 1997; Armstrong et al. 2013). This wide range reflects the lack of good quality prevalence data.

The core neuropathological feature of CBD is elevated levels of tau protein (see a more detailed outline of this in subsection 2.6.1). Similar to AD, tau accumulation is thought to drive atrophy in CBD. Structural T1-weighted MRI scans have revealed levels of atrophy are asymmetric with the motor, frontal and parietal cortices being primarily affected (Boxer et al. 2006).

Disease pathology as measured by neuroimaging could improve the accuracy of diagnosis markedly as there is less overlap between the neuropathological features of CBD and other neurodegenerative diseases than there is in the clinical presentation. This in turn, is likely to provide neuropathological insight and speed up the development of disease-modifying treatments.

2.5 Traumatic brain injury

TBI is becoming a heavy socio-economic burden throughout the world. Although, high-quality prevalence figures are hard to obtain, it was recently estimated that 3.7 million people have suffered TBI in Europe alone (Gustavsson et al. 2011). The financial cost of caring for these patients is becoming prohibitively high.

There has been some controversy over the definition of TBI (Roozenbeek, Maas, and Menon 2013). Menon et al. 2010 introduced the following definition; “TBI is defined as an alteration in brain function, or other evidence of brain pathology, caused by an external force”. In the definition, the authors add explanation that the external force could be the head being struck by an object, the head striking

an object, the brain undergoing an acceleration movement without direct external trauma to the head, a foreign body penetrating the brain, forces generated from or events such as a blast or explosion. In my opinion, the definition given by Menon et al. 2010 has some ambiguity, particularly surrounding what is defined to be an "alteration in the brain", but it does provide the first attempt to define TBI in one simple statement, which is necessary in order to obtain better prevalence figures.

Patients suffering TBI often go on to have poor outcomes after the initial injury. Alongside, increased morbidity and mortality rates (Tagliaferri et al. 2006), patients often develop behavioural problems many years after the initial injury (Sharp, Scott, and Leech 2014; Mckee and Daneshvar 2015). It is well known that TBI is a risk factor for developing progressive disorders of cognitive impairment leading to dementia (Fleminger et al. 2003; Plassman et al. 2000; Lye and Shores 2000). Indeed, TBI is has been estimated to cause a 2-4 fold increase in risk of developing dementia in later life (Medicine 2009; Shively et al. 2012). It is also a risk factor for a wide range of neurodegenerative diseases such as AD, Parkinsons disease, amyotrophic lateral sclerosis (ALS), and Creutzfeldt–Jakob disease (CJD) (Mckee and Daneshvar 2015). Post-mortem studies have revealed Aβ plaques and NFT are found in subjects who suffered a single or multiple TBI (Gentleman et al. 1997; Ikonomovic et al. 2004; DeKosky et al. 2007; McKee, Cantu, et al. 2009; Mez et al. 2017) and some believe this to be the link between TBI and dementia (Shively et al. 2012; Mez et al. 2017). More evidence that long-term effects of TBI can include neurodegeneration comes from chronic traumatic encephalopathy (CTE). CTE is a neurodegenerative disease caused by repeated mild TBI often resulting from sports and blast injuries (McKee, Cantu, et al. 2009). The tau pathology of CTE is unique from other neurodegenerative diseases in that its has a different spatial distribution in the brain (see section 2.6.1) (Stein, Alvarez, and McKee 2014).

One of the greatest problems with studying the chronic effects of TBI is that it is difficult to determine whether a TBI caused neurodegeneration and cognitive

decline or whether it just happened before already inevitable neurodegenerative disease such as AD. If dementia is caused by TBI, then the connection between the acute injury and the chronic phase is still poorly understood and a greater understanding of the pathophysiological changes and their causes is paramount. This knowledge will guide the development of therapeutics to mediate these changes and give potentially patients a better outcome after TBI.

2.6 Imaging tau *in vivo* using PET

A consistent finding in histopathological studies of neurodegenerative diseases is the presence of misfolded tau protein. It was first isolated as the major constituent of NFT in AD by Grundke-Iqbal et al. 1986. In this section, I review the developments and challenges of imaging tau protein *in vivo* using PET. First, I consider the target of interest. Tau has different presentations *in vivo* in both in its spatial distribution and its structure. These presentations cause the level of radiotracer binding to vary greatly between different disease groups. Second, I introduce the desirable features for a tau PET radiotracer and finally I review tau PET radiotracers which have been used to date. Importantly, by combining information from both *in vivo* and post-mortem studies I investigate limitations of the current tau tracers.

2.6.1 Tau in neurodegenerative diseases

Tau is a microtuble associated protein. In healthy brain, microtubules aid in the structural integrity and morphology of neurons and the assembly and stability of microtubules, in turn, are maintained by microtubule-associated proteins (H.-G. Lee et al. 2005). Tau occurs in 6 different isoforms which are split into two classes; 3-repeat (3R) and 4-repeat (4R) isoforms. In healthy brain, the ratio between 3R and 4R tau is 1:1. When tau accumulates, this ratio is often affected. Tau can aggregate in different conformations such as paired helical filaments (PHF) and straight filaments. I will briefly outline the key features of the tau deposits seen in AD, TBI and CBD.

Tau accumulation in TBI and AD As I have previously mentioned, NFT which are primarily formed of hyperphosphorylated tau protein are one of two pathological hallmarks of AD and similarly, TBI subjects often have widespread tau pathology at post-mortem (McKee, Cantu, et al. 2009; D. H. Smith, V. E. Johnson, and Stewart 2013). Aggregated tau is thought to play key role in neurodegeneration as post-mortem studies have shown that there is a strong correlation between the NFT load and cognitive ability in a variety of neurodegenerative diseases (Nelson et al. 2012; Ikonomovic et al. 2004; Mitsis et al. 2014; McKee, Cantu, et al. 2009). Hyperphosphorylation is thought to lower the ability of tau to bind with microtubules which in turn causes tau aggregation (Grundke-Iqbal et al. 1986). Tau aggregation causes PHF and NFT to form in the intracellular space (Hoenig et al. 2017). The aggregates are formed of both 3R and 4R isoforms however McKee, Stein, et al. 2013 have reported less 3R tau in CTE. The spatial distribution of tau in AD has been extensively studied. A characterisation into 6 Braak stages (Stage I to Stage VI) was performed by H. Braak and E. Braak 1991 using post-mortem data from 60 subjects. Initially, tau deposits are confined to the entorhinal cortex but as the disease progresses, the rest of the temporal lobe is affected and by the Stage VI tau pathology is seen in the whole isocortex. A full characterisation in subjects with only a single TBI has yet to be performed, however the spatial distribution of tau in CTE has been studied where McKee, Stein, et al. 2013 discovered distinctive perivascular NFT and an irregular cortical distribution of tau but with higher concentrations observed in the sulci of the cortex.

Tau in CBD Patients with CBD, like AD and TBI, have elevated levels of tau which are thought to play a key role in the disease. There are however, differences in the way it accumulates. The accumulated tau is hyperphosphorylated 4R-tau only and accumulates to form swollen, achromatic neurons and astrocytic plaques (Komori 1999; Wakabayashi and Takahashi 2004) rather than PHF and NFT. The spatial distribution of the aggregated tau is also different. The most affected areas are the frontal lobe, parietal lobe and the basal ganglia and accumulation occurs in both the grey and the white matter (Forman et al. 2002).

In stark contrast to AD, the occipital lobe remains devoid of tau pathology (Forman et al. 2002).

In summary, the role of tau in neurodegenerative diseases is far from being elucidated however all the evidence from post-mortem studies points to it playing a key role in pathogenesis. Post-mortem assessments give an accurate measurement of tau levels post-mortem but a key step in understanding more will be quantifying tau pathology *in vivo*.

2.6.2 Radiotracer design for tau PET

An ideal radiotracer for neuroimaging will be non-toxic, cost-effective and easily synthesised molecule which is lipophilic enough to cross the blood-brain barrier (Villemagne and Okamura 2014). Further, it should exhibit a high selectivity and specificity for the target of interest, exhibit a low level of non-specific binding and therefore produce a high signal-to-noise ratio (Villemagne, Furumoto, et al. 2014). Finally, tracers should be rapidly cleared from the blood (Laruelle, Slifstein, and Huang 2003; Pike 2009). A tracer which is cleared rapidly is described as having fast kinetics and this is important for a tracer as it means the system gets closer to equilibrium in the duration of a scan and allows for more accurate quantification.

For tau tracers, selectivity is an especially important issue. Developed tau tracers have been designed to bind to the structure of PHF however this structure is not unique (Okamura, Harada, et al. 2014). Aβ has a similar structure and the availability of Aβ deposits is thought to be approximately 5-20 times greater than that of tau Villemagne and Okamura 2014. Simulations suggest that this implies that a tau tracer will require at least a 20-50 fold selectivity for PHF over Aβ to give reliable data in the presence of both pathologies (Schafer et al. 2012).

As has previously been mentioned, there are two classes of aggregated tau - 3R and 4R - and level of expression of each of these classes is different in different neurodegenerative diseases. Only by characterising the binding to both these classes, is it possible to decide what an elevated signal implies. If one wants to

quantify the total tau load on a subject, then tau tracers need to have similar affinities for both classes. In future, it may be useful to develop tracers which are specific to different isoforms.

Several novel tracers have been developed with the aim of giving reliable quantitative data on the expression of tau *in vivo*. Here, a brief review of the data produced is presented.

[^{18}F]FDDNP In the early part of the previous decade the first attempts to develop a tracer for imaging AD pathology were made. [^{18}F]FDDNP was one of the early candidates (Agdeppa, Kepe, Liu, Flores-Torres, et al. 2001; Agdeppa, Kepe, Liu, G. W. Small, et al. 2003; G. W. Small et al. 2006). One of the first drawbacks when considering this tracer for imaging tau is that it is not selective for tau over Aβ (Shoghi-Jadid et al. 2002) which means interpretation of increased signal is difficult. More importantly however, this tracer was found to show little to no binding to Aβ or tau in multiple *in vitro* studies (Thompson et al. 2009; Ni et al. 2013). This means the *in vivo* signal seen using the tracer could well be to do with non-displaceable binding. This is backed up when the tracer is compared with Aβ tracers *in vivo*. One is unable to differentiate between cognitively impaired groups and healthy controls using [^{18}F]FDDNP as all groups show similar uptake (Tolboom et al. 2009). Thus, this tracer is not suitable for giving accurate quantification of tau pathology *in vivo*.

Quinoline derivatives - [^{18}F]THK523, [^{18}F]THK5105, [^{18}F]THK5117 and [^{18}F]THK5351 In an attempt to address the lack of selectivity of tau over Aβ, Fodero-Tavoletti, Okamura, et al. 2011 developed a radiolabelled ligand for imaging tau specifically. [^{18}F]THK523 showed binding co-localised with tau pathology in autoradiographic studies and low binding to Aβ plaques. However, *in vivo*, it was found to have high levels of non-specific binding to white matter (Villemagne, Furumoto, et al. 2014) which makes visual interpretation of the scans difficult. Further, *in vitro* results suggest that there is little binding to lesions in non-AD tauopathies (Fodero-Tavoletti, Furumoto, et al. 2014).

[^{18}F]THK523 was iterated on, in an attempt to increase the selectivity and reduce the level of non-specific binding. Two compounds were discovered which showed favourable properties *in vitro*, namely [^{18}F]THK5105 and [^{18}F]THK5117 (Okamura, Furumoto, et al. 2013). Initial studies of [^{18}F]THK5105 in humans were promising; regional SUVr values in the temporal lobe were 10% higher in subjects with AD compared to healthy controls and uptake correlated with cognitive parameters unlike many Aβ imaging studies. Almost identical results were achieved by the same lab a year later using [^{18}F]THK5117 (Harada, Okamura, Furumoto, Furukawa, Ishiki, Tomita, Hiraoka, et al. 2015). Whilst these were important findings, I am of the opinion that choosing to quantify the images with SUVr without having ascertained the optimum imaging time window was premature. Indeed, this was further investigated by Jonasson et al. 2016 and it was found that SUVr overestimated binding when compared to full kinetic analysis with an arterial input function. It was also tested in subjects with non-AD neurodegenerative diseases including a subject with CBD (Chiotis et al. 2016) and initial results showed high retention and a different spatial pattern of uptake to AD.

Yet more compound optimisation produced another tracer, [^{18}F]THK5351. Initial *in vitro* and *in vivo* experiments showed the tracer showed an even greater selectivity for tau over Aβ and the highest signal-to-noise ratio of all the tested compounds (Harada, Okamura, Furumoto, Furukawa, Ishiki, Tomita, Tago, et al. 2016). Importantly, the tracer was tested in non-AD neurodegenerative diseases (CBD and progressive supranuclear palsy) *in vivo* (Kikuchi et al. 2016; Ishiki et al. 2017). Both studies showed greater uptake in patient groups when compared with controls.

All this evidence suggests that [^{18}F]THK5351 could be a good tracer for quantifying tau accumulation *in vivo*. However, Ng et al. 2017 published a paper this year showing problems with the selectivity of the tracer. 60% of the specific signal of the tracer can be blocked by selegiline which is a compound known to block monoamine oxidase B (MAO-B). This is strong evidence that there is "off-target" specific binding and therefore interpretation of increased signal is

difficult. This is particularly true since MAO-B is known to increase with age and cognitive measures often decline with age. Any correlation between decline in cognitive performance and increased tracer binding could result from off-target binding rather than increased tau. Off-target binding may well also explain the apparent discrepancy between binding *in vitro* and *in vivo* in non-AD neurodegenerative diseases as it possible that the increased binding seen in studies involving subjects with CBD and progressive supranuclear palsy could have resulted from increased MAO-B rather than a greater tau burden.

[^{11}C]PBB3 [^{11}C]PBB3 is the tracer that has a higher affinity for tau (Kimura, Ichise, et al. 2015) than all the tracers I have previously discussed. There are however, some serious drawbacks. The main one being that, it has been shown metabolites of [^{11}C]PBB3 cross the blood brain barrier (Hashimoto et al. 2015; Kimura, Ichise, et al. 2015). This means the metabolite can enter the brain but is unlikely to bind to tau. This causes problems with quantification. In addition to this, typically the concentration in the plasma available to cross the blood brain barrier is taken from the parent compound. This is not true with [^{11}C]PBB3 and therefore calculations of volumes of distribution will be invalid. Attempts have been made to quantify tau in the brain despite the existence of metabolites that enter the brain (Kimura, Ichise, et al. 2015; Kimura, Endo, et al. 2016), however validation of these novel methods is difficult. Only with post-mortem studies of subjects who recently had a [^{11}C]PBB3 scan would one really be able to ascertain this information. Until this has been performed, all results should be treated with caution. In addition, the blood-brain barrier penetration is low and therefore the signal to noise ratio in the tissue is poor.

Finally, this compound is radiolabelled with [^{11}C]. Even if the quantification of tau could be validated, its wider use could be hindered by the fact that it requires a cyclotron on-site for its implementation. A compound with a longer half-life would be more desirable.

[^{18}F]AV1451 and [^{18}F]T808 The most widely used radiotracer today for imaging tau is [^{18}F]AV1451. It was introduced by Xia et al. 2013 under its original name of [^{18}F]T807. The tracer showed strong binding *in vitro* to the aggregated PHF form of tau in human brain sections and immunohistochemistry showed that the tracer was selective to tau pathology with no visible binding of Aβ deposits. In mice, the tracer crossed the blood-brain barrier and exhibited fast kinetics (Xia et al. 2013).

At a similar time the results from a study using [^{18}F]T808, another potential tracer developed by the same group with a similar structure to [^{18}F]T807, were published (Chien, Szardenings, et al. 2014). Whilst the study showed that it has faster kinetics, it was reported that there was a high level of defluorination and as it stands, the defluorination will halt the progression of this tracer.

Chien, Bahri, et al. 2013 used [^{18}F]T807 to scan three healthy controls and three cognitively impaired subjects. The reported cortical uptake of the tracer demonstrated a spatial distribution that correlated well with the known pattern of tau. In addition to this, the group noted that there was low retention in white matter and the level of uptake correlated well with the disease severity.

The intellectual property of the production of [^{18}F]T807 was bought by Avid radiopharmaceuticals and as such the tracer has been renamed [^{18}F]AV1451.

2.6.3 [^{18}F]AV1451 in AD and non-AD studies

AD studies The most widely studied disease with [^{18}F]AV1451 is AD. As previously mentioned, the first in man study conducted by Chien, Bahri, et al. 2013 concentrated on AD and MCI but only with small numbers. Since then, larger studies have been conducted, most notably by Avid radiopharmaceuticals themselves (K. A. Johnson, Schultz, et al. 2016). Consistent with Chien, Bahri, et al. 2013, they found elevated neocortical uptake of the tracer in Alzheimer's disease patients when compared to controls.

Of particular note, has been the investigation into the relationship between Aβ and tau. Five studies have focussed on this relationship using PET only by scanning subjects with both [^{18}F]AV1451 and an established Aβ radiotracer (K. A. Johnson, Schultz, et al. 2016; Lockhart et al. 2017; Vemuri, Lowe, et al. 2017; Tosun et al. 2017). They all show a weak positive correlation between increased tau binding and Aβ burden. This result is interesting but in my opinion, the more important question is how they interact. Is one a downstream event from the other? Looking further ahead, it will be interesting to see whether we can provide evidence for or against the hypothetical model for biomarkers introduced by Jack Jr, Knopman, Jagust, Shaw, et al. 2010. To elucidate this, extensive longitudinal studies will have to be performed. Similarly to previous findings from post-mortem data, these studies found that, unlike Aβ, tau burden correlates well with cognitive scores (Ossenkoppele et al. 2016; K. A. Johnson, Schultz, et al. 2016; Pontecorvo et al. 2017).

Recently, there has also been a focus on how [^{18}F]AV1451 will be used in the clinic (Jack Jr., Bennett, et al. 2016; Jack Jr., Wiste, et al. 2017). Jack Jr., Wiste, et al. 2017 tried to define cut-off points for abnormal tracer uptake levels. This strategy is appealing as it will give a simple positive or negative outcome from a scan in a similar way to what is common for an Aβ PET scan. However, I think this method may be too simplistic as the combination of the spatial distribution and the intensity of the signal may hold more information when attempting to track a subjects' tau pathology. In their seminal paper, H. Braak and E. Braak 1991, could only define three different levels of Aβ accumulation but could define six Braak stages for tau based on its spatial distribution.

Non-AD studies *In vivo*, use of [^{18}F]AV1451 outside of AD has been far less extensive. Isolated studies have looked at progressive supranuclear palsy (Cho et al. 2017; Passamonti et al. 2017; R. Smith, Schain, et al. 2017; R. Smith, Schöll, Honer, et al. 2017), cerebral amyloid angiopathy (Kim et al. 2017), dementia with lewy bodies (Kantarci et al. 2017) and CBD (R. Smith, Schöll, Widner, et al. 2017).

In progressive supranuclear palsy, the results are inconclusive. An increased binding in patient groups when compared to controls was observed in midbrain and the basal ganglia (Passamonti et al. 2017). However, the binding did not correlate with the severity of the symptoms but did correlate with age in both healthy controls and patients (R. Smith, Schain, et al. 2017). Combining these results with the fact that K. A. Johnson, Schultz, et al. 2016 report a high signal in the substantia nigra in both AD and healthy controls which is inconsistent with the tau distribution found in AD post-mortem studies (H. Braak and E. Braak 1991; Thal, Attems, and Ewers 2014), this raises the possibility of off-target specific binding for [^{18}F]AV1451.

The study performed by R. Smith, Schöll, Widner, et al. 2017 involved scanning 8 patients with CBD, 17 healthy control and 31 AD patients with the aim of characterising the differences in uptake between the groups. They were able to distinguish the three groups by their scans; AD subjects showed elevated uptake in cortical areas as expected when compared to controls whereas increased uptake was confined to the corticobasal tract and basal ganglia in subjects with CBD. In all subjects (both patients and healthy controls), there was high uptake in the basal ganglia which again raises the question of how much of the signal is specific to tau. The main PET outcome measure in this study was SUVr. I think to use this measure without validation is premature. Signal intensity could be affected by the time window chosen. A validation of the use of simplified methods such as reference tissue models or SUVr has yet to be performed in subjects with CBD.

***In vitro*, post-mortem and CSF studies** The main concern raised from results from *in vivo* experiments using [^{18}F]AV1451 regards the selectivity of the tracer for tau. In the development of tau tracers there has been extensive work characterising the selectivity over Aβ but less looking at characterising any other off-target binding. Following the *in vivo* results, two groups researched this

and independently observed off-target binding to neuromelanin (Marquié, Normandin, Vanderburg, et al. 2015; Lowe et al. 2016). This also resulted in increased understanding of the level of binding to different isoforms and formations of tau. It was shown that, binding is highest in paired helical filaments in diseases which have both 3R and 4R isoforms (Lowe et al. 2016) such as AD. There was a lower affinity of the tracer for straight filaments and low binding in non-paired helical filament containing sections of brains of subjects with progressive supranuclear palsy and CBD (Marquié, Normandin, Vanderburg, et al. 2015). This initial work was followed up by Marquié, Normandin, Meltzer, et al. 2017 where *in vivo* [^{18}F]AV1451 binding for a subject with progressive supranuclear palsy was compared with post-mortem quantification. It was shown that all the binding observed *in vivo* was either due to paired helical filaments in the entorhinal cortex (which the authors hypothesised was part of the normal ageing process) or off-target binding to neuromelanin. A similar study was performed by R. Smith, Puschmann, et al. 2016 but in a subject with a mutation in the MAPT gene which is involved in the encoding of tau. They found a statistically significant correlation between regional [^{18}F]AV1451 SUVr and the post-mortem regional quantification of tau. Consistent with previous results however, this was not true in the putamen where the SUVr was high but there was little detected tau pathology post-mortem. More recently, more selectivity issues with the tracer have been identified as it has been shown that it binds to monoamine oxidase A (MAO-A) (Vermeiren et al. 2017). MAO-A binding is more problematic as its expression is co-localised with tau pathology in many diseases.

The *in vitro* work so far with [^{18}F]AV1451 allows us to have confidence tau in paired helical filaments in the cortex will produce a robust signal *in vivo*, however this is only part of the tau burden and any straight filaments will show little to no signal. Also, any inferences made based on results from the basal ganglia should be treated with caution as the selectivity of the tracer in these regions is poor. Lowe et al. 2016 make the important point that clinical use of the tracer in different disease types will only be possible following a full characterisation of

the binding sites.

***In vivo* quantification of [^{18}F]AV1451** As has been previously mentioned, the majority of studies involving [^{18}F]AV1451 have used SUVr as the primary outcome measure. This simplified measure is attractive as it is cost-effective and easy to compute but its use should be validated against full quantitative analysis with an arterial input function.

Two studies have focussed on obtaining the optimum kinetic modelling approach for [^{18}F]AV1451 (Wooten et al. 2017; Golla et al. 2017). Both studies recruited healthy controls and AD patients and Wooten et al. 2017 also included three subjects that had suffered a TBI. The results between the studies are broadly consistent; both found the optimum model to be a reversible 2-tissue compartmental model when considering all the subjects as one group (although Golla et al. 2017 found the reversible 1-tissue compartmental model to be optimal if only the healthy controls were considered and Wooten et al. 2017 found this to be true in some subjects showing little uptake). The correlation between SRTM and the 2-tissue compartmental model was found to be strong ($R^2 = 0.87$ (Golla et al. 2017)) and this was also true for SUVr ($R^2 = 0.96$ (Wooten et al. 2017) and $R^2 = 0.84$ Golla et al. 2017)). Wooten et al. 2017 showed that the system reaches "pseudoequilibrium" at a late time window of 80-100 min and therefore this should be used as the optimum time window for SUVr. I would claim that if a system is in "pseudoequilibrium" then it has not reached equilibrium and therefore an even later scanning window may be better in that it will be independent of the scanning window chosen. Where I agree with the authors however, is that I think 80-100 mins represents an optimum trade off between a good quantification and a scanning protocol which is easy to implement.

The body of *in vitro* literature analysing the binding characteristics of [^{18}F]AV1451 has shown different behaviour of the tracer in progressive supranuclear palsy and CBD. It therefore is important to perform similar studies to those conducted by Wooten et al. 2017 and Golla et al. 2017 in these disease groups to have confidence in using simplified methods for quantification in future studies.

2.7 Outline of the remainder of the thesis

In the first two chapters, I have introduced the imaging modalities of MRI and PET and shown how they can be used to study neurodegeneration. In this section I will outline how this thesis aims to add to research in this field.

In chapters 4 and 5, I model the spatiotemporal distribution of Aβ in AD using two different models. In chapter 4, I use a network diffusion model similar to the one used by Raj, Kuceyeski, and Weiner 2012 but I improve the model by adding parameters for production and clearance. In chapter 5, the methodology of chapter 4 is improved to produce a chronological dataset representing the spatiotemporal distribution of Aβ in AD. This dataset is then modelled using a novel four-parameter logistic growth model and the results are used to infer characteristics that drive the observed stereotypical spatiotemporal distribution of Aβ. Parametric maps for two of the four parameters in the logistic growth model are generated in chapter 5 by fitting the model at the voxel-level and in chapter 6 these maps are used to define a novel outcome measure for the global Aβ burden, amyloid load $A\beta_L$ which can be obtained from static [^{18}F]AV45 scans. This outcome measure is compared to mean cortical SUVr in both cross-sectional and longitudinal data. In chapter 7 the focus switches from Aβ to tau. An image analysis pipeline is developed to quantify [^{18}F]AV1451 uptake *in vivo* in healthy controls and CBD. SRTM and static images are investigated to find out if less invasive and more cost-effective scanning protocols are possible options for future studies. In chapter 8, SRTM is used to quantify [^{18}F]AV1451 uptake at the ROI and voxel-level in a large study which aims to investigate whether suffering a TBI increases tau expression. The thesis is concluded in chapter 9 and recommendations for future studies are made.

[^{18}F]

Chapter 3

Datasets and preprocessing

This thesis performs mathematical modelling on a variety of different types of PET data. This chapter is dedicated to providing detail of these data were preprocessed so that the mathematical modelling could be performed. Each section outlines not only the data and the preprocessing but also where in the thesis this data is used.

3.1 Static [^{18}F]AV45 Aβ PET imaging data

Chapters 4, 5 and 6 use freely available large static [^{18}F]AV45 PET imaging data to analyse the progression of Aβ in AD. All of this work requires the images downloaded from these databases to be preprocessed and spatially normalised to MNI152 space. In this section, the databases themselves are introduced and methodology for registering the images to MNI152 space is explained.

3.1.1 Alzheimer's disease neuroimaging initiative

Static [^{18}F]AV45 images and structural T1-weighted MRI were downloaded from the Alzheimer's disease neuroimaging initiative (ADNI). ADNI describe the initiative in the following way,

"The ADNI was launched in 2003 as a public-private partnership, led by Principal Investigator Michael W. Weiner, MD. The primary goal of ADNI has been to test whether serial MRI imaging, PET, other biological markers, and clinical and neuropsychological

assessment can be combined to measure the progression of mild cognitive impairment and early Alzheimer's disease. For up-to-date information, see www.adni-info.org."

ADNI is a multi-centre imaging initiative and as such the structural MRI and [^{18}F]AV45 images were obtained on a range of different scanners. PET and MRI are visually QC'd for excessive motion, artefacts and to ensure the entire brain is in the field of view before the images are made available to download (Jagust, Landau, et al. 2016).

[^{18}F]AV45 PET scans consisted of a 20-minute scan window 50 minutes after injection of a target dose of 370 MBq of [^{18}F]AV45 according to the standardised ADNI protocol.

There were 3 image pre-processing steps applied to the data prior to entry into the ADNI imaging database (For full details, see http://adni.loni.usc.edu /methods/pet-analysis/pre-processing). Briefly, four five min frames are co-registered and averaged. The resulting image is converted to a 160x160x96 voxel static image with voxel dimension of 1.5mmx1.5mmx1.5mm. Finally, an 8mm full width half maximum gaussian filter was applied (corresponding to the lowest resolution scanner used in the study). Finally, the intensities were normalised to the grey matter cerebellum as defined using Freesurfer which created SUVr images. I downloaded these SUVr from the ADNI database and used them in the subsequent analyses.

This thesis used both longitudinal and cross-sectional data from ADNI which were downloaded from the ADNI website.

Cross-sectional ADNI dataset

All work in Chapters 4, 5 and some work in Chapter 6 was performed on static [^{18}F]AV45 images obtained from 769 subjects in the ADNI imaging database.

For each patient, a structural T1-weighted MRI and a static PET image and a diagnosis was downloaded where the diagnosis was one of four categories;

	HC	EMCI	LMCI	AD	Total Study
Number	211	233	203	132	769
Age (std dev)	73.9 (7.23)	73.2 (7.69)	74.2 (8.56)	75.7 (6.92)	74.1 (7.71)

TABLE 3.1: Size and ages of different groups in the cross-sectional ADNI dataset

healthy control (HC), early mild cognitive impairment (EMCI), late mild cognitive impairment (LMCI) or Alzheimer's disease (AD). The sizes and ages of the different groups are summarised in Table 3.1.

Longitudinal ADNI dataset

147 subjects from the cross-sectional study with the diagnosis of EMCI underwent a follow-up MRI and [^{18}F]AV45 scan two years after baseline (mean 1.96 years standard deviation 0.12 years). These were also downloaded and are used for the longitudinal data analysis in Chapter 6.

3.1.2 Dallas lifespan brain study

A separate cross-sectional dataset consisting of structural MRI and static [^{18}F]AV45 scans were downloaded from the Dallas lifespan brain study. The organisers describe the aims of this project as,

"The Dallas Lifespan Brain Study (DLBS) is a major effort designed to understand the antecedents of preservation and decline of cognitive function at different stages of the adult lifespan, with a particular interest in the early stages of a healthy brain's march towards Alzheimer Disease. The DLBS aims to (1) understand how brain atrophy as well as accumulation of amyloid and tau affects healthy aging and cognition, (2) understand how the brain develops "neural scaffolds" to support cognition, and also (3) develop a corpus of research on the cognitive neuroscience of middle age. The DLBS is one of the most complete studies of the aging mind that is available, particularly in the United States, and can address many important hypotheses regarding the cognitive neuroscience of aging."

The dataset used here consisted of 147 subjects aged between 20 and 89 years (mean age 62.8 years). The study imaging protocol is outlined in full on the Dallas lifespan brain study website - http://fcon_1000.projects.nitrc.org /indi/retro/dlbs.html

Here I will just outlined the key elements. Each participant received a structural MRI on a Philips 3T scanner and a static [^{18}F]AV45 scan conducted on a Siemens ECAT HR PET scanner. All participants were injected with a target dose 370 MBq of [^{18}F]AV45. The structural MRI and [^{18}F]AV45 were not performed on the same day and the time between the two scans ranged from 0.3 to 19 months. The static PET images were formed by averaging two five minute frames that were obtained 50 min post-injection. Reconstruction of the image was done using filtered back projection and a 6mm full-width half maximum Gaussian filter. These reconstructed images were downloaded from the Dallas lifespan brain study database.

3.1.3 Spatial normalisation of static [^{18}F]AV45 Aβ images into MNI152 space

[^{18}F]AV45 static images were nonlinearly registered into Montreal Neurological Institute 152 space (MNI152 space) using a diffeomorphic nonlinear registration (DARTEL) (Ashburner 2007). Initially, the structural MRI images were segmented into grey matter and white matter using the software package SPM12 using the unified segmentation algorithm (Ashburner and K. J. Friston 2005) - see Figure 1.1 for a typical output. The segmented images were used to create a DARTEL template. Separate DARTEL templates were created for the cross-sectional ADNI data and the Dallas lifespan brain study images. DARTEL flowfields from each subjects' MRI to the group DARTEL template were formed and the group average template was then registered to MNI152 space using an affine registration. Each [^{18}F]AV45 SUVr image was registered to the their corresponding structural MRI using a rigid-body registration. Finally, the individuals' DARTEL flow field and template transformation was applied without modulation resulting in [^{18}F]AV45 images in MNI152 space. The spatially normalised maps were spatially smoothed (8mm full width at half maximum

Gaussian kernel). Each registration was visually assessed to check the quality of the registration. 10 registrations failed QC from the original 779 images in the ADNI cross-sectional data meaning there 769 subjects were included in the analysis (see Table 3.1). One registration out of 148 failed QC in the Dallas lifespan brain study meaning the dataset consisted of the 147 images outlined in sub-section 3.1.2.

As the Dallas lifespan brain study images had not had their intensities normalised by a reference region this was done after the images had been spatially normalised. The grey matter cerebellum was defined using the combination of an atlas and template grey matter probability map. Reference region voxels were defined to be the intersection between voxels that had a grey matter probability greater than 0.5 and those that were in the cerebellum region of the CIC atlas (Tziortzi et al. 2011). Image intensities were divided by the mean intensity of the reference region voxels to create SUVr images.

3.2 Calculating regional SUVr

Regional SUVr and a mean cortical SUVr were calculated for the cross-sectional ADNI data for three different parcellations of the brain using the CIC neuroanatomical atlas (Tziortzi et al. 2011); one which had 90 cortical and subcortical regions, one which was restricted to 76 cortical regions and one which had nine large regions covering the whole brain. The ROIs were applied to the spatially normalised SUVr images in order to derive regional SUVr values for each subject. The cortical SUVr value was obtained by calculating the mean SUVr value for all 76 cortical regions (weighted by region volume).

3.3 Dynamic [^{18}F]AV1451 PET imaging data

In Chapter 7, the kinetics of the novel tau PET radiotracer are investigated in a study involving subjects suffering from CBD and in Chapter 8 the same tracer is

used to attempt to quantify tau accumulation *in vivo* in subjects who have suffered a TBI Both of these studies use dynamic [^{18}F]AV1451 PET data. In this section, this data is introduced and the preprocessing and motion correction steps are outlined. The result from these steps is dynamic motion corrected 2 mm isotropic images which are co-registered to each subjects structural MRI which are used to for the kinetic modelling analysis that is performed in Chapters 7 and Chapter 8

3.3.1 Tau in CBD

16 subjects (8 healthy controls, 8 CBD) underwent a structural T1-weighted MRI scan and a dynamic 120 minute [^{18}F]AV1451 PET scan which were performed at Imanova Ltd, London, UK.

T1-weighted structural MRI Scans were acquired on a Siemens Magnetom MAGNETOM TrioTim syngo MR B17-3T MRI scanner and PET scans were performed on a Siemens Biograph Hi-Rez 6 PET-CT scanner. A slow bolus intravenous injection (20 seconds) of [^{18}F]AV1451 was administered to each subject. Dynamic emission data were acquired continuously for 120 minutes following the injection. The dynamic images were reconstructed into 29 frames (8x15 seconds, 3x60 seconds, 5x120 seconds, 5x300 seconds, and 8x600 seconds), using filtered back projection and smoothed with a Gaussian filter of 5 mm.

Blood sampling was performed for [^{18}F]AV1451 through an arterial line inserted in the radial artery to generate arterial plasma input data. For the initial 15 minutes radioactivity levels in blood was continuously measured through an automatic blood sampling system, followed by samples at 5, 10, 20, 40, 50, 60, 80 and 100 minutes during the scan (further detail in Chapter 6).

The injected dose in MBq was recorded along with the subjects' age, body weight and gender (see Tables 3.2 and 3.3).

3.3.2 Tau in TBI

33 subjects (11 healthy controls, 22 TBI) underwent a structural T1-weighted MRI scan and a dynamic 100 minute [^{18}F]AV1451 PET scan which were again performed at Imanova Ltd, London, UK.

T1-weighted MRI scans were acquired with a Siemens Magnetom MAGNETOM TrioTim syngo MR B17, 3T MRI scanner.

PET scans were performed on a Siemens Biograph Hi-Rez 6 PET-CT scanner. A slow bolus intravenous injection (20 seconds) of [^{18}F]AV1451 was administered to each subject. Dynamic emission data were acquired continuously for 100 minutes following the injection.

The dynamic images were reconstructed into 27 frames (8x15 seconds, 3x60 seconds, 5x120 seconds, 5x300 seconds, and 6x600 seconds), using filtered back projection and smoothed with a Gaussian filter of 5 mm.

The injected dose in MBq was recorded along with the subjects' age, body weight and gender. The time since injury was also recorded for subjects that had suffered a TBI (see Tables 3.4 and 3.5).

3.4 Preprocessing and motion correction of [^{18}F]AV1451 PET images

All preprocessing and motion-correction was done using MIAKAT^{TM} (R. N. Gunn, Coello, and Searle 2016) which is a fully quantitative suite of analysis tools for PET neuroimaging data.

3.4.1 Isotropic images

After reconstruction it was checked that all frames of the dynamic PET images contained 2 mm isotropic voxels.

A 2 mm isotropic version of the structural MRI image was created (by reslicing the original image) for registration purposes.

3.4.2 Motion correction

Motion correction of the images was performed using frame-by-frame correction meaning each frame was registered to the reference frame (frame 16) using a rigid body registration in SPM12. This motion correction is the chosen method of the MIAKAT. It would be possible to register frame two to frame one and then register each subsequent frame to the previously aligned frame but given the results from the reference frame methodology it was not investigated. The quality of the registrations, however, were QC'd for each image and using a single reference frame produced good quality registrations for all subjects. The registration parameters (translations in the x, y and z directions and rotations pitch roll and yaw) were recorded and used to QC the level of motion along with visual assessment of the scans. Subjects that showed high motion were removed from any further analysis. High motion was determined qualitatively by using plots of the registration parameters. If any of the translation parameters changed by more than 10 mm in between one frame and the next or if any of the rotation parameters changed by more than 10 degrees between one frame and the next, then the subject was removed from further analysis. Example motion parameters can be seen for subjects that passed and failed QC in Figures 3.1 and 3.2 respectively.

The motion-corrected images were subsequently registered to the subjects' down-sampled T1-weighted MRI using a rigid-body registration resulting in a motion-corrected dynamic image in T1 space with voxel dimensions of 2 mm x 2 mm x 2 mm.

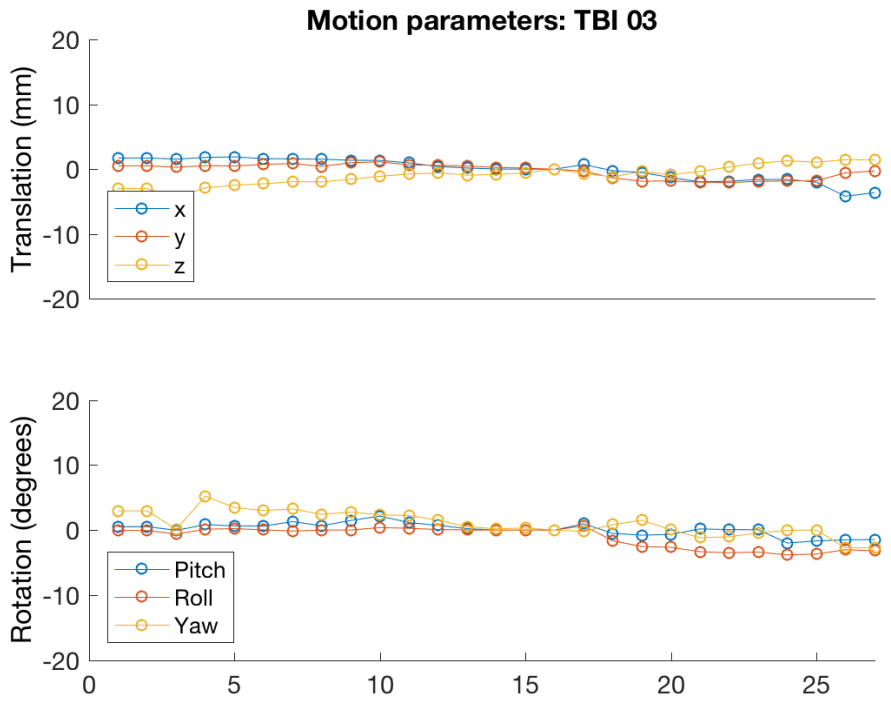


FIGURE 3.1: Motion parameters for an example subject who had suffered a TBI. This subject passed QC.

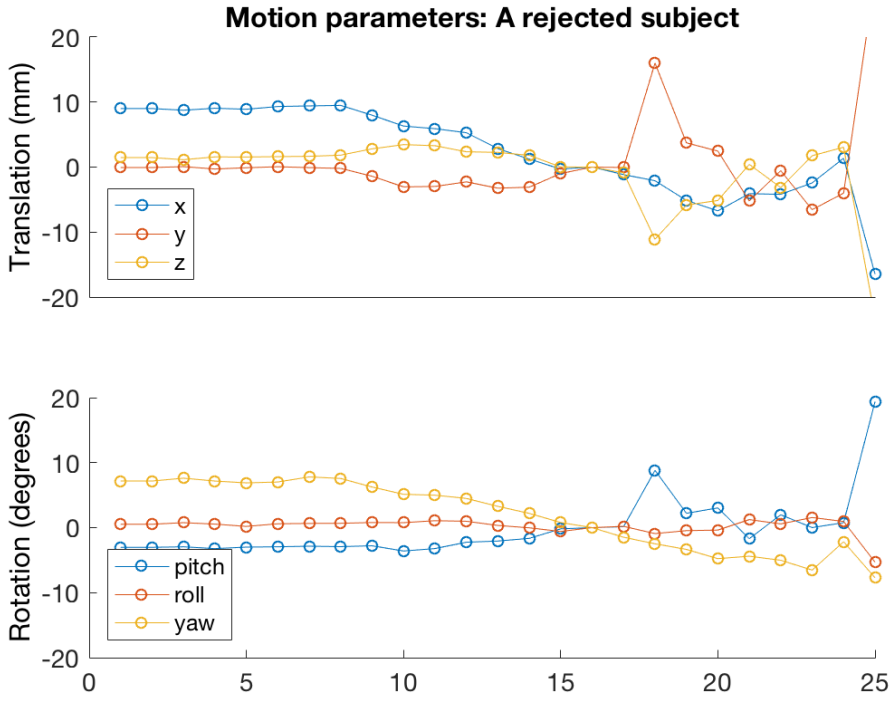


FIGURE 3.2: Motion parameters from a subject taken from the study involving patients with CBD that wasn't included in the analysis in Chapter 7 due to excessive motion.

	Age (yrs)	Gender	Injected Dose (kBq)	Body weight (kg)
HC 01	65	female	165.09	69.9
HC 02	62	male	156.47	67.3
HC 03	73	male	160.02	61.5
HC 04	58	female	138.92	69.5
HC 05	37	female	165.48	50.5
Mean (s.d.)	61 (13)	n/a	157.96 (9.91)	61.92(8.5)

TABLE 3.2: Demographics for the healthy controls included in the Tau in CBD analysis in chapter 7.

	Age (yrs)	Gender	Injected Dose (MBq)	Body weight (kg)
CBD 01	58	female	161.15	59.6
CBD 02	70	male	161.35	72.4
CBD 03	71	male	158.35	92.4
CBD 04	80	female	170.92	60.0
CBD 05	72	female	161.79	52.8
Mean (s.d.)	70 (7.9)	n/a	162.71 (4.78)	67.4 (15.6)

TABLE 3.3: Demographics for the CBD subjects included in the Tau in CBD analysis in chapter 7.

3.4.3 Overview of subjects included in kinetic modelling of [^{18}F]AV1451 in CBD analysis (Chapter 7)

10 of the 16 subjects were included in the analysis presented in Chapter 7 because four of the 16 subjects (2 healthy controls and 2 CBD) recruited failed to complete over 100 min of the 120 min scan and two subjects (1 healthy control and 1 CBD) failed QC of the motion correction and therefore were not included. Both rejected subjects had extensive within frame motion (see Figure 3.2) which means the motion correction steps which only account for between frame motion will not be sufficient.

Ancillary information for the 10 subjects (five healthy controls and five CBD) included in the analysis in Chapter 7 is detailed in Tables 3.2 and 3.3. There were no significant differences in the age ($p > 0.1$), injected dose ($p > 0.3$) and body weight ($p > 0.6$) of the healthy controls and subjects diagnosed with CBD and both groups contained 2 males and 3 females.

	Age (yrs)	Gender	Injected Dose (MBq)	Body weight (kg)
HC 01	60	male	222.46	115.0
HC 02	44	male	212.52	50.0
HC 03	59	female	212.18	44.4
HC 04	43	male	231.35	88.4
HC 05	58	male	214.31	82.6
HC 06	29	female	225.64	65.8
HC 07	51	female	238.34	69.9
HC 08	55	female	225.88	59.6
HC 09	65	female	165.09	69.9
HC 10	62	male	156.47	67.3
HC 11	73	male	160.02	61.5
Mean (s.d.)	53 (11)	n/a	210.42 (27.53)	71.3 (20.3)

TABLE 3.4: Demographics for the healthy controls included in the Tau in TBI analysis in chapter 8.

3.4.4 Overview of subjects included in kinetic modelling of [^{18}F]AV1451 in TBI (Chapter 8)

31 of the 32 subjects were included in the analysis for Chapter 8 because one subject showed extensive atrophy in the Cerebellum and grey matter Cerebellum was chosen as the reference region for the study analysis in Chapter 8 (for more details please see 8.2). The atrophy was likely to cause the results to be heavily biased and therefore the subject was removed from the analysis.

Three of the healthy controls in this study are the same subjects that were included in the study of patients with CBD (HC 09, HC 10 and HC 11 from the TBI study are HC 01, HC 02 and HC 03 from the CBD study).

Ancillary information for the 31 subjects (11 healthy controls and 21 traumatic brain injury) included in the analysis in Chapter 8 is detailed in Tables 3.4 and 3.5. There were no significant differences in the age ($p > 0.2$), injected dose ($p > 0.07$) and body weight ($p > 0.05$) of the healthy controls and subjects who had suffered a TBI. Six out of the 11 healthy controls were male (55%) and 14 of the 21 TBI subjects were male (67%).

The time since injury for the TBI subjects ranged from 19 to 51 years meaning all patients were not suffering from any acute effects from the injury.

	Age (yrs)	Time since injury (yrs)	Gender	Injected Dose (MBq)	Body weight (kg)
TBI 01	45	36	female	196.12	61.2
TBI 02	44	29	male	217.65	80.9
TBI 03	61	35	female	208.25	75.4
TBI 04	39	28	female	207.78	54.9
TBI 05	49	27	male	232.85	109.3
TBI 06	72	51	male	226.12	90.8
TBI 07	41	31	female	210.26	61.5
TBI 08	66	31	male	217.42	72.0
TBI 09	54	34	male	225.69	83.3
TBI 10	57	35	female	225.34	58.5
TBI 11	43	20	male	218.46	88.9
TBI 12	40	32	male	231.18	101.0
TBI 13	57	35	male	222.66	118.5
TBI 14	31	18	female	207.6	59.0
TBI 15	39	19	male	211.44	78.5
TBI 16	55	32	male	222.03	95.9
TBI 17	46	31	female	233.52	85.2
TBI 18	43	35	male	216.58	106.7
TBI 19	55	20	male	232.18	88.3
TBI 20	48	37	male	228.07	101.0
TBI 21	58	37	male	207.08	95.7
Mean (s.d.)	50 (10)	31 (7.6)	n/a	218.97 (10.36)	84.12 (18.30)

TABLE 3.5: Demographics for the TBI subjects included in chapter 8.

3.5 Conclusion

This chapter has outlined the datasets that the rest of this thesis will use for analysis.

I have introduced two cross-sectional and one longitudinal [^{18}F]AV45 Aβ static imaging datasets that have been downloaded from freely available databases. I described how these images were preprocessed to produce spatially normalised SUVr images in MNI152 space. These images will be used in Chapters 4, 5 and 6.

I also introduced two dynamic [^{18}F]AV1451 tau datasets which have been acquired at Imanova Ltd. UK. One dataset includes healthy controls and CBD patients and the other has healthy controls and subjects who have suffered a TBI. The image preprocessing and motion correction steps were outlined and applied to both datasets. The resulting motion-corrected isotropic images in T1-weighted MRI space will be used in Chapters 7 and 8.

Chapter 4

Spatiotemporal Modelling of Misfolded Proteins using a Network Diffusion Model

In the previous three chapters I have introduced the imaging modalities of PET and MRI, discussed the role of Aβ in AD and described the ADNI PET dataset. In this chapter mathematical modelling will be used to attempt to describe the accumulation of Aβ in AD at the population level using the ADNI dataset.

4.1 Outline and aims

In chapter 2, I introduced the stereotypical pattern of Aβ accumulation that was characterised by H. Braak and E. Braak 1991 and commented that by combining mathematical modelling and PET data one could attempt to characterise this pattern using *in vivo* data. The aim of this chapter and chapter 5 is to develop a mathematical model which characterises regional SUVr values as AD progresses.

In this chapter, I introduce the concept of modelling the brain as a weighted graph in section 4.2 and how this is calculated using DTI data. This graph subsequently provides a framework for a spreading model to describe the spatiotemporal distribution of Aβ in AD. In section 4.3, I combine the strengths

of previous models outlined by Raj, Kuceyeski, and Weiner 2012 and Iturria-Medina, Sotero, et al. 2014 to create a new network diffusion model which incorporates three processes - Aβ production, Aβ clearance and distal spreading of Aβ across brain regions. In an attempt to assess the accuracy of the new model, I explain how the cross-sectional ADNI dataset introduced in Chapter 3 is transformed to a dataset representing the spatiotemporal distribution of Aβ at the population level in section 4.3. I go on to define a model space by considering different options for each of the three processes that are hypothesised to be occurring in the network diffusion model in section 4.4 and each of the models in the model space is fitted to the transformed cross-sectional dataset to evaluate its validity. Finally, information theory is used to determine the optimal model in section 4.6. Subsequently in section 4.7, strengths and weaknesses of both the network diffusion model and the experimental approach are discussed and improvements are suggested for further study.

4.2 Modelling the brain as a weighted graph

Graph theory has recently been used extensively in neuroscience but its origins lie in pure mathematics. As such, it comes with its own nomenclature which I will adhere to here. In mathematics, a graph is an ordered pair, $G = (V, E)$ where $V = \{v_i | i \in \mathbb{Z}\}$ is a set of nodes and $E = \{e_{i,j} | i, j \in V\}$ a set of edges connecting the nodes. In a weighted graph any edge $e_{i,j}$ has an associated $c_{i,j} \in \mathbb{R}_{\geq 0}$ which represents the strength of that edge.

In this work, 76 cortical regions defined in the CIC atlas (Tziortzi et al. 2011) of the brain are modelled as the set of nodes V, and the white matter connections form the set of edges, E. The number of tracts in the white matter connection between any two cortical regions represents the weight of each edge. These assumptions means that I am modelling each region as having uniform concentration of Aβ at a given time in the disease.

DTI is an MRI technique which provides a detailed map of the white matter tracts (outlined in more detail in Chapter 2). This can be combined with an atlas

to create a connectivity matrix between regions. Each entry in the connectivity matrix represents the strength of the connection between two regions. As the graph is undirected $c_{i,j} = c_{j,i}$ for all $i, j \in V$ and therefore the connectivity matrix is symmetrical about the leading diagonal.

The DTI data used in this work was provided by Carnegie Melon University and was averaged over 60 subjects (For full details on the acquisition parameters see Yeh and Tseng 2011). This DTI image was downloaded and a connectivity matrix for the 76 regions in the CIC atlas was calculated with the kind help of Yasser Iturria-Medina. Figure 4.1 outlines the methods used to model the brain as a weighted graph.

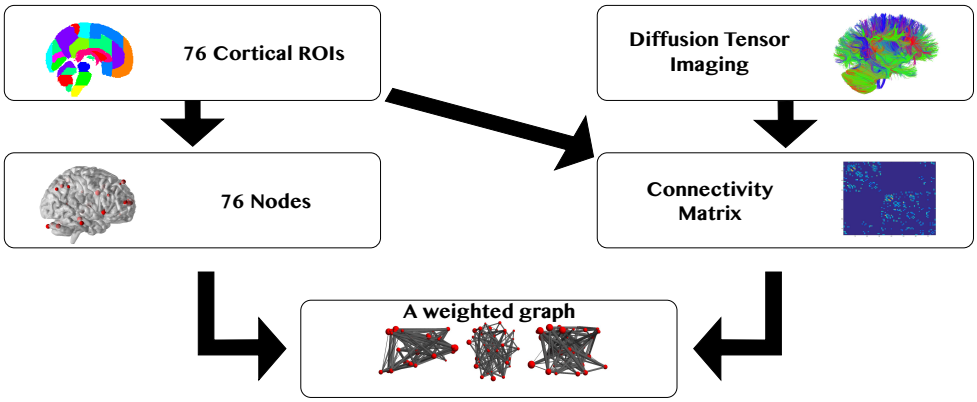


FIGURE 4.1: The workflow applied to model the brain as a weighted graph.

4.3 Network diffusion model

The network diffusion model I proposed to model Aβ accumulation is governed by a set of differential equations. The rate of change of concentration of Aβ in region i, $\frac{dP_i}{dt}$ is hypothesised to depend on three distinct processes; local production, local clearance and distal spreading between regions. Production is hypothesised to occur at a constant rate however each region can have an individual production rate, clearance was hypothesised to be proportional to the concentration but as with production regions can have different clearance rates. Distal spreading between regions i and j was hypothesised to be a function of

the connection strength between regions and the difference in concentration in those regions. Using these hypotheses, $\frac{dP_i}{dt}$ is given by

$$\frac{dP_i}{dt} = v_i - k_i P_i + \gamma[(\sum_{j \in G} c_{i,j} P_j) - \deg(i) P_i] \tag{4.1}$$

where P_i is the concentration of Aβ in region i, v_i is the production rate in region i, k_i is the clearance rate in region i, γ is a scaling constant for the connectivity, $c_{i,j}$ is the connection strength between regions i and j, G is the set of all regions and $\deg(i) = \sum_{j \in G} c_{i,j}$ is the sum of all weights of the edges attached to region i.

4.4 Investigating the model space

The network diffusion model in Equation 4.1 has a large amount of flexibility and it is important to ascertain the optimum number of parameters in order to obtain a parsimonious model. With this aim, I defined ten models each having different options for the involvement of production, clearance and distal spreading as shown in Figure 4.2.

Production was hypothesised to occur either only in one region, in all regions with the same production rates or in all regions with each region having its own individual production rate. Similarly, clearance was hypothesised that the clearance rates were either regionally varying or constant were constant across all regions. Finally, I considered models that did and did not include spreading between regions. The model space was then defined as all the permutations of each of the different options for production, clearance and distal spreading. The number of parameters to be estimated in the different models ranges from 2 to 153.

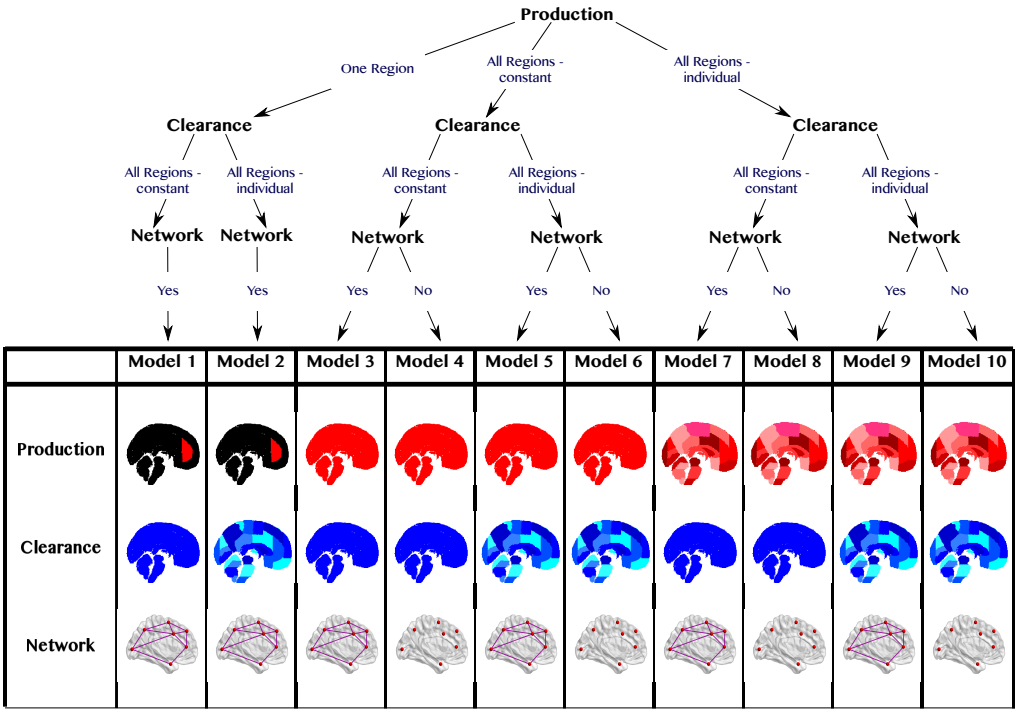


FIGURE 4.2: A graphic illustrating the model space that was investigated

4.5 Creation of a dataset representing the spatiotemporal distribution of Aβ at the population level

In order to test the validity of each of the models in the model space, one would ideally have longitudinal Aβ PET data where each subject received PET scans each year for a period of over 15 years. This dataset currently doesn't exist and so in this work I aimed to convert the large cross-sectional dataset obtained from ADNI introduced in Chapter 3 into a dataset which represents the spatiotemporal distribution of Aβ in AD at the population level.

With this aim, it was hypothesised that the age at which Aβ production begins in AD, t^*, is different between subjects but that after that there is a common spatiotemporal distribution for the accumulation across subjects. A t^* was calculated for each subject using a 2-parameter model from the model space; local production in all regions but at a constant rate across all regions, local clearance which is fixed across all regions and no connectivity. I fixed the clearance and production values to produce a biologically plausible output. The resulting curve plateaued at SUVr = 1.8 at a time of 30 years after production started

which was similar to values obtained by Jack et al. 2013 from longitudinal data.

With these values for production and clearance fixed, a t^* for each subject in the ADNI dataset was obtained by optimising t^* so that the model best fit all the regional SUVr of that subject using a trust-region reflective algorithm in MATLAB©.

Having determined t^* for each subject, regional SUVr were plotted against the age of the subject (on the scan date) minus t^* for every subject in the ADNI dataset. For this analysis, 76 cortical regions were used and the calculation of the regional SUVr values is outlined in section 3.2. The result is 76 plots representing each of the 76 cortical regional where each plot consists of 769 points (one for each subject in the ADNI dataset) where each point is a subjects regional SUVr plotted against their Age at the scan date minus their t*. The effect is that the x-axis is a time axis which is adjusted so that zero represents the time at which accumulation begins.

4.5.1 Fitting the model to the chronological dataset

Each of the ten models defined in the model space (displayed in Figure 4.2) was fitted to the transformed dataset using a trust-reflective region algorithm in MATLAB©.

The fit by each of the ten models was evaluated using the bayesian information criteria (BIC).

$$BIC = n \ln\left(\frac{RSS}{n}\right) + k \ln(n)$$

where n is the number of data points, k is the number of parameters in the model and RSS is the residual sum of squares. The model with the lowest BIC value is deemed optimal. The first term in the BIC is a function of the sum of squares of residuals and determines the goodness of fit of the model. The second term is a term which penalises the model for its complexity and this is the term which ensures the optimal model avoids overfitting.

4.6 Results

4.6.1 Calculating t^*

The variable t^* was successfully obtained for each of the 769 subjects. t^* represents an age at which the deposition of Aβ aggregates is estimated to begin. Thus, for each subject $age - t^*$ is the time in years that the model calculates that Aβ aggregates have been accumulating for. The mean $age - t^* = 4.21$ years (std $= 3.07$ years).

A scatter plot for each region was created by plotting the regional SUVr against $age - t^*$ for each subject. The result is 76 scatter plots (one for each region) aiming to represent the spatiotemporal distribution of the concentration of Aβ at the population level. The coherence of the majority of plots suggests that there is a stereotypical accumulation pattern, however the level of coherence varied across the regions. Figure 4.3 shows the scatter plots for 9 regions. The coherence of the data is poor in regions such as the inferior temporal gyrus and calcarine cortex but strong in the dorsal anterior cingulate.

4.6.2 Identifying the most parsimonious model

Each of the ten models outlined in Figure 4.2 was fitted to the data. The sum of squares of the residuals of the model was calculated across all 76 regions. This was used to calculate a BIC value, BIC_i for each model i and these were used to assess the quality of the fit for each model. Model 9 had the lowest BIC of the models tested and therefore was deemed to be the most parsimonious and by our criteria was determined to be the best model.

The ΔBIC_i for each model i was calculated where $\Delta BIC_i = BIC_i - \min(BIC)$ and $\min(BIC)$ is the BIC value of Model 9. As ΔBIC_i increases, the probability that model i is the optimal model decreases. Kass and Raftery 1995 stated that there is "strong evidence" that the model with lower BIC value is better when the $\Delta BIC > 10$. The smallest ΔBIC value across the models tested was 3510

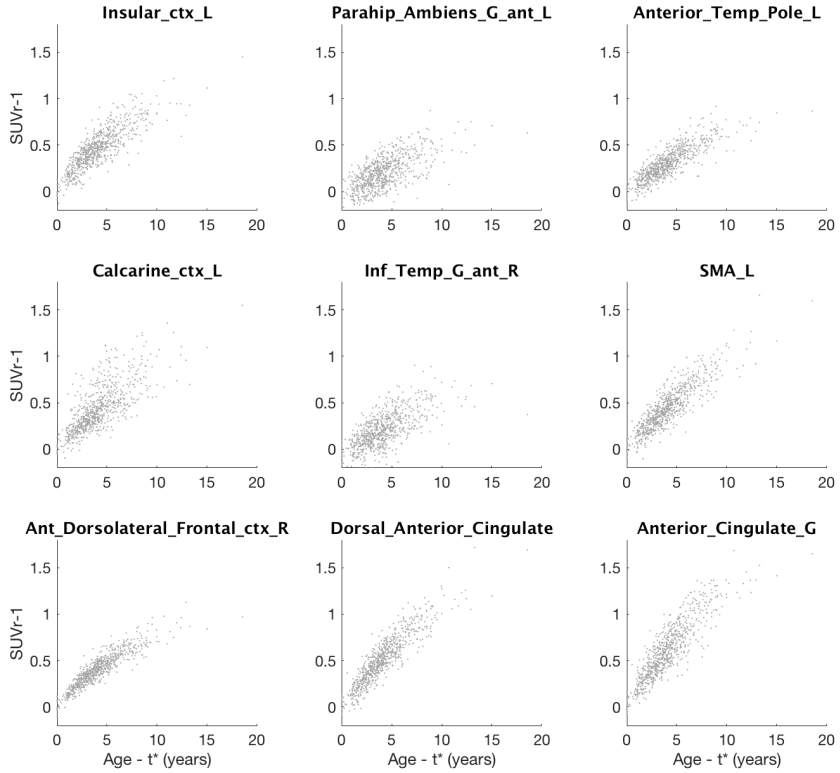


FIGURE 4.3: Example scatter plots created after finding t^* for each subject. $Age - t^*$ is the estimated time since accumulation began. Each plot gives the estimated regional accumulation at the population level.

	Production	Clearance	Network	No. of params	SSQ	ΔBIC_i
Model 1	One ROI	Global	Yes	3	1590	51500
Model 2	One ROI	Local	Yes	78	1590	52400
Model 3	All ROIs - Global	Global	Yes	3	1620	52500
Model 4	All ROIs - Global	Global	No	2	1620	52500
Model 5	All ROIs - Global	Local	Yes	78	1470	47700
Model 6	All ROIs - Global	Local	No	77	979	24000
Model 7	All ROIs - Local	Global	Yes	78	690	3510
Model 8	All ROIs - Local	Global	No	77	743	7880
Model 9	All ROIs - Local	Local	Yes	153	640	0
Model 10	All ROIs - Local	Local	No	152	688	4190

TABLE 4.1: A table showing the results of fitting each of the different models to the dataset. Models were ranked by the BIC value. The rightmost column shows the Delta BIC for each model where $\Delta BIC_i = BIC_i - \min(BIC)$ and $\min(BIC)$ is the lowest value across all the models. Model 9 has the lowest BIC values and all other models had a ΔBIC of greater than 3500.

(see Table 4.1) and therefore one has good confidence that Model 9 was the best model of the ten fitted to the data.

Local production was the most important feature for a good fit to the model. The SSQ was <800 for all models tested with local production and >800 for all models without local production.

Model 9 can accurately describe the scatter plots created after obtaining t^*. Fits of Model 9 can be seen in Figure 4.4. Model 9 is the most highly parametrised model of the 10 tested. The variable production rates allow enough flexibility to accurately fit high, medium and low accumulating regions and the individual clearance rates allow the model to have different shape curves although the predicted curves is always hyperbolic.

4.7 Limitations

The spatiotemporal distribution of Aβ was modelled with a network diffusion model on a weighted graph in a similar way to previous analyses and whilst this approach is attractive, it is important to understand the assumptions made and the limitations.

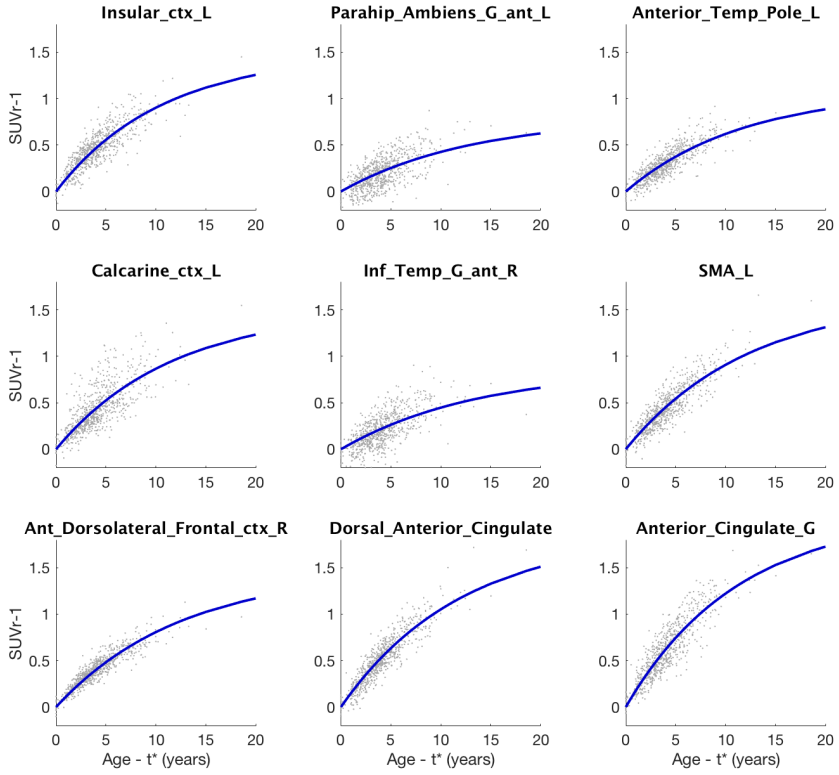


FIGURE 4.4: Plots for 9 regions showing the fit of Model 9 to the data. The model can accurately describe the data in regions with high and low uptake.

4.7.1 Network diffusion model on a weighted graph

In this experiment, it was assumed firstly, that the concentration in any region can be be collapsed to a concentration at a given node. This means that it is assumed that within an ROI from the CIC atlas (Tziortzi et al. 2011) the uptake was uniform. Whilst this is an oversimplification as uptake within regions regions is heterogeneous, the parcellation into 76 anatomical regions means that this heterogeneity is limited.

It was hypothesised that Aβ accumulation could be effectively modelled by a network diffusion model on the created weighted graph. This was motivated by previous work conducted by Raj, Kuceyeski, and Weiner 2012. The network diffusion model fitted to the process included three processes; Aβ production, Aβ clearance and spreading between regions. Many biological processes could be involved in all three of these processes and may not be limited to being involved in only one process. The aim of this work was to provide information whether the stereotypical accumulation pattern observed in AD can be accurately modelled. Understanding biological mechanisms underlying each of these processes, ie, studying the mechanism which clears Aβ from the brain is beyond the scope of this work.

4.7.2 The parameter $Age - t^*$

Currently, a longitudinal dataset with multiple time-points across the full Aβ accumulation period does not exist. Therefore, in order to study the accumulation of Aβ over a 30-year period it was necessary to create a dataset representing the spatiotemporal distribution on Aβ at the population level. In this work, this was done by calculating an t^* for each subject in the cross-sectional data. This t^* was the age at which accumulation was calculated to begin. Subsequently, $Age - t^*$ was the length of time that Aβ had been accumulating for. Once $Age - t^*$ was calculated for each subject, it was possible to plot the regional SUVr versus $Age - t^*$ for each subject. After plotting this for every subject, a set

of 76 plots (one for each cortical region) representing the accumulation of Aβ at the population level was obtained.

Clearly, the parameter t^* is important when constructing the dataset and also in the results that follow. t^* was found by fitting a simple version of the network diffusion model where all parameters apart from t^* were fixed to give a biologically plausible accumulation period of 30 years and maximum value for SUVr = 1.8. This approach suffers from some severe disadvantages which mean interpretation of the results in this chapter is difficult. The main disadvantage is that I have used the model both to construct the data and then to fit to it. This means that the second stage of fitting is likely to produce good fits to the data and it is difficult to know whether a network diffusion model is in fact accurately describes Aβ accumulation. Secondly, the $Age - t^*$ calculated for each subject is heavily dependent on the chosen parameters for production and clearance in the 2-parameter model fitted initially. As previously discussed these were chosen to give biologically plausible results but they are still arbitrarily chosen. It is possible to create plausible results with different values for production and clearance. Identification of these parameters is therefore impossible and as the values for the production clearance and spreading in the second phase of fitting are dependent on these results, it follows that these too will suffer from problems of identifiability.

To improve the methodology it would be far more robust if the creation of the dataset to which the ten models were fitted was completed without the use of any kind of network diffusion model, ideally with information from longitudinal data to increase its plausibility. This idea will be expanded upon in Chapter 5.

4.7.3 The optimum network diffusion model

In the second phase of optimising the network diffusion model, ten different versions of the model were fitted to the dataset created in the first phase. The ten different models had different options for the production, clearance and

spreading parameters. The optimum model was decided upon using the BIC because the best model is not necessarily the one which gives the lowest sum of squares of residuals. Rather, the best model is the one which provides the most parsimonious fit to the data meaning that it provides the best balance between the number of parameters and the goodness of fit of the model. The model didn't include lagged start times for production which could have added further flexibility however, these weren't included because identifiability of parameters was difficult due to the high dimensionality of the models tested and lagged start time would have made this worse.

There are a number of different information criteria such as the Akaike information criteria and the deviance information criteria. The choice to use the BIC was taken as it has been shown to be better when considering nested models and when the aim is explanatory power rather than predictive power (Burnham and Anderson 2004). In this study however, the AIC and the BIC picked the same model as being the most parsimonious. Information criteria are one way to assess the parsimony and fit of a model but a more robust way would be to cross-validate the model on an independent dataset. One could, for instance, fit the model on half the dataset presented and then assess the fit on the other half. This wasn't performed here because I wanted to use the whole dataset for the fitting to achieve the best estimate of the parameters but this does mean the validation of the best model is difficult.

4.8 Conclusion

In this chapter, the spatiotemporal distribution of Aβ has been modelled using a network diffusion model. Ten different models were defined and fitted and the most parsimonious model was obtained using information criteria.

In order to fit the ten different models we were required to fit a t^* for each subject first. This t^* represents the age at which the model estimates the accumulation of insoluble aggregates of β-amyloid began. The fitting of t^* is dependent on the values arbitrarily chosen for production and clearance. This then will

affect the fitting of each of the ten models. Interpreting the results is therefore difficult.

To improve the work, it is important to identify t^* without using the model and this idea will be explained in the next chapter.

Chapter 5

Spatiotemporal modelling of Aβ using a four-parameter logistic growth model

In the previous chapter, the spatiotemporal distribution of Aβ in AD was modelled using a network diffusion model but the results were difficult to interpret due to problems with the identifiability of parameters. In this chapter, the weaknesses of the methodology in Chapter 4 are addressed. Results from a previously published longitudinal study are combined with the ADNI cross-sectional dataset to create a dataset showing the spatiotemporal distribution of Aβ at the population level — a 'chronological dataset'. A four-parameter logistic growth model is introduced and used to model the chronological dataset and different versions of the logistic growth model are fitted to the data to obtain the most parsimonious fit to the data. By examining the parameterisation of the optimum model I am able to provide evidence that Aβ does not spread from a small number of seed regions over an extended period during its accumulation but rather that it accumulates at the same time across all regions with regions having different maximum possible concentrations of Aβ.

5.1 Aims and outline

The model for the spatiotemporal distribution of Aβ used in the previous chapter included parameters for production, clearance and spreading. Due to difficulties in parameter identification, it was difficult to draw conclusions on the importance of each of these processes and in particular, it was impossible to determine whether the spreading component was a key aspect of the model fitting.

In this chapter, I aim to model the spatiotemporal distribution of Aβ in AD using a novel logistic growth model. With this aim, in section 5.2, I introduce a four parameter logistic growth model. By using data from a previously published longitudinal study I describe how a chronological dataset representing the spatiotemporal distribution of Aβ in AD is created in section 5.3. In a similar way to chapter 4, in section 5.4 I define a model space consisting of 16 models which allow me to test the competing hypotheses for Aβ accumulation in section 5.5. The optimal model is fitted at the voxel level in section 5.10 which produces parametric maps for two spatially varying parameters from the logistic growth model which will be used in the next chapter. Finally, in section 5.8 the results are discussed and potential confounds are identified.

5.2 Logistic growth model of Aβ accumulation

This section introduces a logistic growth model to describe the accumulation of Aβ in the human brain. The model assumes that the growth rate of Aβ concentration is proportional to the product of the current concentration of Aβ and a term limiting growth due to the carrying capacity of the local environment (Verhulst 1844). The model is defined by the following differential equation,

$$\frac{dA\beta(t)}{dt} = rA\beta(t)\left(1 - \frac{K}{A\beta(t)}\right) \tag{5.1}$$

where $A\beta(t)$ is the concentration of Aβ at time t, r is the uninhibited exponential growth rate and K is the carrying capacity.

Solving the differential equation yields a function for the concentration of Aβ over time,

$$A\beta(t) = \frac{K}{1 + e^{-r(t-T_{50})}} \tag{5.2}$$

where T_{50} is the time of half maximal concentration (i.e. $A\beta(T_{50} = \frac{K}{2})$.

In vivo, SUVr is the outcome measure which includes the Aβ concentration, $A\beta(t)$. In order to model SUVr directly, it is necessary to account for the non-specific binding present in the SUVr outcome measure,

$$SUVr(t) = NS + A\beta(t) \tag{5.3}$$

where NS is the non-specific component of the imaging outcome measure SUVr.

Combining equations 5.2 and 5.3 yields,

$$SUVr(t) = NS + \frac{K}{1 + e^{-r(t-T_{50})}} \tag{5.4}$$

This equation describes the temporal evolution of the *in vivo* PET Aβ signal over time (with the four parameters NS, r, T_{50} and K). The graph displayed in Figure 5.1 shows a curve over a 30 year period with $T_{50} = 15$ years, $K = 2$, $NS = 1$ and $r = 1$.

5.3 Construction of a chronological dataset

The main disadvantage of the methodology in Chapter 4 was that the network diffusion model was fitted twice; firstly, to generate a dataset representing the spatiotemporal distribution of Aβ in AD and secondly, to model the generated dataset. This caused the results from the second step to be dependent on the

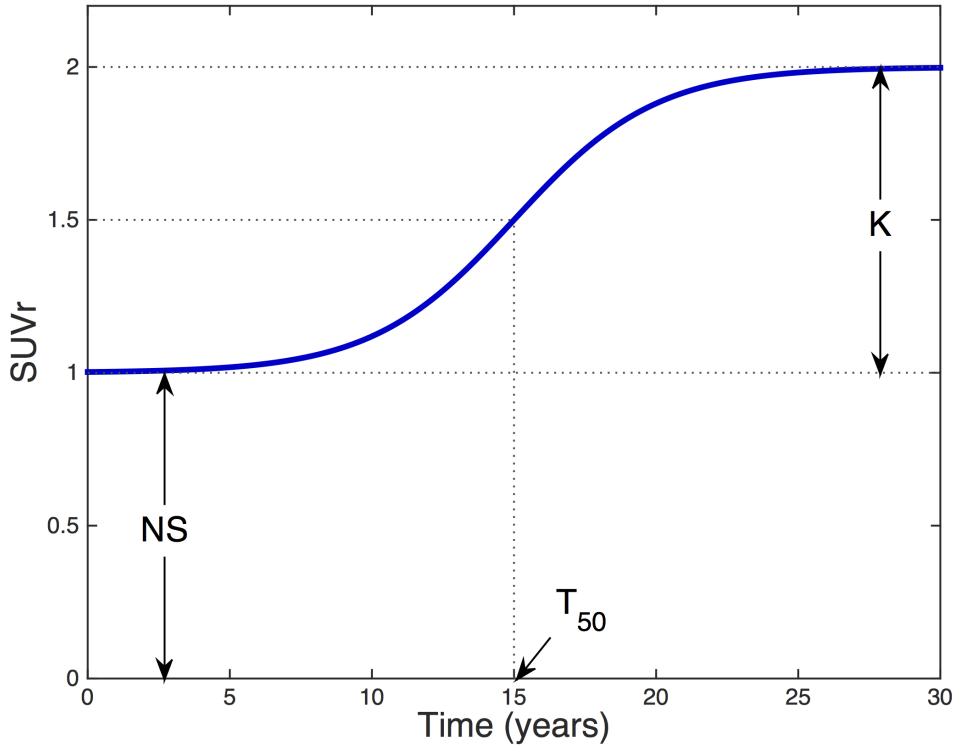


FIGURE 5.1: The logistic growth model describing the PET imaging signal over time as a function of the PET tracer's non-specific binding (NS), the carrying capacity (K), the time of half maximal Aβ concentration (T_{50}) and the uninhibited exponential growth rate (r).

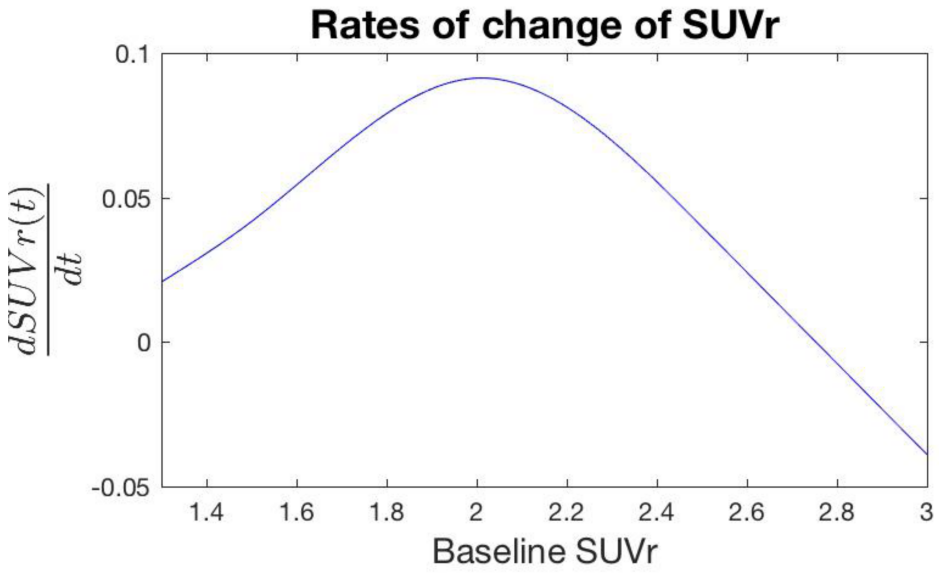


FIGURE 5.2: The cubic spline function found by Jack et al. 2013 which describes rates of change of mean cortical SUVr as a function of the baseline value. In this work, I followed the methodology described by Jack et al. 2013 to create a functional form for the temporal evolution of mean cortical SUVr in AD by integrating this cubic spline function with respect to time.

inputs from the first. To address this, in this chapter, a time through the accumulation process for each subject i, t_i, is calculated independently (ie, without using any version of the logistic growth model) using a previously published functional form describing the temporal changes of [^{11}C]PiB mean cortical SUVr in AD (Jack et al. 2013). The functional form was derived by fitting a cubic spline function to rates of change of mean cortical SUVr in a longitudinal study. The cubic spline was kindly provided to me by Clifford Jack and can be seen in Figure 5.2. Following the methodology of Jack et al. 2013, I integrated this cubic spline function with respect to time to obtain a functional form for the temporal evolution of [^{11}C]PiB mean cortical SUVr in AD .

The set of calculated times, $T = \{t_i\}$, were then used to generate a dataset representing the spatiotemporal distribution of Aβ in AD at the population level - from here on this will be termed the 'chronological dataset'.

It is important to evaluate whether the subjects from the two samples (the longitudinal study from Jack et al. 2013 and the cross-sectional ADNI study) are part of the same population. Demographics for both studies are summarised

Characteristic	Jack et al. 2013	ADNI
Number	260	769
Age - median (min max)	79 (70 94)	73 (55 91)
Male - n (%)	162 (62)	438 (57)
Number of MCI/AD patients - n (%)	55 (21)	558 (73)
APOE e4 positive - n (%)	87 (33)	342 (44)
MMSE - median (min max)	28 (23 30)	28 (19 30)

TABLE 5.1: The characteristics of the subjects taken from both the longitudinal study performed by Jack et al. and the cross-sectional data obtained from ADNI. These two datasets are combined to create a chronological dataset.

in Table 5.1 and one can see that they are well matched in all categories apart from age where the subjects in the longitudinal study were older. However, both studies have a wide enough range of ages that they include subjects at all stages of the accumulation process.

5.3.1 Transformation of the functional form for use with [^{18}F]AV45 data

The functional form provided to me by Jack et al. 2013 was derived from a longitudinal Aβ imaging data using [^{11}C]-PiB rather than [^{18}F]-AV45. Previous work scanning the same subjects with both [^{11}C]-PiB and [^{18}F]-AV45 has shown that there is a strong linear relationship between [^{11}C]-PiB and [^{18}F]-AV45 SUVr values (Landau, Breault, et al. 2013,Landau, Thomas, et al. 2014) and that a linear equation can appropriately convert between the different PET tracers according to

$$AV45_{SUVr} = aPiB_{SUVr} + b \tag{5.5}$$

Therefore, a transformation of the [^{11}C]-PiB derived functional form into [^{18}F]-AV45 SUVr units was performed so that the resultant function, $SUVr(t)$ ranged between the median of the 2.5th and 97.5th mean cortical [^{18}F]-AV45 SUVr percentiles for the cross-sectional ADNI dataset ($a = 0.72$ and $b = 0.02$).

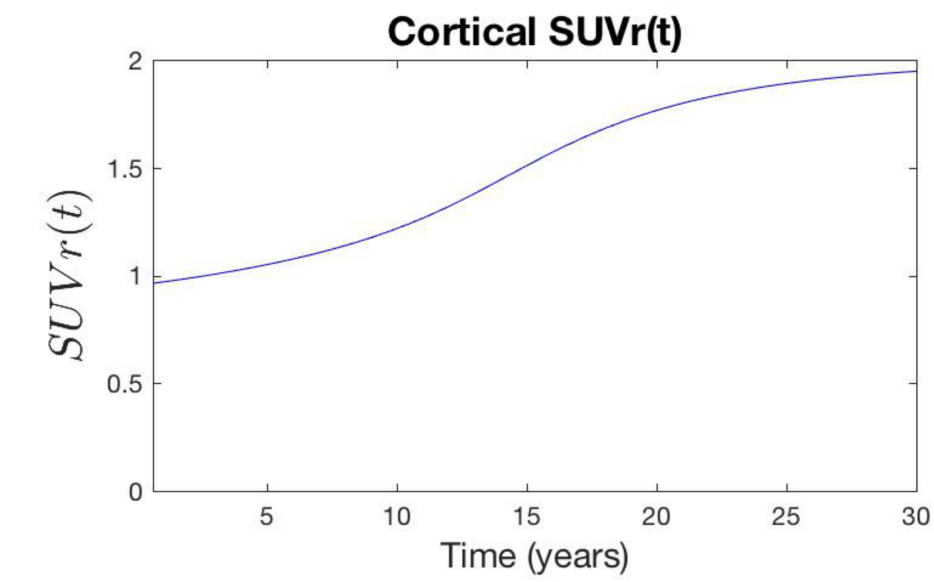


FIGURE 5.3: The functional form for the temporal evolution of mean cortical SUVr in AD over a 30 year period. The curve is produced by integrating the cubic spline function shown in Figure 5.2 and subsequently applying a linear transformation to account for differences between [^{11}C]PiB and [^{18}F]AV45

Figure 5.3 shows the resulting curve which describes the temporal evolution of mean cortical SUVr as measured with [^{18}F]AV45 in AD. The curve has a sigmoidal shape with the fastest accumulation occurring between 10 and 20 years after accumulation begins. As Jack et al. 2013 noted, this curve reaches a plateau SUVr value of approximately 2.

5.3.2 Finding the time through the disease process, t_i and generation of the chronological dataset

The time point in the chronology of the disease process t_i was determined for each subject by taking their mean cortical SUVr value (calculated in section 3.2) and looking up from this function what time this corresponded to in the range 0 to 30 years. This generated a chronological data set for the spatiotemporal accumulation of Aβ by associating an individual time in the 30 year disease cascade with each of the [^{18}F]AV45 images.

Figure 5.5 shows a histogram of the times t_i calculated for each of the 769 subjects. The set of times T appear to be normally distributed and have a mean of 11.8 years and a standard deviation of 5.12 years. Importantly though, there

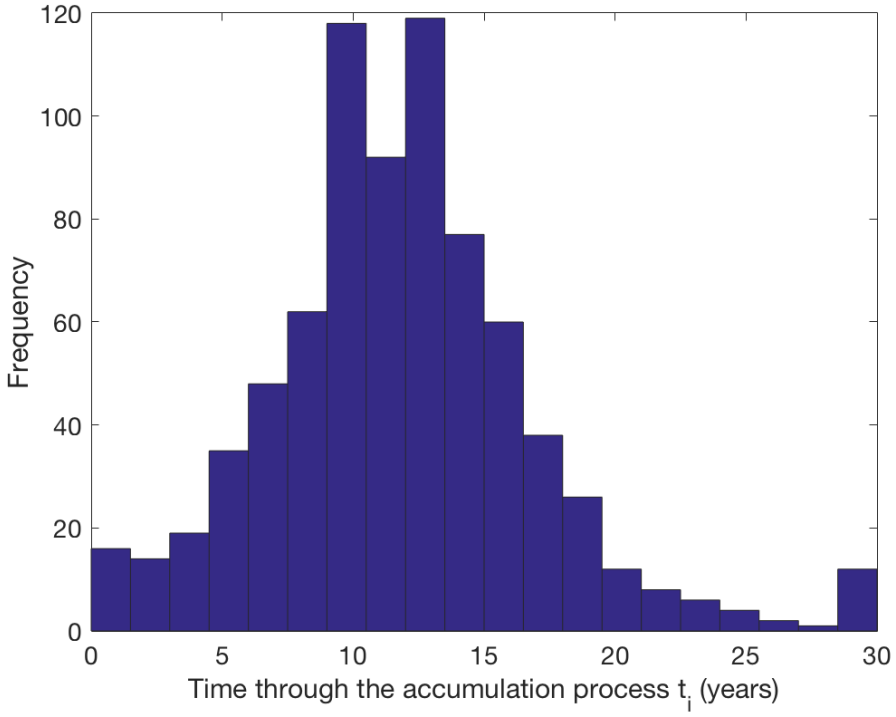


FIGURE 5.4: A histogram to show the distribution of the set $T = \{t_i\}$. This distribution is normal with mean of 11.8 years and standard deviation of 5.12 years. There are subjects in all the bins meaning that the cross-sectional data appears to have subjects at al stages of the accumulation process.

are data points existing at all times throughout the disease process. The test-retest variability of mean cortical [^{18}F]AV45 SUVr values has been calculated to be less than 3% (Joshi et al. 2012) which would translate to a variability of 0.68 years in calculated t_i for the median SUVr value of 1.3 in the cross-sectional dataset. This result means one can have good confidence that the calculation of t_i is robust and that therefore the chronological dataset can be used to study the spatiotemporal distribution of Aβ in AD.

An ROI level chronological dataset was formed in a similar way to chapter 4. Regional SUVr (calculated in section 3.2) were plotted against t_i for each subject for 90 cortical and subcortical regions and resulting in plots for the temporal evolution of regional SUVr in AD. The plots exhibited coherent but different trajectories within individual regions providing evidence of a stereotypical spatiotemporal distribution at the population level - see Figure 5.5. As with

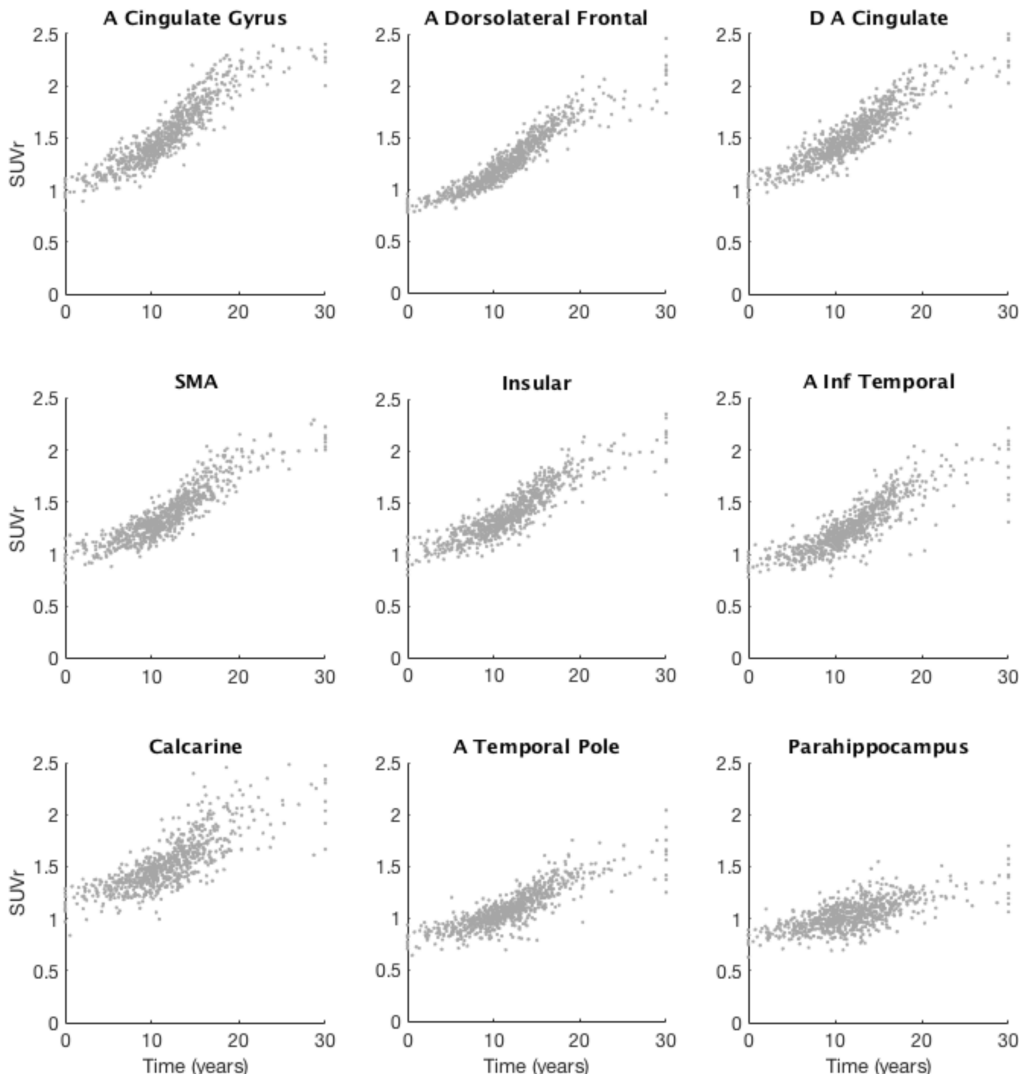


FIGURE 5.5: The chronological [^{18}F]-AV45 Aβ PET data in 9 regions. The trajectories in regions are coherent providing strong evidence that there is a stereotypical accumulation pattern for Aβ in AD. (D: Dorsal, A: Anterior, Inf: Inferior).

the previous chapter the level of coherence varied across regions. Higher accumulating regions such as the anterior cingulate gyrus and anterior dorsolateral frontal cortex having the least variability and low accumulating regions such as the parahippocampus exhibiting higher variability. The overall coherence of the regional curves shows that there is not only a stereotypical temporal accumulation at a global level but also that relative to that, each region has a stereotypical accumulation curve which is consistent across subjects.

5.4 Model space

To investigate the different hypotheses for the underlying process driving Aβ accumulation, it is important to find out whether each of the four model parameters is constant across different brain regions or whether they are regionally different. Of particular interest is the parameter T_{50} because if the T_{50} varies between regions then the model is consistent with longer term spreading from seed regions as seed regions would have a lower T_{50} than other regions because accumulation would start there first. If however, T_{50} is constant across the brain it is consistent with local tissue properties driving the accumulation process.

In order to determine whether each of the 4 model parameters were constant across the whole brain or varied by region, sixteen different models were investigated corresponding to all the permutations of using either "Global" (the parameter is constant across all brain regions) or "Local" (the parameter varies by region) parameter values for each of the four model parameters. The full set of models are summarised in Table 5.2 and contain between 4 and 360 parameters.

Figure 5.6 provides examples of curves for 3 different simulated regions (red curve, green curve and blue curve) for each of the 16 different models. In Model 1, K, r, T_{50} and NS are all Global parameters and as such all regions have the same trajectory. Model 16 by contrast has all parameters as Local which means an individual four-parameter logistic growth model is fitted to each region. Models with a Local T_{50} (grey background) are consistent with long-term spreading from seed regions. One would expect, the red curves to be representative of a seed region trajectory as they have the shorter T_{50}. whereas models Global T_{50} have a white background.

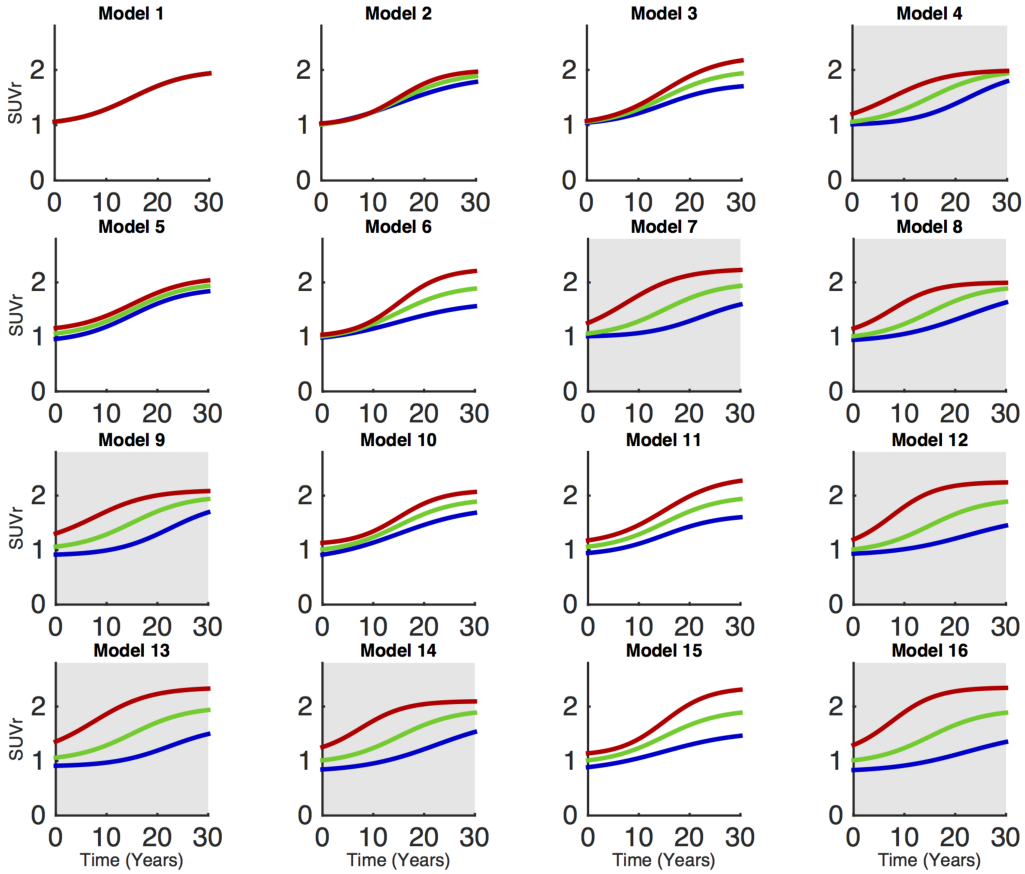


FIGURE 5.6: 16 logistic growth models of Aβ accumulation with example curves from 3 distinct brain regions. Models in grey have regionally different T_{50} values and are consistent with spreading from seed regions whilst the models in white are consistent with local tissue properties driving the Aβ accumulation process.

5.4.1 Fitting the logistic growth model to the chronological dataset and investigation of the model space

Each of the models was fitted to the regional chronological data using a nonlinear trust-region reflective algorithm implemented in MATLAB (The Mathworks Inc, Natwick, CA) that minimised the residual sum of squared errors subject to $A\beta(0) < 0.1$. This bound was introduced as it is assumed that the level of Aβ at the beginning of the accumulation was small and solutions violating this would not be modelling the whole accumulation process.

Model selection was performed using the BIC to select the most parsimonious model and a posterior probability of each model being optimum was ascertained from the weights of each model. The formula for the posterior probability (Schwarz 1978; Neath and Cavanaugh 2012) of a model M_j in a model space D with n different models, $Pr(M_j|D)$ is give in Equation 5.6.

$$Pr(M_j|D) = \frac{e^{\Delta BIC_j}}{\sum_{i=1}^{n} e^{\Delta BIC_i}} \tag{5.6}$$

where, $\Delta BIC_k = BIC_k - \min BIC$ and $\min BIC$ is the smallest BIC value of all the models in the model space D.

The posterior probability provides the probability that M_j is the optimum of all the models in the model space if all models are assumed to have equal priors.

5.5 ROI level results

Each of the logistic growth models was fitted to the chronological *in vivo* PET data to investigate the spatiotemporal evolution of the signal in the AD process. The 16 logistic growth models were successfully fitted and Model 11 was identified as the most parsimonious description of the data as determined by the BIC (see Table 5.2). The difference in BIC between Model 11 and all the other models (ΔBIC_i) is at least 137. As was mentioned in the previous chapter, evidence is considered strong when BIC is greater than 10 (Kass and Raftery 1995).

Model	K	r	T_{50}	NS	Parameters	SSQ	ΔBIC_i
Model 1	Global	Global	Global	Global	4	2288	96900
Model 2	Global	Local	Global	Global	93	1612	73600
Model 3	Local	Global	Global	Global	93	925.1	35200
Model 4	Global	Global	Local	Global	93	823.6	27200
Model 5	Global	Global	Global	Local	93	667.6	12600
Model 6	Local	Local	Global	Global	182	741.7	20900
Model 7	Local	Global	Local	Global	182	690.6	16000
Model 8	Global	Local	Local	Global	182	668.9	13800
Model 9	Global	Global	Local	Local	182	607.7	7120
Model 10	Global	Local	Global	Local	182	574.1	3180
Model 11	Local	Global	Global	Local	182	548.3	0
Model 12	Local	Local	Local	Global	271	654.3	13300
Model 13	Local	Global	Local	Local	271	547.6	908
Model 14	Global	Local	Local	Local	271	545.5	642
Model 15	Local	Local	Global	Local	271	541.6	137
Model 16	Local	Local	Local	Local	360	540.6	1030

TABLE 5.2: The 16 parameterisations of the logistic growth model of Aβ accumulation used to analyse the chronological [^{18}F]-AV45 SUVr PET data at a regional level with the corresponding sum of squared residuals (SSQ) and ΔBIC_i. 90 cortical and subcortical regions were included and parameters were either restricted to a single value across all regions (Global) or fitted individually for each region (Local). ΔBIC_i gives a measure of the parsimony of each model in relation to the smallest BIC value. Model 11 (Local K, Global r, Global T_{50} and Local NS) gives the most parsimonious fit to the data.

The posterior probability that Model 11 is the best choice of the models tested is also high (p>0.999999).

The model was able to accurately describe the time course of Aβ accumulation in all regions. A selection of 9 regions with different levels of Aβ accumulation are displayed in Figure 5.7, demonstrating the ability of the model to accurately describe distinct regional time courses. The fits to all 90 regions are shown in Figures 5.8 and 5.9.

Model 11 requires that local regional values for Aβ carrying capacity and tracer non-specific binding vary. In contrast, the time to half maximal Aβ (T_{50}) and the uninhibited exponential growth rate (r) are constant across brain regions in this model. This suggests that regional variability in Aβ carrying capacities determine the distribution of Aβ concentration as regions with higher carrying capacities will accumulate more Aβ over time. These results support the hypothesis that regional Aβ accumulation is limited by properties of the local

tissue environment. The observation that the data is best explained by a model with a global T_{50} provides evidence against the spreading hypothesis, as long-term spreading from seed regions would imply shorter T_{50} for seed regions and therefore require models with a local T_{50} such as Model 12.

For Model 11, the largest carrying capacities were obtained in the anterior cingulate gyrus, precuneus and frontal operculum cortex (1.55, 1.50 and 1.46 SUVr units respectively), intermediate values were obtained in parts of the frontal cortex and the insular cortex (1.13 and 1.19) and lower values thalamus and the brain stem (0.48 and 0.38). The global time of half accumulation, T_{50} was 14.9 years and the uninhibited exponential growth rate $r = 0.20$ years^{-1} were constant across all regions.

5.6 Alternative brain parcellations

In order to confirm that the results presented are not dependent on the chosen parcellation of the brain, the same methodology was performed on two more parcellations of the brain. The first was restricted to only the 76 cortical regions of the 90 regions originally presented and the second had 9 large regions covering the whole brain (calculation of these regional SUVr values is covered in section 3.2). Tables analogous to Table 5.2 for each of these parcellations are shown in Tables 5.3 and 5.4.

As with the 90 region parcellation, Model 11 is found to be the most parsimonious as evaluated by the BIC in both the additional parcellations of the brain. These results provide strong evidence that Model 11 is the optimum model for the chronological dataset out of the 16 fitted regardless of which neuroanatomical atlas or parcellation one chooses.

5.7 Parametric imaging

Having identified Model 11 (Global r and T_{50} and Local NS and K) as the optimal model based on the regional analysis, the model was then fitted at the voxel

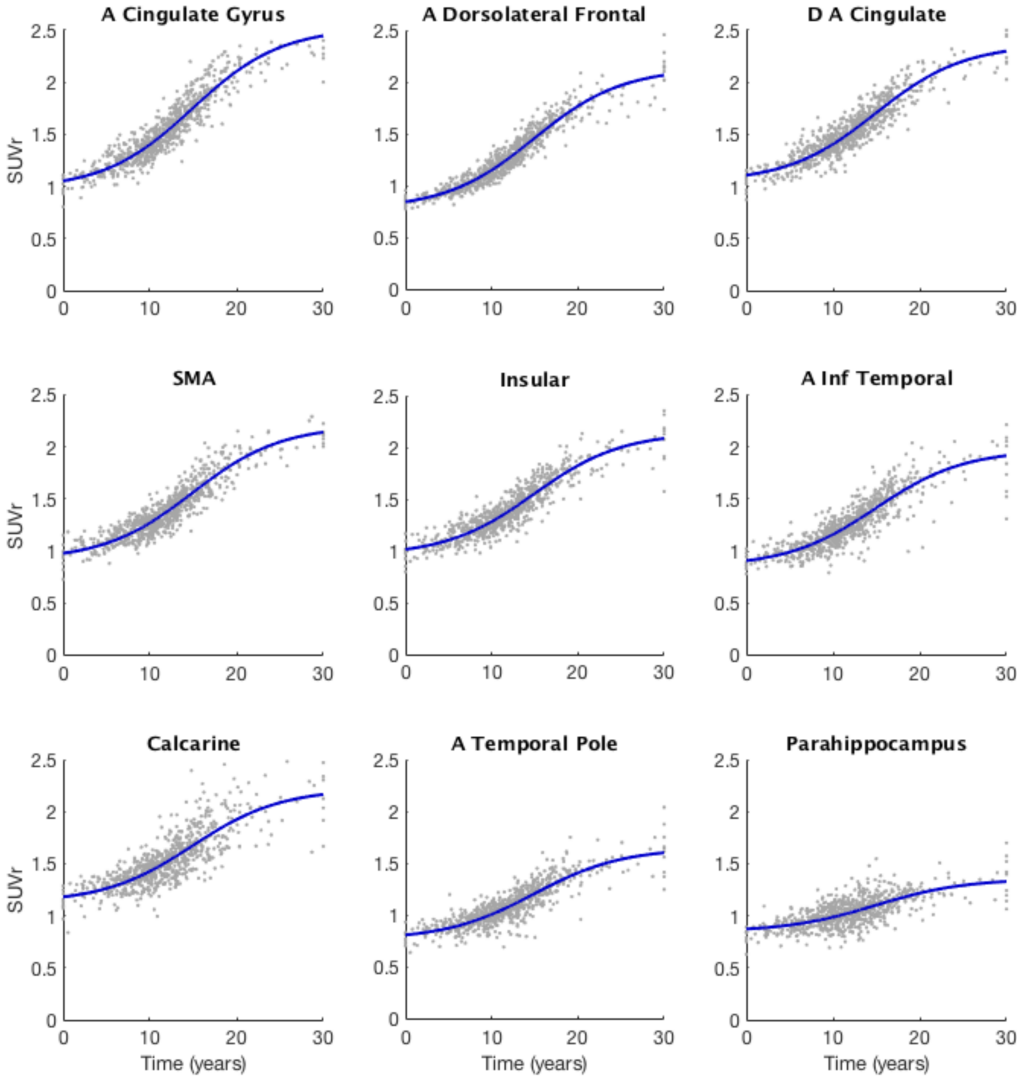


FIGURE 5.7: Model fitting of the most parsimonious logistic growth model (Model 11) to the chronological [^{18}F]-AV45 Aβ PET data in 9 regions taken from the 90 region parcellation of the CIC atlas (Tziortzi et al. 2011) (D: Dorsal, A: Anterior, Inf: Inferior). The model accurately describes the data including regions of high accumulation (top row), medium accumulation (middle row) and low accumulation (bottom row).

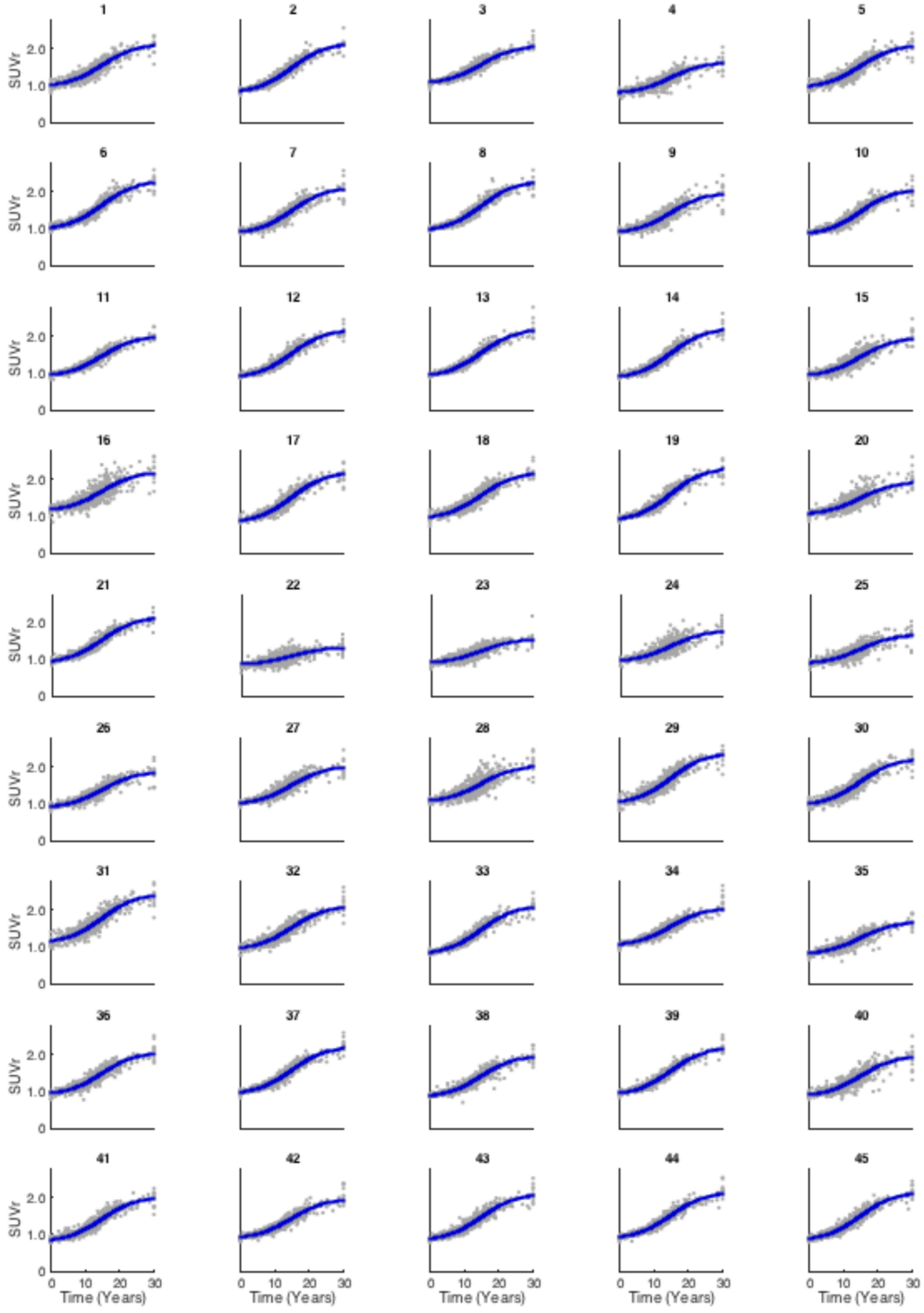


FIGURE 5.8: The fit of Model 11 to the chronological dataset for ROIs 1-45 of the 90 region parcellation of the CIC atlas (Tziortzi et al. 2011). The model accurately describes all trajectories but the level of coherence in the data is variable across regions

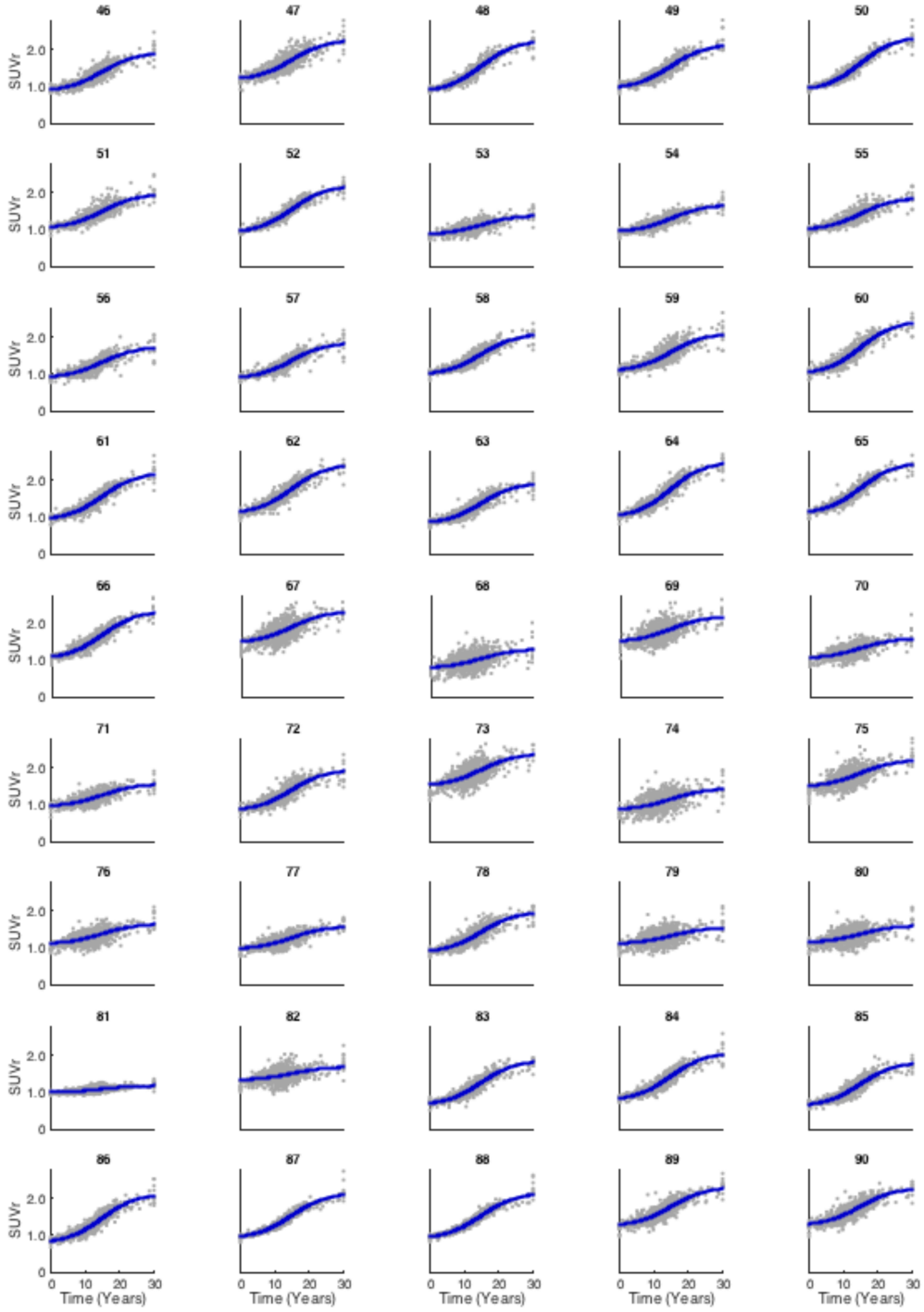


FIGURE 5.9: The fit of Model 11 to the chronological dataset for ROIs 46-90 of the 90 region parcellation of the CIC atlas (Tziortzi et al. 2011). The model accurately describes all trajectories but the level of coherence in the data is variable across regions. In particular, the subcortical regions have a higher level of variability.

Model	K	r	T_{50}	NS	Parameters	SSQ	ΔBIC_i
Model 1	Global	Global	Global	Global	4	1257	74800
Model 2	Global	Local	Global	Global	79	895.3	55800
Model 3	Local	Global	Global	Global	79	484.3	19900
Model 4	Global	Global	Local	Global	79	456.4	16400
Model 5	Global	Global	Global	Local	79	400.4	8740
Model 6	Local	Local	Global	Global	154	392.0	8330
Model 7	Local	Global	Local	Global	154	394.3	8670
Model 8	Global	Local	Local	Global	154	403.8	10100
Model 9	Global	Global	Local	Local	154	381.8	6790
Model 10	Global	Local	Global	Local	154	347.4	1270
Model 11	Local	Global	Global	Local	154	339.9	0
Model 12	Local	Local	Local	Global	229	371.3	5980
Model 13	Local	Global	Local	Local	229	339.6	758
Model 14	Global	Local	Local	Local	229	339.7	791
Model 15	Local	Local	Global	Local	229	336.7	273
Model 16	Local	Local	Local	Local	304	336.1	977

TABLE 5.3: An equivalent table to Table 5.2 but using a set of 76 cortical ROIs only (this corresponds to the removal of the sub-cortical regions from the previous set of 90 ROIs where there is lower accumulation)

Model	K	r	T_{50}	NS	Parameters	SSQ	ΔBIC_i
Model 1	Global	Global	Global	Global	4	434.4	12700
Model 2	Global	Local	Global	Global	12	227.7	8320
Model 3	Local	Global	Global	Global	12	126.9	4280
Model 4	Global	Global	Local	Global	12	106.2	3040
Model 5	Global	Global	Global	Local	12	94.15	2210
Model 6	Local	Local	Global	Global	20	103.5	2940
Model 7	Local	Global	Local	Global	20	90.90	2040
Model 8	Global	Local	Local	Global	20	86.13	1660
Model 9	Global	Global	Local	Local	20	74.93	700
Model 10	Global	Local	Global	Local	20	77.40	925
Model 11	Local	Global	Global	Local	20	67.72	0
Model 12	Local	Local	Local	Global	28	84.44	1600
Model 13	Local	Global	Local	Local	28	67.64	62.1
Model 14	Global	Local	Local	Local	28	67.62	60.5
Model 15	Local	Local	Global	Local	28	67.05	1.40
Model 16	Local	Local	Local	Local	36	67.01	68.2

TABLE 5.4: An equivalent table to Table 5.2 but using a set of 9 ROIs which are much larger regions and cover the whole brain

level to generate parametric images of the tracer's non-specific signal (NS) and the regional Aβ carrying capacity (K). Parameter values for r and T_{50} were fixed from the regional analyses ($r = 0.20$ years^{-1} and $T_{50} = 14.9$ years) and individual voxel time course were fitted using a linearisation of the model in order to ensure fast and robust fitting.

In order to achieve this, Equation 5.2 was transformed to,

$$SUVr(t) = \begin{pmatrix} 1 & \frac{1}{1+e^{t_1-T_{50}}} \\ \vdots & \vdots \\ 1 & \frac{1}{1+e^{t_{769}-T_{50}}} \end{pmatrix} \begin{pmatrix} NS_{vox} \\ K_{vox} \end{pmatrix} \tag{5.7}$$

where NS_{vox} and K_{vox} are the non-specific binding and carrying capacity for the voxel respectively. This is an equation of the form,

$$b = Ax \tag{5.8}$$

and therefore was solved in MATLAB using the function 'mldivide' which uses QR decomposition to solve a system of linear equations.

Parametric images of the carrying capacity and tracer non-specific binding were generated which can be seen in Figure 5.10. The carrying capacity parametric image **K** closely maps to the grey matter regions of the brain but with higher cortical carrying capacities in frontal regions. This map is consistent with post-mortem data (H. Braak and E. Braak 1991; Thal, Rüb, et al. 2002 and previous imaging studies of AD Klunk et al. 2004; Camus et al. 2012; Clark, Schneider, and Bedell 2011; K. A. Johnson, Sperling, et al. 2013. The non-specific binding parametric map **NS** is similar to a white matter image and this reflects known non-specific binding properties of the tracer. As Yang, Rieves, and Ganley 2012 stated, when Aβ scans are visually classified, images that have the highest binding in the white matter should be classified as negative scans. The strong binding here is just high levels of non-specific binding.

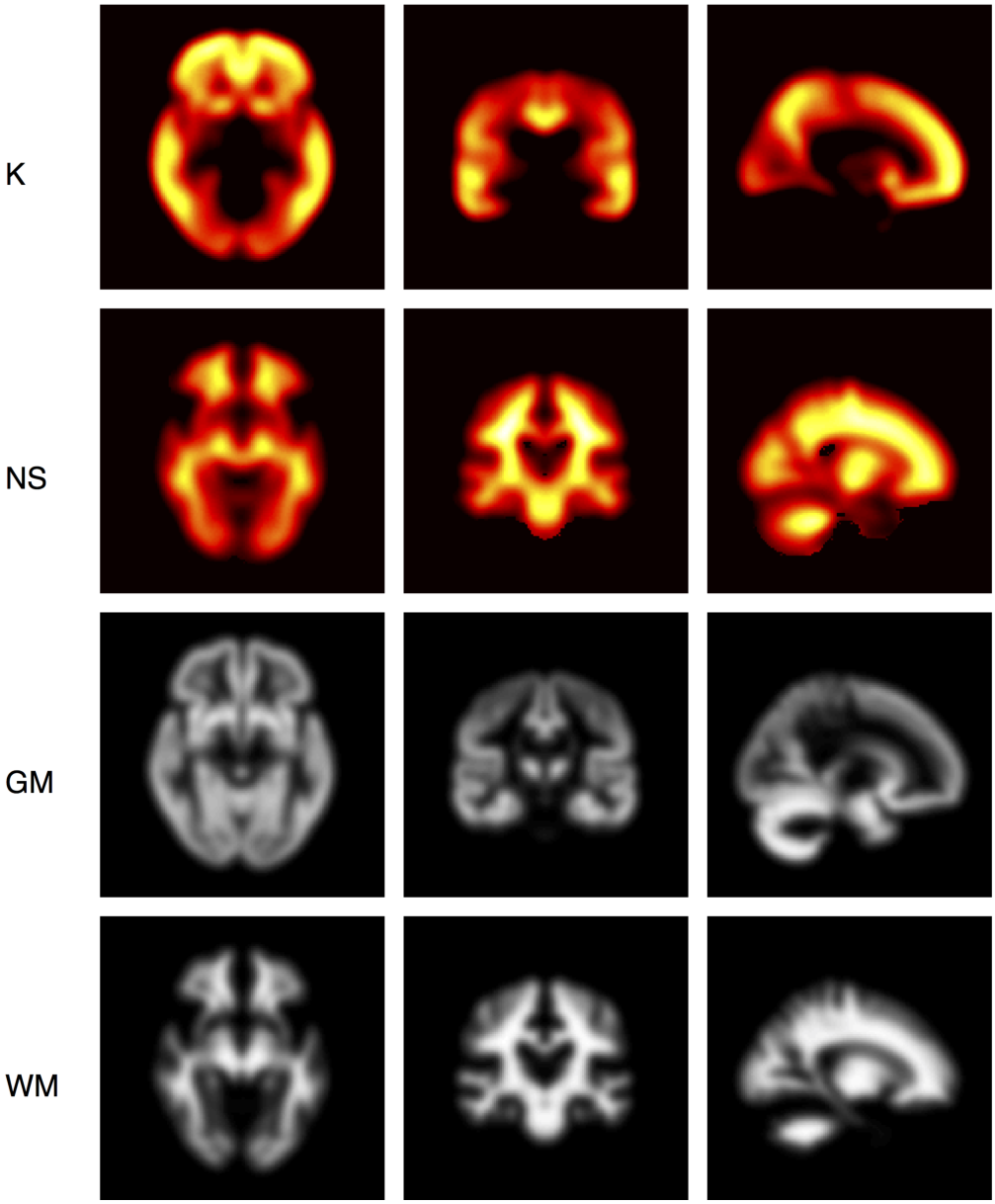


FIGURE 5.10: Parametric images displayed as orthographic projections for the carrying capacity K and the tracer non-specific binding (NS) obtained from fitting Model 11 at the voxel level. Grey matter (GM) and white matter (WM) maps are displayed for reference. The highest carrying capacities are found in the frontal lobe and the lowest are observed in the cerebellum, occipital lobe and the brain stem. The non-specific image is consistent with the known non-specific binding of [^{18}F]AV45 to white matter.

5.8 Discussion

In this chapter, I have mathematically modelled the spatiotemporal distribution of Aβ in the brain as AD pathology increases with a high degree of accuracy using a logistic growth model. The results support the hypothesis that the regional accumulation of Aβ originates at the same time with the same growth rate for all regions. The results support the hypothesis that the heterogeneous Aβ concentrations first characterised by H. Braak and E. Braak 1991 are caused by a particular property of the local tissue environment, rather than longer term spreading from seed regions, as this would require different growth rates or times to half maximal Aβ concentration (e.g. for long term spreading T_{50} would be expected to be earlier in seed regions).

First and foremost, the analysis shows that the spatiotemporal distribution of Aβ in AD can be accurately modelled using a four-parameter logistic growth model, where the carrying capacity and non-specific binding vary across the brain but the growth rate and time of half maximal concentration are constant. A model with these characteristics was clearly identified as the most parsimonious model using the BIC model selection criteria and the optimal model was shown to be independent of the chosen parcellation of the brain. Interestingly, this model has previously been shown to be able to characterise the accumulation of Aβ *in vitro* (C.-C. Lee et al. 2007).

In order to apply the logistic growth model, I formed a modelling pipeline which combined cross-sectional and longitudinal data to form a 'chronological dataset' which represented the typical accumulation of Aβ across the population. This modelling approach was confined to only Aβ imaging in AD but a similar methodology could be applied to other PET tracers and other diseases. One requires large datasets of both longitudinal and cross-sectional data as was obtained here but with more PET data being acquired all the time, this will become feasible for many tracers in the near future.

There are a number of limitations of the current work that should be considered. Firstly, in order to model the accumulation of Aβ in AD at the population level it was assumed that there is a consistent spatiotemporal distribution for all subjects within the cross sectional ADNI cohort, which may be an oversimplification. However, the clear coherence of individual trajectories in all brain regions and previous post-mortem data provides confidence that this assumption is reasonable. Secondly, when creating the chronological dataset, it was assumed that the subjects in the longitudinal data and the cross-sectional study are all following the same accumulation trajectory. Table 5.1 shows demographics for both the studies. Both studies have scans from healthy controls, MCI and AD patients and the subjects in the two studies are well matched on all the characteristics apart from the number of cognitively impaired subjects which is less in the longitudinal study. However, the most important factor is that the longitudinal data contains subjects across the full spectrum of the disease process which means that it is appropriate to apply the whole cortex SUVr canonical function derived from the longitudinal data to the cross-sectional data. Thirdly, quantification was done with SUVr and this does not account for brain atrophy during the 30-year period and the impact this may have on Aβ signal. Studies have shown that the rate of atrophy is greatest in medial temporal regions where the rate is 0.6 % per year (std = 0.7) for healthy controls increasing to 1.5 % per year (std = 0.7) in AD. With these atrophy rates, it is unlikely that atrophy would have a significant impact on the model identification and conclusions presented. Further, and perhaps more importantly, it has been shown that the majority of Aβ accumulation occurs prior to atrophy effects becoming significant (Jack Jr, Knopman, Jagust, Petersen, et al. 2013). Fourthly, the models investigated in this chapter have each parameter as either being local or global. It would be interesting to see if there is an intermediate model where groups of regions are modelled to behave similarly. These intermediate models weren't investigated and so it is possible that a more parsimonious model than Model 11 does exist for the data.

There are a number of different information criteria such as the Akaike information criteria and the deviance information criteria. The choice to use the BIC was taken as it has been shown to be better when considering nested models and when the aim is explanatory power rather than predictive power (Burnham and Anderson 2004). In this study, the AIC picked Model 15 as being the most parsimonious model. This model also has a global T_{50} but the uninhibited exponential growth rate r is a local parameter.

As stated in chapter 4, information criteria are one way to assess the the parsimony and fit of a model but a more robust way would be to cross-validate the model on an independent dataset. This wasn't performed here as the whole dataset was used for the fitting to achieve the best estimate of the parameters however this means the validation of the best model is difficult.

The spatiotemporal modelling of longitudinal data with the logistic growth model that has been introduced here could have much wider utility. In particular, it will be important to investigate the trajectory of Aβ accumulation in other dementias and neurodegenerative diseases where different patterns of Aβ are observed to ascertain whether the temporal process is the same but the spatial distribution is simply driven by different regional carry capacities or whether the accumulation process is actually different.

5.9 Conclusion

In conclusion, the *in vivo* spatiotemporal distribution of Aβ in AD can be mathematically modelled using a four-parameter logistic growth model where the Aβ carrying capacity is heterogeneous across the brain but the exponential growth rate and time of half maximal Aβ concentration are constant. This suggests that the heterogeneous Aβ accumulation in AD results from different regional carrying capacities, rather than longer term spreading from a small number of seed regions. By fitting this model at the voxel-level it is possible to create parametric maps **K** and **NS** for the Aβ carrying capacity and the non-specific binding respectively. **K** has the highest intensities in frontal regions of the cortex and

in **NS** has the highest intensities in the white matter which reflect the known non-specific binding properties of [^{18}F]AV45. Future work, could include using the mathematical modelling approach introduced here to characterise the spatiotemporal distribution of other misfolded proteins such as tau. In the next chapter, the two parametric images are used to define a new imaging outcome measure to quantify the global Aβ burden in AD.

Chapter 6

Amyloid load, $A\beta_L$: a novel outcome measure for the global Aβ burden in AD

In the previous chapter, I provided evidence that, Aβ accumulation in AD is a global process which occurs at the same time in all brain regions and that heterogeneity in [^{18}F]AV45 uptake across the brain are the result of heterogeneity in Aβ carrying capacities and non-specific binding. I produced parametric maps for the Aβ carrying capacity and non-specific binding. In this chapter, building on the implications of the logistic growth model and these parametric maps I define a new outcome measure to quantify the global Aβ burden and an algorithm to calculate it from Aβ scans.

6.1 Quantifying Aβ burden using mean cortical SUVr

Mean cortical SUVr and composite SUVr (with grey matter cerebellum reference region) are outcome measures which are easily calculated from a static PET scan and are frequently used in Aβ imaging to quantify the global Aβ burden in the brain. Once the static image has been converted into an SUVr image (as outlined in Chapter 3), the mean cortical SUVr is defined to be the mean intensity of the voxels in a cortical target ROI. Usually, this ROI would be calculated by combining a grey matter probability map (obtained by segmenting a structural

MRI image) with a set of cortical regions taken from an atlas. For a composite SUVr, a similar methodology is used but one would select a set of regions from the atlas which cover most but not all of the cortex. For example, the occipital lobe (where there is stereotypically less signal) can be excluded (Jagust, Landau, et al. 2016).

Mean cortical SUVr and composite SUVr have been used as the primary outcome measures in large cross-sectional studies, longitudinal studies and even phase 3 trials of potential therapeutics (Clark, Schneider, and Bedell 2011; D. F. Wong et al. 2010; Jagust, Landau, et al. 2016; Sevigny et al. 2016).

6.1.1 Limitations of mean cortical SUVr

As I have shown in chapter 5, Aβ accumulation does occurs at different levels across the entire cortex. Indeed, as H. Braak and E. Braak 1991 noted, some small areas of the cortex remain free of Aβ deposits even at a late stage in the disease process. Further, I showed that even within ROIs, stereotypically there is heterogeneity in Aβ concentration. Therefore, using the whole cortex as a target region for an outcome measure is suboptimal. By including voxels with little accumulation, one is reducing the signal to noise ratio.

In addition to the poor signal to noise ratio, harmonisation of a global SUVr measure is challenging in large multi-centre studies as one has to ensure that every centre uses a target ROI defined in the same way. Interpreting differences in reported SUVr between studies is even more difficult because they may represent differences in concentrations in Aβ but could also be a result of defining the target region differently. It would be preferable to have a biomarker for the global level of Aβ which doesn't define a target region, as this would reduce the methodological bias incurred by having to define a target ROI.

Finally, when calculating mean cortical SUVr, there is no automatic output which checks whether the methodology was computed correctly or whether it is appropriate to use it as an outcome measure. For instance, if there are large lesions in the brain or the atlas was poorly applied to the image, the mean cortical SUVr

values could be low despite high concentrations of Aβ. This would not be automatically detected during the calculation of mean cortical SUVr and this could then bias any study level results.

6.2 Aims and outline

The aim of this chapter is to introduce a new outcome measure to quantify the global Aβ burden on the brain that is specific to regions where Aβ accumulates, doesn't require the definition of a target region and includes an automatic check of how well the computation was performed.

The remainder of the chapter is organised as follows; initially, in section 6.3, I define a new parameter $A\beta_L$ for the quantification of the global Aβ burden that is a natural consequence of the logistic growth model identified in chapter 5. An automated method for calculating $A\beta_L$ is presented in section 6.4. The method involves modelling SUVr images as a linear combination of the two previously derived template images and the quality of this modelling is evaluated in section 6.5. Finally, $A\beta_L$ is compared to the mean cortical SUVr as an outcome measure to quantify the global Aβ burden in cross-sectional data in section 6.6 and in longitudinal data in section 6.7.

6.3 Definition of Amyloid Load, $A\beta_L$

Results from chapter 5, showed that SUVr at time, t, $SUVr(t)$ is effectively modelled by

$$SUVr(t) = NS + \frac{K}{1 + e^{-r(t-T_{50})}} \tag{6.1}$$

where r and T_{50} are the global values of the exponential growth rate and time of half maximal concentration and NS and K are local values for the non-specific binding and Aβ carrying capacity

Since r and T_{50} are constant across the brain, $\frac{1}{1 + e^{-r(t-T_{50})}}$ is also constant across the brain for a given t and therefore at the population level the SUVr value

in a voxel i, $SUVr_i(t)$ can be written as,

$$SUVr_i(t) = NS_i + A\beta_L K_i \tag{6.2}$$

where NS_i is the non-specific binding in voxel i, K_i is the Aβ carrying capacity in voxel i and $A\beta_L = \frac{1}{1+e^{-r(t-T_{50})}}$ is a scalar ranging from 0 to 1 and is constant across the brain.

Therefore, images SUVr at all timepoints in the accumulation process can be written as,

$$\mathbf{SUVr}(t) = \mathbf{NS} + A\beta_L \mathbf{K} \tag{6.3}$$

where $\mathbf{SUVr}(t)$ is a typical SUVr image at time t, **NS** is the non-specific binding parametric image and **K** is the carrying capacity parametric image.

$A\beta_L$ is the scalar which multiplies the $A\beta$ specific carrying capacity image with 0 corresponding to zero $A\beta$ burden and 1 corresponding to the point of maximal Aβ concentration.

To account for global differences in the level of non-specific binding between subjects it was hypothesised that any [^{18}F]AV45 image that had been spatially normalised into MNI152 space could be approximated using a linear combination of the carrying capacity parametric image, **K** and the non-specific binding parametric image **NS**. Therefore any SUVr image can be approximated by $\mathbf{SUVr}_{fit}$, where,

$$\mathbf{SUVr}_{fit} = ns\mathbf{NS} + A\beta_L \mathbf{K} \tag{6.4}$$

where, ns is a scalar fitting the global level of non-specific binding, **NS** is the non-specific binding parametric image, $A\beta_L$ is the scaling factor of the carrying capacity image and **K** is the carrying capacity parametric image.

Since the carrying capacity image **K** relates to the maximal Aβ concentration, the scaling factor is defined as Amyloid Load ($A\beta_L$) which is a biomarker for global the Aβ concentration.

6.4 Automated method of calculating $A\beta_L$

As outlined in Chapter 3, initially SUVr images were created using grey matter cerebellum as a reference region. These images were spatially normalised to MNI152 space using DARTEL (Ashburner 2007).

After spatially normalising the [^{18}F]AV45 SUVr images, a fully automated algorithm was used to calculate $\mathbf{SUVr}_{fit}$ for each image by optimising the values for α and $A\beta_L$ so that the sum of squares of residuals between the voxel intensities of the spatially normalised [^{18}F]AV45 SUVr image and $\mathbf{SUVr}_{fit}$ was minimised. This was achieved by forming the overdetermined system of linear equations shown in Equation 6.5 and solving it in MATLAB using QR decomposition.

$$\begin{pmatrix} NS_1 & K_1 \\ \vdots & \vdots \\ NS_{end} & K_{end} \end{pmatrix} \begin{pmatrix} ns \\ A\beta_L \end{pmatrix} = \begin{pmatrix} SUVr_1 \\ \vdots \\ SUVr_{end} \end{pmatrix} \tag{6.5}$$

where NS_i, K_i and are the i $^{\text{th}}$ voxel intensities in the **NS** image, **K** image and [^{18}F]AV45 SUVr image in MNI space respectively.

Following the optimisation step, the algorithm produces four outputs as summarised in Figure 6.1. The values of ns and $A\beta_L$ are recorded, the $\mathbf{SUVr}_{fit}$ image is written to file and a difference image is also produced by calculating $\mathbf{SUVr} - \mathbf{SUVr}_{fit}$.

$A\beta_L$ was calculated using this algorithm for all subjects in the ADNI cross-sectional data, the ADNI longitudinal data and Dallas Lifespan study databases (for more information see chapter 3).

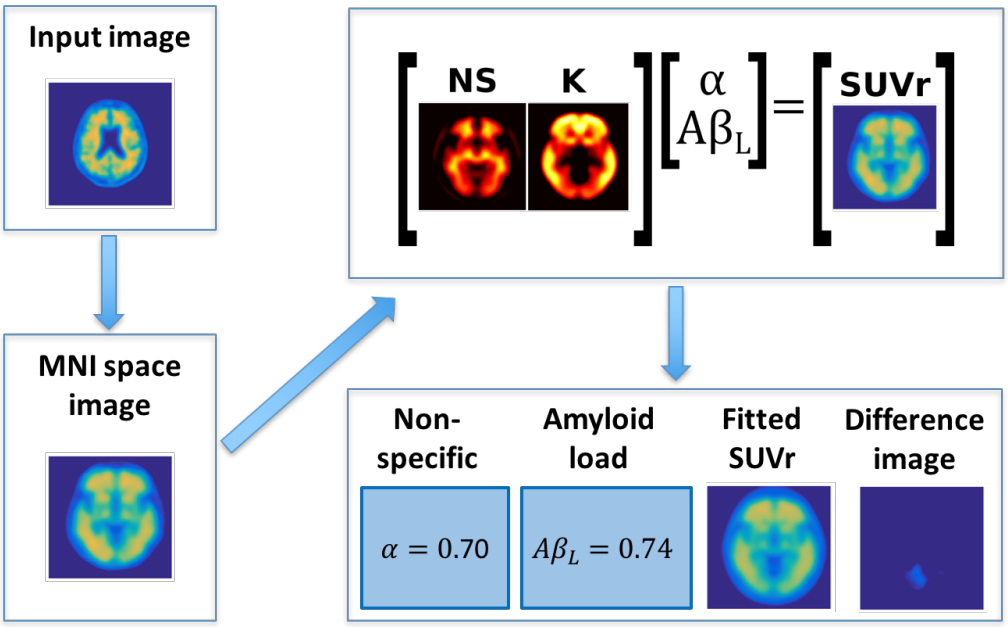


FIGURE 6.1: Workflow of how $A\beta_L$ is calculated: the input image is initially spatially normalised to MNI152 space and then a linear regression is performed using the two parametric maps. There are four outputs; α, $A\beta_L$, the fitted SUVr image $\mathbf{SUVr}_{fit}$ and a difference image equal to $\mathbf{SUVr} - \mathbf{SUVr}_{fit}$

6.5 Evaluating $\mathbf{SUVr}_{fit}$ images

The quality of the fit of $\mathbf{SUVr}_{fit}$ was analysed by evaluating the percentage of voxels in the brain which satisfied $|\mathbf{SUVr} - \mathbf{SUVr}_{fit}| > 0.3$. Clearly, the larger this percentage, the poorer the fit.

6.5.1 ADNI cross-sectional data

The mean percentage of voxels in the brain with $|\mathbf{SUVr} - \mathbf{SUVr}_{fit}| > 0.3$ for the 769 subjects from the ADNI data was 4.6%. 96% of the 769 subjects had fewer than 20% of voxels which satisfied $|\mathbf{SUVr} - \mathbf{SUVr}_{fit}| > 0.3$ meaning that over 80% of voxels in 96% of subjects were well modelled. The highest percentage in all the subjects was 38.0%. There was no correlation between the calculated $A\beta_L$ and the percentage of voxels which satisfied $|\mathbf{SUVr} - \mathbf{SUVr}_{fit}| > 0.3$.

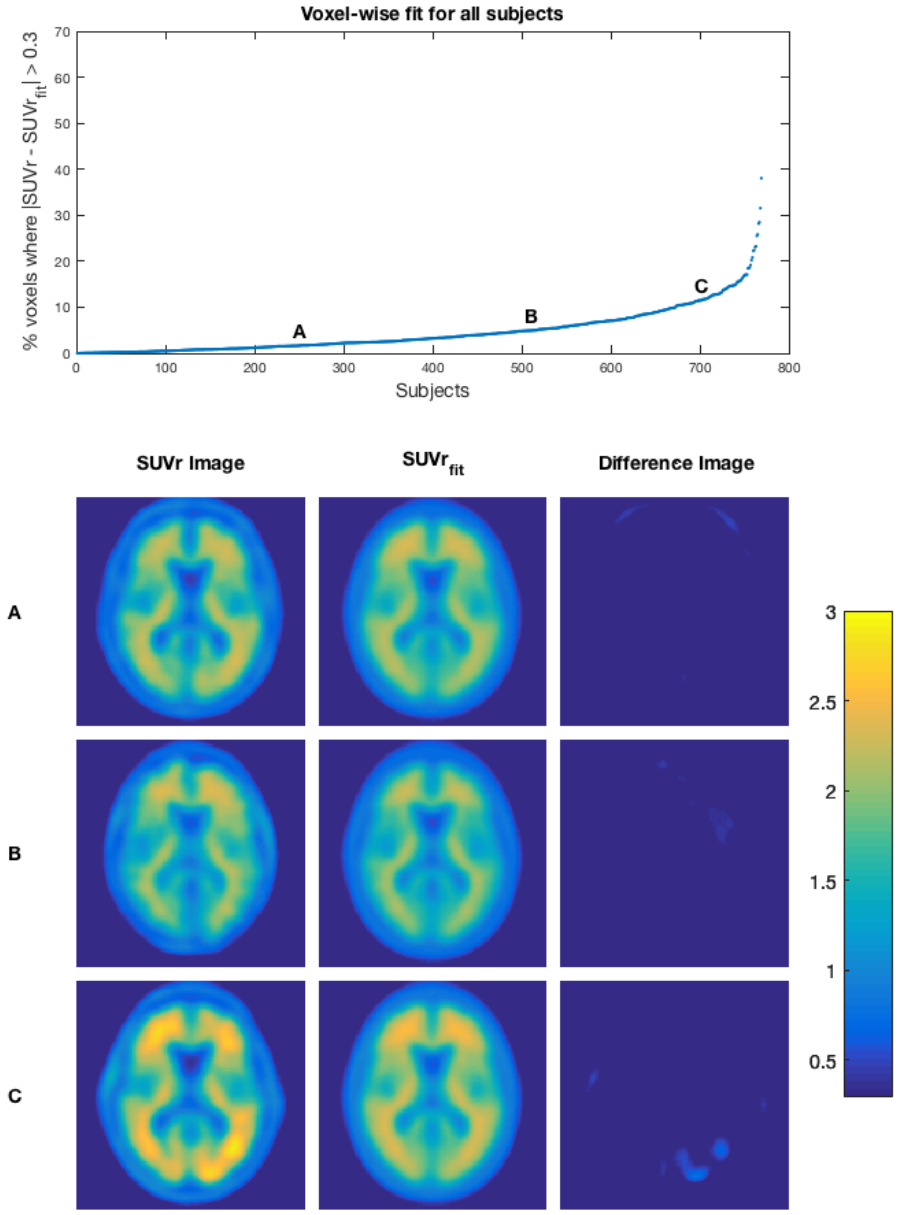


FIGURE 6.2: A figure showing the quality of the fit of $\mathbf{SUVr}_{fit}$ images. The top plot shows percentage of voxels in the brain which satisfied $|\mathbf{SUVr} - \mathbf{SUVr}_{fit}| > 0.3$ for each of the 769 subjects. The subjects are ordered by this percentage. 3 subjects (A, B, C) are labelled on the graph and below the corresponding **SUVr**, $\mathbf{SUVr}_{fit}$ and difference images are displayed. Overall, the linear combination of parametric images can effectively model the scans from the ADNI cross-sectional imaging data.

6.5.2 Dallas lifespan study

141 of the 146 subjects (96.5%) in the Dallas Lifespan study had fewer than 10% of voxels which satisfied $|\mathbf{SUVr} - \mathbf{SUVr}_{fit}| > 0.3$. The highest percentage in all the subjects was 36.0% and like the ADNI cross-sectional data, there was no correlation between the calculated $A\beta_L$ and the quality of the fit.

The quality of the fitting is similar in the Dallas lifespan study data to the cross-sectional ADNI data. The template images **K** and **NS** were created using the ADNI cross-sectional data and this result shows that the same template images can be used in other studies rather than having to calculate study specific templates for **K** and **NS**. This is vital in order for $A\beta_L$ to be applied more generally as an outcome measure to quantify the global Aβ burden.

6.5.3 Using the difference image to QC the quality of $\mathbf{SUVr}_{fit}$ in future studies

The difference image produced by the algorithm allows one to analyse how well the SUVr image data were modelled. This feature could provide useful information as to whether a particular scan has an abnormal $A\beta_L$ due to poor fitting rather than abnormal concentrations of Aβ. This information is lacking when using mean cortical SUVr.

As an example, consider a simulated example in Figure 6.4 where I have artificially set all the voxels in two ROIs in the frontal cortex to zero (similar to what we might expect from a lesioned region of the brain). The difference image calculated clearly picks out the 'lesioned' voxels as being poorly fitted. In a real setting, this would allow one to act accordingly. For instance, it would be possible to only calculate $A\beta_L$ on well fitted voxels or remove the subject from any subsequent analysis if the poor fitting voxels were more widespread. The percentage of voxels in which $|\mathbf{SUVr} - \mathbf{SUVr}_{fit}| > 0.3$ for this simulated case was 23.3% and the $A\beta_L$ dropped from 54% from the original image to 33% once the simulated lesions were applied. This decrease in $A\beta_L$ would bias any study

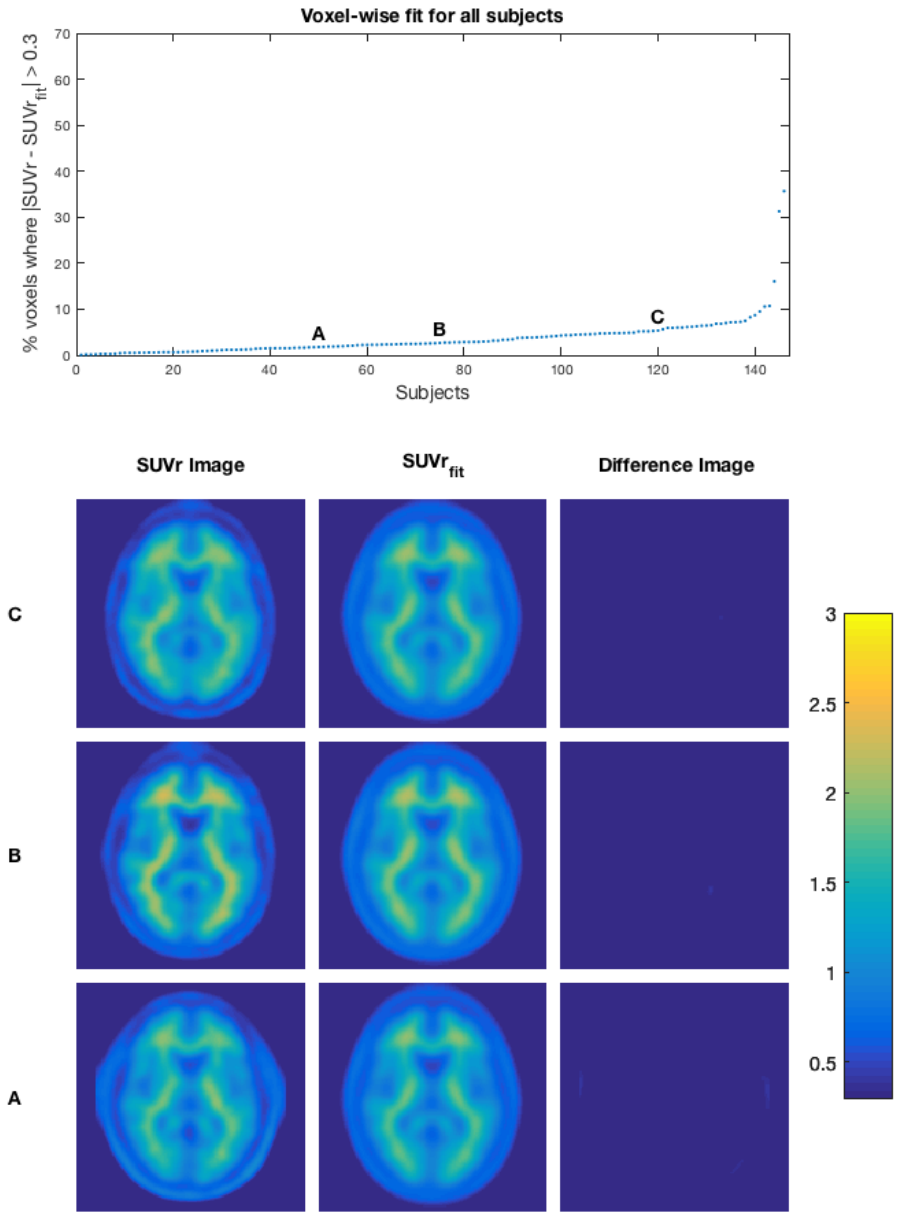


FIGURE 6.3: An equivalent figure to Figure 6.2 but using the cross-sectional Dallas Lifespan Brain study. As with the ADNI cross-sectional data, linear combinations of the parametric template images can effectively model the data

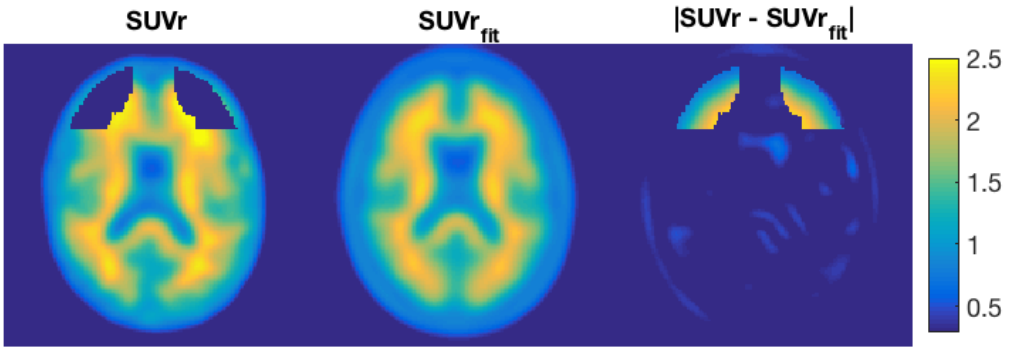


FIGURE 6.4: Using the difference image to check $A\beta_L$ calculation. **Left**: Two frontal ROIs have had the intensities set to zero to simulate a heavily lesioned brain. **Middle**: The fitted image calculated with this adaptation of the original image. **Right**: The difference image between $\mathbf{SUVr}_{fit}$ and the 'lesioned' brain. One can clearly identify the bright intensities in the simulated lesions showing the poor fitting here.

level analysis performed and therefore it is necessary to implement a QC step which rejects images like this where the fit is poor.

A possible QC algorithm for checking the quality of the fit of $\mathbf{SUVr}_{fit}$ in studies with a large number of scans could look at the percentage of voxels in which $|\mathbf{SUVr} - \mathbf{SUVr}_{fit}| > 0.3$ initially. Then visually QC the difference images for all subjects where the percentage of poorly fitted voxels exceeds 10%. If this algorithm was followed for the ADNI cross-sectional data, 97 scans would have to be visually QC'd instead of 769. This approach requires further validation before it can be used with confidence as the example shown here is a simulation case and it is difficult to tell the ability to detect abnormalities in more subtle real-life cases from this example.

6.6 $A\beta_L$ as an outcome measure in the cross-sectional ADNI data

The distributions of $A\beta_L$ within the four different classifications (HC, EMCI, LMCI, AD) in ADNI were calculated and compared to analogous distributions for the mean cortical SUVr. Boxplots for each of the distributions are presented

in Figure 6.5 and the effect sizes between the different groups for mean cortical SUVr and $A\beta_L$ are shown in Table 6.1 and Table 6.2 respectively. Here, the Hedges' g effect size presented. The equation for the Hedges' g effect size between two distributions X_1 and X_2 is,

$$\text{Hedges' g} = \frac{|\mu_2 - \mu_1|}{s^*} \tag{6.6}$$

where, μ_2 is the mean of X_2, μ_1 is the mean of X_1 and s^* is the pooled standard deviation. The pooled standard deviation of two distributions X_1 and X_2, s^* is defined to be,

$$s^* = \sqrt{\frac{(n_1 - 1)s_1^2 + n_2 - 1)s_2^2}{n_1 + n_2 + 2}} \tag{6.7}$$

where, n_1 is the sample size of X_1, n_2 is the sample size of X_2, s_1 is the standard deviation of X_1 and s_2 is the stardard deviation of X_2.

Both mean cortical SUVr and $A\beta_L$ increase from healthy controls to EMCI, LMCI and finally AD in the ADNI population but $A\beta_L$ has greater sensitivity between all classification groups. The mean increase in effect size when comparing $A\beta_L$ with mean cortical SUVr was 56% and the greatest increase was observed between LMCI and EMCI.

	EMCI	LMCI	AD
Effect size vs HC	0.21	0.43	0.97
Effect size vs EMCI		0.23	0.77
Effect size vs LMCI			0.5

TABLE 6.1: Effect sizes for SUVr.

	EMCI	LMCI	AD
Effect size vs HC	0.24	0.71	1.5
Effect size vs EMCI		0.49	1.2
Effect size vs LMCI			0.64

TABLE 6.2: Effect sizes for $A\beta_L$.

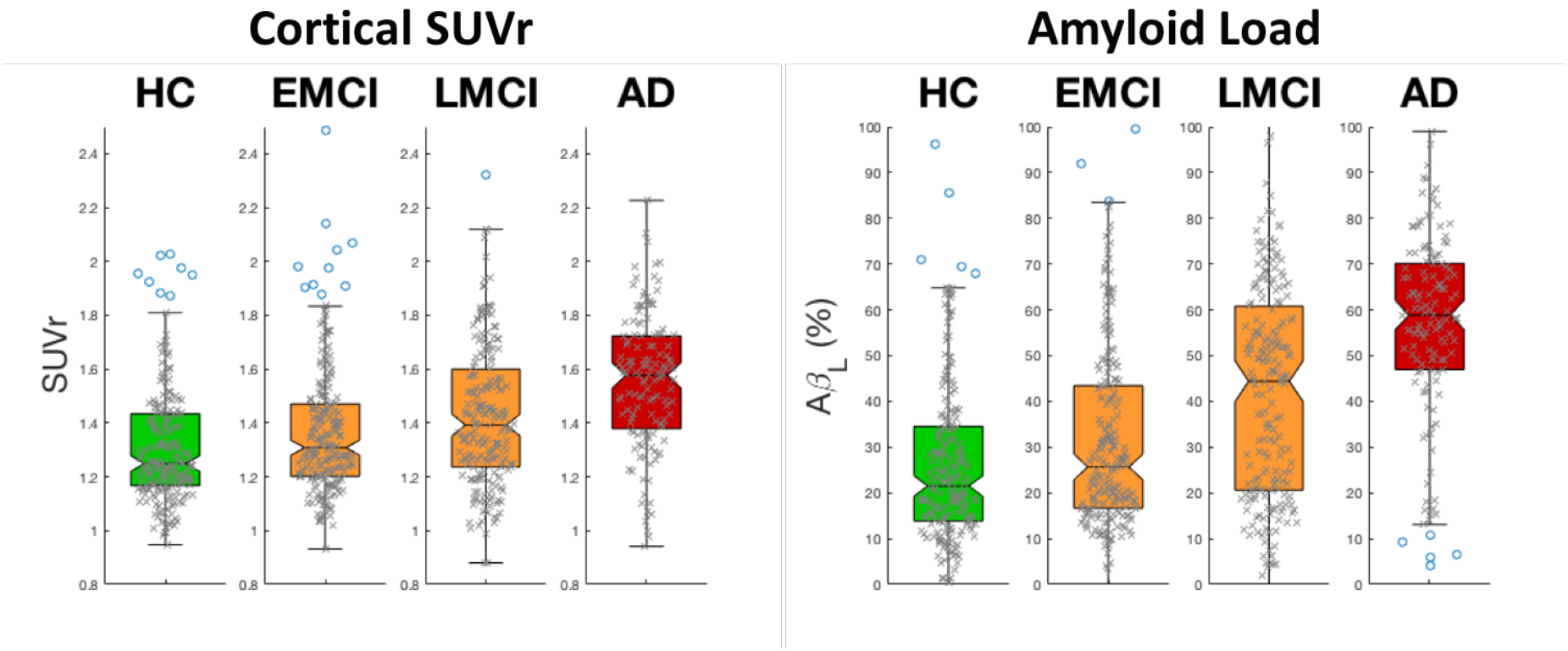


FIGURE 6.5: Boxplots of the distributions of mean cortical SUVr and $A\beta_L$ within four groups - HC: Healthy controls, EMCI: Early mild cognitive impairment, LMCI: Late mild cognitive impairment and AD: Alzheimer's disease. With increased progression through the disease process, there is an increase in both mean cortical SUVr and $A\beta_L$ but the effect sizes between the groups are all greater for $A\beta_L$ (see Tables 6.1 and 6.2).

6.6.1 ns in the cross-sectional ADNI data

The global scaling factor for the non-specific binding ns decreases as subjects progress from HC to AD. Figure 6.6 shows the distributions of ns for all classifcations. The mean ns in healthy controls was 1.06 and this reduced to 0.89 in Alzheimer's disease subjects.

There are two possible explanations for this reduction. Firstly, it could be an increase in the level of non-specific binding in the reference region (grey matter Cerebellum) in AD subjects when compared to controls. If this was the case however, one would expect to see a similar effect on $A\beta_L$ which is not the case. In fact, $A\beta_L$ increases which would imply that either there is no change in the level of non-specific binding in the reference region between healthy controls and AD patients or that the change is very small in comparison to the change in Aβ concentration in the brain. Secondly, and perhaps more plausibly, the reduction could represent an actual decrease in the level of non-specific binding in AD subjects which could be due to a reduction in tissue density.

6.7 $A\beta_L$ as an outcome measure in ADNI longitudinal data

$A\beta_L$ and mean cortical SUVr were calculated for each of the 147 subjects included in the longitudinal arm of ADNI. The distributions of $A\beta_L$ and mean cortical SUVr can be seen in Figure 6.7. The increase in follow-up mean cortical SUVr was 0.026 compared to baseline with a standard deviation of 0.11 which translates to an effect size of 0.35. The increase in follow-up $A\beta_L$ compared to baseline was 2.0% and the standard deviation was 5.8% which translates to an effect size of 0.49 for $A\beta_L$.

The increase in sensitivity in longitudinal data could prove important in future longitudinal studies as one would be able to detect a significant change with interventional studies with fewer subjects. For instance, in order to statistically detect a 5% change in mean cortical SUVr with an intervention with a power of 80% one would require 359 subjects (where this is calculated using the mean

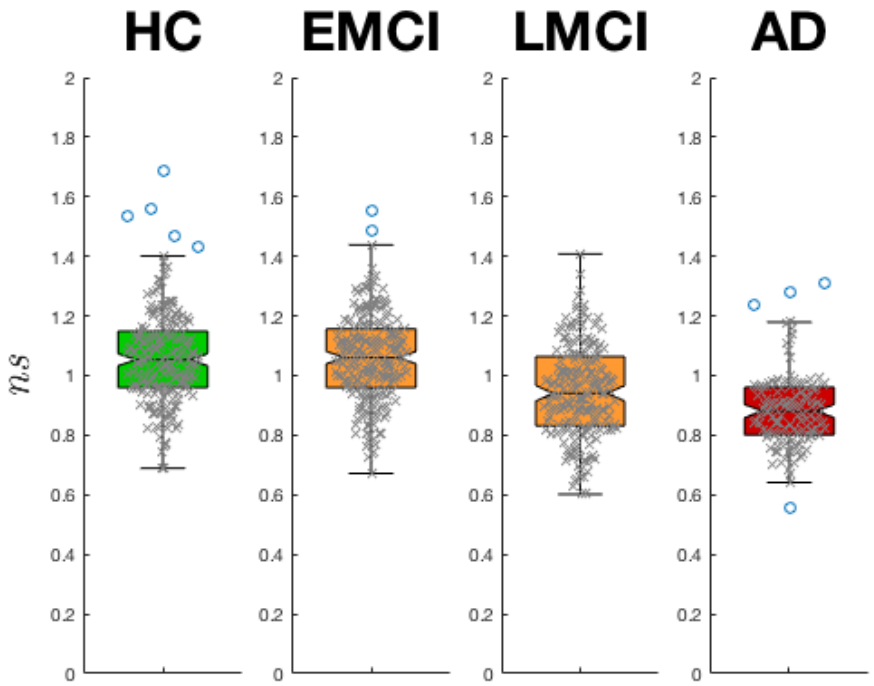


FIGURE 6.6: Boxplots of the distributions of the calculated α for the 4 different groups with decreasing level of cognition. With increased progression through the disease process, there is a decrease in ns.

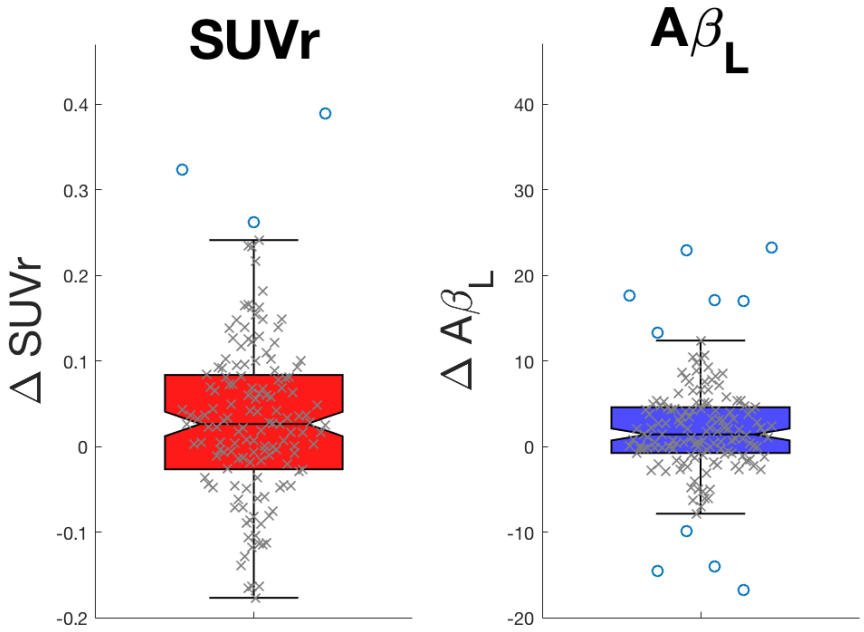


FIGURE 6.7: Boxplots for the distributions of changes in $A\beta_L$ and mean cortical SUVr between baseline and follow-up scans in the longitudinal ADNI data

and standard deviation of mean cortical SUVr in this study) whereas $A\beta_L$ using would only require 81 subjects. This could have a dramatic effect on the financial cost and the number of patients required in interventional studies and clinical trials, such as that conducted by Sevigny et al. 2016 who showed aducanumab reduces the mean composite SUVr in AD over a period of 12 months.

6.8 Discussion

In this chapter, I have introduced the novel sensitive biomarker for quantifying the Aβ burden in the human brain using data from a static PET [^{18}F]AV45 scan. $A\beta_L$ is calculated from insights derived from the logistic growth model identified in chapter 5 by initially modelling an SUVr image as a linear combination of two template images - **K** and **NS**. $A\beta_L$ is determined as the scaling factor of the carrying capacity template image **K**. An automated method of calculating $A\beta_L$ which is fast and robust to execute was also presented. The algorithm produces four outputs, $A\beta_L$, the global level of non-specific binding ns, a fitted SUVr image and a difference image showing the difference between the fitted SUVr image and the actual SUVr image.

In this work, I calculated $A\beta_L$ and mean cortical SUVr for 769 scans of subjects ranging across the full spectrum of disease. The effect sizes between the different disease classifications in the cross-sectional ADNI dataset introduced in chapter 3 were calculated for both outcome measures and larger effect sizes were observed for $A\beta_L$ in every comparison. The mean increase in effect size between the different classifications in the cross-sectional ADNI was 56%. This increase in sensitivity could prove important in future studies as one would require fewer subjects to detect a significant difference between disease groups and healthy controls. The increased power was also observed using the longitudinal data and this would translate into more powerful or smaller sized interventional studies aimed at testing novel therapeutics. To illustrate this point, consider Figure 6.8; it shows the power of mean cortical SUVr and $A\beta_L$ to detect changes in a simulated trial of a potential anti-Aβ therapeutic where the power

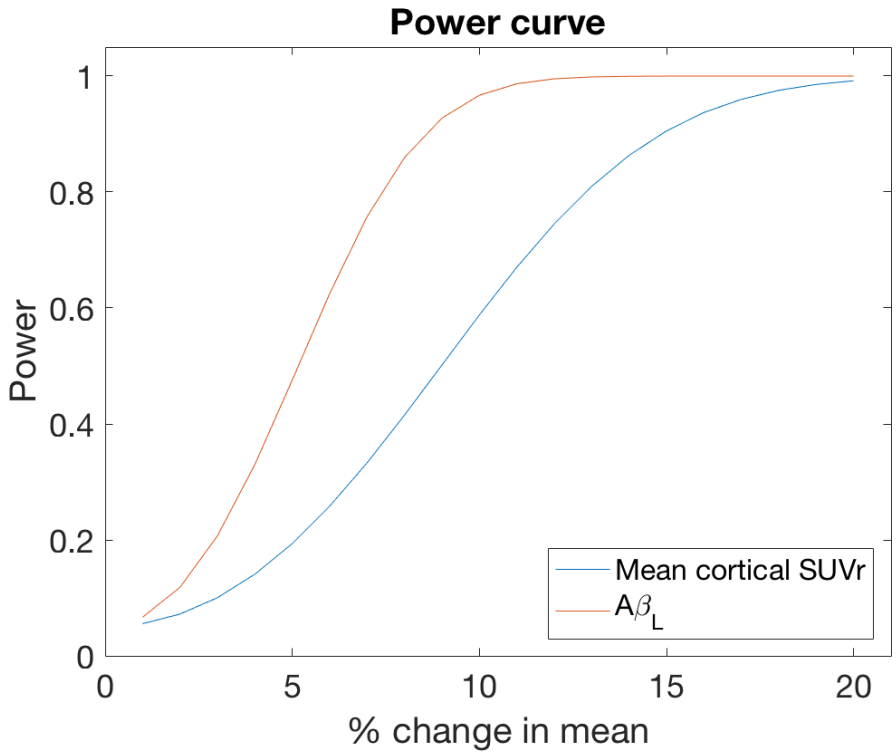


FIGURE 6.8: Power curves for the ability of mean cortical SUVr and $A\beta_L$ to detect changes in global Aβ burden

of each is calculated using the mean and standard deviations found in the longitudinal ADNI data. The power to detect small changes of less than 15% in the global $A\beta$ burden is greatly increased when using $A\beta_L$

The difference image produced by the algorithm allows one to analyse how well the SUVr image data was modelled. This feature can provide useful information as to whether a particular scan has an abnormal $A\beta_L$ due to poor fitting (resulting from poor registration to MNI space or lesions) for instance rather than abnormal concentrations of Aβ. This information is lacking when using mean cortical SUVr. In this work, a voxel was considered to be poorly estimated if the absolute difference in intensity was greater than 0.3. 96% of the SUVr fitted images had fewer than 20% of voxels which were poorly fitted suggesting the SUVr fitted images accurately model the majority of SUVr images. This work however, requires further validation in order to have confidence that all poor registrations are being detected as the work done to date merely provides motivation and a possible methodology. In reality, this will have to be developed further before it can be used.

There are some limitations that should be considered when using this technique in future studies. In particular, for interventional studies, one should consider that if the intervention affects the $A\beta$ concentration in a spatially dependent manner (i.e., does not reduce $A\beta$ uniformly across the brain) then scans may not be modelled effectively using a linear combination of **NS** and **K** after treatment. The quality of fitting pre and post-treatment should be investigated in future work. Caution should be exercised when using disease groups other than AD as the outcome measure was developed using templates derived from modelling the disease progression of AD.

6.9 Conclusion

In this chapter, I have introduced a novel biomarker, $A\beta_L$, for quantifying the global Aβ burden in the brain using an [^{18}F]AV45 scan. Previous approaches have used either mean cortical SUVr or a composite SUVr of large cortical regions.

The novel method introduced to calculate $A\beta_L$ showed that SUVr images can be effectively modelled using a linear combination of the two template images (**NS** and **K**) both in the ADNI dataset where they were generated and an independent dataset.

Finally, I showed that by using $A\beta_L$ it is possible to obtain greater effect sizes both between different clinical groups in cross-sectional data and between baseline and follow-up in longitudinal data. This result has important implications for the number of subjects needed to have sufficient power to detect significant differences in clinical trials.

Chapter 7

Kinetic analysis of [^{18}F]AV1451 Tau PET

In chapter 2, I provided background about the microtubule associated protein tau and its involvement in neurodegenerative diseases including CBD. I also discussed imaging pathological tau using PET. In this chapter, I develop a pipeline to quantitatively analyse imaging data from the novel tau radiotracer [^{18}F]AV1451 in a study of patients with CBD.

7.1 Aims and outline

In chapter 2, when reviewing the previously published literature using [^{18}F]AV1451 I noted that studies optimising the quantification pipeline had been restricted to AD and TBI subjects. This chapter is dedicated to optimising the analysis pipeline for [^{18}F]AV1451 in CBD. Chapter 3 described how dynamic [^{18}F]AV1451 PET images were corrected for motion, an atlas was non-linearly warped from MNI space to subject-space and regional time activity curves were generated.

In this chapter, initially in section 7.2, I obtain a model to accurately quantify the metabolite fraction in the plasma and combined with modelling of the plasma over blood ratio generate an arterial plasma parent input function. This input function is used in conjunction with imaging data to ascertain the optimum compartmental model for [^{18}F]AV1451 in CBD. The optimum model is subsequently used as a gold standard to assess the validity of SRTM in section 7.3

and SUVr in section 7.4. Time stability analysis of SUVr is also performed in section 7.4 to ascertain the optimum scanning window for future [^{18}F]AV1451 studies in CBD.

7.2 Optimum modelling pipeline for quantitative [^{18}F]AV1451 analysis

There are two main stages to optimising the kinetic modelling approach for a radiotracer once one has established the method to generate TACs for a set of chosen ROIs (covered in Chapter 3). The first of these is the determination of an arterial input function from the blood data obtained from a dynamic PET scan and the second is selecting an appropriate kinetic model.

7.2.1 Determination of arterial plasma parent input function

This section will first describe the method to produce an arterial input function. Firstly, the reader is introduced to the blood data obtained and then this information is used to generate an input function. The arterial input function is the modelled concentration of radiotracer in the plasma and it is assumed in all subsequent analysis that only radiotracer in this form can cross the blood-brain barrier.

Blood data from a dynamic PET scan

In all ten scans (5 healthy controls and 5 CBD patients; for more demographics see Chapter 3), arterial blood data was sampled from each patient over the course of the scan. For the first 900 seconds the concentration of radioactivity (kBq/ml) in the blood was recorded every second.

In addition to this, discrete blood samples were taken every 300 seconds between 0 and 1800 seconds and every 600 seconds between 1800 and 7200 seconds. The plasma over blood ratio was calculated for each of these discrete samples.

Finally, the plasma was further analysed at a set of discrete timepoints using high-performance liquid chromatography (HPLC) techniques for each scan to analyse the percentage of the compound which had not been metabolised (it is assumed that only the parent compound can cross the blood brain barrier).

Modelling blood data to create an arterial input function

In the first step, a model is fitted to the plasma over blood ratio data. For this tracer I observed that the ratio stabilises rapidly as has previously been reported (Wooten et al. 2017) and therefore a constant k was fitted to the data. That is,

$$POB(t) = k \tag{7.1}$$

where, $POB(t)$ is the plasma over blood ratio at a time t. This constant ratio was used to find the radioactivity in the plasma over the course of the scan (here it is assumed that the concentration of radiotracer is the same in plasma and blood) by multiplying the blood data points by the constant ratio k.

$$P(t) = kB(t) \tag{7.2}$$

where, $P(t)$ is the concentration of radioactivity in the plasma and $B(t)$ is the concentration of radioactivity in the blood.

A range of different empirical models (all models tested are shown Appendix A) for the fraction of parent compound in plasma $PPF(t)$ were fitted to the metabolite data for all the subjects and the BIC was used to calculate the most parsimonious option. The lowest BIC value for seven of the ten subjects occurred when using a sigmoid function which has three parameters (α, β and γ) written in Equation 7.3

$$y = \frac{\left(1 - \frac{x^3}{x^3+10^\alpha}\right)^\beta + \beta}{1+\gamma} \tag{7.3}$$

This sigmoid function was used as the model for all the subjects and Figure 7.1 shows the fit of the sigmoid function to the metabolite data. One can see that in all cases (including the three subjects where it was not found to be the most parsimonious option), it accurately describes the data however, there is an overestimation (less than 5%) of the true parent fraction at the earliest time-point for 5 subjects. A consistent overestimation across time would lead to an overestimation of the AIF(t) and therefore an underestimation of V_T. The V_T is ultimately dependent on the area under the fitted metabolite curve however, and small overestimations of one point will have a small effect on the this area. Therefore, this level of error will not majorly effect the calculated V_T.

Figure 7.2 shows the mean parent fraction data across all subjects. The mean parent fraction remains above 10% across the length of the scan. The highest variability in the parent fraction across the subjects occurs before 3000 s with the mean value dropping from approximately 85% at 300 seconds to 20% by 3600 s. This shape of the mean parent fraction curve is consistent to those found by Wooten et al. 2017 and Golla et al. 2017 in that it exhbits a sigmoid curve and a flattening of the curve one hour post injection. Wooten et al. 2017 only collected data for 90 min post injection of the tracer and at this point the parent fraction was approximately 25% whereas in this study it was less than 20%. Similar to Golla et al. 2017, at later timepoints the rate of change of parent fraction decreases but the value is still decreasing.

In the final step of creating the arterial input function, the values for the concentration of radioactivity in the plasma are multiplied by the parent fraction modelled to be in the plasma, $PPF(t)$. Therefore,

$$AIF(t) = PPF(t) \cdot P(t) \tag{7.4}$$

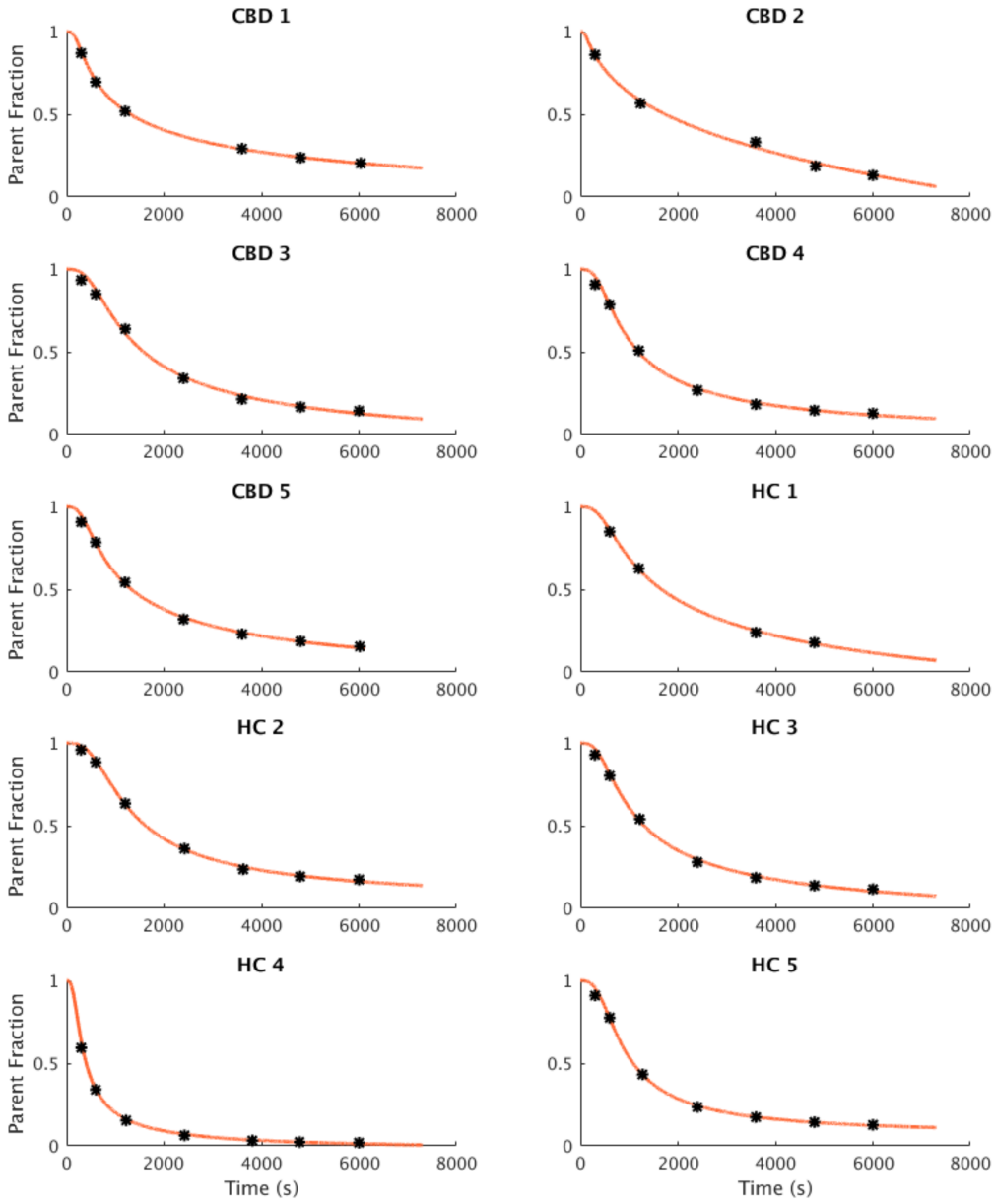


FIGURE 7.1: Fit of the sigmoid function to the parent fraction data for all 10 subjects

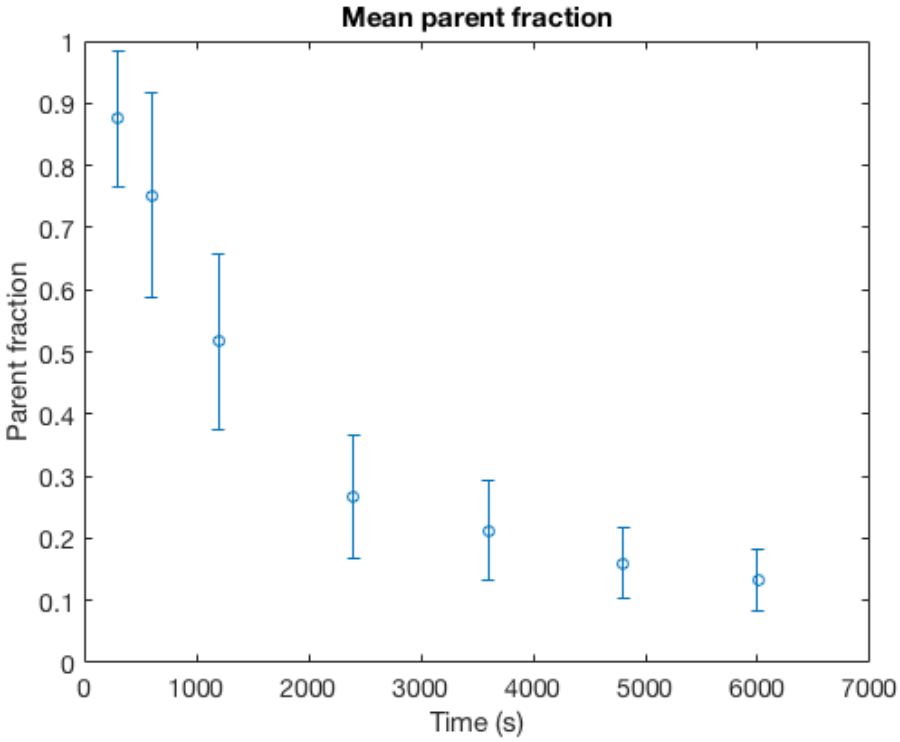


FIGURE 7.2: Mean parent fraction curve across the whole study (error bars show the standard deviation).

where, $AIF(t)$ is the arterial input function and $\cdot$ is the element wise multiplication of the data for a defined set of values for t.

7.2.2 Generation of TACs

Initially, the structural T1-weighted MRI images were segmented using a unified segmentation algorithm (Ashburner and K. J. Friston 2005). The resulting grey matter and white matter probability maps were used to create DARTEL flowfields which define a spatial mapping from each subjects' structural MR image space to the standard MNI152 space. The inverse of these flowfields was calculated and was applied to the CIC atlas (Tziortzi et al. 2011) which produced an atlas image in each individuals' MR structural T1 space which was visually QC'd.

Six ROIs were chosen from the CIC atlas; Parahippocampus, Insular, Hippocampus, Posterior Cingulate Gyrus, Precuneous cortex and Orbitofrontal. These were chosen because they are cortical regions of the brain that have been shown

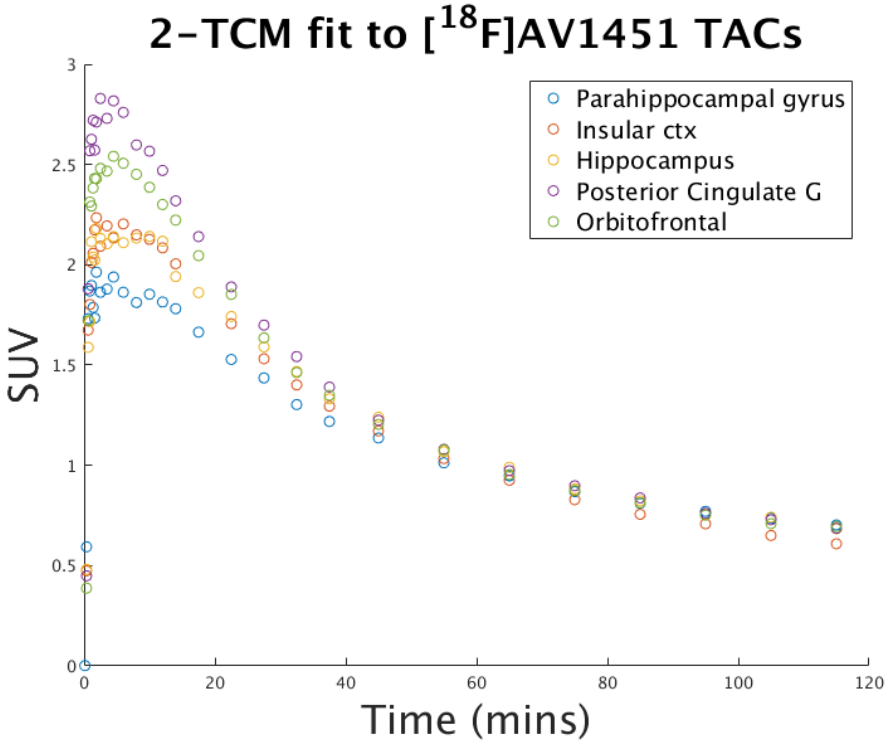


FIGURE 7.3: Regional TACs for the 120 min scan for an example subject for the Precuneous cortex and the Cerebellum. Qualitatively, these regions exhibit different kinetics.

to have tau pathology in CBD *in vitro* (Forman et al. 2002). I am restricting the analysis to cortical regions because quantification of [^{18}F]AV1451 in subcortical regions is unreliable due to tracer off-target specific binding to neuromelanin and MAO-A. In addition to the six target regions, the Cerebellum TACs were also generated to use as a potential reference region.

The regional TACs were generated by applying the atlas to the dynamic motion corrected PET images in T1 space. The mean intensity weighted by the grey matter probability of the voxels in each frame was plotted against the mid-frame time for each frame to generate the final TACs. Example TACs can be seen in Figures 7.3 and 7.4. The TACs are similar to the control subject TACs presented by Wooten et al. 2017. Their peak values are between 2 and 3 SUV units before 20 minutes post injection and reduce to under 1 in the time of the scan. The MCI subjects in the data presented by Wooten et al. 2017 exhibited much greater signal at later timepoints and greater differentiation between regional TACS.

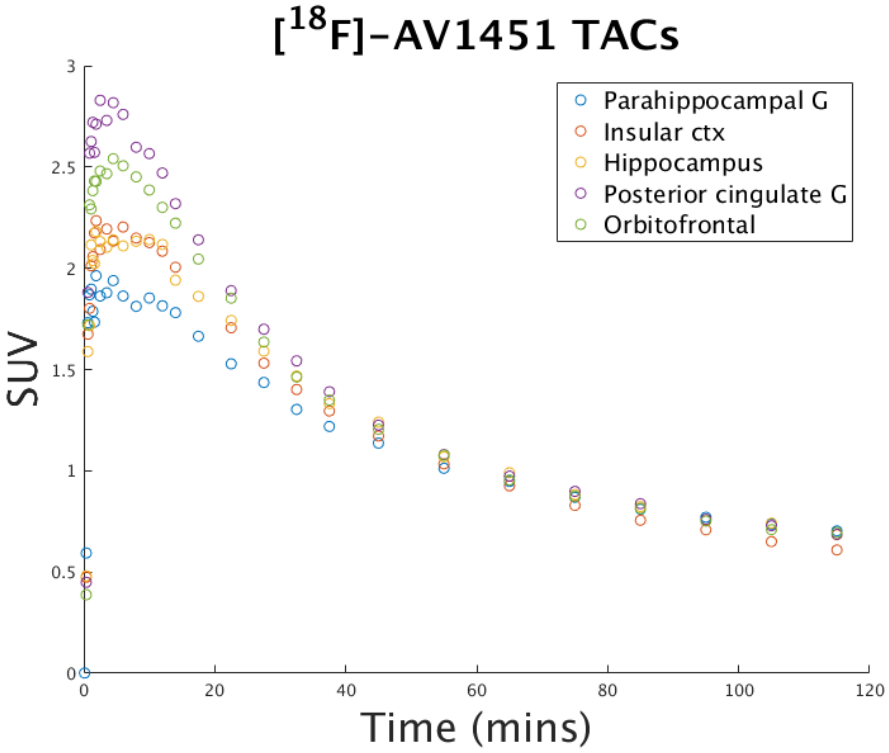


FIGURE 7.4: Regional TACs for the 120 min scan for an example subject for 5 ROIs.

7.2.3 Optimum kinetic model

Having determined an appropriate arterial input function for each of the ten subjects, a set of compartmental models used this as the input to describe the regional TACs generated from the imaging data (see Chapter 3 for further details on how these were generated). Four different compartmental models were tested; the reversible one-tissue compartment model, the irreversible one-tissue compartment model, the reversible two-tissue compartment model and the irreversible two-tissue compartment model.

As with the metabolite data, the best model of the four was determined using the BIC.

In all seven grey matter masked ROIs (Parahippocampal gyrus, Insular cortex, Hippocampus, Posterior cingulate gyrus, Precuneous cortex, Orbitofrontal cortex and Cerebellum) the reversible two-tissue compartment model was found to be the most parsimonious model for describing the TACs which is consistent with previous studies using this tracer (Wooten et al. 2017; Golla et al. 2017. The

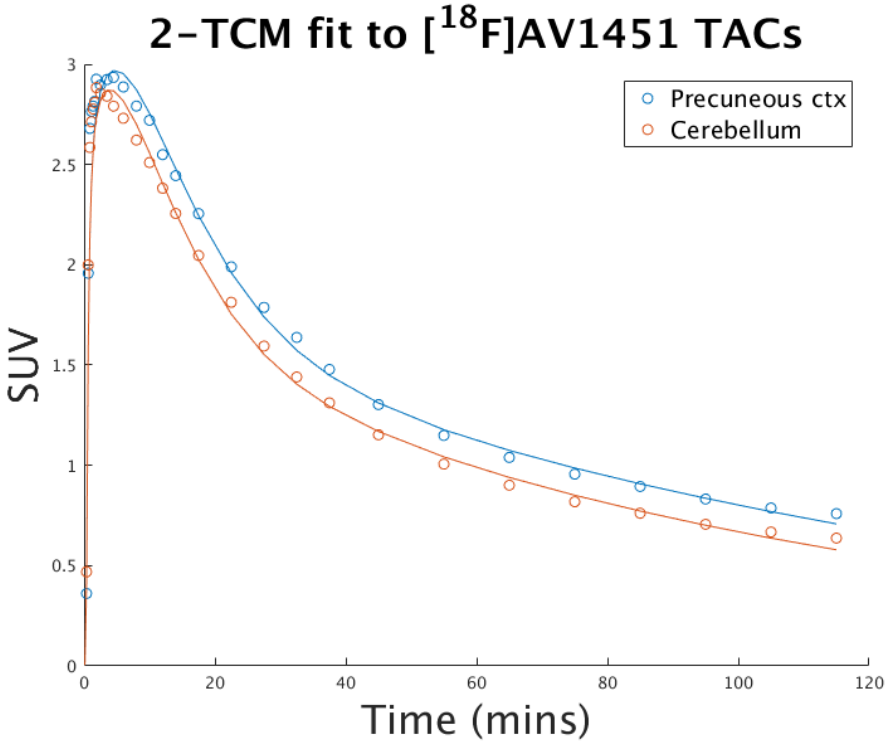


FIGURE 7.5: Fits of the two-tissue compartment model (2-TCM) to time activity curves for a target region (Precuneous cortex) and the potential reference region (grey matter Cerebellum)

blood volume was fixed to be 5%. (Models with a fitted blood volume and zero blood volume were also investigated but resulted in poor fits or biologically implausible blood volume estimates).

Fits of the reversible two-tissue compartment model for an example subject can be seen in Figures 7.5 and 7.6. The fit of the model is good in all regions however there is an underestimation of the TACs between approximately 20 and 40 min post-injection followed by and overestimation between 50 and 90 min and finally an underestimation between 100 and 110 min. The maximum absolute value of any residual across all target regions is less than 0.05 SUV units.

7.2.4 Grey matter cerebellum as a reference region

In AD, the grey matter Cerebellum has been used as a reference region and showed good correspondence with results from full kinetic modelling (Wooten et al. 2017; Golla et al. 2017). It was hypothesised it could also be a good reference region for CBD because it does not intersect with the basal ganglia which

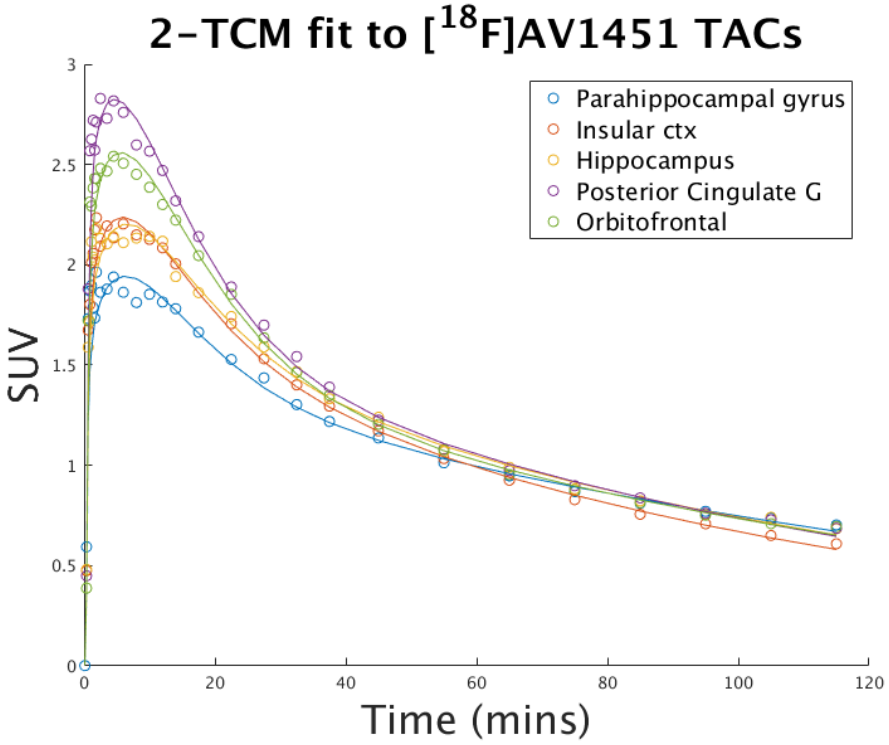


FIGURE 7.6: Fits of the two-tissue compartment model (2-TCM) to TACs from 5 cortical ROIs

seems to show the highest off-target binding signal (K. A. Johnson, Schultz, et al. 2016; Marquié, Normandin, Vanderburg, et al. 2015) and post-mortem studies of CBD patients show low levels of tau in the grey matter Cerebellum (Forman et al. 2002).

The grey matter Cerebellum time activity curves are plotted for all the patients and controls in Figure 7.7. As Wooten et al. 2017 found, all subjects appear to exhibit fast wash-in of radioactivity with high initial SUV peak of 1.75-3 and rapid clearance which occured in the first 10 min of the scan. The CBD subjects have TACs similar to controls but there is a small difference in the late time points with CBD subjects having greater signal than healthy controls. This could be due to differences in specific or non-specific binding of the tracer in the Cerebellum.

Combining our results with previous post-mortem studies and the characteristics of the tracer that have been identified in other disease groups suggests that the grey matter Cerebellum can serve as a reference region for [^{18}F]AV1451 in CBD although one should be aware that there are subtle differences in the

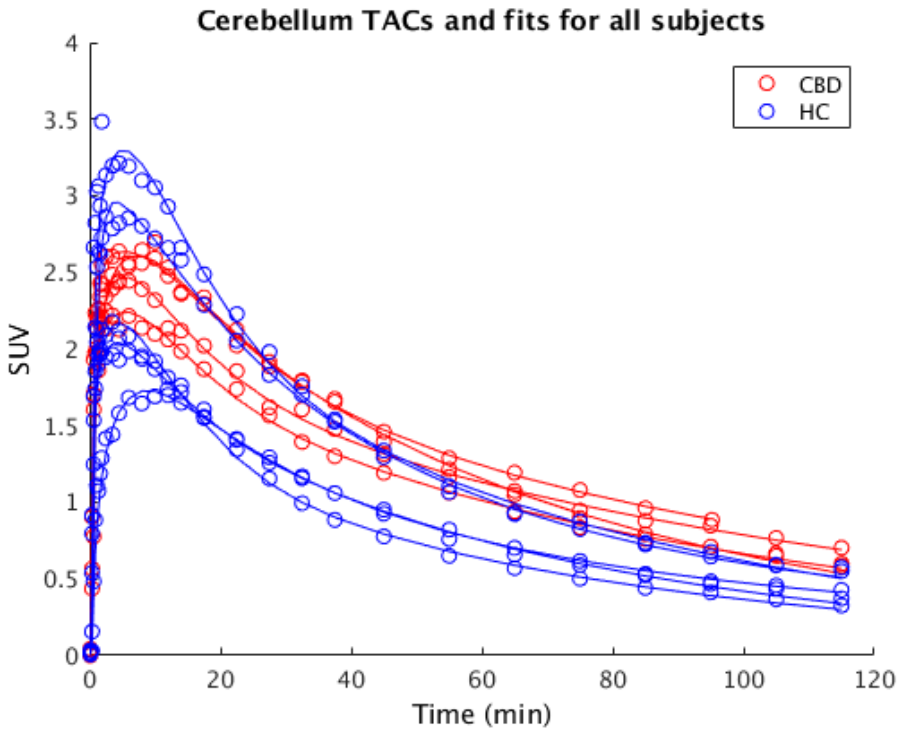


FIGURE 7.7: Plots showing the TACs and 2-tissue compartment model fits for the grey matter Cerebellum region for all subjects.

kinetics in the Cerebellum which could affect the calculation of BP_{ND}.

7.2.5 V_T and BP_{ND} in CBD and healthy controls

Volumes of distribution, V_T, were calculated using the optimum kinetic model (reversible 2-tissue compartmental model with a fixed blood volume of 5%) in both healthy controls and patients. The results are shown in Figure 7.8. There was no statistically significant differences between V_T in patients and controls when they are compared at the group level when using a two-sample t-test.

In addition to calculating volumes of distribution, the reversible 2-tissue compartmental model was used to calculate BP_{ND} values for the six target regions using the indirect method for all subjects using grey matter Cerebellum as a reference region.

$$BP_{NDi} = DVR_i - 1 = \frac{V_{Ti}}{V_{TCerebellum}} - 1 \tag{7.5}$$

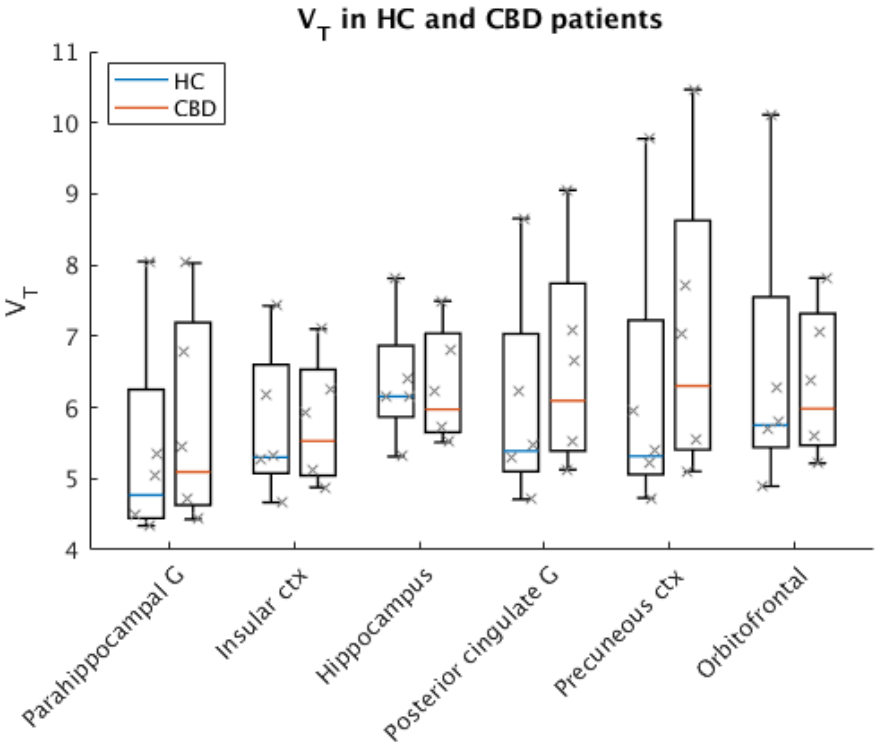


FIGURE 7.8: Boxplots displaying calculated V_T values for CBD patients and healthy controls for six ROIs

where, BP_{NDi} is the binding potential value in a region i, DVR_i is the distribution volume ratio in region i, V_{Ti} is the volume of distribution in region i and $V_{TCerebellum}$ was the volume of distribution in the grey matter Cerebellum reference region.

The BP_{ND} values calculated are summarised in Figure 7.9. As was the case with V_T, no regions show statistically significant increases of binding in patients when compared to controls. However, the medians of the CBD patients are higher than controls in all regions. With these data, it is impossible to tell whether lack of statistical significance is due to the small study size or not. The selected cohort was not used to evaluate differences between patients and controls but rather to find the optimum modelling pipeline for larger future studies.

7.3 Validation of SRTM

This section focusses on assessing the quality of quantification of the same ten subjects when using SRTM with grey matter Cerebellum as a reference region

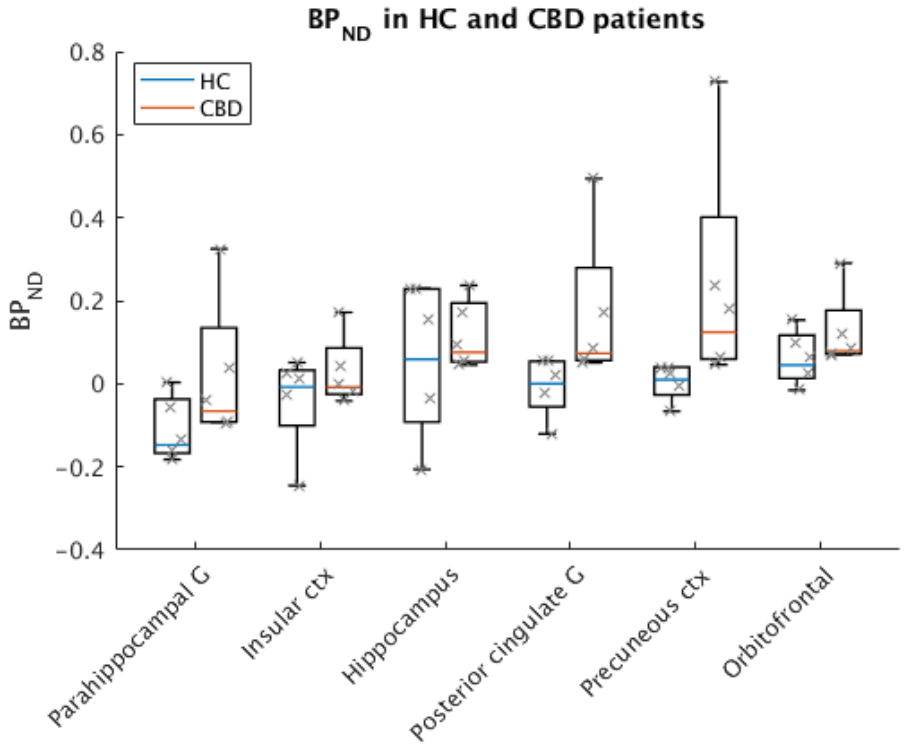


FIGURE 7.9: Boxplots showing calculated BP_{ND} values for CBD patients and controls for six ROIs

instead of full kinetic analysis with an arterial input function. SRTM does not require an arterial input function and so quantification can be achieved without inserting an arterial cannula into a subject. This has two main advantages; it is far less invasive for the patient and it is more cost-effective and logistically easier (especially in larger studies).

Fits of SRTM to the TACs for an example subject for six ROIs when using grey matter Cerebellum as the reference region are displayed in Figures 7.10 and 7.11. The model can accurately describe the TACs in all regions. It should be noted here that the sum of squares of the residuals of the fit to the Cerebellum TAC is zero by design as this is the reference tissue TAC.

In Figure 7.12 the BP_{ND} values calculated using SRTM are correlated with those found using the 2-tissue compartment model. There is a strong positive linear correlation between the gold standard of full kinetic modelling and the SRTM in CBD. The Pearson's coefficient of determination, r^2, for the correlation was 0.86 which is similar to what was found in AD by Wooten et al. 2017 and Golla et al. 2017. Importantly, however the gradient of the best fit line was 0.78 suggesting

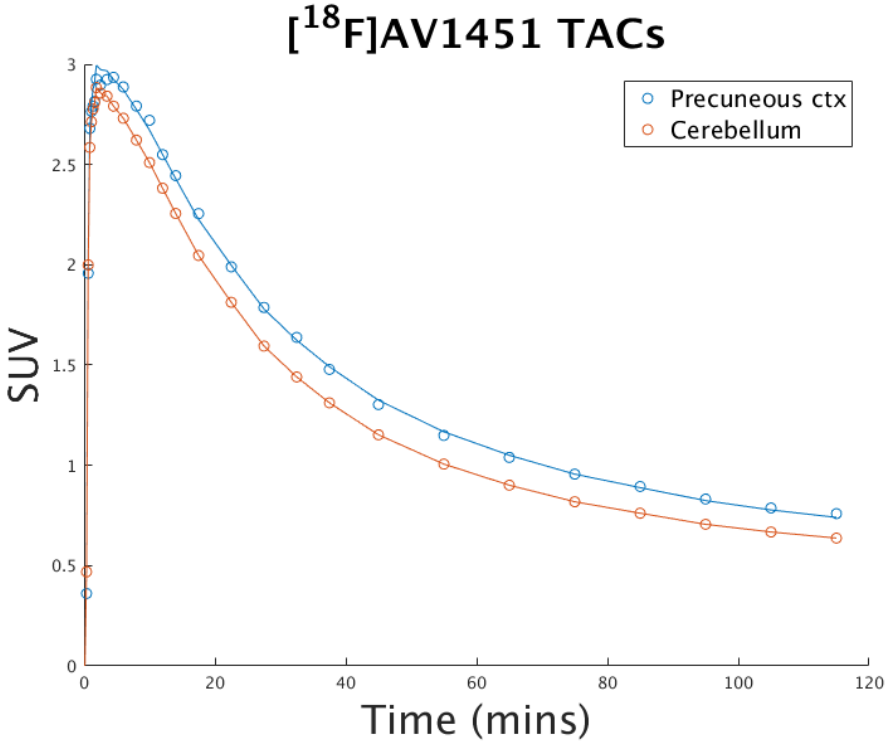


FIGURE 7.10: The fit of SRTM to the TACs of two ROIs. The sum of squares of the residuals of the fit to the Cerebellum TAC is zero as this is the reference tissue TAC.

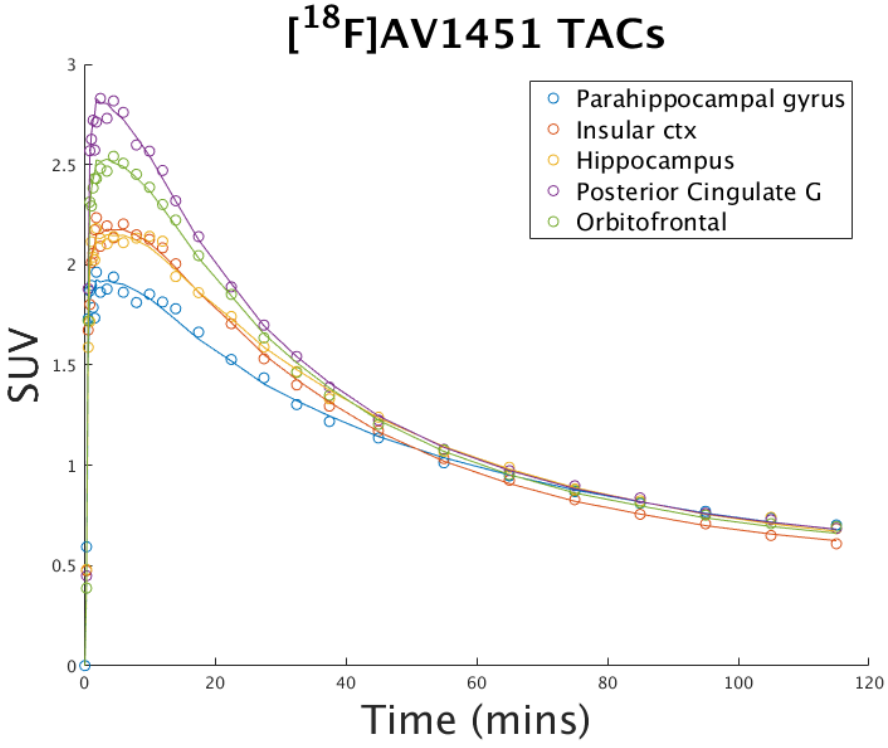


FIGURE 7.11: The fit of SRTM to the TACs of five ROIs. The model accurately describes the TACs in all regions.

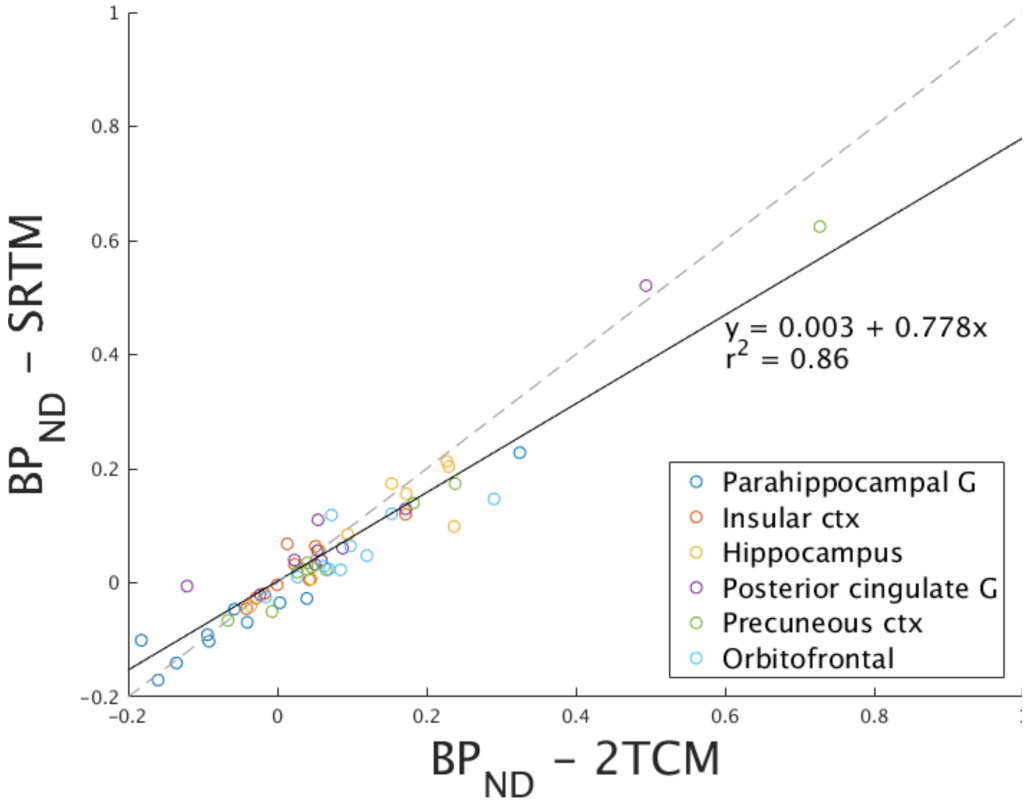


FIGURE 7.12: Correlation between BP_{ND} derived from 2-tissue compartmental model and from SRTM

there is an underestimation of the true BP_{ND} using SRTM.

7.4 Validation of SUVr

I have already shown that SRTM provides a good correlation with full kinetic modelling when using [^{18}F]-AV1451 in healthy controls and patients with CBD. In this section, the potential to use a static imaging protocol for future studies is explored.

Specifically, SUVr with grey matter Cerebellum as a reference region is assessed as an outcome measure from static images.

7.4.1 Finding the optimum SUVr time window

I found the optimum time window for SUVr by evaluating the correlation with BP_{ND} at the group level. SUVr images were generated for a set of 11 20 min

time windows ranging from 0-20 min to 100-120 min (see left hand column of Table 7.1 for list of chosen time windows). This was achieved by creating integral images from the same time windows and dividing the intensities of the voxels in the integral images by the mean value from the Cerebellum grey reference region. The CIC atlas (Tziortzi et al. 2011) was then applied to each of the SUVr images in order to calculate regional SUVr values for the six target ROIs introduced in section 7.2.2.

The Pearson's correlation of determination, r^2 between the SUVr $-$ 1 values and the BP_{ND} values from the full kinetic modelling across all subjects and all ROIs was evaluated for each time window. The results are summarised in Table 7.1. The greatest r^2 values were observed at the late time windows of 90-110 mins and 100-120 mins. However, these were calculated with only nine subjects as one patient only completed 100 min of the 120 min scan. The r^2 of the 80-100 min is 0.83 which is the joint highest of all the time windows which included all patients. In addition to this, the gradient of the line of best fit is the closest to one out of all the time windows in which all the subjects were included.

SUVr time window (mins)	r^2	Gradient	Intercept
0-20	0.01	0.091	-0.102
10-30	0.25	0.542	-0.096
20-40	0.30	0.306	-0.007
30-50	0.78	0.644	0.036
40-60	0.55	0.489	0.031
50-70	0.66	0.592	0.042
60-80	0.83	0.821	0.049
70-90	0.79	0.761	0.052
80-100	0.83	0.841	0.052
90-110 (9 subjects only)	0.85	0.926	0.054
100-120 (9 subjects only)	0.87	1.009	0.045

TABLE 7.1: A table showing Pearson correlations of determination and the parameters from the best linear fit for the correlation of regional SUVr values with BP_{ND} values derived from the two-tissue compartment model for six regions of interest

The optimum time window for the ten subjects analysed was determined to be 80-100 min as this produced the highest r^2 values for a time window that included all subjects but Table 7.1 shows that all time windows after 60 min

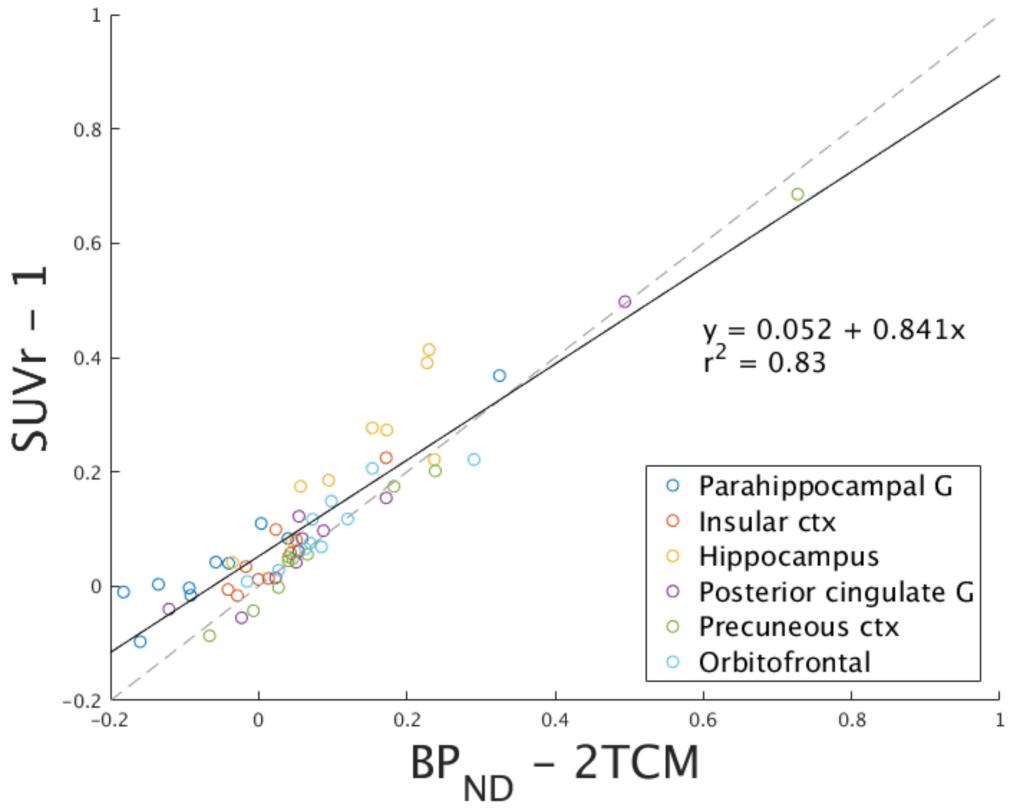


FIGURE 7.13: Correlation between BP_{ND} derived from 2-tissue compartmental model and SUVr-1 calculated from static images

provide similar correlations. Figure 7.13 shows the correlation between SUVr-1 and BP_{ND} as calculated from the 2-tissue compartment model for the optimum time window of 80-100 min.

Time windows before 60 min show both lower r^2 value for the correlation and also a lower gradient. A lower gradient implies lower sensitivity and if one assumes all measurements have the same signal-to-noise ratio, this could reduce the power to detect real biological changes.

7.4.2 Assessing the optimum SUVr time window using individual scan time stability analysis

The strong correlation of SUVr values with BP_{ND} derived from 2-tissue compartmental model at the group level provides evidence that late time windows can provide reliable quantification of the regional tau burden. However, by combining the results for all the subjects into one analysis it is impossible to

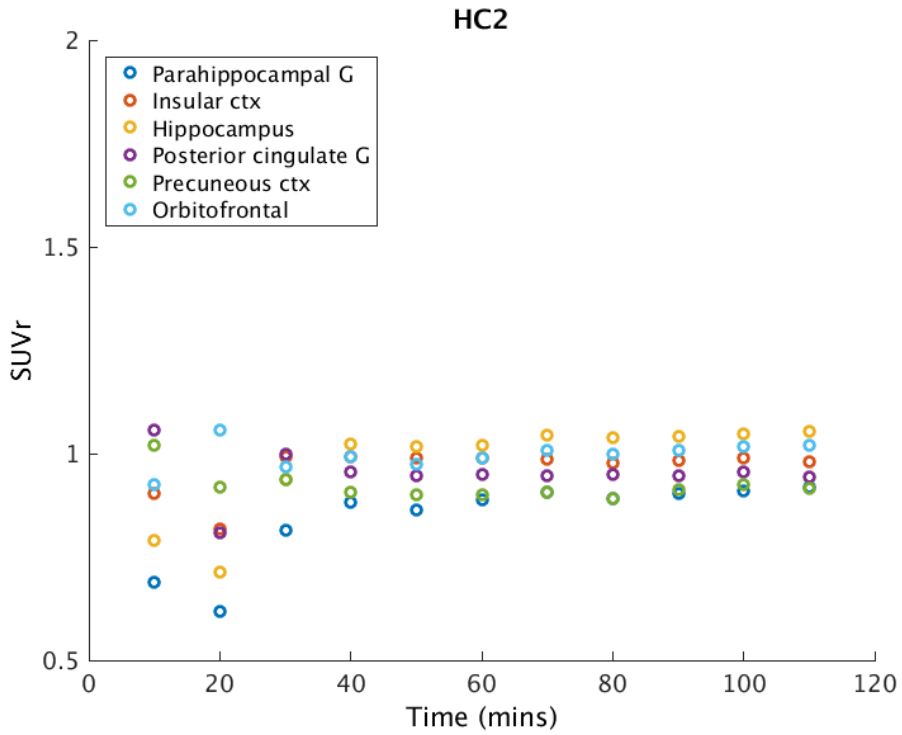


FIGURE 7.14: Plot showing the time stability of regional SUVr values for six ROIs. The x-axis represents the mid-time window time. The values become stable at 40 min (30-50 min time window)

evaluate how the characteristics of individual TACs affect the quality of quantification.

In order to address this, the time stability of the regional SUVr was investigated. Further, for each subject, regional SUVr values were plotted as function of time. These plots show whether, and if so how quickly, the system reaches equilibrium. The time stability plot for a healthy control is shown in Figure 7.14. The regional SUVr values become stable at 40 min meaning that for this subject a 20 min time window of 30-50 min would have yielded similar results to a late time window.

Figures 7.15 and 7.16 show time stability graphs for two of the patients with CBD. The system takes longer to reach an equilibrium with values becoming stable at 70 mins (60-80 min time window) for one patient (Figure 7.15) and not becoming stable in the full scan time window for another (7.16).

There appears to be a relationship between the SUVr values and the time it takes

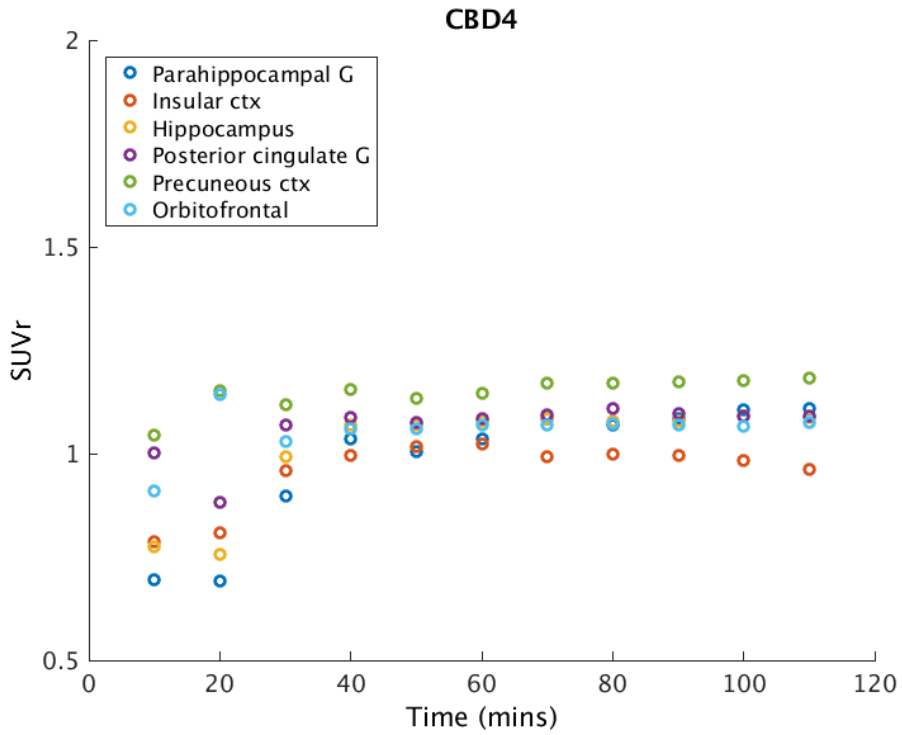


FIGURE 7.15: Plot showing the time stability of regional SUVr values for six ROIs. The values become stable at 70 min (60-0 min time window)

for the values to become stable. Higher SUVr values mean the system takes longer to reach equilibrium with very high values (as seen in Figure 7.16) meaning the values never become stable. Interestingly, this result was also found in AD patients by Wooten et al. 2017. The mechanism causing these results is unclear but one hypothesis could be that the presence of NFT alters the tissue in a way which slows down the kinetics of the tracer and therefore the system fails to reach equilibrium as quickly as when tau is not present.

This individual analysis has shown that although it is possible to achieve a good group level correlation at the ROI level between full kinetic analysis and late time-window SUVr, one should exercise caution as it is likely that SUVr of subjects with high uptake are likely to be time-dependent.

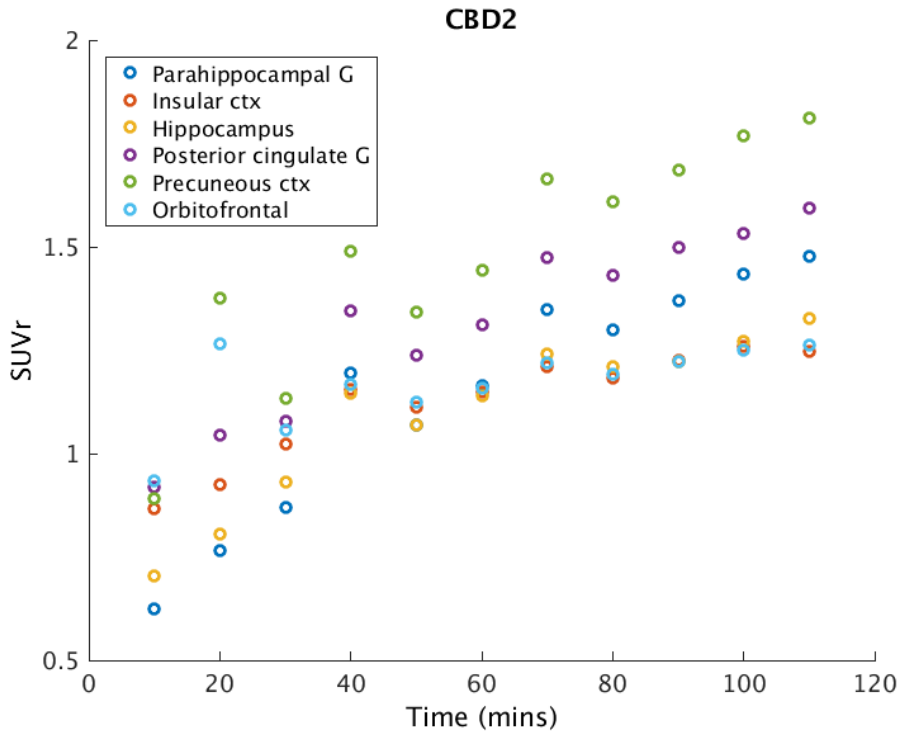


FIGURE 7.16: Plot showing the time stability of regional SUVr values for six ROIs. The values fail to become stable inside the duration of the 120 min scan.

7.5 Conclusion

In this chapter, I have assessed different methods for modelling [^{18}F]AV1451 in CBD. In previous studies, optimum imaging protocols have been identified for studies in AD subjects and patients who have suffered a TBI but no equivalent studies have been performed for other tauopathies. Here, I firstly outlined the method for producing an arterial input function. Metabolite data was accurately fitted using a sigmoid function with three parameters and arterial input functions were successfully created for all subjects successfully. The dynamic imaging data was found to be best fitted using a 2-tissue compartment model with fixed blood volume at the region level when considering seven grey matter regions of interest.

After identifying the optimum kinetic model, I investigated whether it was possible to use SRTM as a method for quantifying tau. This does not require an arterial cannula to be placed and therefore is less invasive for the patient. SRTM

with a grey matter Cerebellum reference region showed a good correlation with full kinetic modelling although gradient of the best linear fit between the two suggested that there may be a consistent underestimation of BP_{ND} values when using SRTM.

Finally, SUVr was evaluated as a method to quantify the tau burden. Initially, different time windows were investigated and 80-100 mins was identified as the optimum time window as it provided the best compromise between including all subjects and a good correlation between SUVr values and BP_{ND} when derived using full kinetic modelling. However, time stability analysis suggested there may be a relationship between the level of uptake and the time taken for the system to reach equilibrium. As such, the ability to detect real biological differences may be diminished in larger studies if one only uses static imaging.

Chapter 8

Application of Tau PET quantification to tau accumulation following a TBI

In the previous chapter, the kinetics of [^{18}F]AV1451 were investigated where full kinetic modelling with an arterial input function, reference tissue models and static imaging methods were applied to a small study consisting of five healthy controls and five patients with corticobasal degeneration. In this chapter, I concentrate on quantifying [^{18}F]AV1451 uptake in a larger TBI study consisting of 32 subjects. The demographics of the study, preprocessing of dynamic [^{18}]-AV1451 images and motion correction steps were explained in Chapter 3. The hypothesis to be tested is that there is increased tracer uptake in subjects who have suffered a TBI when compared to healthy controls. SRTM was used to quantify all the data in this study.

8.1 Aims and outline

In this chapter, I hypothesise that there will be increased [^{18}F]AV1451 uptake in patients who have suffered a TBI as compared to healthy controls. In the study, 32 subjects (21 TBI, 11 healthy controls) underwent a dynamic [^{18}F]AV1451 PET scan without an arterial cannula being placed (more details in Chapter 3). The

hypothesis of increased tau levels in TBI is assessed both at the ROI and voxel level.

The remainder of this chapter is dedicated to implementing SRTM to quantify tracer uptake for all 32 subjects enrolled in the study. In section 8.2, the methodology for defining seven regions of interest including the reference tissue region of interest is outlined. SRTM is then applied at the region of interest level to the generated TACs in section 8.3. A parametric imaging approach is used in section 8.4 which has the ability to detect more sporadic and less anatomically related increases in tracer uptake. Parametric binding potential images are generated and individual z-score images are created for each TBI patient. These show at an individual level in which voxels there is increased uptake when compared to the normal distribution of healthy controls.

8.2 Definition of regions of interest

All preprocessing, motion-correction and model fitting in this analysis was computed using MIAKAT^{TM} (R. N. Gunn, Coello, and Searle 2016) which is a fully quantitative suite of analysis tools for PET neuroimaging data.

8.2.1 Definition of grey matter

Grey matter voxels were determined from the structural MR images of all subjects which were segmented into six different tissue classes using unified segmentation in SPM12 (Ashburner and K. J. Friston 2005). All voxels exceeding a probability of 0.9 in the grey matter probability map were considered to be grey matter voxels.

8.2.2 Registration of atlas image to individual MR space

The grey matter and white matter probability maps were subsequently used to create DARTEL flowfields which define a spatial mapping from each subjects' structural MR image space to the standard MNI152 space. The inverse of these

flowfields was calculated and was applied to the CIC atlas (Tziortzi et al. 2011) which produced a personalised atlas image in each individuals' MR structural T1 space which was visually QC'd.

8.2.3 Reference region

Post-mortem immunohistochemistry in a recent large cross-sectional study has shown relatively low tau levels in the cerebellum of subjects with chronic traumatic encephalopathy (thought to be caused by repeat traumatic brain injuries) (Mez et al. 2017) and therefore grey matter Cerebellum was chosen as the reference region in this study.

The grey matter Cerebellum reference region was defined on the MR image to be the intersection of the grey matter voxels (defined in subsection 8.2.1) and the voxels in the Cerebellum region of interest in the subject space atlas (defined in subsection 8.2.2).

8.2.4 Target regions

Six target ROIs were chosen from the CIC atlas; Parahippocampus, Insular, Hippocampus, Posterior Cingulate Gyrus, Precuneous cortex and Orbitofrontal. These were chosen because they are cortical regions showing high tau levels in chronic traumatic encephalopathy (Mez et al. 2017). As was the case in the previous chapter, I restricted the analysis to cortical regions because quantification of [^{18}F]AV1451 in subcortical regions is unreliable due to tracer off-target specific binding to neuromelanin and MAO-A. As with the reference region, these regions were defined to include all voxels which are in the intersection of grey matter voxels (defined in subsection 8.2.1) and the voxels in the region of interest in the subject space atlas (defined in subsection 8.2.2).

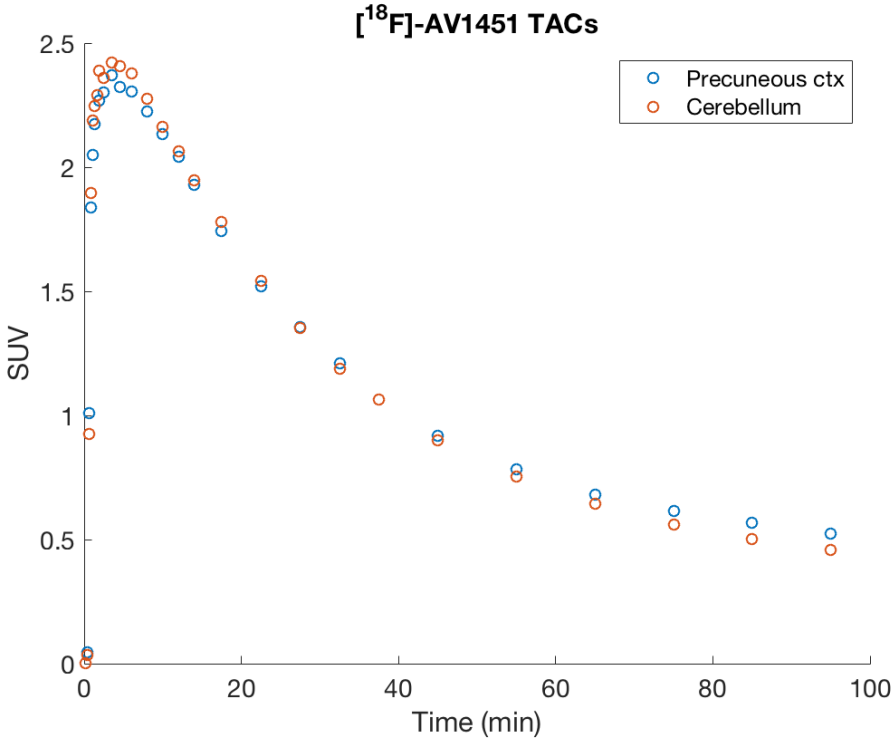


FIGURE 8.1: Time activity curves for a target ROI (Precuneous cortex) and the reference region (Cerebellum). Both regions have been grey matter masked.

8.3 Region of interest analysis using SRTM

TACs were generated for seven regions of interest defined above (the grey matter Cerebellum reference region and six target regions) for each subject by plotting the mean of the intensities of the voxels in the region for each frame.

8.3.1 SRTM fits to TACs

Figures 8.1 and 8.2 show TACs for the seven regions for an example subject. The peak SUV value varied between regions from approximately 1.8 in the Parahippocampus to approximately 2.5 in the Precuneous cortex.

SRTM was applied to the TACs using the grey matter Cerebellum reference region as the reference region. Figures 8.3 and 8.4 show the fit of SRTM to the TACs for an example subject. The model uses the grey matter Cerebellum reference region TAC as an input and therefore the sum of squares of residuals for

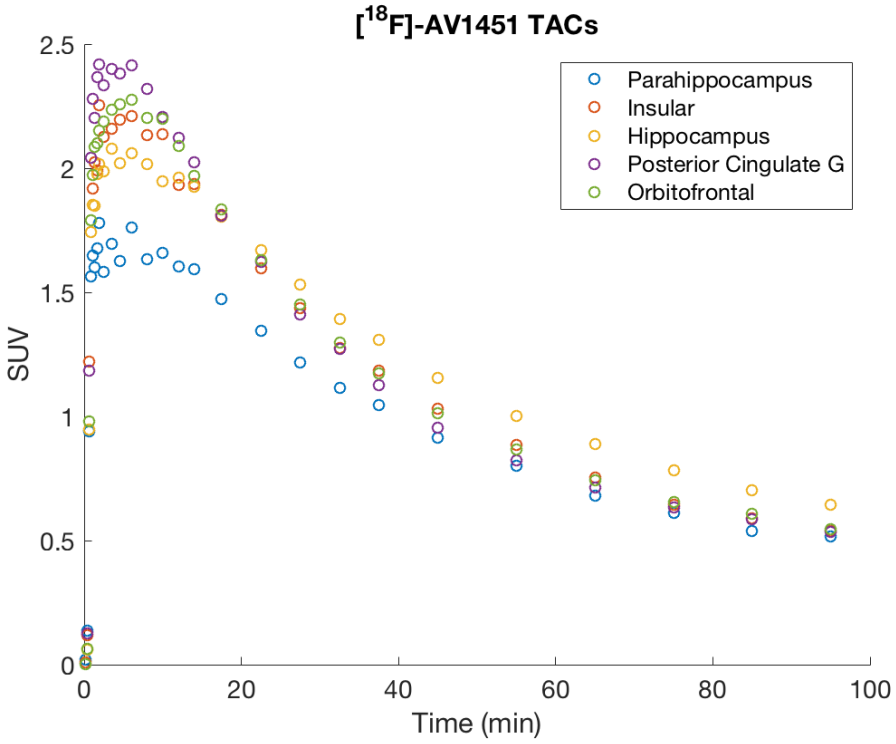


FIGURE 8.2: TACs for five grey matter ROIs

the Cerebellum region is zero (Figure 8.3). In the target regions, the model accurately describes all the TACs and can account for the different kinetics shown across regions.

8.3.2 Distributions of BP_{ND} in healthy controls and TBI

Regional BP_{ND} values from SRTM were generated for each subject. The distributions of BP_{ND} values across all the chosen target regions in healthy controls and patients who had suffered a TBI are summarised using boxplots in Figure 8.5. No regions show significantly higher uptake in patients who have suffered a TBI.

However, subjects who had suffered a TBI did show an increased range of BP_{ND} values in all regions.

Overall, the BP_{ND} values ranged from -0.27 to 0.29 in TBI subjects. These values are lower than those seen in studies involving AD patients (Golla et al. 2017) but similar to the majority of values found for patients suffering from CBD shown

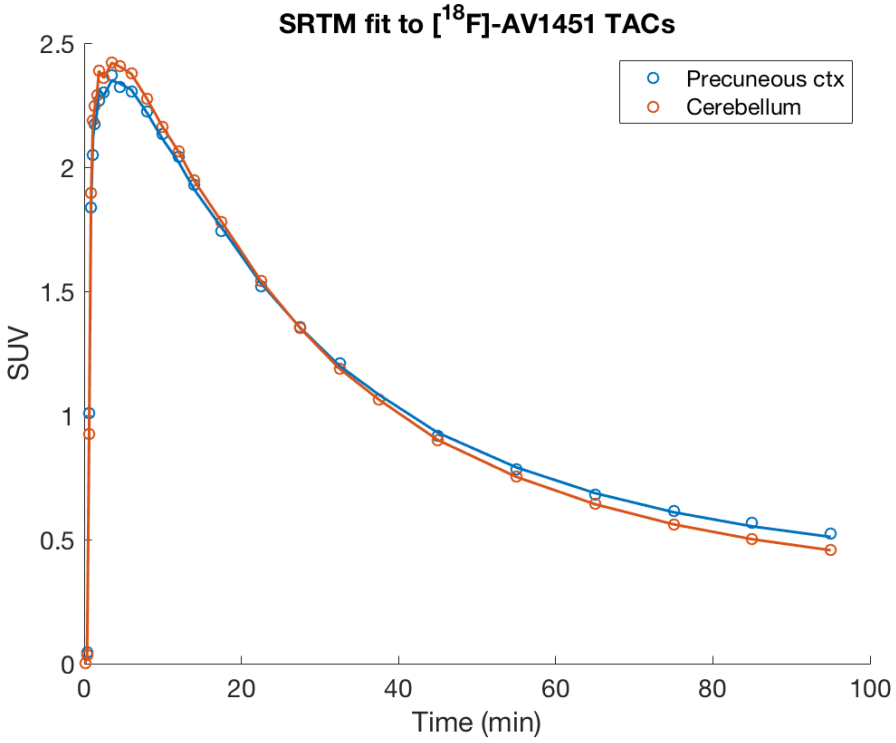


FIGURE 8.3: The fit of SRTM to two TACs for an example subject. The Cerebellum is the reference region in this analysis resulting in the sum of squares of residuals equalling zero by design.

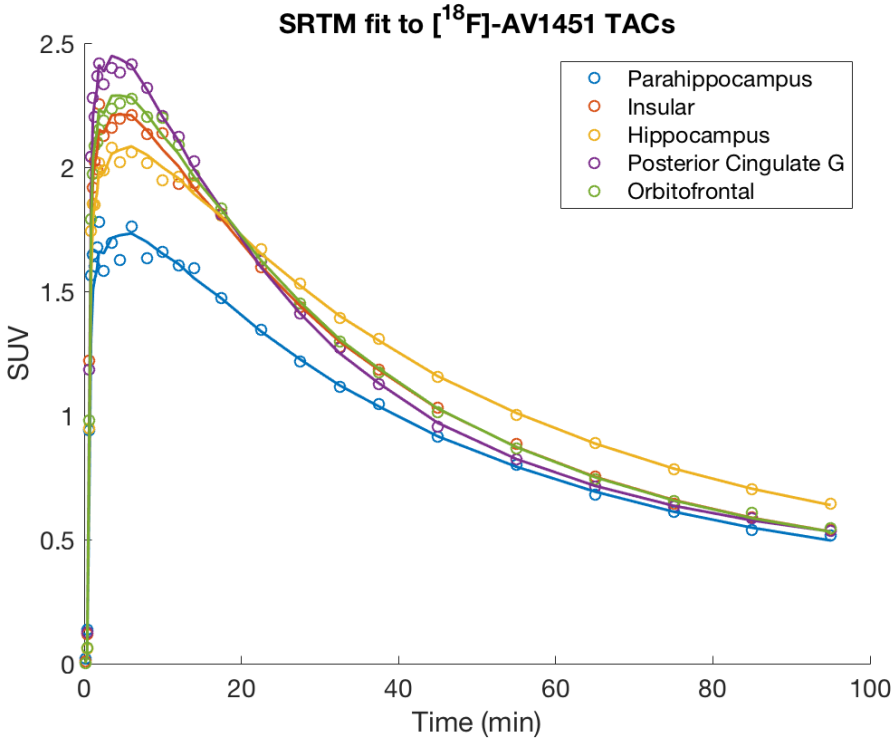


FIGURE 8.4: The fit of SRTM to five TACs for an example subject. The model can accurately describe TACs in each region.

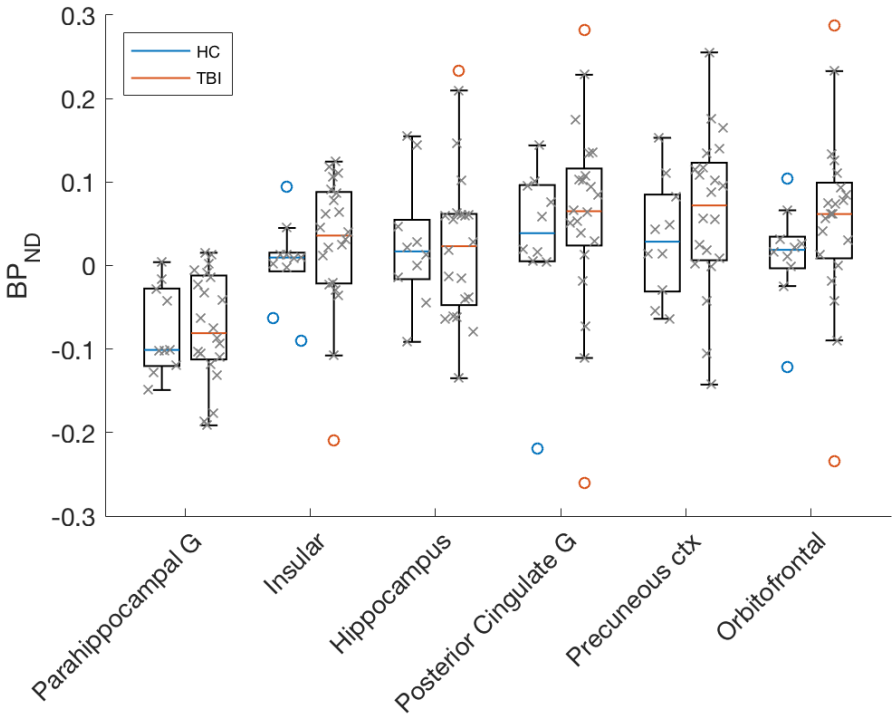


FIGURE 8.5: BP_{ND} values as calculated using STRM across six regions in healthy controls and TBI: At the region of interest level there is no difference in the tracer binding potentials between groups. In all regions, there is a higher range of BP_{ND} values in the TBI group than in controls suggesting that level of uptake in TBI is variable and potentially not spatially consistent across patients

in the previous chapter in Figure 7.9. This high variability is not surprising given the heterogeneous nature TBIs in the sample. This analysis suggests that elevated tracer uptake may not be spatially consistent across subjects.

In healthy controls the variance is lower but there are outliers at both ends of the distribution. This high variability could come from differing levels MAO-A which [^{18}F]AV1451 has recently been shown to bind to (Vermeiren et al. 2017).

8.4 Voxel-level analysis

The ROI analysis showed high variability in the uptake of [^{18}F]AV1451 in TBI and I suggested this could be the result of heterogeneity in the nature of injury which may cause different spatial patterns of uptake for each patient. In this section, this is analysed further by modelling the PET data at the voxel level.

8.4.1 Voxel level fitting of SRTM

The grey matter Cerebellum TAC was used as the reference TAC to apply SRTM at the voxel level. SRTM was fitted at the voxel level using a basis function method as outlined in R. N. Gunn, Lammertsma, et al. 1997. The result was parametric images for binding potential for each subject.

The BP_{ND} parametric images were spatially normalised to MNI152 space using the previously derived DARTEL flowfields from subject space to MNI152 space (calculated in section 8.2.2). The flowfields were applied to the BP_{ND} parametric images without modulation (meaning the image intensities were preserved) using a 8mm x 8mm x 8mm smoothing gaussian kernel.

8.4.2 Parametric BP_{ND} images

Figures 8.6, 8.7 and 8.8 show orthographic projections of the BP_{ND} images for all subjects included in the study.

Figure 8.6 shows the BP_{ND} images for the 11 healthy controls. The highest binding potentials are found in the Striatum for almost all subjects which is consistent with the autoradiographic study conducted by Marquié, Normandin, Vanderburg, et al. 2015 showing off-target binding to neuromelanin in this region.

Figures 8.7 and 8.8 show the BP_{ND} images for the 21 TBI patients. As with the healthy controls, there is a strong signal in the striatum which is likely to be a result of off-target binding to neuromelanin and MAO-A. In the cortical regions, BP_{ND} values vary between subjects with some subjects (such as TBI 03, TBI 04, TBI 10, TBI 15 and TBI 16) showing a strong and widespread signal and others exhibiting binding potentials similar to controls. In subjects where there is widespread uptake, the highest binding potentials are seen in the temporal and parietal lobes.

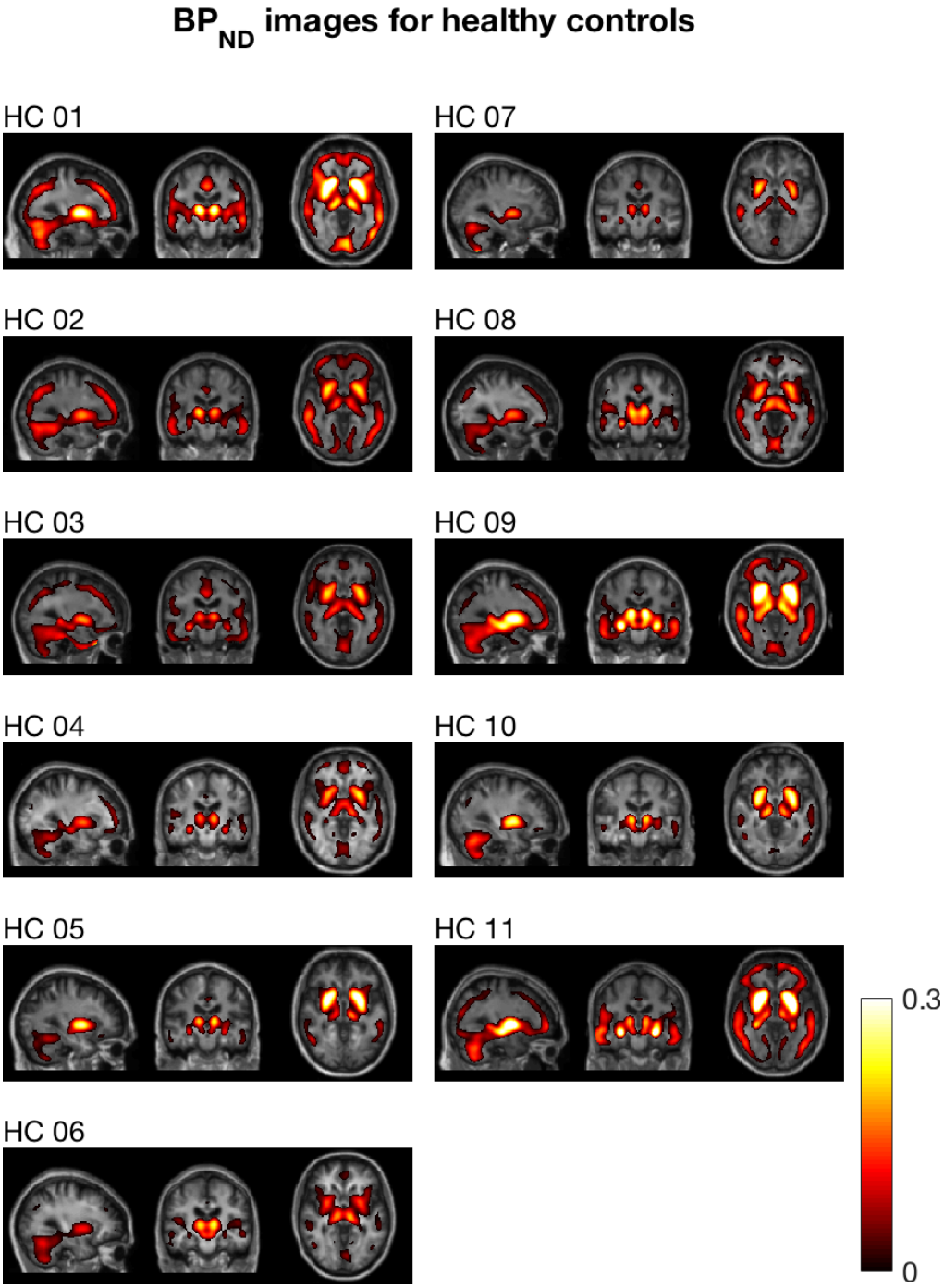


FIGURE 8.6: Orthographic projections of parametric BP_{ND} images for healthy controls; consistent with previous studies, there is high uptake in the striatum which is likely to be due to off-target binding to neuromelanin and MAO-A.

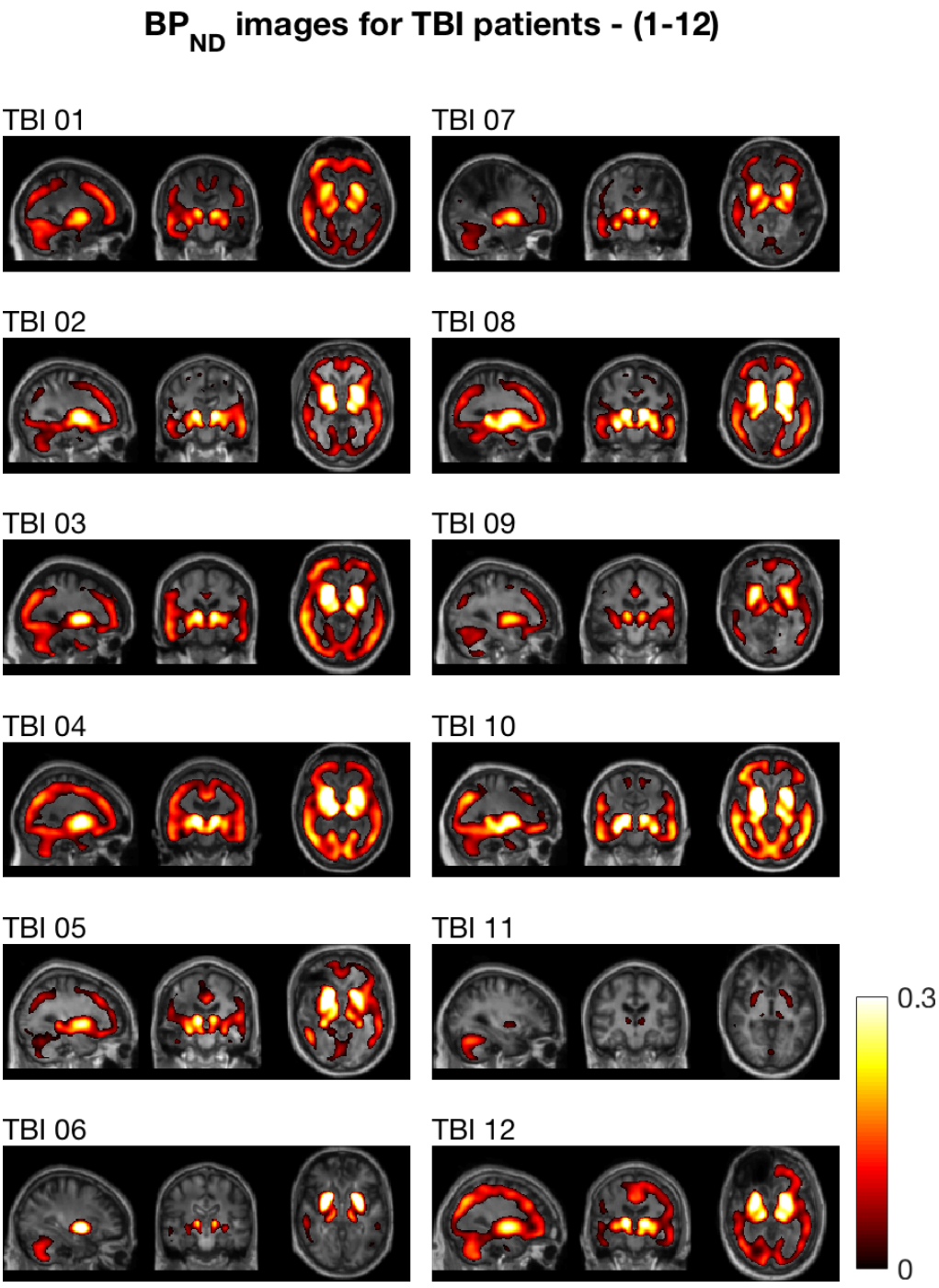


FIGURE 8.7: Orthographic projections of parametric BP_{ND} images for TBI patients (1-12); tracer uptake is variable across patients with some showing a strong and widespread cortical signal such as TBI 03, TBI 04 and TBI 10 but others with few voxels having positive binding potentials such as TBI 06 and TBI 11. In the subjects with strong signal, the highest binding potentials occur in the temporal and parietal lobes

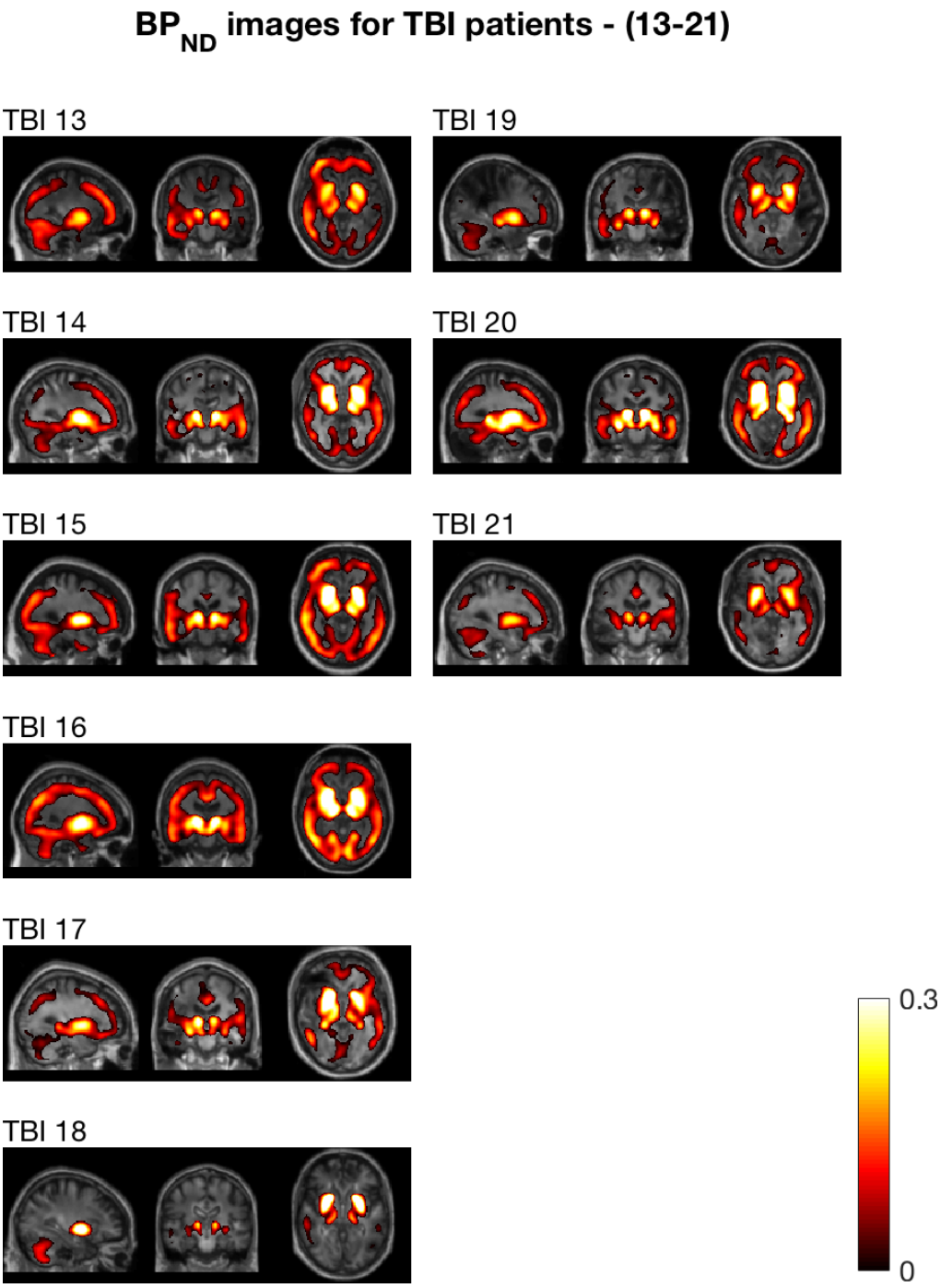


FIGURE 8.8: Orthographic projections of parametric BP_{ND} images for TBI patients (13-21); as with page 1, tracer uptake is variable across patients with some showing a strong and widespread cortical signal such as TBI 15 and TBI 16 but others with few voxels having positive binding potentials such as TBI 18.

8.4.3 Z-score images

It is difficult with just visual inspection of the BP_{ND} images of the TBI patients to see in which voxels there are abnormally high values. To investigate this question quantitatively, the BP_{ND} images in MNI152 space were used to create Z-score images for the 21 traumatic brain injury subjects. These images allow us to analyse the spatial distribution of increased [^{18}F]AV1451 binding when compared to the normal distribution of healthy controls at the individual level.

Characterising the normal distribution of healthy controls

The normal distribution of healthy controls was characterised by generating mean and standard deviation images from the 11 healthy controls. The intensities in each voxel of the mean and standard deviation images were the mean and standard deviation of the distribution of intensities in the corresponding voxel across all healthy control subjects. These images can be seen in Figure 8.9. The key feature picked up from all the individual healthy control BP_{ND} images, is that there is are high BP_{ND} values in the Striatum. As previously mentioned, this is likely to be the result of off-target binding to neuromelanin and MAO-A.

The standard deviation images shows the highest variability in BP_{ND} values in the healthy controls is also in the Striatum which could simply be a result of differing levels of neuromelanin and MAO-A. The magnitude of intensities in the standard deviation image is greater than the intensities of mean image for many voxels. This implies that there is a high level of variability of tracer uptake in healthy controls which means that the power to detect differences between patient groups and healthy controls is likely to be low and therefore large studies will be required to reach statistical significance.

Generating Z-score images for TBI subjects

Z-score images were generated for each of the 21 TBI subjects and 11 Healthy controls. The intensities in the Z-score images are themselves Z-scores and

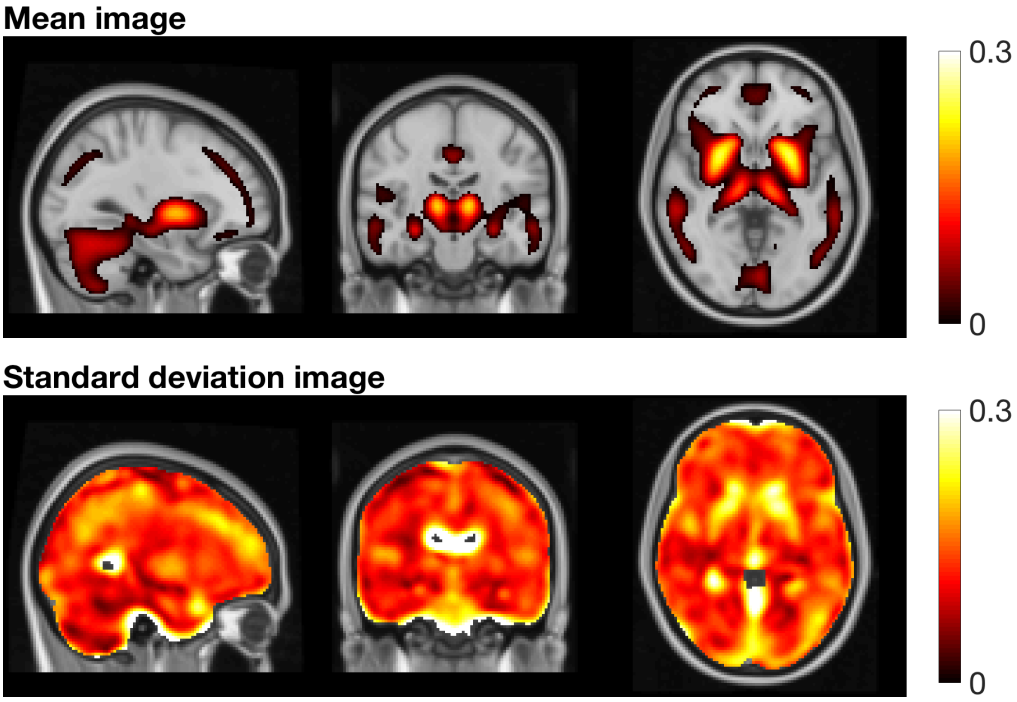


FIGURE 8.9: Orthographic projections of the mean and standard deviation images of healthy controls; the highest binding potentials in the mean image are in the striatum which are likely to be caused by off-target binding to neuromelanin. Interestingly, in this location there is high variability across subjects as shown by the high intensities in the standard deviation image.

therefore the intensity for a TBI subject i in voxel j, is the Z-score, Z_{i_j}, and is calculated by

$$Z_{i_j} = \frac{x_{i_j} - \mu_j}{\sigma_j} \tag{8.1}$$

where x_{i_j} is the BP_{ND} for subject i in voxel j of the spatially normalised parametric BP_{ND} image, μ_j is the intensity in voxel j of the mean HC image and σ_j is the intensity of voxel j in the standard deviation image.

Figures 8.10 and 8.11 show all the Z-score images calculated. When comparing them to the BP_{ND} images the most striking difference is that there aren't high Z-values in the Striatum whereas this is where the highest BP_{ND} values are seen. This shows that, although there are high binding potentials in the Striatum, there are no differences between patients and controls. As before this could be explained by the binding resulting from neuromelanin rather than tau although this shows that this off-target binding is consistent between patients and controls.

As with the BP_{ND} parametric images, there is a heterogeneity in the Z-score images which reflects of the heterogeneity of the sample. There is heterogeneity across subjects in both the Z-scores and the spatial distribution of high Z-scores. Subjects TBI 03, TBI 10, TBI 12 and TBI 15 all have high Z-scores in the cortex whereas TBI 04 and TBI 16 show high Z-scores in white matter regions. The properties of the tracer dictate that high Z-scores in the cortex are more likely to result from increased levels of tau (Marquié, Normandin, Vanderburg, et al. 2015).

8.4.4 Group comparison of Z-scores

The Z-score images shown in figures 8.10 and 8.11 show that the spatial distribution of high z-scores is heterogeneous in the TBI sample. This is consistent with the high range of BP_{ND} values for TBI subjects in the ROI analysis.

Z-score images were used to test whether the tracer uptake is increased in TBI subjects without defining a target ROI. A voxel was classified as being outside

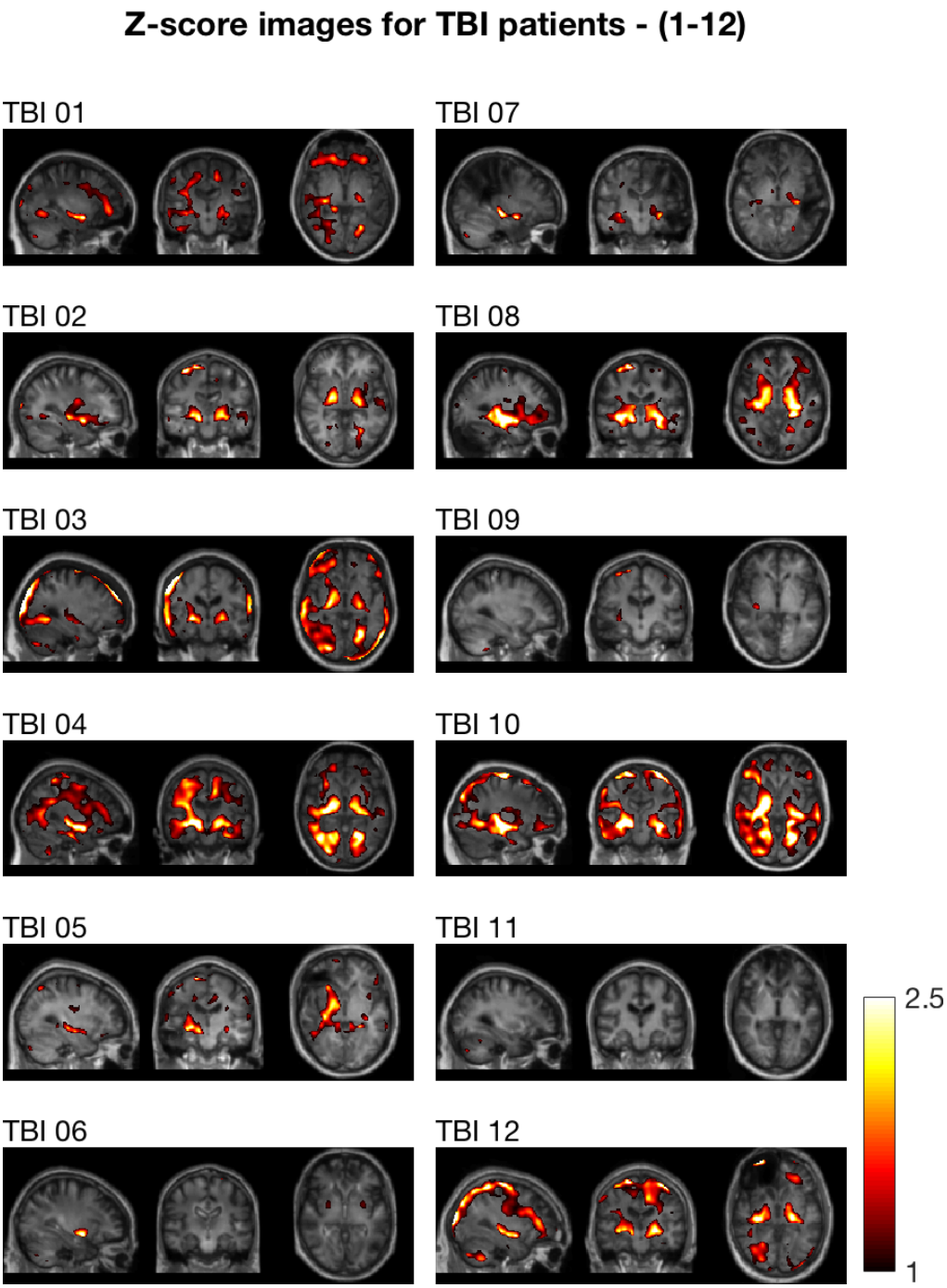


FIGURE 8.10: Orthographic projections of Z-score images for TBI patients (1-12) as calculated against the normal distribution of healthy controls. Both the location and z-values are variable across the patients.

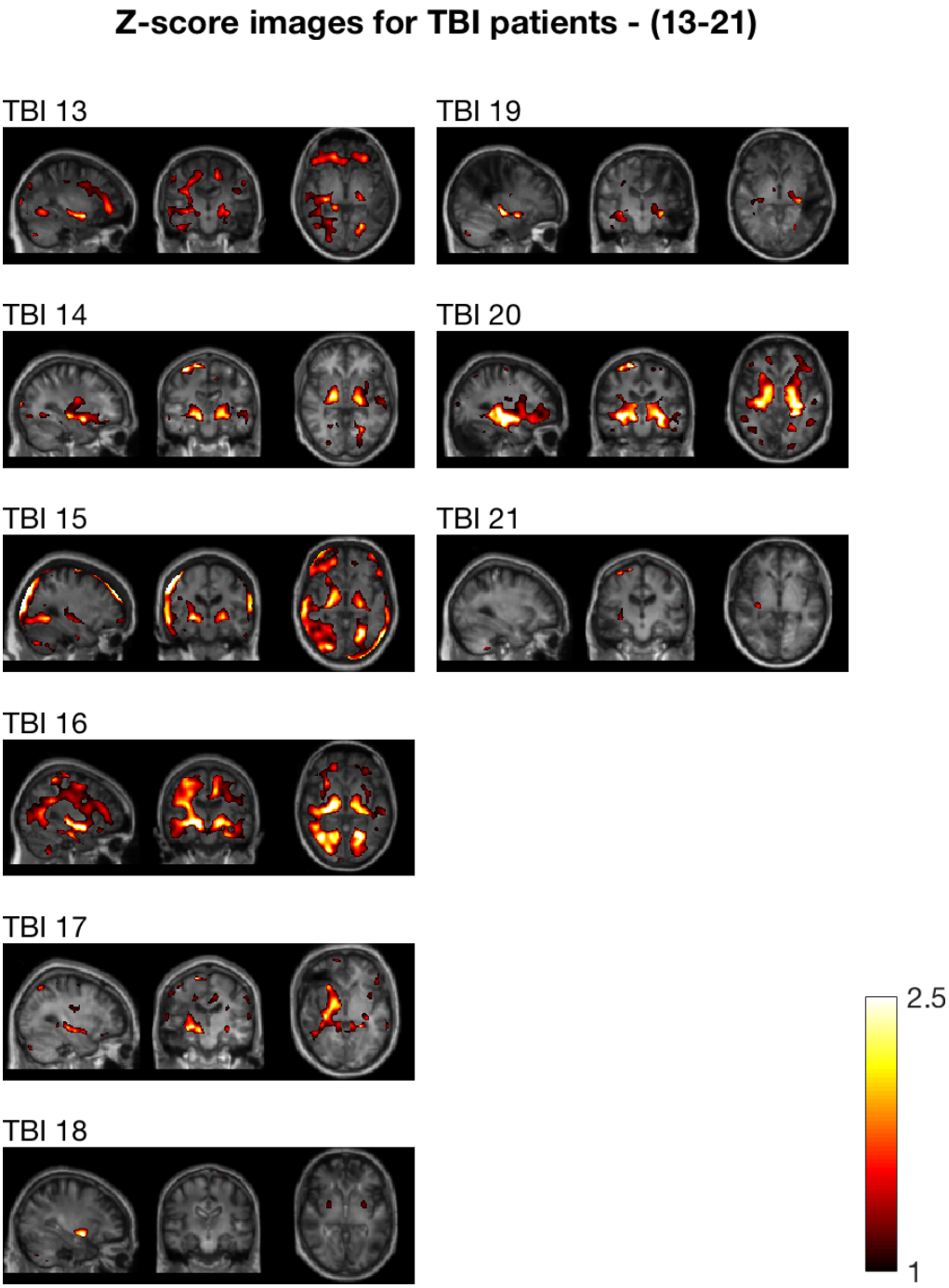


FIGURE 8.11: Orthographic projections of Z-score images for TBI patients (13-21) as calculated against the normal distribution of healthy controls. Both the location and z-values are variable across the patients.

HC 01	37
HC 02	6
HC 03	33
HC 04	0
HC 05	1
HC 06	0
HC 07	0
HC 08	0
HC 09	3
HC 10	0
HC 11	30
Mean	10
S.D.	15.1789

TABLE 8.1: A table showing the number of voxels in the Z-score images of each Healthy conrol over the threshold value of 1.96.

the normal range if the Z-score was greater than 1.96. For each subject in the study the number of abnormal voxels was counted and results are shown in tables 8.1 and 8.2.

The table shows that less than 40 voxels lie outside the normal range for all healthy controls whereas only 5 of 21 subjects in the TBI subjects have less that 40 voxels which are classified as abnormal. A non-parametric Mann-Whitney rank sum statistical test was used to test whether the number of abnormal voxels was higher in TBI than controls because the distributions are not normal. There is a statistically significant difference in the distributions ($p < 6.3e\text{-}4$).

This result shows that at the group level, there is increased tracer uptake in TBI compared to healthy controls but that the spatial distribution of that increased uptake is heterogeneous. There are TBI subjects that show uptake similar to healthy controls which again shows the heterogeneity of the TBI.

8.5 Discussion

In this chapter, I applied SRTM to dynamic [^{18}F]AV1451 PET imaging data in a study involving 21 TBI patients and 11 healthy controls. The aim was to quantify the tau burden *in vivo* for all subjects and assess whether it was increased in the subjects who had suffered TBI.

TBI 01	900
TBI 02	320
TBI 03	4689
TBI 04	2222
TBI 05	304
TBI 06	72
TBI 07	34
TBI 08	1532
TBI 09	223
TBI 10	6737
TBI 11	0
TBI 12	2660
TBI 13	1570
TBI 14	470
TBI 15	27
TBI 16	297
TBI 17	376
TBI 18	0
TBI 19	0
TBI 20	356
TBI 21	127
Mean	1091
S.D.	1744

TABLE 8.2: A table showing the number of voxels in the Z-score images of each Healthy conrol over the threshold value of 1.96.

8.5.1 Quantifying specific binding of [^{18}F]AV1451 with the SRTM

SRTM with a grey matter Cerebellum reference region was chosen to model the dynamic [^{18}F]AV1451 data based on a combination of results from Chapter 7 and previous studies using the tracer in AD and TBI [Wooten et al. 2017; Golla et al. 2017]. The model could accurately describe regional TACs for six cortical target regions and the tracer specific binding was quantified by the BP_{ND} outcome measure.

The four assumptions made by SRTM are that there is no specific binding in the reference tissue, the kinetics of both the reference region and target regions can be described by a one-tissue compartment model, the blood volume contribution to the signal is negligible and that there is the same level of non-specific binding in the reference and target regions (Salinas, Searle, and R. N. Gunn 2015).

It is possible that the first assumption is violated in this case as there could be tau deposition in the grey matter Cerebellum of subjects who have suffered a TBI. Tau deposition in the reference region would mean a global underestimation of the BP_{ND} in the target regions (both at the region of interest and voxel level). However, if there is tau deposition, post-mortem studies suggest the concentration would be low and any other reference region would likely be worse affected (Mez et al. 2017; McKee, Cantu, et al. 2009). As the subjects in this study did not have an arterial line placed, a reference region method is required and therefore SRTM was used following its validation in chapter 7.

The second assumption is likely to be violated to a certain extent. In the previous chapter, I showed that the kinetics of [^{18}F]AV1451 are best described using a two-tissue compartment model in all regions in a study involving subjects with CBD and this model has also been found to be optimal in other studies involving subjects with AD (Golla et al. 2017). The potential bias this may cause has been investigated by Salinas, Searle, and R. N. Gunn 2015 and in this scenario (with both target and reference region exhibiting the same kinetics and target binding potential of < 2) the bias is likely to be less than 10%.

The blood volume contribution to the signal will inevitably be non-zero and a blood volume of 10% would produce an underestimation of the BP_{ND} by approximately 10%. In reality, it is likely that the blood volume is below 10% and therefore the bias coming from assuming a negligible blood volume will be bounded at 10%.

The fourth assumption is important and if it is violated, it can result in a large error in BP_{ND}. Using this data alone, it is impossible to assess to what extent the non-displaceable binding is consistent across the brain. It is sensible however, to assume this a similar level on non-displaceable binding since both target and reference regions were both grey matter masked in the same manner.

8.5.2 Tracer specific binding in TBI

One of the aims of this chapter was to assess whether there was increased tracer specific binding for subjects who have suffered a TBI.

Overall, the tracer uptake in TBI is lower and more spatially heterogeneous than that seen in neurodegenerative diseases such as AD (Golla et al. 2017) and the regional BP_{ND} values were not statistically significantly different between healthy controls and subjects who had suffered a TBI at a group level in any of the target regions. There was however, a higher range of BP_{ND} values for all regions in TBI subjects. Visually inspecting the parametric BP_{ND} images for the TBI subjects allows one to see the heterogeneity in both the spatial distribution and the level of tracer uptake. The Z-score images show that all but one of the TBI subjects had voxels where the BP_{ND} was higher than healthy controls by more than one standard deviation (of the normal distribution of healthy controls). Further, 25% of the patients showed widespread cortical increases in tracer uptake compared to the normal distribution of healthy controls. The group level analysis of the Z-score images showed a statistically significant difference in the number of abnormal voxels (defined as being voxels with a Z-score of over 1.96). Approximately 25% of the TBI subjects however, had similar numbers of abnormal voxels as healthy controls.

By collating all the results, I would say that there is increased binding of the tracer at the group level. However, the individual Z-score images show the value of not grouping all subjects together in this way because one has the ability to explore significant tau levels in a heterogeneous population. Thus, a more informative conclusion can be drawn when looking at each patient individually; that being, there is increased tracer uptake in some TBI subjects and the spatial distribution of increased binding is not spatially consistent across subjects. This inconsistency may be caused by the differing nature of how the brain injury was sustained.

8.5.3 Quantifying tau in TBI with [^{18}F]AV1451

The ultimate aim of this chapter was to quantify tau *in vivo* using [^{18}F]AV1451 and test the hypothesis that there is an increased tau burden on subjects who have suffered a TBI. Until this point I have only written about the tracer specific signal. Here, I consider whether tracer specific signal represents tau concentration *in vivo*.

Before discussing the tracer specificity issues, it is important to remember that tracer quantification for all PET scans has some potential systematic errors. Partial volume effects mean that the apparent uptake in a given voxel could be underestimated as the signal is erroneously "spilled over" to adjacent voxels. Quantification in future studies could be improved by applying partial volume correction methods. Further, imperfections in motion correction, MR image segmentation and atlas registration cause inaccuracies in quantification although all of these stages were visually QC'd to minimise any biases.

More fundamentally than the errors affecting all PET scans for this chapter is the selectivity of [^{18}F]AV1451 for tau. More explicitly, is it true that increased specific binding of the tracer implies a higher concentration of tau? In the last two years, post-mortem and radiographic studies have shown that, there is off-target specific binding of [^{18}F]AV1451 to both neuromelanin (Marquié, Normandin, Vanderburg, et al. 2015) and MAO-A (Vermeiren et al. 2017). The

concentration of neuromelanin in the cortex is low and therefore by restricting the investigation in this study to cortical regions, I have reduced the likelihood of this confound. The spatial distribution of monoamine oxidase A is however more widespread (J. Tong et al. 2013) and further this has been shown to be affected by smoking (Zanotti-Fregonara et al. 2014). It is impossible to determine what percentage of the specific binding of the tracer results from tau.

In addition, it is important to consider whether [^{18}F]AV1451 binds to tau in all its forms. Marquié, Normandin, Vanderburg, et al. 2015; Marquié, Normandin, Meltzer, et al. 2017 showed that [^{18}F]AV1451 exhibits strong binding to the tau in paired helical filament form but negligible binding to straight filaments. This means that an increase in the concentration of paired helical filament tau will increase the specific binding of [^{18}F]AV1451 but that it is possible that an elevated tau load won't necessarily result in increased tracer uptake.

A set of second generation tau tracers are being developed which aim to address the off-target binding of [^{18}F]AV1451. Early results using, [^{18}F]MK6240, a tracer developed by Merck Co, show no off-target binding to neuromelanin or MAO-A (Hostetler et al. 2016) and the promise of increased tau selectivity. Future studies should focus on using these second generation tracers to improve the reliability of the quantification of tau *in vivo*.

8.6 Conclusion

In this chapter, I used SRTM to quantify the *in vivo* concentration of tau in a study which aimed to assess whether suffering a TBI resulted in tau accumulation in the brain.

The SRTM with a grey matter Cerebellum reference region was applied at both the ROI level to TACs derived from the CIC atlas (Tziortzi et al. 2011) and at the voxel-level using a basis function method. The model produced good fits to the TACs and these fits were used to generate BP_{ND} values for each region for all subjects. There was not a statistically significant difference in the tracer

binding between TBI subjects and healthy controls in any of the chosen ROIs at the group level. Parametric images for BP_{ND} showed the level of binding was heterogeneous across all subjects who suffered a TBI both because of the level of binding and the spatial distribution of the increased binding. By making Z-score images, it was possible to conclude that there is increased binding at the gropu level but also that it is best to consider TBI cases individually rather than as one group. Some patients exhibited widespread elevated binding, others showed only moderate increases and some showed binding patterns similar to controls.

The study aimed to quantify tau and I discussed the selectivity of the tracer for tau and which forms of tau are being imaged. It was concluded that, studies using this tracer have the problem that elevated binding could result from increases in tau, neuromelanin or MAO-A. In TBI, it is likely that some of the increased signal is a result of elevated tau but that more selective tau tracers would be required to confirm that.

Chapter 9

Conclusions and future work

Accumulation of insoluble aggregates of misfolded proteins such as Aβ and tau is a consistent finding in many neurodegenerative diseases. PET imaging provides a technique to non-invasively investigate the concentration of misfolded proteins *in vivo*. This thesis has shown how mathematical modelling can be used to understand aggregation and robustly quantify PET data.

The spatiotemporal distribution of Aβ in AD was modelled in two different ways in chapters 4 and 5. Based on previous models, a network diffusion model was introduced in chapter 4 which had parameters for Aβ production, Aβ, clearance and distal spreading of Aβ across the brain. Models with different options for each of these were fitted to cross-sectional PET imaging data obtained from ADNI and the BIC was used to decide on the most parsimonious model. Unfortunately, the results from this chapter are difficult to interpret due to problems with the identifiability of parameters. Importantly though, the methodology in this chapter formed the foundation for chapter 5. A similar framework was used to fit a four-parameter logistic growth model to a chronological dataset which was formed by assigning an individual time through the accumulation process to each subject in the cross-sectional ADNI data based on their mean cortical SUVr. The optimum model for the chronological dataset had regionally consistent exponential growth rate r and time of half maximal accumulation T_{50} but variable levels of non-specific binding NS and Aβ carrying capacity K which provided evidence that the spatiotemporal distribution of Aβ in AD results from properties of the local tissue environment rather than

long-term spreading from seed regions. By fitting the logistic growth model at the voxel-level, parametric maps for the non-specific binding and Aβ carrying capacity were generated and these reflected known features of both Aβ accumulation in AD and [^{18}F]AV45 binding characteristics. Future studies in this field could apply the logistic growth model to longitudinal data from subjects who have received multiple scans over a long time period and data from other misfolded proteins such as tau. A full spatiotemporal characterisation of the PET biomarkers in AD could aid with understanding the disease and developing novel therapeutics to either slow or even reverse neurodegeneration.

In chapter 6, a novel outcome measure, $A\beta_L$ was defined to quantify the global Aβ burden in AD. Spatially normalised SUVr images were effectively modelled using a linear combination of the parametric maps for Aβ carrying capacity (**K**) and non-specific binding (**NS**) and $A\beta_L$ was defined to be scaling factor of **K**. An automated algorithm calculated $A\beta_L$ for both cross-sectional and longitudinal data and compared it to mean cortical SUVr. Greater effect sizes were obtained using $A\beta_L$ for both datasets which could mean that future studies could have greater power to detect biological changes *in vivo* which could prove particularly useful in trials of novel anti-Aβ therapeutics. In order to have confidence in using $A\beta_L$ more widely, further validation studies are required. Particularly, it will be important to understand when modelling an SUVr image as a a linear combination of **K** and **NS** is inappropriate. Looking further ahead, it will be interesting to see if a similar methodology could be used for other Aβ radiotracers such as [^{18}F]Flutametamol and [^{18}F]Florbetaben.

Chapters 7and 8 were focussed on the kinetic modelling of the novel tau PET radiotracer [^{18}F]AV1451. In chapter 7, an optimal kinetic modelling pipeline for quantifying tracer upatake in CBD was developed which included generating an arterial input function and finding the best compartmental model. The two-tissue compartment model with a 5% blood volume was chosen as the best model for quantifying the imaging data. Binding potential derived using SRTM and SUVr $-$ 1 both provided good correlations with binding potentials derived from full kinetic modelling with an arterial input function at the group level

which suggested these simplified methods could be useful in future studies. It was also seen however, that SUVr values failed to stabilise within 120 mins in subjects that exhibited high uptake and therefore SUVr values may be time-dependent. SRTM was used as way to model TACs in chapter 8 and this modelling facilitated the generation of both regional binding potentials and voxel-wise parametric maps for BP_{ND} in 32 subjects in a study evaluating tau expression following TBI. There were no differences in BP_{ND} at the ROI level but there was a greater variation in tracer uptake in patients. At the voxel-level binding in the Striatum existed for both patients and controls which was consistent with known off-target binding of the tracer to neuromelanin and MAO-A (Marquié, Normandin, Meltzer, et al. 2017; Vermeiren et al. 2017) but it was difficult to assess which voxels in the cortex had elevated binding in TBI subjects. To address this, Z-score images were created for each subject which showed great variability in the level of binding both in the intensities and the spatial distribution. This heterogeneity could well have been caused by heterogeneity in the biomechanics of the brain injury itself. It was concluded that there was an increase in binding in the TBI group when looking at Z-score images at the group level but also that it was far more informative to consider patients individually due to the heterogeneous nature of TBI. As was discussed in this thesis, selectivity issues of the [^{18}F]AV1451 mean that it is difficult to interpret increased tracer binding in terms of tau and future studies should focus on using second generation tau tracers that have been developed to avoid off-target binding to neuromelanin, MAO-A and MAO-B.

To conclude, I think this thesis shows the value of combining mathematical modelling and neuroimaging data as together they provide a powerful tool to robustly study neurodegeneration with applications in exploring disease pathology and developing novel therapeutics.

Appendix A

List of PPF models fitted

One parameter

$$y = e^{-\beta x}$$

$$y = \beta$$

Two parameters

$$y = \alpha e^{-\beta x}$$

$$y = \alpha e^{-\beta x} + 1 - \alpha$$

$$y = \alpha x + \beta$$

Three parameters

$$y = \alpha(1 - e^{-\beta x}) + \gamma$$

$$y = \alpha e^{-\beta x} + (1 - \alpha)e^{-\gamma x}$$

$$y = \left(1 - \frac{x^3}{x^3 + 10^{\alpha}}\right)\beta + \gamma^2$$

$$y = \frac{\left(1 - \frac{x^3}{x^3 + 10^{\alpha}}\right)^{\beta} + \gamma}{1 + \gamma}$$

Four parameters

$$y = \alpha e^{-\beta x} + \gamma e^{-\delta x}$$

Appendix B

Permissions summary table

Page No.	Type of work	Name of work	Source of work	Copyright holder	Permission requested on	Permission yes/no
7	Fig	Example DTI image	O'Donnell and Westin 2011	Elsevier	4/12/2017	Yes
31	Fig	Atrophy figure	Vemuri and Jack 2010	BioMed Central Ltd	n/a	Creative commons license
33	Fig	PiB figure	Klunk et al. 2004	John Wiley and Sons	4/12/2017	Yes
36	Fig	Braak staging	H. Braak and E. Braak 1991	Springer	4/12/2017	Yes

Bibliography

Agdeppa, E D, V Kepe, J Liu, S Flores-Torres, et al. (2001). "Binding characteristics of radiofluorinated 6-dialkylamino-2-naphthylethylidene derivatives as positron emission tomography imaging probes for beta-amyloid plaques in Alzheimer's disease." In: *The Journal of neuroscience : the official journal of the Society for Neuroscience* 21.24.

Agdeppa, E D, V Kepe, J Liu, G W Small, et al. (2003). "2-dialkylamino-6-acylmalononitrile substituted naphthalenes (DDNP analogs): Novel diagnostic and therapeutic tools in Alzheimer's disease". In: *Molecular Imaging and Biology* 5.6, pp. 404–417. DOI: 10.1016/j.mibio.2003.09.010.

Alessio, A and P Kinahan (2006). "PET image reconstruction". In: *Nuclear Medicine* 1.figure 1, pp. 1–22. ISSN: 0031-9155. DOI: 10.1088/0031-9155/54/12/007.Iterative.

Alzheimer, A (1907). "Uber eine eigenartige Erkrankung der Hirnrinde." In: *Allegemeine Zeitschrift fur Psychiatrie und physchish-Gerichtliche Medizin* 64, pp. 146–148.

Armstrong, M J. et al. (2013). "Criteria for the diagnosis of corticobasal degeneration". In: *Neurology* 80.5, pp. 496–503. ISSN: 00283878. DOI: 10.1212/WNL.0b013e31827f0fd1.

Ashburner, J (2007). "A fast diffeomorphic image registration algorithm". In: *NeuroImage* 38.1, pp. 95–113. ISSN: 1053-8119. DOI: http://dx.doi.org/10.1016/j.neuroimage.2007.07.007.

Ashburner, J and K Friston (2003). "Rigid Body Registration". In: *Human Brain Function: Second Edition*, pp. 635–653. ISBN: 9780122648410. DOI: 10.1016/B978-012264841-0/50034-2.

Ashburner, J and K J Friston (2005). "Unified segmentation". In: *NeuroImage* 26.3, pp. 839–851. ISSN: 1053-8119. DOI: http://dx.doi.org/10.1016/j.neuroimage.2005.02.018.

Assaf, Y and O Pasternak (2008). "Diffusion Tensor Imaging (DTI)-based White Matter Mapping in Brain Research: A Review". In: *Journal of Molecular Neuroscience* 34.1, pp. 51–61. ISSN: 1559-1166. DOI: 10.1007/s12031-007-0029-0.

Barnes, J et al. (2015). "Alzheimer's disease first symptoms are age dependent: Evidence from the NACC dataset". In: *Alzheimer's & Dementia* 11.11, pp. 1349–1357. ISSN: 1552-5260. DOI: https://doi.org/10.1016/j.jalz.2014.12.007.

Barthelemy, M et al. (2005). "Dynamical patterns of epidemic outbreaks in complex heterogeneous networks". In: *J Theor Biol* 235.2, pp. 275–288. DOI: 10.1016/j.jtbi.2005.01.011.

Basser, P J (1995). "Inferring microstructural features and the physiological state of tissues from diffusion-weighted images". In: *NMR in Biomedicine* 8.7, pp. 333–344. ISSN: 10991492. DOI: 10.1002/nbm.1940080707.

Basser, P J, J Mattiello, and D LeBihan (1994). "MR diffusion tensor spectroscopy and imaging". In: *Biophysical Journal* 66.1, pp. 259–267. ISSN: 00063495. DOI: 10.1016/S0006-3495(94)80775-1.

Basser, P J, S Pajevic, et al. (2000). "In vivo fiber tractography using DT-MRI data". In: *Magnetic Resonance in Medicine* 44.4, pp. 625–632. ISSN: 07403194. DOI: 10.1002/1522-2594(200010)44:4<625::AID-MRM17>3.0.CO;2-O.

Basser, P J and C Pierpaoli (1998). "A simplified method to measure the diffusion tensor from seven MR images". In: *Magn Reson Med* 39.6, pp. 928–934. ISSN: 0740-3194. DOI: 10.1002/mrm.1910390610.

– (2011). "Microstructural and physiological features of tissues elucidated by quantitative-diffusion-tensor MRI". In: *Journal of Magnetic Resonance* 213.2, pp. 560–570. ISSN: 10907807. DOI: 10.1016/j.jmr.2011.09.022.

Bero, A W et al. (2011). "Neuronal activity regulates the regional vulnerability to amyloid-β 2 deposition". In: *Nature Neuroscience* 14.6, pp. 750–756. DOI: 10.1038/nn.2801.

Blumenfeld, H (2010). *Neuroanatomy through Clinical Cases*, p. 1033. ISBN: 9788578110796. DOI: 10.1017/CBO9781107415324.004. arXiv: arXiv:1011.1669v3.

Boxer, A L et al. (2006). "Patterns of brain atrophy that differentiate corticobasal degeneration syndrome from progressive supranuclear palsy". In: *Archives of Neurology* 63.1, pp. 81–6. ISSN: 0003-9942. DOI: 10.1001/archneur.63.1.81.

Braak, H and E Braak (1991). "Neuropathological stageing of Alzheimer-related changes". In: *Acta Neuropathol* 82.4, pp. 239–259.

Brettschneider, J et al. (2015). "Spreading of pathology in neurodegenerative diseases: a focus on human studies". In: *Nat Rev Neurosci* 16.2, pp. 109–120. DOI: 10.1038/nrn3887.

Buckner, R L, J R Andrews-Hanna, and D L Schacter (2008). *The brain's default network: Anatomy, function, and relevance to disease*. DOI: 10.1196/annals.1440.011.

Buckner, R L, A Z Snyder, et al. (2005). "Molecular, Structural, and Functional Characterization of Alzheimer's Disease: Evidence for a Relationship between Default Activity, Amyloid, and Memory". In: *The Journal of Neuroscience* 25.34, pp. 7709–7717. DOI: 10.1523/JNEUROSCI.2177-05.2005.

Burnham, K P and D R Anderson (2004). "Multimodel inference: Understanding AIC and BIC in model selection". In: *Sociological Methods and Research* 33.2, pp. 261–304. DOI: 10.1177/0049124104268644.

Camus, V et al. (2012). "Using PET with 18F-AV-45 (florbetapir) to quantify brain amyloid load in a clinical environment". In: *Eur J Nucl Med Mol Imaging* 39.4, pp. 621–631. DOI: 10.1007/s00259-011-2021-8.

Catani, M et al. (2002). "Virtual in Vivo Interactive Dissection of White Matter Fasciculi in the Human Brain". In: *NeuroImage* 17.1, pp. 77–94. ISSN: 10538119. DOI: 10.1006/nimg.2002.1136.

Chien, D T, S Bahri, et al. (2013). "Early clinical PET imaging results with the novel PHF-tau radioligand [F-18]-T807". In: *J Alzheimers Dis* 34.2, pp. 457–468. DOI: 10.3233/JAD-122059.

Chien, D T, A K Szardenings, et al. (2014). "Early clinical PET imaging results with the novel PHF-tau radioligand [F18]-T808". In: *J Alzheimers Dis* 38.1, pp. 171–184. DOI: 10.3233/JAD-130098.

Chiotis, K et al. (2016). "Imaging in-vivo tau pathology in Alzheimer's disease with THK5317 PET in a multimodal paradigm". In: *European Journal of Nuclear Medicine and Molecular Imaging* 43.9, pp. 1686–1699. DOI: 10.1007/s00259-016-3363-z.

Cho, H et al. (2017). "Subcortical 18F-AV-1451 binding patterns in progressive supranuclear palsy". In: *Movement Disorders* 32.1, pp. 134–140. DOI: 10.1002/mds.26844.

Clark, C M, J Schneider, and B J Bedell (2011). "Use of florbetapir-pet for imaging β-amyloid pathology". In: *JAMA* 305.3, pp. 275–283. ISSN: 0098-7484.

Conturo, T E et al. (1999). "Tracking neuronal fiber pathways in the living human brain". In: *Proceedings of the National Academy of Sciences* 96.18, pp. 10422–10427. ISSN: 0027-8424. DOI: 10.1073/pnas.96.18.10422. arXiv: NIHMS150003.

Crystal, H et al. (1988). "Clinico-pathologic studies in dementia: Nondemented subjects with pathologically confirmed Alzheimer's disease". In: *Neurology* 38.11, pp. 1682–1687.

Damadian, R (1971). "Tumor Detection by Nuclear Magnetic Resonance". In: *Science* 171.3976, 1151 LP –1153.

DeKosky, S T et al. (2007). "Association of increased cortical soluble abeta42 levels with diffuse plaques after severe brain injury in humans." In: *Archives of neurology* 64.4, pp. 541–4. ISSN: 0003-9942. DOI: 10.1001/archneur.64.4.541.

Domert, J et al. (2014). "Spreading of amyloid-β peptides via neuritic cell-to-cell transfer is dependent on insufficient cellular clearance". In: *Neurobiology of Disease* 65, pp. 82–92. ISSN: 0969-9961. DOI: http://dx.doi.org/10.1016/j.nbd.2013.12.019.

Fahey, F H (2010). "Positron emission tomography instrumentation". In: *Radiologic Clinics of North America* 39.5, pp. 919–929. ISSN: 00338389. DOI: 10.1016/S0033-8389(05)70320-1.

Farde, L et al. (1989). "Kinetic analysis of central [11C]raclopride binding to D2-dopamine receptors studied by PET-a comparison to the equilibrium analysis." In: *Journal of cerebral blood flow and metabolism : official journal of the International Society of Cerebral Blood Flow and Metabolism* 9.5, pp. 696–708. ISSN: 0271-678X. DOI: 10.1038/jcbfm.1989.98.

Fields, R D (2010). "Change in the Brain's White Matter". In: *Science* 330.6005, pp. 768–769. ISSN: 0036-8075. DOI: 10.1126/science.1199139.

Filley, C M and R D Fields (2016). "White matter and cognition: making the connection". In: *Journal of Neurophysiology* 116.5, pp. 2093–2104. ISSN: 0022-3077. DOI: 10.1152/jn.00221.2016.

Fleminger, S et al. (2003). "Head injury as a risk factor for Alzheimer's disease: the evidence 10 years on; a partial replication". In: *Journal of Neurology, Neurosurgery & Psychiatry* 74.7, pp. 857–862. DOI: 10.1136/jnnp.74.7.857.

Flier, W M van der et al. (2011). "Early-onset versus late-onset Alzheimer's disease: the case of the missing APOE e4 allele". In: *The Lancet Neurology* 10.3, pp. 280–288. ISSN: 1474-4422. DOI: https://doi.org/10.1016/S1474-4422(10)70306-9.

Fodero-Tavoletti, M T, S Furumoto, et al. (2014). "Assessing THK523 selectivity for tau deposits in Alzheimer's disease and non-Alzheimer's disease tauopathies." In: *Alzheimer's research & therapy* 6.1, p. 11. ISSN: 1758-9193. DOI: 10.1186/alzrt240.

Fodero-Tavoletti, M T, N Okamura, et al. (2011). "18F-THK523: A novel in vivo tau imaging ligand for Alzheimer's disease". In: *Brain* 134.4, pp. 1089–1100. ISSN: 00068950. DOI: 10.1093/brain/awr038.

Forman, M S et al. (2002). "Signature tau neuropathology in gray and white matter of corticobasal degeneration". In: *American Journal of Pathology* 160.6, pp. 2045–2053.

Fox, N C et al. (1999). "Correlation between rates of brain atrophy and cognitive decline in AD." In: *Neurology* 52.8, pp. 1687–1689. ISSN: 0028-3878. DOI: 10.1212/WNL.52.8.1687.

Friston, K J et al. (1995). "Spatial registration and normalization of images". In: *Human Brain Mapping* 3.3, pp. 165–189.

Furst, A J and A Fellgiebel (2011). "White matter degeneration in normal and pathologic aging: The pattern matters". In: *Neurology* 77.1, pp. 14–15. ISSN: 1526632X. DOI: 10.1212/WNL.0b013e3182231455.

Gentleman, S M et al. (1997). "A beta 42 is the predominant form of amyloid beta-protein in the brains of short-term survivors of head injury." eng. In: *Neuroreport* 8.6, pp. 1519–1522. ISSN: 0959-4965 (Print).

Glenner, G G and C W Wong (1984). "Alzheimer's disease: Initial report of the purification and characterization of a novel cerebrovascular amyloid protein". In: *Biochemical and Biophysical Research Communications* 120.3, pp. 885–890. DOI: 10.1016/S0006-291X(84)80190-4.

Goate, A et al. (1991). "Segregation of a missense mutation in the amyloid precursor protein gene with familial Alzheimer's disease". In: *Nature* 349.6311, pp. 704–706.

Golla, S S V et al. (2017). "Quantification of Tau Load Using [18F]AV1451 PET". In: *Molecular Imaging and Biology*, pp. 1–9. ISSN: 1860-2002. DOI: 10.1007/s11307-017-1080-z.

Gregersen, N et al. (2006). "Protein Misfolding and Human Disease". In: *Annual Review of Genomics and Human Genetics* 7.1, pp. 103–124. ISSN: 1527-8204. DOI: 10.1146/annurev.genom.7.080505.115737.

Grundke-Iqbal, I et al. (1986). "Microtubule-associated protein tau. A component of Alzheimer paired helical filaments." In: *Journal of Biological ...* 261.13, pp. 6084–6089. ISSN: 0021-9258. DOI: 10.1074/jbc.M111.271320.

Gunn, R N, C Coello, and G E Searle (2016). "Molecular Imaging And Kinetic Analysis Toolbox (MIAKAT) - A Quantitative Software Package for the Analysis of PET Neuroimaging Data". In: *Journal of Nuclear Medicine* 57.supplement 2, p. 1928.

Gunn, R N, S R Gunn, and V J Cunningham (2001). "Positron emission tomography compartmental models". In: *Journal of Cerebral Blood Flow and Metabolism* 21.6, pp. 635–652.

Gunn, R N, S R Gunn, F E Turkheimer, et al. (2002). "Positron emission tomography compartmental models: A basis pursuit strategy for kinetic modeling". In: *Journal of Cerebral Blood Flow and Metabolism* 22.12, pp. 1425–1439.

Gunn, R N, Q Guo, et al. (2011). "Advances in biomathematical modeling for PET neuroreceptor imaging". In: *Drug Discovery Today: Technologies* 8.2–4, e45–e51. DOI: http://dx.doi.org/10.1016/j.ddtec.2012.01.001.

Gunn, R N, A A Lammertsma, et al. (1997). "Parametric Imaging of Ligand-Receptor Binding in PET Using a Simplified Reference Region Model". In: *NeuroImage* 6.4, pp. 279–287. ISSN: 1053-8119. DOI: http://dx.doi.org/10.1006/nimg.1997.0303.

Gustavsson, A et al. (2011). "Cost of disorders of the brain in Europe 2010". In: *European Neuropsychopharmacology* 21.10, pp. 718–779. DOI: 10.1016/j.euroneuro.2011.08.008.

Haas, M et al. (2016). "Big data to smart data in AD: Real-world examples of advanced modeling and simulation". In: *Alzheimer's & Dementia: The Journal of the Alzheimer's Association*. ISSN: 1552-5260. DOI: 10.1016/j.jalz.2016.05.005.

Hafkemeijer, A, J van der Grond, and S A R B Rombouts (2012). "Imaging the default mode network in aging and dementia". In: *Biochimica et Biophysica Acta - Molecular Basis of Disease* 1822.3, pp. 431–441. DOI: 10.1016/j.bbadis.2011.07.008.

Harada, R, N Okamura, S Furumoto, K Furukawa, A Ishiki, N Tomita, K Hiraoka, et al. (2015). "[18F]THK-5117 PET for assessing neurofibrillary pathology in Alzheimer's disease". In: *European Journal of Nuclear Medicine and Molecular Imaging* 42.7, pp. 1052–1061. DOI: 10.1007/s00259-015-3035-4.

Harada, R, N Okamura, S Furumoto, K Furukawa, A Ishiki, N Tomita, T Tago, et al. (2016). "18F-THK5351: A novel PET radiotracer for imaging neurofibrillary pathology in Alzheimer disease". In: *Journal of Nuclear Medicine* 57.2, pp. 208–214. DOI: 10.2967/jnumed.115.164848.

Hardy, J A and G A Higgins (1992). "Alzheimer's disease: the amyloid cascade hypothesis". In: *Science* 256.5054, pp. 184–185. DOI: 10.1126/science.1566067.

Hardy, J and D Allsop (1991). "Amyloid deposition as the central event in the aetiology of Alzheimer's disease". In: *Trends in Pharmacological Sciences* 12.10, pp. 383–388. ISSN: 01656147. DOI: 10.1016/0165-6147(91)90609-V.

Hashimoto, H et al. (2015). "Identification of a major radiometabolite of [11C]PBB3". In: *Nuclear Medicine and Biology* 42.12, pp. 905–910. DOI: 10.1016/j.nucmedbio.2015.08.006.

Hendee, W R and E R Ritenour (2003). *Medical Imaging Physics:* Liss (Alan) Inc. ISBN: 9780471461135.

Heurling, K et al. (2017). "Quantitative positron emission tomography in brain research". In: *Brain Research* 1670.Supplement C, pp. 220–234. ISSN: 0006-8993. DOI: https://doi.org/10.1016/j.brainres.2017.06.022.

Hill, D L et al. (2001). "Medical image registration." In: *Physics in Medicine and Biology* 46.3, R1–R45. ISSN: 0031-9155. DOI: 10.1088/0031-9155/46/3/201. arXiv: arXiv:1011.1669v3.

Hoenig, M C et al. (2017). "Tau pathology and cognitive reserve in Alzheimer's disease". In: *Neurobiology of Aging* 57, pp. 1–7. DOI: 10.1016/j.neurobiolaging.2017.05.004.

Hostetler, E D et al. (2016). "Preclinical Characterization of 18F-MK-6240, a Promising PET Tracer for In Vivo Quantification of Human Neurofibrillary Tangles". In: *Journal of Nuclear Medicine* 57.10, pp. 1599–1606. DOI: 10.2967/jnumed.115.171678.

Ikonomovic, M D et al. (2004). "Alzheimer's pathology in human temporal cortex surgically excised after severe brain injury". In: *Experimental Neurology* 190.1, pp. 192–203. DOI: 10.1016/j.expneurol.2004.06.011.

Innis, R B et al. (2007). "Consensus nomenclature for in vivo imaging of reversibly binding radioligands". In: *J Cereb Blood Flow Metab* 27.9, pp. 1533–1539. ISSN: 0271-678X.

Ishiki, A et al. (2017). "Tau imaging with [18F]THK-5351 in progressive supranuclear palsy". In: *European Journal of Neurology* 24.1, pp. 130–136. DOI: 10.1111/ene.13164.

Iturria-Medina, Y and A C Evans (2015). "On the central role of brain connectivity in neurodegenerative disease progression". In: *Frontiers in Aging Neuroscience* 7.MAY. DOI: 10.3389/fnagi.2015.00090.

Iturria-Medina, Y, R C Sotero, et al. (2014). "Epidemic Spreading Model to Characterize Misfolded Proteins Propagation in Aging and Associated Neurodegenerative Disorders". In: *PLoS Computational Biology* 10.11. Ed. by Olaf Sporns, e1003956. ISSN: 1553-734X. DOI: 10.1371/journal.pcbi.1003956.

Jack Jr., C R, D A Bennett, et al. (2016). "A/T/N: An unbiased descriptive classification scheme for Alzheimer disease biomarkers". In: *Neurology* 87.5, pp. 539–547. DOI: 10.1212/WNL.0000000000002923.

Jack Jr, C R, D S Knopman, W J Jagust, R C Petersen, et al. (2013). "Tracking pathophysiological processes in Alzheimer's disease: an updated hypothetical model of dynamic biomarkers". In: *The Lancet Neurology* 12.2, pp. 207–216. DOI: http://dx.doi.org/10.1016/S1474-4422(12)70291-0.

Jack Jr, C R, D S Knopman, W J Jagust, L M Shaw, et al. (2010). "Hypothetical model of dynamic biomarkers of the Alzheimer's pathological cascade". In: *The Lancet Neurology* 9.1, pp. 119–128. DOI: http://dx.doi.org/10.1016/S1474-4422(09)70299-6.

Jack Jr., C R, H J Wiste, et al. (2017). "Defining imaging biomarker cut points for brain aging and Alzheimer's disease". In: *Alzheimer's and Dementia* 13.3, pp. 205–216. DOI: 10.1016/j.jalz.2016.08.005.

Jack, C R et al. (2013). "Brain β-amyloid load approaches a plateau". In: *Neurology* 80.10, pp. 890–896. DOI: 10.1212/WNL.0b013e3182840bbe.

Jagust, W J, S M Landau, et al. (2016). "The Alzheimer's Disease Neuroimaging Initiative 2 PET Core: 2015". In: *Alzheimer's & Dementia: The Journal of the Alzheimer's Association* 11.7, pp. 757–771. ISSN: 1552-5260. DOI: 10.1016/j.jalz.2015.05.001.

Jagust, W J and E C Mormino (2011). "Lifespan brain activity, β-amyloid, and Alzheimer's disease". In: *Trends in Cognitive Sciences* 15.11, pp. 520–526. ISSN: 1364-6613. DOI: http://dx.doi.org/10.1016/j.tics.2011.09.004.

James, M L and S S Gambhir (2012). "A Molecular Imaging Primer: Modalities, Imaging Agents, and Applications". In: *Physiological Reviews* 92.2, 897 LP – 965.

Jellison, B J. et al. (2004). *Diffusion Tensor Imaging of Cerebral White Matter: A Pictorial Review of Physics, Fiber Tract Anatomy, and Tumor Imaging Patterns*. DOI: 10.1038/nrn2776.

Johnson, K A, A Schultz, et al. (2016). "Tau positron emission tomographic imaging in aging and early Alzheimer disease". In: *Annals of Neurology* 79.1, pp. 110–119. ISSN: 1531-8249. DOI: 10.1002/ana.24546.

Johnson, K A, R A Sperling, et al. (2013). "Florbetapir (F18-AV-45) PET to assess amyloid burden in Alzheimer's disease dementia, mild cognitive impairment, and normal aging". In: *Alzheimer's and Dementia* 9.5 SUPPL. ISSN: 15525260. DOI: 10.1016/j.jalz.2012.10.007. arXiv: NIHMS150003.

Jonasson, M et al. (2016). "Tracer kinetic analysis of (S)-18F-THK5117 as a PET tracer for assessing tau pathology". In: *Journal of Nuclear Medicine* 57.4, pp. 574–581. DOI: 10.2967/jnumed.115.158519.

Joshi, A D et al. (2012). "Performance Characteristics of Amyloid PET with Florbetapir F 18 in Patients with Alzheimer's Disease and Cognitively Normal Subjects". In: *Journal of Nuclear Medicine* 53.3, pp. 378–384. DOI: 10.2967/jnumed.111.090340.

Kantarci, K et al. (2017). "AV-1451 tau and β-amyloid positron emission tomography imaging in dementia with Lewy bodies". In: *Annals of Neurology* 81.1, pp. 58–67. DOI: 10.1002/ana.24825.

Karran, E, M Mercken, and B D Strooper (2011). "The amyloid cascade hypothesis for Alzheimer's disease: an appraisal for the development of therapeutics". In: *Nat Rev Drug Discov* 10.9, pp. 698–712. ISSN: 1474-1776.

Kass, R E and A E Raftery (1995). "Bayes Factors". In: *Journal of the American Statistical Association* 90.430, pp. 773–795. ISSN: 01621459. DOI: 10.2307/2291091.

Kepe, V et al. (2013). "Amyloid-β positron emission tomography imaging probes: a critical review." In: *Journal of Alzheimer's disease : JAD* 36.4, pp. 613–31. ISSN: 1875-8908. DOI: 10.3233/JAD-130485. arXiv: NIHMS150003.

Kety, S S (1951). "The theory and applications of the exchange of inert gas at the lungs and tissues." In: *Pharmacological Reviews* 3.1, pp. 1–41. ISSN: 0031-6997.

Kikuchi, A et al. (2016). "In vivo visualization of tau deposits in corticobasal syndrome by 18 F-THK5351 PET". In: *Neurology* 87.22, pp. 2309–2316. DOI: 10.1212/WNL.0000000000003375.

Kim, H J et al. (2017). "18F-AV-1451 PET Imaging in Three Patients with Probable Cerebral Amyloid Angiopathy". In: *Journal of Alzheimer's Disease* 57.3, pp. 711–716. DOI: 10.3233/JAD-161139.

Kimura, Y, H Endo, et al. (2016). "A new method to quantify tau pathologies with 11C-PBB3 PET using reference tissue voxels extracted from brain cortical gray matter". In: *EJNMMI Research* 6.1. DOI: 10.1186/s13550-016-0182-y.

Kimura, Y, M Ichise, et al. (2015). "PET quantification of tau pathology in human brain with 11C-PBB3". In: *Journal of Nuclear Medicine* 56.9, pp. 1359–1365. DOI: 10.2967/jnumed.115.160127.

Klunk, W E et al. (2004). "Imaging Brain Amyloid in Alzheimer's Disease with Pittsburgh Compound-B". In: *Annals of Neurology* 55.3, pp. 306–319. ISSN: 03645134. DOI: 10.1002/ana.20009.

Komori, T (1999). "Tau-positive glial inclusions in progressive supranuclear palsy, corticobasal degeneration and Pick's disease." In: *Brain pathology (Zurich, Switzerland)* 9.4, pp. 663–679. ISSN: 1015-6305. DOI: 10.1111/j.1750-3639.1999.tb00549.x.

Kouri, N et al. (2011). "Corticobasal degeneration: a pathologically distinct 4R tauopathy". In: *Nature Reviews Neurology* 7.5, pp. 263–272. ISSN: 1759-4758. DOI: 10.1038/nrneurol.2011.43.

Krishnamoorthy, S, J P Schmall, and S Surti (2016). "PET physics and instrumentation". In: *Basic Science of PET Imaging*, pp. 173–197. ISBN: 9783319400709. DOI: 10.1007/978-3-319-40070-9_8. arXiv: arXiv:1011.1669v3.

Kwee, T C, D A Torigian, and A Alavi (2013). "Overview of positron emission tomography, hybrid positron emission tomography instrumentation, and positron emission tomography quantification." In: *Journal of thoracic imaging* 28.1, pp. 4–10. ISSN: 1536-0237. DOI: 10.1097/RTI.0b013e31827882d9.

Lammertsma, A A (2012). "Compartmental Modeling in Emission Tomography BT - Handbook of Particle Detection and Imaging". In: ed. by Claus Grupen and Irène Buvat. Berlin, Heidelberg: Springer Berlin Heidelberg, pp. 1065–1081. ISBN: 978-3-642-13271-1. DOI: 10.1007/978-3-642-13271-1_42.

– (2017). "Forward to the Past: The Case for Quantitative PET Imaging". In: *Journal of Nuclear Medicine* 58.7, pp. 1019–1024. DOI: 10.2967/jnumed.116.188029.

Lammertsma, A A, C J Bench, et al. (1996). "Comparison of Methods for Analysis of Clinical [11C]Raclopride Studies". In: *J Cereb Blood Flow Metab* 16.1, pp. 42–52. ISSN: 0271-678X.

Lammertsma, A A and S P Hume (1996). "Simplified Reference Tissue Model for PET Receptor Studies". In: *NeuroImage* 4.3, pp. 153–158. ISSN: 1053-8119. DOI: http://dx.doi.org/10.1006/nimg.1996.0066.

Landau, S M, C Breault, et al. (2013). "Amyloid-β Imaging with Pittsburgh Compound B and Florbetapir: Comparing Radiotracers and Quantification Methods". In: *Journal of nuclear medicine : official publication, Society of Nuclear Medicine* 54.1, pp. 70–77. ISSN: 0161-5505. DOI: 10.2967/jnumed.112.109009.

Landau, S M, A Fero, et al. (2015). "Measurement of Longitudinal β-Amyloid Change with 18F-Florbetapir PET and Standardized Uptake Value Ratios". In: *Journal of Nuclear Medicine* 56.4, pp. 567–574. DOI: 10.2967/jnumed.114.148981.

Landau, S M, B A Thomas, et al. (2014). "Amyloid PET imaging in Alzheimer's disease: a comparison of three radiotracers". In: *European Journal of Nuclear Medicine and Molecular Imaging* 41.7, pp. 1398–1407. ISSN: 1619-7089. DOI: 10.1007/s00259-014-2753-3.

Laruelle, M, M Slifstein, and Y Huang (2003). "Relationships between radiotracer properties and image quality in molecular imaging of the brain with

positron emission tomography". In: *Molecular Imaging and Biology* 5.6, pp. 363–375. DOI: 10.1016/j.mibio.2003.09.009.

Lee, C-C et al. (2007). "A Three-Stage Kinetic Model of Amyloid Fibrillation". In: *Biophysical Journal* 92.10, pp. 3448–3458. ISSN: 0006-3495. DOI: 10.1529/biophysj.106.098608.

Lee, H-G et al. (2005). "Tau phosphorylation in Alzheimer's disease: pathogen or protector?" In: *Trends in molecular medicine* 11.4, pp. 164–9. ISSN: 1471-4914. DOI: 10.1016/j.molmed.2005.02.008.

Lee, V M-Y, M Goedert, and J Q Trojanowski (2001). "Neurodegenerative Tauopathies". In: *Annual Review of Neuroscience* 24.1, pp. 1121–1159. ISSN: 0147-006X. DOI: 10.1146/annurev.neuro.24.1.1121. arXiv: 01/0621-1121 [0147-006X].

Li, F et al. (2014). "Kinetic modeling in PET imaging of hypoxia". In: *American Journal of Nuclear Medicine and Molecular Imaging* 4.6, pp. 490–506. ISSN: 2160-8407.

Litvan, I et al. (1997). "Accuracy of the clinical diagnosis of corticobasal degeneration: a clinicopathologic study." In: *Neurology* 48.1, pp. 119–25. ISSN: 0028-3878. DOI: 10.1212/WNL.48.1.119.

Lockhart, S N et al. (2017). "Elevated 18F-AV-1451 pet tracer uptake detected in incidental imaging findings". In: *Neurology* 88.11, pp. 1095–1097. DOI: 10.1212/WNL.0000000000003724.

Logan, J et al. (1990). "Graphical Analysis of Reversible Radioligand Binding from Time - Activity Measurements Applied to [N-11C-Methyl]-(-)-Cocaine PET Studies in Human Subjects". In: *Journal of Cerebral Blood Flow & Metabolism* 10.5, pp. 740–747. ISSN: 0271-678X. DOI: 10.1038/jcbfm.1990.127.

Lowe, V J et al. (2016). "An autoradiographic evaluation of AV-1451 Tau PET in dementia". In: *Acta Neuropathologica Communications* 4.1. DOI: 10.1186/s40478-016-0315-6.

Lye, T C and A E Shores (2000). "Traumatic Brain Injury as a Risk Factor for Alzheimer's Disease: A Review". English. In: *Neuropsychology Review* 10.2, pp. 115–129. ISSN: 1040-7308. DOI: 10.1023/A:1009068804787.

Mahapatra, R K et al. (2004). *Corticobasal degeneration*. DOI: 10.1016/S1474-4422(04)00936-6.

Marquié, M, M D Normandin, A C Meltzer, et al. (2017). "Pathological correlations of [F-18]-AV-1451 imaging in non-alzheimer tauopathies". In: *Annals of Neurology* 81.1, pp. 117–128. DOI: 10.1002/ana.24844.

Marquié, M, M D Normandin, C R Vanderburg, et al. (2015). "Validating novel tau positron emission tomography tracer [F-18]-AV-1451 (T807) on postmortem brain tissue". In: *Annals of Neurology* 78.5, pp. 787–800. DOI: 10.1002/ana.24517.

Masters, C L et al. (2015). "Alzheimer's disease". In: *Nature Reviews Disease Primers* 1. DOI: 10.1038/nrdp.2015.56.

McKee, A C, R C Cantu, et al. (2009). "Chronic traumatic encephalopathy in athletes: Progressive tauopathy after repetitive head injury". In: *Journal of Neuropathology and Experimental Neurology* 68.7, pp. 709–735. DOI: 10.1097/NEN.0b013e3181a9d503.

Mckee, A C and D H Daneshvar (2015). "The neuropathology of traumatic brain injury". In: *Handbook of Clinical Neurology* 127, pp. 45–66. ISSN: 22124152. DOI: 10.1016/B978-0-444-52892-6.00004-0. arXiv: 15334406.

McKee, A C, T D Stein, et al. (2013). "The spectrum of disease in chronic traumatic encephalopathy". In: *Brain* 136.1, pp. 43–64. ISSN: 14602156. DOI: 10.1093/brain/aws307.

Medicine, Institute of (2009). *Gulf War and Health: Volume 7: Long-Term Consequences of Traumatic Brain Injury*. English. Washington, DC: The National Academies Press. ISBN: 978-0-309-12408-9. DOI: 10.17226/12436.

Menon, D K et al. (2010). "Position statement: Definition of traumatic brain injury". In: *Archives of Physical Medicine and Rehabilitation* 91.11, pp. 1637–1640. DOI: 10.1016/j.apmr.2010.05.017.

Mez, J et al. (2017). "Clinicopathological Evaluation of Chronic Traumatic Encephalopathy in Players of American Football". In: *JAMA* 318.4, pp. 360–370. ISSN: 0098-7484. DOI: 10.1001/JAMA.2017.8334.

Mintun, M A et al. (1984). "A quantitative model for the in vivo assessment of drug binding sites with positron emission tomography". In: *Annals of Neurology* 15.3, pp. 217–227. ISSN: 1531-8249. DOI: 10.1002/ana.410150302.

Mitsis, E M et al. (2014). "Tauopathy PET and amyloid PET in the diagnosis of chronic traumatic encephalopathies: Studies of a retired NFL player and of a man with FTD and a severe head injury". In: *Translational Psychiatry* 4.9. DOI: 10.1038/tp.2014.91.

Möllenhoff, K, A-M Oros-Peusquens, and J N Shah (2012). "Introduction to the Basics of Magnetic Resonance Imaging BT - Molecular Imaging in the Clinical Neurosciences". In: ed. by Gerhard Gründer. Totowa, NJ: Humana Press, pp. 75–98. ISBN: 978-1-61779-989-1. DOI: 10.1007/7657_2012_56.

Mori, S, B J Crain, et al. (1999). "Three-dimensional tracking of axonal projections in the brain by magnetic resonance imaging." In: *Annals of neurology* 45.2, pp. 265–9. ISSN: 0364-5134. DOI: 10.1002/1531-8249(199902)45:2<265::AID-ANA21>3.0.CO;2-3.

Mori, S and J Zhang (2006). "Principles of Diffusion Tensor Imaging and Its Applications to Basic Neuroscience Research". In: *Neuron* 51.5, pp. 527–539. ISSN: 0896-6273. DOI: https://doi.org/10.1016/j.neuron.2006.08.012.

Mori, S and P C M van Zijl (2002). "Fiber tracking: principles and strategies – a technical review". In: *NMR in Biomedicine* 15.7-8, pp. 468–480. ISSN: 1099-1492. DOI: 10.1002/nbm.781.

Mueller, S G et al. (2005). "Ways toward an early diagnosis in Alzheimer's disease: The Alzheimer's Disease Neuroimaging Initiative (ADNI)". In: *Alzheimer's & Dementia* 1.1, pp. 55–66. ISSN: 1552-5260. DOI: http://dx.doi.org/10.1016/j.jalz.2005.06.003.

Murray, M E et al. (2011). "Neuropathologically defined subtypes of Alzheimer's disease with distinct clinical characteristics: a retrospective study". In: *The Lancet Neurology* 10.9, pp. 785–796. ISSN: 1474-4422. DOI: https://doi.org/10.1016/S1474-4422(11)70156-9.

Nasrallah, I and J Dubroff (2013). *An overview of PET neuroimaging*. DOI: 10.1053/j.semnuclmed.2013.06.003.

Nath, S et al. (2012). "Spreading of Neurodegenerative Pathology via Neuron-to-Neuron Transmission of β-Amyloid". In: *The Journal of Neuroscience* 32.26, pp. 8767–8777. DOI: 10.1523/JNEUROSCI.0615-12.2012.

Neath, A A and J E Cavanaugh (2012). "The Bayesian information criterion: background, derivation, and applications". In: *Wiley Interdisciplinary Reviews: Computational Statistics* 4.2, pp. 199–203. ISSN: 1939-0068. DOI: 10.1002/wics.199.

Nelson, P T et al. (2012). "Correlation of Alzheimer Disease Neuropathologic Changes With Cognitive Status: A Review of the Literature". In: *Journal of neuropathology and experimental neurology* 71.5, pp. 362–381. ISSN: 0022-3069. DOI: 10.1097/NEN.0b013e31825018f7.

Newberg, A B et al. (2012). "Initial clinical comparison of 18F-florbetapir and 18F-FDG PET in patients with alzheimer disease and controls". In: *Journal of Nuclear Medicine* 53.6, pp. 902–907. DOI: 10.2967/jnumed.111.099606.

Ng, K P et al. (2017). "Monoamine oxidase B inhibitor, selegiline, reduces 18F-THK5351 uptake in the human brain". In: *Alzheimer's Research and Therapy* 9.1. DOI: 10.1186/s13195-017-0253-y.

Ni, R et al. (2013). "Amyloid tracers detect multiple binding sites in Alzheimer's disease brain tissue". In: *Brain* 136.7, pp. 2217–2227. DOI: 10.1093/brain/awt142.

Nussbaum, J M et al. (2012). "Prion-like behaviour and tau-dependent cytotoxicity of pyroglutamylated amyloid-[bgr]". In: *Nature* 485.7400, pp. 651–655. ISSN: 0028-0836.

O'Donnell, L J and C-F Westin (2011). "An Introduction to Diffusion Tensor Image Analysis". In: *Neurosurgery Clinics of North America* 22.2, pp. 185–196. ISSN: 1042-3680. DOI: https://doi.org/10.1016/j.nec.2010.12.004.

Ogawa, S et al. (1990). "Brain magnetic resonance imaging with contrast dependent on blood oxygenation". In: *Proceedings of the National Academy of Sciences* 87.24, pp. 9868–9872.

Okamura, N, S Furumoto, et al. (2013). "Novel 18F-Labeled Arylquinoline Derivatives for Noninvasive Imaging of Tau Pathology in Alzheimer Disease". In: *Journal of Nuclear Medicine* 54.8, pp. 1420–1427. DOI: 10.2967/jnumed.112.117341.

Okamura, N, R Harada, et al. (2014). "Tau PET imaging in Alzheimer's disease". In: *Current neurology and neuroscience reports* 14.11, p. 500. DOI: 10.1007/s11910-014-0500-6.

Ossenkoppele, R et al. (2016). "Tau PET patterns mirror clinical and neuroanatomical variability in Alzheimer's disease". In: *Brain* 139.5, pp. 1551–1567. DOI: 10.1093/brain/aww027.

Palop, J J, J Chin, and L Mucke (2006). "A network dysfunction perspective on neurodegenerative diseases." In: *Nature* 443.7113, pp. 768–773. ISSN: 0028-0836. DOI: 10.1038/nature05289.

Passamonti, L et al. (2017). "18F-AV-1451 positron emission tomography in Alzheimer's disease and progressive supranuclear palsy". In: *Brain* 140.3, pp. 781–791. ISSN: 0006-8950.

Patlak, CS and R G Blasberg (1985). "Graphical Evaluation of Blood-to-Brain Transfer Constants from Multiple-Time Uptake Data. Generalizations". In: *Journal of Cerebral Blood Flow & Metabolism* 4, pp. 584–590. ISSN: 0271-678X. DOI: 10.1038/jcbfm.1985.87.

Phelps, M E et al. (1979). "Tomographic measurement of local cerebral glucose metabolic rate in humans with (F-18)2-fluoro-2-deoxy-D-glucose: Validation of method". In: *Annals of Neurology* 6.5, pp. 371–388. ISSN: 1531-8249. DOI: 10.1002/ana.410060502.

Pike, V W (2009). "PET radiotracers: crossing the blood-brain barrier and surviving metabolism". In: *Trends Pharmacol Sci* 30.8, pp. 431–440. DOI: 10.1016/j.tips.2009.05.005.

Plassman, B L et al. (2000). "Documented head injury in early adulthood and risk of Alzheimer's disease and other dementias". In: *Neurology* 55.8, pp. 1158–1166. DOI: 10.1212/WNL.55.8.1158.

Plewes, D B and W Kucharczyk (2012). "Physics of MRI: A primer". In: *Journal of Magnetic Resonance Imaging* 35.5, pp. 1038–1054. ISSN: 1522-2586. DOI: 10.1002/jmri.23642.

Pontecorvo, M J et al. (2017). "Relationships between flortaucipir PET tau binding and amyloid burden, clinical diagnosis, age and cognition". In: *Brain* 140.3, pp. 748–763. ISSN: 0006-8950.

Price, J L and J C Morris (1999). "Tangles and plaques in nondemented aging and 'preclinical' alzheimer's disease". In: *Annals of Neurology* 45.3, pp. 358–368. ISSN: 03645134. DOI: 10.1002/1531-8249(199903)45:3<358::AID-ANA12>3.0.CO;2-X.

Prince, M et al. (2013). *The global prevalence of dementia: A systematic review and metaanalysis*. DOI: 10.1016/j.jalz.2012.11.007. arXiv: NIHMS150003.

Prusiner, S B (1984). "Some Speculations about Prions, Amyloid, and Alzheimer's Disease". In: *New England Journal of Medicine* 310.10, pp. 661–663. ISSN: 0028-4793. DOI: 10.1056/NEJM198403083101021.

Raj, A, A Kuceyeski, and M Weiner (2012). "A Network Diffusion Model of Disease Progression in Dementia". In: *Neuron* 73.6, pp. 1204–1215. ISSN: 0896-6273. DOI: http://dx.doi.org/10.1016/j.neuron.2011.12.040.

Rebeiz, J J, E H Kolodny, and E P Richardson (1968). "Corticodentatonigral degeneration with neuronal achromasia." In: *Archives of neurology* 18.1, pp. 20–33. ISSN: 0003-9942. DOI: 10.1001/archneur.1968.00470310034003.

Roozenbeek, B, A I R Maas, and D K Menon (2013). "Changing patterns in the epidemiology of traumatic brain injury". In: *Nat Rev Neurol* 9.4, pp. 231–236. ISSN: 1759-4758.

Rowe, C C et al. (2010). "Amyloid imaging results from the Australian Imaging, Biomarkers and Lifestyle (AIBL) study of aging". In: *Neurobiology of Aging* 31.8, pp. 1275–1283. DOI: 10.1016/j.neurobiolaging.2010.04.007.

Saha, G B (2016). *Basics of PET imaging: Physics, chemistry, and regulations, third edition*, pp. 1–282. ISBN: 9783319164236. DOI: 10.1007/978-3-319-16423-6.

Saidlitz, P et al. (2014). "Amyloid imaging in Alzheimer's disease: A literature review". English. In: *The journal of nutrition, health & aging* 18.7, pp. 723–740. ISSN: 1279-7707. DOI: 10.1007/s12603-014-0507-3.

Salinas, C A, G E Searle, and R N Gunn (2015). "The simplified reference tissue model: model assumption violations and their impact on binding potential". In: *J Cereb Blood Flow Metab* 35.2, pp. 304–311. ISSN: 0271-678X.

Schafer, K N et al. (2012). "Selectivity requirements for diagnostic imaging of neurofibrillary lesions in Alzheimer's disease: a simulation study". In: *Neuroimage* 60.3, pp. 1724–1733. DOI: 10.1016/j.neuroimage.2012.01.066.

Scheltens, P et al. (2016). "Alzheimer's disease". In: *The Lancet* 388.10043, pp. 505–517. ISSN: 0140-6736. DOI: https://doi.org/10.1016/S0140-6736(15)01124-1.

Schild, H (1990). *MRI Made Easy*. Berlin.

Schmitz, R E, A M Alessio, and P E Kinahan (2009). "The Physics of PET/CT scanners". In: *PET and PET/CT: a clinical guide*, pp. 1–14. ISBN: 1588904008.

Schwarz, G (1978). "Estimating the dimension of a model". In: *The Annals of Statistics* 6.2, pp. 461–464. ISSN: 0090-5364. DOI: 10.1214/aos/1176344136.

Selkoe, D J (1991). "The Molecular of Pathology Disease". In: *Neuron* 6, pp. 487–498. ISSN: 08966273. DOI: 10.1016/0896-6273(91)90052-2.

Sevigny, J et al. (2016). "The antibody aducanumab reduces Aβ plaques in Alzheimer's disease". In: *Nature* 537.7618, pp. 50–56. ISSN: 0028-0836. DOI: 10.1038/nature19323.

Sharp, D J, G Scott, and R Leech (2014). "Network dysfunction after traumatic brain injury". In: *Nat Rev Neurol* 10.3, pp. 156–166. ISSN: 1759-4758.

Shively, S et al. (2012). "Dementia resulting from traumatic brain injury: what is the pathology?" In: *Archives of neurology* 69.10, pp. 1245–51. ISSN: 1538-3687. DOI: 10.1001/archneurol.2011.3747. arXiv: NIHMS150003.

Shoghi-Jadid, K et al. (2002). "Localization of neurofibrillary tangles and beta-amyloid plaques in the brains of living patients with alzheimer disease". In: *American Journal of Geriatric Psychiatry* 10.1, pp. 24–35. DOI: 10.1097/00019442-200201000-00004.

Shung, K K, M B Smith, and B M W Tsui (1992). "CHAPTER 4 - Magnetic Resonance Imaging BT - Principles of Medical Imaging". In: San Diego: Academic Press, pp. 213–271. ISBN: 978-0-12-640970-3. DOI: https://doi.org/10.1016/B978-0-12-640970-3.50009-0.

Sluimer, J D, F H Bouwman, et al. (2010). "Whole-brain atrophy rate and CSF biomarker levels in MCI and AD: A longitudinal study". In: *Neurobiology of*

Aging 31.5, pp. 758–764. ISSN: 01974580. DOI: 10.1016/j.neurobiolaging.2008.06.016.

Sluimer, J D, W M Flier, et al. (2009). "Accelerating regional atrophy rates in the progression from normal aging to Alzheimer's disease". In: *European Radiology* 19.12, pp. 2826–2833. ISSN: 1432-1084. DOI: 10.1007/s00330-009-1512-5.

Small, G W et al. (2006). "PET of brain amyloid and tau in mild cognitive impairment". In: *New England Journal of Medicine* 355.25, pp. 2652–2663. DOI: 10.1056/NEJMoa054625.

Small, S A and K Duff (2008). *Linking Aβ and Tau in Late-Onset Alzheimer's Disease: A Dual Pathway Hypothesis*. DOI: 10.1016/j.neuron.2008.11.007.

Smith, D H, V E Johnson, and W Stewart (2013). "Chronic neuropathologies of single and repetitive TBI: substrates of dementia?" In: *Nat Rev Neurol* 9.4, pp. 211–221. ISSN: 1759-4758.

Smith, R, A Puschmann, et al. (2016). "18F-AV-1451 tau PET imaging correlates strongly with tau neuropathology in MAPT mutation carriers". In: *Brain* 139.9, pp. 2372–2379. DOI: 10.1093/brain/aww163.

Smith, R, M Schain, et al. (2017). "Increased basal ganglia binding of 18F-AV-1451 in patients with progressive supranuclear palsy". In: *Movement Disorders* 32.1, pp. 108–114. DOI: 10.1002/mds.26813.

Smith, R, M Schöll, M Honer, et al. (2017). "Tau neuropathology correlates with FDG-PET, but not AV-1451-PET, in progressive supranuclear palsy". In: *Acta Neuropathologica* 133.1, pp. 149–151. DOI: 10.1007/s00401-016-1650-1.

Smith, R, M Schöll, H Widner, et al. (2017). "In vivo retention of 18 F-AV-1451 in corticobasal syndrome". In: *Neurology* 89.8, pp. 845–853. DOI: 10.1212/WNL.0000000000004264.

Sokoloff, L et al. (1977). "The [14 C]Deoxyglucose Method for the Measurement of Local Cerebral Glucose Utilization: Theory, Procedure, and Normal Values in the Conscious and Anesthetized Albino Rat". In: *Journal of Neurochemistry* 28.5, pp. 897–916. ISSN: 0022-3042. DOI: 10.1111/j.1471-4159.1977.tb10649.x.

Spires-Jones, T L and B T Hyman (2014). "The Intersection of Amyloid Beta and Tau at Synapses in Alzheimer's Disease". In: *Neuron* 82.4, pp. 756–771. ISSN: 0896-6273. DOI: https://doi.org/10.1016/j.neuron.2014.05.004.

Stein, T D, V E Alvarez, and A C McKee (2014). "Chronic traumatic encephalopathy: a spectrum of neuropathological changes following repetitive brain trauma in athletes and military personnel". In: *Alzheimer's Research & Therapy* 6.1, p. 4. ISSN: 1758-9193. DOI: 10.1186/alzrt234.

Tagliaferri, F et al. (2006). "A systematic review of brain injury epidemiology in Europe". In: *Acta Neurochirurgica* 148.3, pp. 255–267. DOI: 10.1007/s00701-005-0651-y.

Thal, D R, J Attems, and M Ewers (2014). "Spreading of amyloid, tau, and microvascular pathology in alzheimer's disease: Findings from neuropathological and neuroimaging studies". In: *Journal of Alzheimer's Disease* 42, S421–S429. DOI: 10.3233/JAD-141461.

Thal, D R, U Rüb, et al. (2002). "Phases of Aβ-deposition in the human brain and its relevance for the development of AD". In: *Neurology* 58.12, pp. 1791–1800.

Thompson, P W et al. (2009). "Interaction of the amyloid imaging tracer FDDNP with hallmark Alzheimer's disease pathologies". In: *Journal of Neurochemistry* 109.2, pp. 623–630. DOI: 10.1111/j.1471-4159.2009.05996.x.

Tolboom, N et al. (2009). "Detection of Alzheimer pathology in vivo using both11C-PIB and18F-FDDNP PET". In: *Journal of Nuclear Medicine* 50.2, pp. 191–197. DOI: 10.2967/jnumed.108.056499.

Tong, J et al. (2013). "Distribution of monoamine oxidase proteins in human brain: Implications for brain imaging studies". In: *Journal of Cerebral Blood Flow and Metabolism* 33.6, pp. 863–871. DOI: 10.1038/jcbfm.2013.19.

Tong, S, A M Alessio, and P E Kinahan (2010). "Image reconstruction for PET/CT scanners: past achievements and future challenges". In: *Imaging in medicine* 2.5, pp. 529–545. ISSN: 1755-5191. DOI: 10.2217/iim.10.49.

Tosun, D et al. (2017). "Association between tau deposition and antecedent amyloid-β accumulation rates in normal and early symptomatic individuals". In: *Brain* 140.5, pp. 1499–1512. DOI: 10.1093/brain/awx046.

Tziortzi, A C et al. (2011). "Imaging dopamine receptors in humans with [11C]-(+)-PHNO: Dissection of D3 signal and anatomy". In: *NeuroImage* 54.1, pp. 264–277. ISSN: 1053-8119. DOI: http://dx.doi.org/10.1016/j.neuroimage.2010.06.044.

Vemuri, P and C R Jack (2010). "Role of structural MRI in Alzheimer's disease". In: *Alzheimer's Research & Therapy* 2.4, p. 23. ISSN: 1758-9193. DOI: 10.1186/alzrt47.

Vemuri, P, V J Lowe, et al. (2017). "Tau-PET uptake: Regional variation in average SUVR and impact of amyloid deposition". In: *Alzheimer's & Dementia: Diagnosis, Assessment & Disease Monitoring* 6, pp. 21–30. ISSN: 2352-8729. DOI: 10.1016/j.dadm.2016.12.010.

Verhulst, P-F (1844). *Recherches mathematiques sur la loi d'accroissement de la population [microform] / par P.-F. Verhulst*. Memoires de l'Academie royale des sciences des lettres et des beaux-arts de Belgique ; t. 18. [Belgium.

Vermeiren, C et al. (2017). "T807, a reported selective tau tracer, binds with nanomolar affinity to monoamine oxidase a". In: *Alzheimer's & Dementia: The Journal of the Alzheimer's Association* 11.7, P283. ISSN: 1552-5260. DOI: 10.1016/j.jalz.2015.07.381.

Villemagne, V L, S Furumoto, et al. (2014). "In vivo evaluation of a novel tau imaging tracer for Alzheimer's disease". In: *European Journal of Nuclear Medicine and Molecular Imaging* 41.5, pp. 816–826. DOI: 10.1007/s00259-013-2681-7.

Villemagne, V L and N Okamura (2014). "In vivo tau imaging: obstacles and progress". In: *Alzheimers Dement* 10.3 Suppl, S254–64. DOI: 10.1016/j.jalz.2014.04.013.

Wakabayashi, K and H Takahashi (2004). "Pathological heterogeneity in progressive supranuclear palsy and corticobasal degeneration". In: *Neuropathology*. Vol. 24. 1, pp. 79–86. ISBN: 0919-6544 (Print)0919-6544 (Linking). DOI: 10.1111/j.1440-1789.2003.00543.x.

Winter, Y et al. (2010). "Incidence of Parkinson's disease and atypical parkinsonism: Russian population-based study". In: *Movement Disorders* 25.3, pp. 349–356. ISSN: 1531-8257. DOI: 10.1002/mds.22966.

Wong, D F et al. (2010). "In vivo imaging of amyloid deposition in Alzheimer disease using the radioligand 18F-AV-45 (florbetapir [corrected] F 18)". In: *J Nucl Med* 51.6, pp. 913–920. DOI: 10.2967/jnumed.109.069088.

Wooten, D W et al. (2017). "Pharmacokinetic Evaluation of the Tau PET Radiotracer 18F-T807 (18F-AV-1451) in Human Subjects". In: *Journal of Nuclear Medicine* 58.3, pp. 484–491. DOI: 10.2967/jnumed.115.170910.

Xia, C F et al. (2013). "[(18)F]T807, a novel tau positron emission tomography imaging agent for Alzheimer's disease". In: *Alzheimers Dement* 9.6, pp. 666–676. DOI: 10.1016/j.jalz.2012.11.008.

Yang, L, D Rieves, and C Ganley (2012). "Brain Amyloid Imaging — FDA Approval of Florbetapir F18 Injection". In: *New England Journal of Medicine* 367.10, pp. 885–887. ISSN: 0028-4793. DOI: 10.1056/NEJMp1208061.

Yeh, F-C and W-Y I Tseng (2011). "NTU-90: A high angular resolution brain atlas constructed by q-space diffeomorphic reconstruction". In: *NeuroImage* 58.1, pp. 91–99. ISSN: 1053-8119. DOI: http://dx.doi.org/10.1016/j.neuroimage.2011.06.021.

Zanotti-Fregonara, P et al. (2014). "Imaging of monoamine oxidase-A in the human brain with [11C]befloxatone: quantification strategies and correlation with mRNA transcription maps". In: *Nuclear Medicine Communications* 35.12. ISSN: 0143-3636.